ACTIVE CONTROL OF TURBULENCE-INDUCED HELICOPTER VIBRATION

DAVID ANDERSON

Thesis submitted to the Faculty of Engineering, University of Glasgow, for the Degree of Doctor of Philosophy. All aspects of the work contained herein are original in content except where indicated.

This thesis is based on research conducted between October 1994 and October 1997 at the Department of Aerospace Engineering, University of Glasgow.

David Anderson, March 1999.

Abstract

Helicopter vibration signatures induced by severe atmospheric turbulence have been shown to differ considerably from nominal, still air vibration. The perturbations of the transmission frequency have significant implications for the design of passive and active vibration alleviation devices, which are generally tuned to the nominal vibration frequency. This thesis investigates the existence of the phenomena in several *realistic* atmospheric turbulence environments, generated using Computational Fluid Dynamic (CFD) engineering software and assimilated within a high-fidelity rotorcraft simulation, RASCAL. The RASCAL simulation is modified to calculate blade element sampling of the gust, enabling thorough, high frequency analyses of the rotor response. In a final modification, a numerical, integration-based inverse simulation algorithm, GENISA is incorporated and the augmented simulation is henceforth referred to as HISAT. Several implementation issues arise from the symbiosis, principally because of the modelling of variable rotorspeed and lead-lag motion. However, a novel technique for increasing the numerical stability margins is proposed and tested successfully.

Two active vibration control schemes, higher harmonic control 'HHC' and individual blade control 'IBC', are then evaluated against a 'worst-case' sharp-edged gust field. The higher harmonic controller demonstrates a worrying lack of robustness, and actually begins to contribute to the vibration levels. Several intuitive modifications to the algorithm are proposed but only disturbance estimation is successful. A new simulation model of coupled blade motion is derived and implemented using MATLAB and is used to design a simple IBC compensator. Following bandwidth problems, a redesign is proposed using H_∞ theory which improves the controller performance. Disturbance prediction/estimation is attempted using artificial neural networks to limited success. Overall, the aims and objectives of the research are met.

Acknowledgements

I'd like to express my deepest thanks to Dr Stewart Houston for his exceptional guidance, support and supervision throughout the course of this research and also for his motivation and encouragement in getting me to write this dissertation. I would also like to thank Dr Douglas Thomson for fielding my endless questions on inverse simulation and for having the restraint to not throw me out of his office! Special mention must also go to Dr Steve Rutherford, Dave Ewing and Garry Leacock for participating in those incredibly beneficial brainstorming sessions, even if we did get a little side-tracked at times. Dr Chris O'Neill also deserves many thanks for his Monday morning motivation classes, as do Dr John Maclean and Dr Nick Brignall from Marconi. There are many others within the Aerospace Department and beyond who contributed in helping to make this possible, you know who you are, many thanks.

Many thanks must also go to the Centre for Systems and Control at the University of Glasgow for providing me with the research grant and to DERA Bedford for volunteering additional sponsorship. My gratitude to these two bodies for their financial and intellectual contributions cannot be understated.

I'd like to thank Charles and Rae Anderson, my parents, for their loving support throughout some painful times and for their unending belief that one day this thesis would be submitted, even though at times I doubted their judgement.

Most of all, I'd like to thank my beautiful and beloved wife Theresa, who has stoically supported me throughout my academic career and continues to do so to this day. She has been my rock of faith throughout all of the ups and downs, successes and failures I've experienced with this work. The love and gratitude I feel for her cannot be expressed in mere words, so perhaps dedicating this work to her will in some small way make up for my linguistic inadequacy.

David Anderson - March, 1999.

Contents

ABSTRACT *ii*

ACKNOWLEDGEMENTS *iii*

CONTENTS *iv*

NOMENCLATURE *ix*

CHAPTER I

ACTIVE CONTROL OF TURBULENCE-INDUCED HELICOPTER VIBRATION. 1

1.1 INTRODUCTION. 1

1.2 REVIEW OF VIBRATION ALLEVIATION AND CONTROL LITERATURE 3

1.2.1 The Creation and Transmission of Helicopter Vibration. 4

1.2.2 Passive vibration alleviation. 10

1.2.3 Active vibration control. 13

1.3 AIMS OF THE RESEARCH 16

1.4 THE STRUCTURE OF THIS THESIS 17

1.5 SUMMARY OF CHAPTER I. 20

CHAPTER II

A DESCRIPTION OF THE RASCAL HELICOPTER SIMULATION MODEL. 21

2.1 INTRODUCTION TO RASCAL. 21

2.2 RIGID-BODY DYNAMICS. 23

2.3 ROTOR FORCES AND MOMENTS. 25

2.3.1 Introduction. 25

2.3.2 Blade Element Theory. 26

2.3.3 Blade Element Velocity. 27

2.3.4 Blade Acceleration. 30

2.3.5 Blade Aerodynamics. 31

2.3.6 Total Forces and Moments. 36

2.4 BLADE EQUATIONS OF MOTION. 37

2.4.1 Multiblade Co-ordinate Transformation. 39

2.5 ROTOR WAKE MODEL. 40
2.5.1 Static Inflow Models. 41
2.5.2 Dynamic Inflow models. 42
2.5.2.1 *Perturbation model.* 42
2.5.2.2 *Peters HaQuang model.* 44
2.6 FUSELAGE AERODYNAMICS. 45
2.6.1 Polynomial expansion. 45
2.6.1.1 *Absolute forces and moments.* 45
2.6.1.2 *Aerodynamic coefficient expansion.* 46
2.6.2 Tabular approach. 47
2.6.2.1 *Forces and moments.* 47
2.6.2.2 *Coefficient abstraction.* 48
2.7 FIN AERODYNAMICS 48
2.8 TAILPLANE AERODYNAMICS 49
2.9 ENGINE AND TRANSMISSION MODEL 50
2.10 ATMOSPHERE MODEL. 51
2.11 CHAPTER SUMMARY AND DISCUSSION. 53

CHAPTER III

INTEGRATION OF A GUST MODULE WITHIN RASCAL. 54

3.1 WHAT IS ATMOSPHERIC TURBULENCE? 54
3.2 TRANSFORMATION OF THE GUST VELOCITIES TO BLADE AXES. 57
3.2.1 Blade element position. 57
3.2.2 Gust velocity in blade axes. 60
3.2.3 Non-rotating components. 61
3.3 THE RESPONSE OF A SINGLE MAIN AND TAILROTOR HELICOPTER TO A SHARP-EDGED GUST. 62
3.4 ANALYSIS OF THE GUST VIBRATION SIGNATURE. 63
3.4.1 Time Domain Calculation of the Phase Shift. 64
3.5 CHAPTER SUMMARY AND DISCUSSION. 67

CHAPTER IV

THE DEVELOPMENT OF ADVANCED TURBULENT ENVIRONMENTS. 68

4.1 ATMOSPHERIC TURBULENCE MODELLING. 68
4.2 TECHNIQUES AND LIMITATIONS OF EXISTING TURBULENCE MODELS. 69
4.2.1 Modelling the Atmosphere Using Discrete gusts. 69
4.2.2 Continuous turbulence models - PSD methods. 71
4.2.3 Statistical Discrete Gust (SDG) Method. 74

4.2.4 Limitations of Statistical Turbulence models. 76
4.3 GENERATING A TURBULENT ENVIRONMENT USING CFD. 77
4.3.1 Merging with a Rotorcraft Simulation. 77
4.3.2 Bilinear Interpolation. 78
4.4 EXAMPLES OF CFD GENERATED OBSTRUCTION-INDUCED TURBULENCE. 79
4.4.1 Flow around a tower block. 80
4.4.2 Flow over a cliff. 80
4.4.3 Flow across a valley. 81
4.4.4 Flow around an offshore oil platform. 81
4.5 ANALYSIS OF THE RESPONSE TO LONGITUDINAL AND LATERAL/DIRECTIONAL TURBULENCE. 82
4.5.1 Uncontrolled flight past a tower block 82
4.5.2 Uncontrolled flight over a cliff top. 83
4.6 CHAPTER SUMMARY AND DISCUSSION. 85

CHAPTER V

THE INVERSE SIMULATION OF RASCAL **86**

5.1 CONTINUING DEVELOPMENT OF HISAT. 86
5.1.1 Advantages of Inverse Simulation. 87
5.1.2 Methods of Inverse Simulation. 88
5.1.3 Inverse Simulation by Differentiation. 90
5.1.4 Inverse Simulation in the Forward Sense using Integration. 91
5.2 DESCRIPTION OF THE GENISA ALGORITHM. 92
5.2.1 Estimation of the System Jacobian. 95
5.3 POLYNOMIAL METHOD OF FLIGHT PATH GENERATION. 96
5.3.1 Boundary Value Polynomials. 96
5.4 SIMPLE EXAMPLE – MAINTAINING TRIM. 97
5.4.1 Analysis of Simulation Time Histories. 98
5.4.2 The importance of the control application interval to stability. 99
5.4.3 Other numerical sensitivities. 100
5.5 ENHANCEMENT OF THE NEWTON STEP. 100
5.5.1 Enhancement of the Newton Step Using the Bisection Algorithm. 101
5.5.2 Applying the Modified Newton Step Technique to Preserving Trim. 102
5.5.3 Tracking Flight Path Accelerations. 103
5.6 CONSTRAINT OSCILLATIONS. 103
5.7 HELICOPTER INVERSE SIMULATION THROUGH ATMOSPHERIC TURBULENCE - HISAT. 106
5.7.1 Precision Flare-to-Hover Manoeuvre. 106
5.8 CHAPTER SUMMARY. 109

CHAPTER VI

STRATEGIES FOR IMPLEMENTING ACTIVE VIBRATION CONTROL. 110

6.1 ACTIVE VIBRATION CONTROL TECHNIQUES. 110

6.2 HIGHER HARMONIC CONTROL. 111

6.3 HARMONIC ANALYSIS OF VIBRATION DATA. 113

6.3.1 Fourier Analysis. 113

6.3.2 Trapezoidal Approximation to the Fourier Integral. 115

6.3.3 High pass filter algorithm. 116

6.4 THE DESIGN OF AN OPTIMAL MULTICYCLIC CONTROLLER. 117

6.4.1 Optimal control methods. 118

6.4.2 Calculation of the Sensitivity Matrix. 119

6.5 PERFORMANCE OF THE HHC ALGORITHM. 120

6.5.1 Baseline Performance of the Variational HHC Algorithm. 120

6.5.2 Attenuation of Step-Gust-Induced Vibration. 121

6.5.3 Stochastic Model (Kalman Filter Implementation). 122

6.5.3 Multi-Harmonic control. 123

6.6 DISTURBANCE FEED-FORWARD HIGHER HARMONIC CONTROL. 125

6.6.1 Description of the Controller. 125

6.6.2 Performance of the Controller. 126

6.7 INDIVIDUAL BLADE CONTROL. 127

6.7.1 Defining the IBC Strategy. 127

6.8 DERIVATION OF THE BLADE EQUATIONS OF MOTION. 128

6.8.1 Inertial Terms. 128

6.8.2 Aerodynamic Terms. 131

6.8.3 SIMULINK Model of Coupled Flap-Lag Motion. 132

6.9 IBC CONTROLLER DESIGN FOR DISTURBANCE REJECTION. 133

6.10 CONTROLLER ASSESSMENT UNDER OPERATIONAL CONDITIONS. 135

6.11 CHAPTER SUMMARY. 137

CHAPTER VII

ACTIVE VIBRATION CONTROL LAW DESIGN USING ADVANCED CONTROL TECHNIQUES. 138

7.1 REVIEW OF HHC & IBC CONTROLLERS. 138

7.2 MODERN OPTIMAL CONTROL LAW DESIGN TECHNIQUES. 139

7.2.1 State-Space Optimal Control Methods. 139

7.2.2 H_∞ Synthesis. 141

7.3 INDIVIDUAL BLADE CONTROL VIA MIXED-SENSITIVITY H_∞ SYNTHESIS. 142

7.3.1 Closed-Loop Performance Parameters. 142

7.3.2 *H_∞ norm.* 143
7.3.3 *Weighting functions and the Mixed Sensitivity Algorithm.* 144
7.3.4 *Plant Augmentation and the H_∞ Small Gain Problem.* 145
7.3.5 *γ – iteration.* 146
7.4 INDIVIDUAL BLADE CONTROL VIA MIXED-SENSITIVITY H_∞ SYNTHESIS. 147
7.4.1 *Design 1: Sensitivity-Only Weighting.* 147
7.4.2 *Design 2: Sensitivity and Complementary Sensitivity Weighting.* 148
7.5 DHHC DISTURBANCE ESTIMATION: - NEURAL NETWORKS. 150
7.5.1 *What are Neural Networks?* 150
7.5.2 *Neuron Models.* 151
7.5.3 *Training the Network – The Backpropogation Algorithm.* 152
7.5.4 *Improving Convergence by Adding a Momentum Term.* 153
7.6 DESIGN AND TRAINING OF A NEURAL NETWORK FOR GUST PARAMETER PREDICTION. 154
7.6.1 *Network Architecture.* 154
7.6.2 *Network Performance.* 154
7.7 CHAPTER SUMMARY. 157

CHAPTER VIII.
CONCLUSIONS AND RECOMMENDATIONS FOR FUTURE WORK. 158
8.1 REVIEW OF THE RESEARCH AIMS. 158
8.2 DEVELOPMENT OF HISAT. 159
8.3 ACTIVE VIBRATION CONTROL. 161
8.4 RECOMMENDATIONS FOR FUTURE WORK. 163

APPENDIX I 164-167
APPENDIX II 168-171
APPENDIX III 172
APPENDIX IV 173-174

FIGURES & TABLES 175-261

REFERENCES 262-271

Nomenclature

Notes :

i. Where a vector has both subscript and superscript, the subscript denotes the location and the superscript the axis set.

ii. Unless explicitly stated, all quantities are given in standard SI units.

iii. In the event of duplication, the meaning of the symbol will be apparent from the context of the text.

iv. subscripts *i,j* combined denote the i^{th} row and j^{th} column of the attached matrix

General

$\underline{a}$	descriptive translational acceleration vector
$\underline{a}_{hg}^{bl}$	translational acceleration of the hinge in blade axes
$\underline{a}_{elem}^{bl}$	translational acceleration of a blade element in blade axes
A_n,A	Fourier coefficient of general blade loading, disc area
A,A_c	system state matrix, constraint oscillation equation state matrix
a	intermittency parameter for the SDG model, local speed of sound
a_0	lift curve slope
b	intensity parameter for the SDG model.
$b_{e,rl}$	distance from the hub to a nominal blade element on blade 1.
c	blade element chord length
C	Fourier cosine integral
C_l, C_d	blade element lift and drag coefficients
C_T,C_L,C_M	non-dimensionalised thrust, rolling and pitching moment coefficients
dp	dynamic pressure
$\underline{d}(t_{k+1})$	vector of harmonic coefficients of the disturbance over the next rotor turn
e, eR	fractional hinge offset, blade root cut-out
E[..]	expectation operator
$\underline{e}(t_k)$	tracking error vector at time t_k
F, $F_{/rev}$	total hub shear force from all N blades, frequency (/rev)
$\underline{F}_{ext}$	vector of all external forces in body axes

$\underline{F}_{elem}^{aero}, \underline{F}_{elem}^{inertial}$	aerodynamic and inertial forces acting on a blade element
g ,$\boldsymbol{g}()$	acceleration due to gravity, nonlinear mapping function
$G(s)$, $G_d(s)$	generalised plant and disturbance transfer functions
$\underline{\boldsymbol{H}}$, $\underline{\dot{\boldsymbol{H}}}$	angular momentum and rate of change of angular momentum
H_g, H_{sdg}	gust gradient length, SDG gust gradient
h_{dist}	non-dimensionalised rotor-to-ground distance
I	Inertia tensor
I_{xx}, I_{yy}, I_{zz}	moments of inertia
I_{xz}	
I_β	blade flap moment of inertia
$\boldsymbol{J}$	system Jacobian, Quadratic cost function
k_{ground}	ground effect factor
k_e	engine droop gain
K_P, K_I, K_D	PID compensator proportional, integral and derivative gains
$\boldsymbol{L}(s)$	open-loop gain
L, LR	turbulence length scale, lapse rate
$\boldsymbol{L,M,N}$	aerodynamic moments about the body axes
$L(\psi)$	blade loading
L_a, M_a	aerodynamic rolling and pitching moments
$\boldsymbol{L}_{aero.}$ $\boldsymbol{N}_{aero}$	roll and yaw aerodynamic moments of the blade about the hinge
[**L**],[**M**]	dynamic inflow gain and apparent mass matrices
M, m	Mach number, aircraft mass
M	Euler transformation matrix
M_θ	blade aerodynamic moment due to pitch angle
$M_{\theta tw}$	blade aerodynamic moment due to blade washout
$M_{\dot{\beta}}$	blade aerodynamic moment due to blade flapping rate
M_{vi}	blade aerodynamic moment due to inflow
N, n	number of blades, summation index
$N_{H,uk}$	average rate of occurrence of gusts
p,q,r	body axes angular rates about the a/c centre of gravity
$\dot{p}, \dot{q}, \dot{r}$	body axes angular accelerations about the a/c centre of gravity
Δp	pressure difference between the upper and lower surfaces of an airfoil
$p(y)$	probability of quantity 'y'
q_d	demanded engine torque
$R(..)$	correlation matrix
R	rotor radius, gas constant
Δr	length of a blade element
$\underline{\boldsymbol{r}}_{hub/cg}$	position vector of the rotor hub with respect to the cg

$\underline{r}_{hg\,/\,hub}$	position vector of the blade hinge with respect to the rotor hub
$\underline{r}_{elem\,/\,hg}$	position vector of a blade element with respect to the blade hinge
s	Laplace variable
S	blade element area, Fourier sine integral
$\boldsymbol{S}$, $\boldsymbol{S}(s)$	variational sensitivity matrix, closed loop sensitivity function
T, T_{mom}	period for one main rotor revolution, temperature, rotor thrust
$\underline{T}_{ext}$	vector of external torques
$\boldsymbol{T}$, $\boldsymbol{T}(s)$	rotor system harmonic jacobian, complementary sensitivity function
T_1, T_2, T_3	direction cosine transformation matrices into hub, hinge and blade axes respectively.
$\underline{u}\ (x)$	gust velocity as a function of longitudinal distance
$\underline{u}$	vector of body axes translational velocities, vector of control inputs
$\underline{u}_B$, $\underline{u}_E$	velocity vectors in body and earth axes respectively
u, v, w	translational velocities (body axes)
$\dot{\underline{u}}$	vector of body axes translational accelerations
$\dot{u}$, $\dot{v}$, $\dot{w}$	centre of gravity accelerations in body axes
$\underline{u}_{hub}^{body}$	translational velocity of the hub in body axes
$\underline{u}_{hub}^{hub}$	translational velocity of the hub in hub axes
$\underline{u}_{hub}^{hg}$	translational velocity of the hub in hinge axes
$\underline{u}_{hg}^{hg}$	translational velocity of the hinge in hinge axes
$\underline{u}_{hg}^{bl}$	translational velocity of the hinge in blade axes
$\underline{u}_{elem}^{bl}$	translational velocity of a blade element in blade axes
$\underline{u}_{g}^{a/c}$	gust vector in body axes
u_g, v_g, w_g	Gust velocities in inertial frame
u_g^{table} , v_g^{table}	gust velocity field table entries
u_k	self similar gust family
u_p	perpendicular component of blade velocity
u_t	tangential component of blade velocity
V_f	aircraft velocity
V_{mw}	mean wind speed
$V_{hub,p}$	velocity of the hub at point p
v_{i0}, v_{1c}, v_{1s}	uniform, longitudinal and lateral inflow coefficients
$\underline{w}(t_k)$	vector of exogenous disturbances
$\boldsymbol{W}$	higher harmonic control weighting matrix
$\boldsymbol{W}_S, \boldsymbol{W}_R, \boldsymbol{W}_T$	sensitivity, control sensitivity and complementary sensitivity weighting functions
w	neural weighting

x	longitudinal distance moved in inertial frame
$x_{g,1}$	x-distance from blade 1 to gust front
$x(t)$	arbitrary time domain signal
$X()$	Fourier transform of ()
$\underline{\boldsymbol{x}}(t_k)$	system state vector at time t_k
$\underline{\boldsymbol{x}}_{hg}^{bl}$	position of the hinge wrt blade element in blade axes
$\underline{\boldsymbol{x}}_{hg}^{hg}$	position of the hinge wrt blade element in hinge axes
$\underline{\boldsymbol{x}}_{hub}^{hg}$	position of the hub wrt blade element in hinge axes
$\underline{\boldsymbol{x}}_{hub}^{hub}$	position of the hub wrt blade element in hub axes
$\underline{\boldsymbol{x}}_{hub}^{a/c}$	position of the hub wrt blade element in body axes
$\underline{\boldsymbol{x}}_{cg}^{a/c}$	position of the cg wrt blade element in body axes
$\underline{\boldsymbol{x}}_{hub}$	hub location wrt a/c co-ordinate system
$\underline{\boldsymbol{x}}_{cg}$	cg location wrt a/c co-ordinate system
$\underline{\boldsymbol{x}}_{E}$	position of the a/c in earth axes wrt earth-fixed datum
$\underline{\boldsymbol{x}}_{bl}^{a/c}$	position of the blade element wrt cg in body axes
$\underline{\boldsymbol{x}}_{bl}^{E}$	position of the blade element wrt earth origin in earth axes
$\underline{\boldsymbol{x}}_{g}^{E}$	gust front location in earth axes
$\underline{\boldsymbol{x}}_{tp}^{E}$	tailplane location in earth axes
$\underline{\boldsymbol{x}}_{fin}^{E}$	fin location in earth axes
$\underline{\boldsymbol{y}}(t_k)$	system output at time t_k
$\underline{\boldsymbol{y}}_{des}(t_k)$	desired system output at time t_k
$\underline{\boldsymbol{Z}}(t_{k+1})$	vector of vibration harmonic coefficients over the next rotor turn

Greek symbols

$\underline{\boldsymbol{\alpha}}_{hub}^{hub}$	angular acceleration vector of the hub in hub axes
$\underline{\boldsymbol{\alpha}}_{hub}^{hg}$	angular acceleration vector of the hub in hinge axes
$\underline{\boldsymbol{\alpha}}_{hg}^{hg}$	angular acceleration vector of the hinge in hinge axes
$\underline{\boldsymbol{\alpha}}_{hg}^{bl}$	angular acceleration vector of the hinge in blade axes
α	angle of attack
$\beta, \dot{\beta}$	rotor blade flap angle (or sideslip angle) and rate
$\ddot{\beta}$	flap angle acceleration

$\beta_0, \beta_{1c}, \beta_{1s}$	multiblade co-ordinate coning, longitudinal and lateral flap angles
δ_3	pitch-flap coupling term
$\delta_{n,mN}$	Kroneker delta.
ϕ, θ, ψ	Euler attitude angles of the aircraft
$\dot{\phi}, \dot{\theta}, \dot{\psi}$	Euler angle rates in body axes
$\Phi(\omega)$	von Karman and Dryden PSD shapes
γ	polytropic index, flight path angle
γ_i	output of the i^{th} iteration of the bisection routine
Γ_i	harmonic analysis and control selection for the i^{th} harmonic
η	learning rate parameter
$\varphi(v)$	activation function
$\lambda_0, \lambda_{1c}, \lambda_{1s}$	non-dimensionalised dynamic inflow coefficients
$\theta_0, \theta_{1s}, \theta_{1c}$	collective, longitudinal and lateral pitch angles
θ_{tr}	tailrotor collective pitch angle
θ_s, ϕ_s	longitudinal and lateral shaft tilt angles
$\underline{\theta}_{HHC}$, $\underline{\theta}(t_k)$	general higher Harmonic control vector, for the k^{th} rotor turn.
$\Delta\underline{\theta}(t_k)$	change in higher harmonic control inputs
$\Delta\underline{\theta}^*(t_k)$	optimal change in higher harmonic control inputs
θ_{nc}, θ_{ns}	the 'n'th order cosine and sine Fourier coefficients of the HHC vector.
ρ	air density
σ_w, σ_{sdg}	gust intensity, SDG gust intensity
τ_{1c}, τ_{1s}	dynamic inflow acceleration lags
$\underline{\omega}$	body axes angular rate vector.
$\underline{\omega}_{hub}$	angular rate vector of the hub in hub axes.
$\underline{\omega}_{hub}^{hg}$	angular rate vector of the hub in hinge axes
$\underline{\omega}_{hg}^{bl}$	angular rate vector of the hinge in blade axes
Ω	rotorspeed, spatial frequency
$\psi_k, \Delta\psi$	azimuth angle of the kth blade, non-dimensional vibration phase shift
$\zeta, \dot{\zeta}$	rotor blade lag angle and rate
$\ddot{\zeta}$	flap angle acceleration
$\zeta_0, \zeta_{1c}, \zeta_{1s}$	multiblade co-ordinate constant, longitudinal and lateral lag angles

Abbreviations

ACF	Actively Controlled trailing edge flap

ACSR	Active Control of Structural Response
ANN (NN)	Artificial Neural Networks
BVI	Blade Vortex Interaction
CFD	Computational Fluid Dynamics
DAVI	Dynamic Antiresonant Vibration Isolator
DHHC	Disturbance feedforward Higher Harmonic Control
FLUENT	Commercial Computational Fluid Dynamics package
GENISA	GENeric Inverse Simulation Algorithm
Helinv	Helicopter inverse simulation algorithm
HISAT	Helicopter Inverse Simulation through Atmospheric Turbulence
HHC	Higher Harmonic Control
HGS	Helicopter Generic Simulation
H_∞	Control design technique based on minimising the H_∞ norm of the closed-loop transfer functions
IBC	Individual Blade Control
LQR	Linear Quadratic Regulator
LQG/LTR	Linear Quadratic Guassian with Loop Transfer Recovery
MATLAB	commercial engineering design package
PID	Proportional-Integral-Derivative control.
PSD	Power Spectral Density
RASCAL	Rotorcraft Aeromechanic Simulation for Control AnaLysis
RQM	Ride Quality Meter
SDG	Statistical Discrete Gust
SIMULINK	Dynamic system simulation package for MATLAB
OAT	Outside Air Temperature

"Those who are enamoured of practice without science are like a pilot who goes into a ship without rudder or compass and never has any certainty where he is going. Practice should always be based upon a sound knowledge of theory".

Leonardo da Vinci

"Lasciate ogni speranza voi ch'entrate"

(All hope abandon, ye who enter here)

Dante Alighieri

CHAPTER I

Active Control of Turbulence-Induced Helicopter Vibration.

1.1 Introduction.

Central to every rotorcraft design, from the simple autogyro to the most sophisticated military or civilian helicopters, is the successful alleviation or control of fuselage vibration induced by the main rotor. Rotorcraft, and helicopters in particular, are not unique in this regard, the minimisation of vibration is a principal design aim for every complex mechanical system with rotating sub-systems. Vibration isolation is especially important for an airborne vehicle, where the safety of passengers and crew should have paramount importance over any commercial or economic factors. If left unchecked, excessive vibration levels will almost certainly contribute to the fatigue and eventual failure of fuselage integrity, which can have catastrophic results. The operability of the onboard sensors will also be impaired through the generation of additional noise, although this problem can be reduced by robust design of the electronics. However, the service life of the aircraft and instrumentation will unquestionably be reduced, requiring significant maintenance and consequently loss of revenue for the operators. That said, general airframe and systems fatigue are not the only undesirable consequences of vibration. The ride quality experienced by the passengers is another metric which directly influences the economic viability of the aircraft.

Helicopters have always suffered when compared to fixed wing aircraft when assessed in terms of the ride quality offered to passengers. Coupled with higher operating costs, this has led to the helicopter occupying a disproportionately small share of the commercial passenger transportation market. In today's expanding business marketplace, with aircraft operator costs benefiting greatly from economies of scale, many more passengers now choose to travel by air rather than the more conventional road and rail networks. This has seen an increased demand for comfortable, reliable and expedient air travel over short distances, a market ideally suited to the helicopter. To compete in this market, passenger comfort has to be improved to a level comparable to the helicopter's fixed-wing counterparts. Ride quality is a subjective and cumulative measure of all facets of passenger comfort, principally noise and vibration levels. Several empirical and subjective vibration discomfort indices exist (*Bramwell, 1976; Gabel, Henderson & Reid, 1971; Griffin, 1977*), however the current standard is set by NASA (*Bradley et.al., 1994*). NASA's metric is known as a collective Ride Quality Meter (RQM), which is essentially an input weighting algorithm that measures the total discomfort experienced by passengers and crew. The fuselage vibration is measured along the longitudinal, lateral and vertical axes as well as in roll and pitch. The RQM combines these signals into a single vibration discomfort index. The noise levels within the cabin and passenger areas are digitally sampled across six octave bands, then passed through the RQM to yield a single noise index. This is added to the vibration index to give the total passenger discomfort level for the aircraft and operating environment. This approach does have one rather serious flaw however. It is necessary to construct a mock-up of the aircraft interior, which naturally can only be accomplished when the design has been completed. If several modifications to the design are necessary, this could prove to be a costly exercise, one that could benefit greatly from accurate computer simulation.

Another design objective, that of precise weapons deployment, exists in the design of helicopters targeted for military applications. Nap-of-the-earth flight and the use of natural terrain for stealth are integral facets of modern helicopter battlefield tactics. Such manoeuvres invariably lead to flight through turbulent airflow, which in turn increases the level of rotor vibration and noise. In addition, the manoeuvrability inherent in modern helicopters means they can be flown through very aggressive manoeuvres, which will lead to a substantially higher disc loading during segments of

the flight. Vibration levels are related to an augmented form of the disc loading (*Bramwell, 1976*) defined as the ratio of vibrating force to the weight of the aircraft. An aircraft fully laden with external stores and weaponry will consequently be more susceptible to large hub vibration loads. Moreover, the current military ethos for battlefield tactics is tending towards long range stand-off engagement as the preferred mode of attack. This has in turn lead to increasingly stringent requirements on the pointing and tracking accuracy of the onboard weapons aiming avionics systems, requirements which are difficult to achieve with excessive vibration levels. Ultimately, helicopter vibration degrades the performance of weapons systems leading to imprecise deployment of munitions and so increasing the probability of inflicting civilian casualties.

It is obvious from the consequences of excessive vibration discussed here that vibration control is an important design parameter for all types of rotorcraft. It is hoped the work presented in this thesis will contribute to the greater understanding of helicopter vibration transmission in typical operating environments and will suggest novel means for actively controlling this response. We begin by conducting a thorough review of the published literature pertaining to helicopter vibration, detailing the source, the transmission and the control thereof.

1.2 Review of Vibration Alleviation and Control Literature

To fully understand what is truly 'state-of-the-art' for vibration minimisation devices, both active and passive, it is essential to understand and appreciate the research into vibration minimisation that has been accomplished to date. A thorough review of the available literature has shown that there are two intertwined avenues of research to the study of helicopter vibration, the cause and the control. Consequently this section will present, where possible, a chronological review of published work first on the causes and then on the control of vibration and will thus 'set the scene' for the remainder of the thesis. Throughout this discussion, where appropriate, detailed explanations of concepts or devices will be given.

This literature review was conducted in the conventional manner, by searching through references contained within several key vibration review papers and also by using a computer search on library and internet based databases. Methodical repetition of this process has yielded a substantial reference base, encompassing many facets of the vibration literature.

1.2.1 The Creation and Transmission of Helicopter Vibration.

The end of the 1940's saw the eventual decline of the autogyro and the emergence of the helicopter as the preferred vehicle for rotary wing flight. The autogyro still had some use as the platform for the first flight-test experiments on rotary wing vibration (*Bailey, 1940*). Theoretical investigations also began around this time (*Wheatley, 1937*) into the higher harmonic dynamics of blade flapping, although an accurate understanding of the aerodynamic forces responsible for harmonic blade loading had still to be attained. Glauert (*1926*), among others, was laying the foundations of modern rotor inflow theory by a combination of theoretical and experimental analysis. Indeed the inflow model he developed is still used in many rotorcraft simulation models today [HGS, Helinv, etc.].

The next significant step in the understanding of blade loading came in 1958 when Jones (*1960*), (see also *Ham, Maser & Zvara, 1958* and *Loewy, 1955*), found that the maximum blade bending stresses occurred when the natural frequency (which varies with rotorspeed) of one or more of the blade modal responses matched an integer multiple of rotorspeed. In addition, the maximum amplitude of these vibrations occurred in the transition region of the speed range, not, as expected, at high speed where the higher harmonic components of lift reach a maximum. Most unexpectedly though, the rotor experiences vibratory blade loads in hover, where no asymmetry of dynamic pressure and hence periodic aerodynamic forcing, exists. These phenomena could not be predicted by the blade aerodynamic theory available at the time. Seeking an alternative explanation, Jones looked to the rotor wake.

The wake produced by a helicopter rotor forms a skewed helix beneath the rotor and, as the mean velocity of the axial flow through the disc is significantly less than the

tip speed, the wake remains close to the rotor disc. Jones studied the effect of the wake generated by an oscillating blade (*Jones, 1958*) on the blade aerodynamic and inertial loading. Each blade is disturbed by the vortices shed in previous revolutions and Jones postulated that if these disturbances were additive, they would tend to sustain the vibration and would be maximum if the vorticity below the blade is the same after each revolution. Jones tested his theory with experiments on a single rotating blade in a controlled wind tunnel, obtaining good correlation of theoretical predictions with experimental results. The main conclusion drawn from this work is that at low speed, the rotor wake is responsible for vibratory blade loading which occurs at a frequency which is an integer multiple of rotorspeed.

Lynn at the Bell helicopter company (*Lynn, 1960*), documented a series of experiments using the Bell stabilising bar modified for use as an in-plane vibration absorber. A hinged version of the stabilising bar successfully attenuated the one-per-rev in-plane stresses by dynamic absorption of the rotor loads. In the fixed frame, the 2/rev vibratory excitation was also alleviated and noting this, Lynn constructed a simple set of equations, which he used to measure the effectiveness of the rotating dynamic absorber by measuring fixed frame vibration.

These equations were in essence the now familiar individual to multiblade co-ordinate transformations. Coupled with the nature of blade aerodynamic loading discovered by Jones (*1960*), a simple mathematical proof can be derived for predicting the frequency at which rotor vibration is transmitted to the fixed frame (through the swashplate) and subsequently into the fuselage. It is the authors intent to present such a proof, as the result has formed the backbone of helicopter vibration research to the present day.

Vibration is defined (*Collins dictionary, 1995*) as "*a periodic motion about an equilibrium position*". To adequately characterise a periodic signal, the amplitude and frequency of the oscillation are necessary. For a helicopter rotor, the amplitude of the oscillation is a complex function of the aerodynamic and inertial loads acting on each rotor blade. As a result, a simple mathematical model for predicting the amplitude of vibration is not possible. However, the fundamental frequency of the transmitted vibration (under normal atmospheric conditions) can be predicted. The loads

experienced by each blade reach a maximum when the blade natural frequency is an integer multiple of the rotorspeed and consequently, can be expressed in terms of a Fourier series (*Newman, 1994*).

$$L(\psi) = \sum_{n=0}^{\infty} A_n \cos n\psi$$

For an N-bladed rotor, the azimuth angle of the k^{th} blade is,

$$\psi_k = \psi + (k-1)\frac{2\pi}{N}$$

and the overall shear force at the hub is given by,

$$F = \sum_{k=1}^{N} \sum_{n=0}^{\infty} A_n \cos n\psi_k$$

This simplified expression makes the assumption that only the rotating vertical shear forces of each blade are responsible for the vertical hub forces, i.e. no contribution from the rotating in-plane shear forces is included. The contribution of in-plane loads is discussed later.

Substituting for ψ_k and defining the summations

$$C = \sum_{k=1}^{N} \cos n\left(\psi + (k-1)\frac{2\pi}{N}\right)$$

$$S = \sum_{k=1}^{N} \sin n\left(\psi + (k-1)\frac{2\pi}{N}\right)$$

leads to,

$$C + iS = e^{in\psi} \cdot \sum_{k=1}^{N} e^{in(k-1)\frac{2\pi}{N}}$$

the terms inside the summation form a geometric series, which when expanded give,

$$C + i\,S = \frac{e^{in\psi}\left(e^{2\pi m i} - 1\right)}{e^{in2\pi/N} - 1}$$

The exponential term in the numerator of the geometric expansion is unitary when n is an integer, leading to $C + iS = 0$. This is obviously false, as the case for $n = 0$ demonstrates, corresponding to steady lift. For a non-zero value of $C + iS$, it is necessary that the denominator is also zero. This requires that,

$$e^{in2\pi/N} = 1$$

$$\Rightarrow i\,n\frac{2\pi}{N} = 2\pi\,im$$

$$\Rightarrow n = m\,N$$

Therefore, for a non-zero result it is necessary that the forcing frequency be an integer multiple of the number of blades. Using L'Hopital's rule,

$$C + i\,S = \lim_{n \to mN}\left[\frac{\frac{\partial}{\partial n}\left(e^{2\pi m i} - 1\right)}{\frac{\partial}{\partial n}\left(e^{in2\pi/N} - 1\right)}\right]$$

$$= N\,e^{in\psi}$$

The hub forces can now be expressed as,

$$F = \sum_{n=0}^{\infty}\left(A_n \cos n\psi_k\right).\delta_{n,mN}$$

where $\delta_{n,mN}$ is the Kroneker delta. To summarise, the rotor blade loads are transmitted to the hub with minimal attenuation if and only if the blade forcing frequency is at an integer multiple of the number of blades. If the forcing frequency is not an integer multiple of rotorspeed, the multiblade summation is

$$C + iS = \frac{\sin \pi n}{\sin(\pi n / N)} \left\{ \cos n\left[\psi + \frac{N-1}{N}\pi\right] + i \sin n\left[\psi + \frac{N-1}{N}\pi\right] \right\}$$

Consequently, the vibration alleviation devices, both passive and active, which have been designed to date, are tuned in some form or another to attenuate vibration transmitted at N/rev.

The rotor wake is not the only contributor to vibration levels. In forward flight there exists an asymmetrical lift distribution around the rotor disc which, if left unattended, results in a rolling moment that increases in magnitude with forward airspeed. To compensate for this moment, the blades are free to flap out of the plane of rotation (either through hinges or an elastomeric bearing) achieving an equilibrium when the lift produced by the resulting angle of attack changes balances the lift generated by azimuthal dynamic pressure variations. The resulting 1/rev cyclical load variation in the rotating reference frame generates force components at higher harmonics of the rotorspeed, including N/rev in the non-rotating reference frame. Thus, the fuselage experiences vibration, which increases in magnitude proportional with lift asymmetry.

Perhaps the most significant contributor to vibration is the interaction between each blade and the tip vortex of the preceding blade. This is known as Blade Vortex Interaction (BVI), a subject of considerable research within the rotorcraft community. (*Ham, 1975*; *Caradonna et.al., 1988*; *Horner et.al., 1993*). The spanwise circulation around each blade forms a vortex at the blade tip, which is convected downstream along the outer perimeter of the wake helix. This vortex is formed when the pressure difference between the lower and upper surfaces of the blade combine at the tip. Although BVI appears throughout the entire flight envelope, it is particularly apparent during transition between low and high-speed forward flight. The inclination of the rotor disc and the wake skew angle combine to create a wake geometry with a small helix pitch, facilitating BVI. It is in this region of the speed range that the helicopter experiences the highest levels of vibration.

Physically, the tip vortex of the preceding blade induces local angle of attack and

dynamic pressure changes that result in a sharp non-linear 'pulse' in the blade aerodynamic loading. Experimental data collated by Hooper (*Hooper, 1984*) shows that BVI occurs near to the blade tip, at blade azimuth angles of between 75° and 115°, irrespective of the blade type, number of blades, forward airspeed etc. In addition to vibration, BVI is responsible for a large portion of rotor aerodynamic noise and blade fatigue.

At the upper end of the speed range, stall and compressibility effects influence the levels of vibration (*Newman, 1994*; *Johnson, 1980*). The reverse flow region on the retreating blade side of the rotor disc increases in effective area with greater forward airspeed. Consequently, more of the retreating blade stalls, the stall inducing a load discontinuity along the blade which compounds the vibratory forces at the hub.

In addition to the vibration generated by the rotor wake and asymmetric aerodynamic loads in forward flight, several other less obvious sources exist. The three most widely recognised are as follows (*Newman, 1994*).

- *Pitch-lag instability.* Should the situation arise that the blade lags rearward when the blade pitch decreases (due to the geometry of the hinges or elastic deformation) and consequently causes a reduction in lift, the rotor will undergo flapwise oscillations. If the phase of the blade flapping and the pitch-lag motion couple together, the rotor tip path plane will destabilise. Usually, the resulting unsteady motion will eventually damp out. This may be the first indication of a degradation of lag damper performance.
- *Classical flutter.* When the chordwise position of the blade CG lies such that blade torsional motion increases the incidence (nose up, inducing an additional aerodynamic force), a coupling between the torsion and bending of the blades is created. The additional aerodynamic lift causes vertical bending of the blade which, if the phase between torsion and bending is favourable, will result in a growth in the amplitude of the induced oscillations. This will increase vibration levels through the additional reaction forces/moments at the hub.
- *Stall flutter.* This condition is triggered when the blade is twisted elastically by some mechanism when the airfoil is close to its stalling incidence. Under the influence of torsional loads, the blade continues to twist until the sectional stalling incidence is reached. At this point, the lift is dramatically reduced and the blade untwists even in the

presence of the additional lift generated by the onset of dynamic stall. Torsional oscillations are generated which, depending on the phasing between pitching moment, incidence and pitch rate, can either exist in a limit cycle, maintain oscillation amplitude or even become divergent.

The cause of vibration of most interest to this research is that due to flight through atmospheric turbulence and in particular to flight at low relative speed through discrete gusts. Turbulence in the atmosphere may be generated from a variety of aerodynamic conditions: weather fronts, microbursts, windshear and obstruction-induced turbulence are but a few of the many sources of atmospheric turbulence. However, irrespective of the source, the net effect of atmospheric turbulence is to modify the forces acting on each aerodynamic surface of an aircraft. For a helicopter, the changes in blade loading induced by turbulence directly influence the vibration levels experienced in the fuselage. The cumulative effect on vibration levels due to flight through turbulence is a major topic of research within this thesis and is explored more thoroughly in ChapterIII.

1.2.2 Passive vibration alleviation.

The devices designed to control helicopter vibration fall into two categories, passive and active. A further two sub categories which are particularly relevant to passive systems can be defined as dynamic absorbers and isolators. The dynamic vibration absorber is essentially a simple mass-spring device connected to a vibrating system for curbing the motion of the parent system. The aim of an absorber is to provide anti-resonant forces to cancel out rotor induced vibration. An isolator, on the other hand, is a device which attempts to decouple the system (fuselage) from the source of vibration (rotor). Various types of passive devices have been designed with both the isolator and dynamic absorber ideologies utilised. The most popular passive devices will be discussed here.

Passive devices are mechanical systems attached to the airframe, hub or rotor blade. They range from complex servohydraulic mechanisms (LIVE, MBB anti-resonance isolator) to a simple tuned spring mounting for the helicopter battery (Westland Sea King). Ideally, vibration should never be permitted to reach the fuselage

i.e. the fuselage should be isolated from the rotor. Mounting the engine, gearbox and rotor assembly on a platform connected to the fuselage via a suspension mechanism is perhaps the simplest isolator. However, good isolation requires a large static deflection of the suspension system (*Newman, 1994*) which is obviously unacceptable. Many helicopters have to perform aggressive manoeuvres, consequently flexible fuselage-gearbox couplings are undesirable. A more sophisticated approach was required, one which maintained the attenuation qualities of a soft mounting without the corresponding large deflection of the suspension system.

In 1963, W.G. Flannely of the Kaman Aircraft Company invented the DAVI (Dynamic Antiresonant Vibration Isolator), a passive device which puts a pendulum in parallel with a spring mount, providing isolation with a much smaller static deflection. Figure *1.1* is a schematic of a DAVI isolator. When correctly tuned, the pendulum mass accelerates in a direction opposite to the exciting force. The resulting reaction force at the fuselage/pendulum attachment point is equal and opposite to the force transmitted through the spring (*Schuett, 1969; Reichert ,1981; Rita, et.al., 1978*). The net result is no forcing and hence no vibration at the fuselage. However, as each device only achieves isolation in one axis (and as full rotor isolation requires isolation in all axes) the system becomes mechanically complex. Other anti-resonance isolators use a hydraulic pendulum (LIVE, MBB Antiresonsnce isolator) for mechanical simplification (*Halwes, 1980; Braun, 1980*). The DAVI concept is extended with the IRIS (Improved Rotor Isolation System) isolation system developed through a Boeing Vertol / Kaman programme, where elastomeric isolators replace the mechanical bearings of the DAVI (*Desjardins & Hooper, 1978*).

Similar to the DAVI is the nodal suspension system (Bell nodamatic™) (*Shipman, 1972, 1973*). The fuselage is suspended under the rotor, engine and gearbox via a tuned vibrating beam, *figure 1.2*. The main rotor vibration excites the beam in the centre, producing two nodes of zero displacement either side of the rotor mount. If the fuselage is attached to the beam at these points, no vibration is transmitted from the rotor.

Unlike passive isolation systems, dynamic absorbers are not designed to decouple the rotor from the fuselage. Rather, the aim is of suppressing the motion of the parent system by rigid attachment of a tuned mass-spring system, supplying a force pattern

which is directly out of phase with the vibration (*Ellis&Jones, 1963*). For fuselage vibration control the helicopter battery is often used as the absorber mass, as in the Wessex and Sea-King aircraft, although a dedicated parasitic mass is sometimes used. The Westland Lynx rotor head absorber is designed to absorb rotor head vibration (*Balmford, 1977*). Bolted to the hub centre, it is attached to the spindle by four composite leaf springs. Tuning weights can be attached to the outer cover to allow frequency modification.

Dynamic absorbers also exist closer to the source of vibration, i.e. on the rotor blades. Centrifugal pendulum absorbers (*Taylor & Teare, 1975; Amer&Neff, 1974*) have been implemented by several companies, specifically Boeing-Vertol, Hughes and MBB. The absorber rotates with the rotor and the pendulums, under the action of the rotor centrifugal force, suppress the motion of certain flapping and in-plane blade modes. This reduces the shear and bending moments experienced at the blade root which directly contribute to fuselage vibration. Unfortunately, each mode requires a separate absorber, which would make a complete vibration absorber system prohibitively complex and expensive.

The final passive device to be discussed here is the BIFILAR dynamic absorber (*Paul, 1969*). It has been used successfully by Sikorsky on several helicopters, notably the Sikorsky Blackhawk S92. Essentially a pendulum device, the BIFILAR is designed to attenuate horizontal and in-plane shear forces at the blade root. For small oscillations, the natural frequency of the BIFILAR, like the pendulum, adjusts with changes in the centrifugal force thus re-tuning the absorber to changes in the rotorspeed. The advantage of the BIFILAR absorber over a simple pendulum device is that it provides a means of reducing the pendulum length without incurring additional weight penalties.

An alternative to designing a separate passive system is to optimise the helicopter configuration in the design phase. The objective here is to minimise vibration through careful design of the rotor assembly, such as increasing the number of blades to reduce disc loading etc. Careful positioning of the chordwise position of the blade centre of gravity can, in some rotor systems, reduce the N/rev vertical hub shear force. Compound configurations, designed to alleviate main rotor aerodynamic loading in high

speed forward flight, also reduce vibration levels (*Fradenburgh & Chuga,1968*). Primarily, the vibration induced by higher harmonic aerodynamic loading is the source most attenuated by the compound.

The benefits of including one or more passive vibration control device are obvious from the discussion presented here. However, passive absorption and isolation devices suffer from several notable problems. Employing a passive system imposes a significant weight penalty, typically 1% of the total aircraft mass. Changes in rotorspeed or aircraft mass can quickly de-tune the absorber/isolator, significantly reducing the effectiveness of the device. In addition, the recent strive for aerodynamically clean hub assemblies (Lynx) precludes the integration of rotor based devices. Finally, technological advances in electronics and servohydraulics, plus cheaper, faster and more reliable microprocessors facilitate using active control.

1.2.3 Active vibration control.

Several review papers exist (*Friedmann & Millot, 1995*; *Pearson et.al.,1994*), which present various active control strategies for the control of helicopter vibration. The following four approaches have collectively generated the most interest within the research community. These are,

i. Higher Harmonic Control (HHC),
ii. Individual Blade Control (IBC),
iii. Actively Controlled trailing edge flap (ACF),
iv. Active Control of Structural Response (ACSR).

Of the four techniques, higher harmonic control has perhaps received the most attention. This is primarily because HHC can be implemented in the non-rotating reference frame through a conventional swashplate, removing the need for specially tailored hardware. This enables experimentation and flight-testing to be performed with only minor modification of the traditional swashplate control mechanism. Only the swashplate actuation system may require any modification and then only to ensure that the actuators will perform reliably across the frequency range demanded by the

harmonic controller.

Essentially, higher harmonic control aims to reduce the fuselage vibration levels by actively manipulating the vibratory aerodynamic loads on the blades. This is achieved by oscillating the pitch of each blade at the primary vibration frequency, with the amplitude and phase of the oscillation determined by the controller. Thus the vibratory aerodynamic and inertial forces and moments are attenuated *before* they have a chance to propagate throughout the airframe, i.e. vibration alleviation is performed *at source*. This is contrary to most passive systems (with the possible exception of BIFILAR and pendulum absorbers) which attempt to minimise vibration *after* it has been generated.

The key to designing a good higher harmonic controller is selecting the control law which will yield the optimum amplitude and phase of the pitch compensation signal.

$$\theta_{HHC} = \theta_{nc} \cos n\psi + \theta_{ns} \sin n\psi$$

A number of approaches have proliferated since 1967 when Shaw (*1967*), (one of the first to investigate this problem), published a treatise on the subject. Since then, a substantial budget of academic and industrial effort and/or resources have been targeted to the HHC cause. Most of the control algorithm research to date has been performed using linear optimal control theory (*Chopra & McCloud, 1981; Molusis et.al.,1981; Achache & Polychroniadis, 1987*), often with state estimation via an optimal observer (Kalman Filter). A detailed discussion and performance evaluation of optimal higher harmonic control algorithms is presented in Chapter VI.

An alternative to conventional swashplate control is Individual Blade Control (IBC). In IBC, each blade is controlled directly in the rotating reference frame, enabling control inputs to be applied over a wide range of frequencies. Originally pioneered by Kretz (*Kretz, 1976*), considerable research on IBC has been undertaken by Ham (*1980, 1983, 1987, 1995*). The benefits which IBC could promise over conventional swashplate control are considerable, and include gust alleviation; attitude stabilisation and vibration alleviation; lag damping augmentation; stall flutter suppression; and

flapping stabilisation in forward flight (*Friedmann & Millot, 1995*). However, as modern time periodic system control theory is currently embryonic (*Calico & Weisel, 1984, 1986*), IBC control is generally derived from simple helicopter rotor dynamic equations of motion. Typically, blade flap angle is the rotor state most often controlled. IBC is discussed in more depth in Chapter VI.

Active control of rotor blade flap (ACF) and active control of structural response (ACSR) constitute the most fashionable of the remaining active control schemes. ACF involves positioning an actively controlled flap near the tip of each blade, allowing direct manipulation of the vibratory aerodynamic forces as and when they act. ACSR controls vibration after the transmission to the fuselage using the principal of superposition. Compensating vibratory forces are input to the fuselage through actuators located at key nodal positions in the airframe. The net result is low magnitude fuselage vibration. Both of these approaches are intrinsically aircraft specific, i.e. they require a detailed knowledge of the aircraft structure (ACSR) or the rotor blade section aerodynamics (ACF). The current study aims to look at several aircraft and therefore requires a control scheme that can be easily ported from one aircraft to the next. For this reason, only HHC and IBC are investigated later in the thesis.

The causes and control of helicopter vibration presented in this literature review contain one common thread throughout:- it is assumed that helicopter vibration is *always* transmitted to the fuselage at a frequency of N/rev. In a paper to the 19th European Rotorcraft forum in 1993 (*Houston & Hamilton, 1993*), Houston presented the vibration response of an individual blade helicopter mathematical model progressively entering an idealised sharp-edged vertical gust. The results showed a somewhat startling vibration spectral distribution - the vibration induced by the gust was not transmitted to the fuselage at N/rev (*figure 1.3*)! When compared to the still air vibration predicted by the simulation, there was a marked increase in the energy contained within the signal, as expected from the increase in aerodynamic loading. However, the split in fundamental frequency about N/rev was unexpected and may have far reaching implications for the design of both active and passive vibration control devices. To date, none of the rotorcraft research community has conducted any study into the existence of this phenomena during actual helicopter operations, or to the effect such a phenomena has on the robustness or performance of the vibration control laws.

1.3 Aims of the Research

In view of the possible implications for vibration minimisation systems, the findings of Houston & Hamilton warrant further investigation. In essence, these results pose three questions. First, does helicopter flight through realistic atmospheric turbulence result in the same kind of frequency distribution as flight through an idealised disturbance? Secondly, how robust are the existing pre-tuned active vibration controllers to gust-induced vibration, which is not transmitted to the fuselage at the fundamental vibratory forcing frequency? Third, is there an effective method for improving the disturbance rejection qualities (if required) of the current advanced active vibration control algorithms?

In answering these questions, it will be necessary to develop a suitable rotorcraft simulation model. Suitability is governed by the complexity of the dynamics required for vibration modelling. The prediction of conventional vibratory blade loading ideally requires the aerodynamic environment surrounding the blades (and in particular the wake), to be simulated using an aeroelastic/free wake rotor model. However, as it is also intended that the results of the simulation should be directly related to actual operational environments, a flight mechanics model is required. The compromise is to use a flight mechanics based simulation model, which embodies an advanced rotor model, rotor-fuselage coupling and can predict fuselage vibration levels. There should also exist within the model a mechanism for testing vibration alleviation control laws, both in still air and through atmospheric turbulence. In addition, it would be advantageous to be able to fly the simulation along some pre-defined aggressive manoeuvres to evaluate the vibration levels in near-limit flight. The model should also be generic in its construction to facilitate comparison of vibration levels experienced by different aircraft. Such a simulation tool would not be limited to fulfilling the research aims but could be used in a variety of other tasks, *figure 1.4*.

A helicopter simulation model that satisfies the requirements outlined above has been developed. Called HISAT (*Helicopter Inverse Simulation through Atmospheric Turbulence*), it is a modified version of RASCAL (*Rotorcraft Aeromechanic Simulation for Control AnaLysis*), a complex, generic, rotorcraft simulation model developed at the University of Glasgow (*Houston, 1991b*). For expediency (and to avoid confusion

throughout the thesis), the author has coined the acronym HISAT to differentiate the modified from the original version of RASCAL. It should be stressed here that HISAT retains the core functionality of RASCAL, but has been enhanced to accommodate atmospheric turbulence and inverse simulation models. To the best of the authors knowledge, no similar simulation device exists which can match HISAT in both complexity and diversity of use. Therefore the development of HISAT alone constitutes a novel and important contribution to the field of rotorcraft simulation.

The aims of this research may then be outlined as follows. First, to develop a suitable mathematical model (HISAT) which could simulate a helicopter performing complex manoeuvres within realistic atmospheric turbulence, akin to that experienced in an operational environment. Secondly, as there exits no flight test or computer simulation data to either validate or rebut the phenomena observed by Houston, HISAT will be used to investigate the vibratory response of a helicopter immersed in a realistic turbulent atmospheric environment. Third, the robustness of two active vibration control techniques, namely higher harmonic and individual blade control, are to be evaluated using a 'worst case' idealised sharp-edged gust. Finally, should improvement in controller performance prove necessary, it is hoped that enhancement of the active control schemes can be attained by employing modern robust and/or intelligent control theory.

1.4 The Structure of this Thesis

The structure of this thesis follows closely to the order in which the research aims were set. Chapter II will present an overview of RASCAL, indicating where prudent the areas where enhancement of the model is required. A comprehensive description was included here, rather than in an appendix as the author felt that presenting the existing structure of the simulation was necessary to explaining why particular paths were chosen or techniques employed during the course of the research. Chapter III details the mechanism for incorporating turbulence effects in the simulation. The results of Houston and Hamilton (*1993*) are duplicated, although not to the same amplitude. A

novel mathematical explanation for the observed split in fundamental forcing frequency is shown to correlate well with the model calculations.

Chapter IV begins with a review of several techniques used to generate turbulence fields, namely discrete gust modelling, continuous Gaussian PSD based models and the Statistical Discrete Gust (SDG) method, with the intention of selecting one to support HISAT. The demand for realism precludes the use of discrete gust modelling techniques, although further insight into the nature of gust-induced vibration is gained. The continuous models are shown to generate turbulence using statistical information extracted from fixed wing, flight test measurements through turbulence, which is not strictly applicable to helicopter rotors. Consequently, none of the accepted turbulence generators appear suitable, so a new and novel approach is employed, using a Computational Fluid Dynamics (CFD) package to generate a realistic turbulence field. The field creation process is outlined alongside several fluid dynamics and grid generation issues that must be addressed. An inspection of the positions, velocities, accelerations and Euler angle time histories for flight through the CFD-generated turbulence fields suggests a successful integration.

The incorporation of an inverse simulation algorithm into the RASCAL-CFD hybrid model is presented in Chapter V. After a short review of various approaches to helicopter inverse simulation, the integration method and in particular the GENISA algorithm, is selected as the best candidate for meeting the inverse simulation goal of successful symbiosis with RASCAL. The GENISA algorithm is then fully explained and developed using a non-linear state space representation of the input-output (controls-flightpath) connection. After presenting the results of some benign manoeuvres, an oscillation is observed in the time histories of the dominant attitude angle for each manoeuvre. An enhancement to GENISA in the form of a Newton-step optimisation algorithm reduces the severity of these oscillations. A linear constraint analysis technique suggests the initial oscillations to be the result of numerical instability in the algorithm, but confirms the smaller motion to be constraint oscillations, which are directly related to inverse simulation. Inverse simulation of an individual blade helicopter with variable rotorspeed and lead-lag hinges has never been performed successfully and consequently, HISAT represents the current state of the art model.

Active vibration control is discussed extensively in Chapter VI. The performance of higher harmonic and individual blade control algorithms when subjected to flight through a sharp-edged gust is compared and evaluated using two criteria: performance and complexity of the control law. The HHC algorithm is shown to give excellent attenuation of still-air vibration but performs extremely poorly when tasked with controlling vibration induced by flight through a sharp-edged gust. Enhancements to the algorithm through the inclusion of a Kalman filter and multi-harmonic inputs fail to yield any performance improvement. However, a novel modification to the algorithm allowing for direct feedforward of a Fourier estimate of the gust, is shown to be extremely proficient. High gain IBC is also proven to be an effective strategy for rejecting gust-induced vibration. However, it is apparent that some improvement of the control law is necessary. Continuing this theme, precise loop shaping via H_∞ synthesis is investigated in Chapter VII alongside intelligent disturbance prediction/estimation using neural network models.

Conclusions to the thesis are drawn in Chapter VIII. It is shown that a successful development of HISAT was achieved, fulfilling the first of the research aims. It will also show that the two other research aims were also met and outlines possible avenues for future research.

1.5 Summary of Chapter I.

It was the intention of this introduction to explain to the reader the importance of vibration minimisation in commercial and military rotorcraft, the causes of this vibration and the control devices and concepts which have been implemented or investigated to date. In addition, the research aims of this dissertation have been presented and can be summarised as follows;

i. Develop a mathematical model suitable for turbulence-induced vibration analysis.
ii. Investigate the response of a helicopter through a realistic atmospheric environment.
iii. Assess the performance of Higher Harmonic and Individual Blade control through several gust fields.
iv. Suggest possible avenues for controller enhancement.

The development of the mathematical model begins with a discussion of RASCAL, the topic of the next chapter.

CHAPTER II

A Description of the RASCAL Helicopter Simulation Model.

This chapter describes the helicopter simulation model, RASCAL, used as the core mathematical model in this research program. The complex nature of the model is illustrated through a detailed discussion of the simulation strategy, with particular emphasis placed upon the techniques used to model the main and tail rotors of the helicopter. Throughout the development, key concepts and development techniques, which have a particular relevance to vibration analysis, will be expanded and placed in context with the state-of-the-art development of vibration simulation software.

2.1 Introduction to RASCAL.

RASCAL (Rotorcraft Aeromechanic Simulation for Control AnaLysis) is the acronym for the helicopter simulation mathematical model used throughout this study. RASCAL is an individual blade/blade element, generic rotorcraft model designed primarily for flight mechanics applications, developed initially by Houston (*1991b*). The aircraft (helicopter, gyroplane, tiltrotor etc.) is modelled as a discrete point mass assembly of fuselage, main rotor, secondary rotor (often tailrotor), tailplane and fins. The dynamic equations of motion are derived directly from Newton's second law (in accordance with common practice in helicopter mathematical modelling intended for

flight mechanics applications) instead of energy or other methods. RASCAL can support up to 10 blades per rotor, each with fully coupled flap and lead/lag degrees of freedom. Each blade can be discretised to a maximum of 10 blade elements, with the aerodynamic calculations at each element capable of predicting stall and compressibility effects. Up to three engines can be individually modelled with separate transmissions to the rotors via geared or independently controlled rotor torque. The wake is modelled by momentum based dynamic inflow algorithms which incorporate ground effect and rudimentary tail surface interaction. The current version of RASCAL is a level 2 helicopter simulation model as defined in Padfield (*1996*) (reproduced in table 2.1), but is constructed in a fashion that will allow the integration of aeroelastic and free-wake models if required. A summary of these and other important features of the model is presented in table 2.2.

The primary function of RASCAL is to predict the rigid body flight mechanics of rotary wing aircraft. It does this by trimming the aircraft using an optimisation algorithm to compute the fuselage orientation and control positions necessary to keep the aircraft in trim (no fuselage accelerations). Once in trim, either the free body response of the aircraft or the response to control inputs (step, doublet etc.) can be simulated. The model also contains a numerical differentiation algorithm, included specifically for calculating stability and control derivatives. Comparisons of some of the longitudinal and lateral/directional derivatives with those obtained from flight test data are shown in *figures 2.1* and *2.2*. These results have been reproduced from Houston (*1994*) and clearly show that RASCAL adequately predicts the helicopter dynamic characteristics to the precision demanded for this investigation.

The remainder of this chapter will present a detailed explanation of the concepts and equations used in the derivation of RASCAL, many of which will be referenced and discussed in later chapters. It is hoped that this exercise will impart the complexity, coupling and nonlinearity of the dynamic response of the helicopter predicted by RASCAL, as these concerns undoubtedly influenced the direction and success of the research.

2.2 *Rigid-Body dynamics.*

By assuming the helicopter to be a rigid structure the commonly used Euler rigid body equations of motion may be employed to describe the motion of the system. The motion of the body in free space can be tracked by the position and orientation of a body axes set fixed in the fuselage with origin at the centre of gravity, *figure 2.3*. This axes set is defined as follows. The positive X-axis lies parallel to the floor and points to the front of the aircraft, positive Y-axis points to starboard and positive Z completes the orthogonal set. The translational (u,v,w) and angular (p,q,r) velocities are defined with respect to these axes as shown. From Newton's second law, the inertial acceleration of a body subject to the application of external forces and moments is given by

$$\dot{\underline{u}} = \underline{\omega} \times \underline{u} + \frac{\sum \underline{F}_{ext}}{m} \tag{2.2.1}$$

where $\dot{\underline{u}}$ is the vector of body axes translational accelerations, $\underline{\omega}$ contains the body axis rotational velocities, m is the total mass of the aircraft, including fuel, stores and passengers and $\sum \underline{F}_{ext}$ represents the sum of all of the external forces {aerodynamic, inertial, propulsive and gravitational} acting on the airframe. From the conservation of angular momentum, the governing equation for angular motion about the body axis set is given by,

$$\dot{\underline{H}} = -\underline{\omega} \times \underline{H} + \sum \underline{\mathbf{T}}_{ext} \tag{2.2.2}$$

and

$$\underline{H} = \mathrm{I}\underline{\omega} \tag{2.2.3}$$

where I is the inertia matrix, $\underline{H}$ is the angular momentum of the system and $\sum \mathrm{T}_{ext}$ is the sum of all external torques acting on the fuselage. Expansion of the general equations for translational motion into the constituent components of the velocity vectors gives,

$$\dot{u} = vr - qw + \frac{F_{ext}^{X}}{m} - g\sin\theta$$

$$\dot{v} = wp - ur + \frac{F_{ext}^{Y}}{m} - g\cos\theta\sin\phi$$

$$\dot{w} = uq - vp + \frac{F_{ext}^{Z}}{m} + g\cos\theta\cos\phi \qquad (2.2.4)$$

where the gravitational forces have been extracted from the cumulative force terms in accordance with standard practice in flight vehicle simulations. Performing a similar operation on the angular equations of motion yields,

$$I_{xx}\dot{p} = (I_{yy} - I_{zz})qr + I_{xz}(\dot{r} + pq) + \boldsymbol{L}$$

$$I_{yy}\dot{q} = (I_{zz} - I_{xx})rp + I_{xz}(r^2 - p^2) + \boldsymbol{M}$$

$$I_{zz}\dot{r} = (I_{xx} - I_{yy})pq + I_{xz}(\dot{p} - qr) + \boldsymbol{N} \qquad (2.2.5)$$

The conversion between an earth-fixed inertial reference co-ordinate axes set and the body axes set (*figure 2.4*) is performed through the Euler Transformation matrix.

$$\underline{\boldsymbol{u}}_B = \mathrm{M}\,\underline{\boldsymbol{u}}_E \qquad (2.2.6)$$

where,

$$\mathrm{M} = \begin{bmatrix} \cos\theta\cos\psi & \cos\theta\sin\psi & -\sin\theta \\ (\sin\phi\sin\theta\cos\psi - \cos\phi\sin\psi) & (\sin\phi\sin\theta\sin\psi + \cos\phi\cos\psi) & \sin\phi\cos\theta \\ (\cos\phi\sin\theta\cos\psi + \sin\phi\sin\psi) & (\cos\phi\sin\theta\sin\psi - \sin\phi\cos\psi) & \cos\phi\cos\theta \end{bmatrix}$$

The Euler angle rates can be expressed in terms of the body-fixed angular rates.

$$\dot{\phi} = p + q\sin\phi\tan\theta + r\cos\phi\tan\theta$$

$$\dot{\theta} = q\cos\phi - r\sin\phi$$

$$\dot{\psi} = q\sin\phi\sec\theta + r\cos\phi\sec\theta \qquad (2.2.7)$$

The absolute, or inertial motion through space (both position and orientation) of the helicopter centre of gravity can be calculated by integrating equations (2.2.1-7). However, the magnitude and direction of the external forces and moments acting on the body have still to be defined. For all classes of airborne vehicle the primary source of external, non-conservative forcing is due to the aerodynamic interaction between the vehicle and the atmosphere. For the helicopter in particular both propulsion and control are achieved through the same medium, the main lifting rotor. Therefore, the mechanisms for generating and modelling this principal source of external forcing will now be discussed.

2.3 Rotor Forces and Moments.

2.3.1 Introduction.

The accuracy of a helicopter simulation is governed by the simplifying assumptions used in the estimation of the main rotor forces and moments. For simulations which are intended to predict the low frequency response of the aircraft to pilot commands or external disturbances, a simple actuator disc representation of the rotor is often adequate. Here, the rotor system is substituted by an equivalent thrust vector which is oriented perpendicular to the plane mapped out by the tip of each blade (tip-path plane) and is assumed to act through the centre of this disc. The magnitude and direction of the thrust vector is determined by the swashplate orientation (pilot inputs) and position of the rotor disc within the flight envelope (airspeed, altitude etc.). The relationship between control inputs and vehicle response is often simulated by employing simple transfer functions. Such simulation models are used in the driver software for real-time flight simulators, as they are fast, simple and cheap to develop.

Predicting medium to high frequency response characteristics requires a much higher fidelity rotor model. To simulate the response of the helicopter to high frequency rotor loads - which will almost certainly vary along the span - the loads (aerodynamic and inertial) are calculated at several radial stations, using a technique known as *blade element* modelling. The aerodynamic environment surrounding each blade also varies significantly with azimuth, which in turn alters the transient response

characteristics of the blade. An important example of this is the cyclically varying aerodynamic damping of the flap degree of freedom which will be discussed thoroughly in Chapter VI. Consequently, each blade should ideally be modelled as a separate dynamic system, which is coupled to the motion of the rotor hub. Mathematical models of this type are known as individual blade models and have been used successfully in a variety of applications (*Houston, 1994., Celi, et.al., 1993*). The section to follow develops the primary tools used in an individual blade - blade element simulation.

2.3.2 Blade Element Theory.

The use of blade element theory is becoming increasingly commonplace with the advent of affordable and powerful digital instruments and computers, which enable increasingly detailed and complex simulations to be performed within a reasonable time scale. As all conventional helicopter rotor blades have a high aspect ratio (specified through rotor performance requirements), blade element theory can be used to predict the rotor forces of most rotorcraft configurations to an acceptable accuracy. This reduces software duplication and allows the direct comparison of the performance of like aircraft by eliminating model specific issues. Although blade element theory has been documented extensively in the literature, there are some fundamental assumptions used in this theory which demand attention.

As stated (and to the best of the authors knowledge), all modern, conventional helicopters have high aspect ratio blades. High aspect ratio blades generate large tip velocities with relatively low rotorspeed, generating the required aerodynamic loads to manoeuvre the aircraft at low engine rpm settings. As a consequence of this geometry, the primary influences of 3-dimensional aerodynamic effects are confined to a small portion of the blade near the tip and to the inboard blade section near the root cut-out (*Johnson, 1980*). The remaining sections of the blade locally experience aerodynamic effects which can be adequately modelled using 2-D aerodynamic lifting line or thin airfoil theory. Blade element theory uses this assumption and makes a further assumption, that the blade may be segmented into a number of individual and distinct

elements, *figure* 2.5, each element analysed as a 2-D airfoil section. The local aerodynamics on one blade element are illustrated in the free-body diagram of *figure 2.6*. For most flight dynamics applications it is sufficient to represent the aerodynamic forces solely by sectional lift and drag. However, by predicting the position of the aerodynamic centre of each element and calculating the sectional aerodynamic moment (from thin airfoil theory), an aeroelastic or pitch-link model may easily be assimilated. There now follows a more detailed development of the inertial and aerodynamic forces and moments acting on each blade.

2.3.3 Blade Element Velocity.

The velocity of a blade element with respect to inertial space is required principally for the calculation of the blade aerodynamics. It is derived initially from flight path considerations such as the flight velocity, the turn rate, the flight path angle and the sideslip angle etc. By defining these variables, it is a simple operation to calculate the translational and rotational velocities of the centre of gravity along the body axis. It is by this method that the initial conditions of the fuselage states are defined. (The response of the c.g. from $t = t_o \rightarrow t_f$ is subsequently found by integrating equations 2.2.4-5). Assuming the body axis velocities,

$$\underline{u} = [u\ v\ w]^T \quad \text{and} \quad \underline{\omega} = [p\ q\ r]^T \tag{2.3.1}$$

are known, the velocity of the hub in body axes is given by,

$$\underline{u}_{hub}^{body} = \underline{u} + \underline{\omega} \times \underline{r}_{hub/cg} \tag{2.3.2}$$

In most rotary wing aircraft, the rotor shaft is inclined with respect to the fuselage through rotations in pitch and roll. This is to ensure that while travelling at speeds at or around the ideal cruise speed, the fuselage is approximately level. Note that to increase and maintain airspeed the rotor disc must tilt forward to provide the component of

thrust required. Therefore, as it is convenient to express the motion of a system in axes native to that system, the velocity of the hub in hub axes is,

$$\underline{\boldsymbol{u}}_{hub}^{hub} = \mathrm{T}_1 \underline{\boldsymbol{u}}_{hub}^{body} \quad \text{and} \quad \underline{\boldsymbol{\omega}}_{hub} = \mathrm{T}_1 \underline{\boldsymbol{\omega}} \tag{2.3.3}$$

where,

$$T_1 = \begin{bmatrix} cos\theta_s & 0 & -sin\theta_s \\ sin\theta_s sin\phi_s & cos\phi_s & cos\theta_s sin\phi_s \\ sin\theta_s cos\phi_s & -sin\phi_s & cos\theta_s cos\phi_s \end{bmatrix}$$

and θ_S, ϕ_S are the shaft tilt angles. This transformation is illustrated in *figure 2.7*. The next transformation is that from the non-rotating to rotating hub plane, a transformation which is physically realised through the bearings of a swashplate (for modelling purposes the swashplate and hub are assumed to be co-located). The translational rotating velocities are,

$$\underline{\boldsymbol{u}}_{hub}^{hg} = \mathrm{T}_2 \underline{\boldsymbol{u}}_{hub}^{hub} \tag{2.3.4}$$

where,

$$\mathrm{T}_2 = \begin{bmatrix} \sin\psi & -\cos\psi & 0 \\ \cos\psi & \sin\psi & 0 \\ 0 & 0 & 1 \end{bmatrix}$$

The superscript *hg*, which is an abbreviation of 'hinge', refers to the axis orientation that rotates with the blades in the hub plane. This notation was chosen as it facilitates the notation when describing the integration of a suitable a gust module within RASCAL. This will become apparent in the discussion of turbulence integration in Chapter III. The transformation of the hub angular velocity to hinge axes must include the rotor angular velocity provided by the engines,

$$\boldsymbol{\omega}_{hub}^{hg} = \boldsymbol{\omega}_{hub} + [0\ 0\ \Omega]^{\mathrm{T}} \tag{2.3.5}$$

The transformation from the non-rotating to rotating planes is illustrated in *figure 2.8* with $\psi = 45°$. The hinge is offset from the hub by a distance,

$$\underline{r}_{hg/hub} = [0 \;\; -eR \;\; 0]^T \tag{2.3.6}$$

The velocity at the hinge is then,

$$\underline{u}_{hg}^{hg} = \underline{u}_{hub}^{hg} + \underline{\omega}_{hub}^{hg} \times \underline{r}_{hg/hub} \tag{2.3.7}$$

The final axis transformation is through the blade hinge arrangement (assuming coincident flap and lead/lag hinges) from hinge to blade axes, *figure 2.9*, thus.

$$\underline{u}_{hg}^{bl} = T_3 \underline{u}_{hg}^{hg} \quad \text{and} \quad \underline{\omega}_{hg}^{bl} = T_3 \underline{\omega}_{hub}^{hg} + [\dot{\beta} \; \dot{\theta} \; \dot{\zeta}]^T \tag{2.3.8}$$

where,

$$T_3 = \begin{bmatrix} \cos\zeta & sin\zeta & 0 \\ -cos\beta sin\zeta & cos\beta cos\zeta & sin\beta \\ sin\beta sin\zeta & -cos\zeta sin\beta & cos\beta \end{bmatrix}$$

In this transformation, it is implicitly assumed that the blades experience only rigid deformation about each hinge. The more complex aeroelastic analysis would typically involve the modal decomposition of the motion of the blade through generalised co-ordinates in flap and lag at each radial station. However, recent studies have shown, (*Turnour & Celi, 1996*), that blade aeroelastic distortion has a negligible effect on the response of the aircraft from within a flight mechanics context. Consequently, the simpler rigid blade assumption is used throughout the derivation of the model. Finally, the velocity experienced at a blade element is,

$$\underline{u}_{elem}^{bl} = \underline{u}_{hg}^{bl} + \underline{\omega}_{hg}^{bl} \times \underline{r}_{elem/hg} \tag{2.3.9}$$

where, $$\underline{r}_{elem/hg} = [0 - r_{elem} \; 0]^T$$

It is prudent at this point to emphasise that the velocity components derived here result from the kinematic expansion of the motion of the entire helicopter system through space. No aerodynamic - and in particular wake influences - are included. The influence of the wake predominantly effects the perpendicular component of velocity, *figure 2.6* and can be superimposed upon the kinematic motion of the blade vis,

$$u_p = u_p^{kinematic} - u_p^{wake} \qquad (2.3.10)$$

where u_p^{wake} is the velocity induced at the blade element by the vorticity within the rotor wake and $u_p^{kinematic}$ is the $\underline{k}^{th}$ component of $\underline{u}_{elem}^{bl}$. Similarly, u_t from *figure 2.6* is the $\underline{i}^{th}$ component of $\underline{u}_{elem}^{bl}$. The calculation of u_p^{wake} is presented in section 2.6.

2.3.4 Blade Acceleration.

A complete description of the forces acting on each individual blade must include the inertial forces generated by motion of the blade mass. Indeed, components of inertial force such as the centripetal rotor force are crucial in the construction of blade models and the understanding of blade dynamics. Continuing from the development of blade velocity, blade element acceleration will now be derived. As a suitable starting point, consider the general expression for the acceleration of a point B defined with respect to an origin at A,

$$\underline{a}_{B/A} = \underline{a}_A + \frac{d^2 \underline{r}_{B/A}}{dt^2} \qquad (2.3.10)$$

Expansion of this term yields,

$$\underline{a}_{B/A} = \underline{a}_A + \frac{\partial^2 \underline{r}_{B/A}}{\partial t^2} + \underline{\alpha} \times \underline{r}_{B/A} + 2\underline{\omega} \times \frac{\partial \underline{r}_{B/A}}{\partial t} + \underline{\omega} \times \left(\underline{\omega} \times \underline{r}_{B/A}\right) \qquad (2.3.11)$$

In a rigid structure, the position of point B with respect to the origin at A does not alter with time and so the acceleration can be rewritten as,

$$\underline{a}_{B/A} = \underline{a}_A + \underline{\alpha} \times \underline{r}_{B/A} + \underline{\omega} \times \left(\underline{\omega} \times \underline{r}_{B/A}\right) \tag{2.3.12}$$

where,

$$\underline{\alpha} = \underline{\dot{\omega}} = \left[\dot{p}\ \dot{q}\ \dot{r}\right]^{\mathrm{T}}$$

Taking the centre of gravity of the entire helicopter as the origin,

$$\underline{a}_A = \underline{a}_{cg} = \frac{\partial \underline{u}}{\partial t} + \underline{\omega} \times \underline{u} \tag{2.3.13}$$

Then, by the same process of axis transformations used to derive the components of the velocity vector, the acceleration of a blade element is given by,

$$\underline{a}_{elem}^{bl} = \underline{a}_{hg}^{bl} + \underline{\alpha}_{hg}^{bl} \times \underline{r}_{elem/hg} + \underline{\omega}_{hg}^{bl} \times \left(\underline{\omega}_{hg}^{bl} \times \underline{r}_{elem/hg}\right) \tag{2.3.14}$$

It should be noted that the angular acceleration of the blade about the hinge includes terms derived from the blade degrees of freedom, i.e.

$$\underline{\alpha}_{hg}^{bl} = \mathrm{T}_1 \underline{\alpha}_{hg}^{hg} + \left[\ddot{\beta}\ \ddot{\theta}\ \ddot{\zeta}\right]^{\mathrm{T}}$$

and,

$$\underline{\alpha}_{hg}^{hg} = \underline{\alpha}_{hub}^{hg} = \mathrm{T}_2 \underline{\alpha}_{hub}^{hub} + \left[0\ 0\ \dot{\Omega}\right]^{\mathrm{T}}$$

2.3.5 *Blade Aerodynamics.*

From the fundamental assumptions of blade element theory outlined in section 2.3.1.1, the equations for the sectional aerodynamic forces are,

$$dL = \frac{1}{2} c \rho \left(u_t^2 + u_p^2\right) C_l \Delta r$$

$$dD = \frac{1}{2} c\rho\left(u_t^2 + u_p^2\right) C_d \Delta r \tag{2.3.15}$$

and the total aerodynamic force on each blade is obtained by integrating the differential forces along the blade span, vis.

$$L = \int_{eR}^{R} dL\, dr$$

$$D = \int_{eR}^{R} dD\, dr \tag{2.3.16}$$

where, ρ is the local air density, $\left(u_t^2 + u_p^2\right)$ is the local airspeed experienced by the section squared, C_l (C_d) are the aerodynamic coefficients and Δr is the length of the blade element. It is apparent from the above equations that the aerodynamic forces are governed by four parameters:

i) The effective area of the blade section, which for $\Delta r \Rightarrow 0$ simplifies to the chord length of the section, c,
ii) the local Mach Number and
iii) the aerodynamic coefficients C_l *and* C_d.

The first parameter is a combination of the constraints imposed by the blade geometry (and in particular the chord length distribution along the blade span) and the number of elements chosen to represent the blade. For most applications, choosing as little as ten elements per blade yields accurate results. Increasing the number of elements beyond this point significantly increases the run time of the simulation without any appreciable increment in modelling accuracy (*Houston, 1991; Johnson, 1980*).

The Mach number of the airflow is the next parameter to influence the magnitude of the aerodynamic forces. The Mach number (airspeed divided by the local speed of sound) is the preferred measure of velocity for use in aerodynamic calculations as it encompasses the compressibility of the airflow at high speed within a single velocity parameter. The benefit of adopting this approach will become apparent when

discussing the prediction of the aerodynamic coefficients later in this chapter. The Mach number is,

$$M = \frac{\sqrt{(u_t^2 + u_p^2)}}{a} \tag{2.3.17}$$

and the local speed of sound is given by

$$a = \sqrt{\gamma R T} \tag{2.3.18}$$

where γ is the polytropic index, R is the gas constant and T is the local air temperature. The expressions for the tangential and perpendicular blade velocities due to the aircraft motion were derived and discussed in § 2.3.3. It should be noted however that the perpendicular velocity component includes the induced velocity from the rotor wake.

From *figure 2.6*, the angle of attack of each element is composed of two angles, the geometric blade pitch angle θ_{be} and the inflow angle ϕ_{be}. The blade pitch angle is a combination of the blade root pitch - derived from the multiblade description of the control angles, i.e.

$$\theta_r = \theta_0 + \theta_{1s}\sin\psi + \theta_{1c}\cos\psi + \delta_3\beta \tag{2.3.19}$$

(including any pitch-flap coupling) - and the washout or geometric twist, θ_{tw} to give,

$$\theta_{be} = \theta_r + \theta_{tw} r_{be} \tag{2.3.20}$$

where the subscript '*be*' denotes blade element and r_{be} is the radial position of that element. The inflow angle is a trigonometric combination of the perpendicular and tangential velocities u_t and u_p, therefore,

$$\alpha_{be} = \theta_{be} + \phi_{be} = \theta_{be} + \tan^{-1}\left(\frac{u_p}{u_t}\right) \tag{2.3.21}$$

Hence, the calculation of the blade sectional aerodynamic forces and moments reduces to the calculation of the local velocities u_t and u_p, from which the angle of attack can be derived. Once the Mach number and angle of attack are known, the aerodynamic coefficients can be calculated.

The induced lift (and drag) coefficients are the mechanisms whereby stall and compressibility effects are incorporated into the calculation of the blade aerodynamic forces. The inclusion of these effects is essential for all but the most basic analysis of blade loading and therefore mandatory for vibration prediction. However, many low order models achieve a successful coherence with flight data using thin airfoil theory to predict the coefficients. In thin airfoil theory, the mean camber line of the airfoil is replaced with a vortex sheet constructed of individual vortex filaments, the combined vorticity of which matches the bound circulation of the airfoil. The lift per unit span, L', is defined as the integral of the pressure difference between the upper and lower surfaces of the airfoil from the leading to trailing edge of the airfoil.

$$L' = \int_0^c \Delta p \, dx \tag{2.3.22}$$

For a symmetric airfoil the lift coefficient reduces to the simple result,

$$C_l = 2\pi\alpha \equiv a_0\alpha \tag{2.3.23}$$

This approximation is valid only for sections experiencing small angles of attack. However, a helicopter rotor undergoes large angle of attack changes with azimuth position and forward flight speed, leading, in some circumstances, to stall conditions on the inboard retreating section of the blade, which is not predicted by thin airfoil theory. Nonlinear aerodynamic conditions such as blade stall and compressibility were identified in Chapter I as belonging to the class of primary contributors to main rotor vibration. It is therefore apparent that a more specialised theory is required, but first a general explanation of the physics of airfoil stall and compressibility is warranted.

An airfoil is designed specifically to promote different accelerations on the airflow over the upper and lower surfaces, creating a pressure differential and hence lift.

Considering only a potential flow solution for the moment, the airflow is accelerated to a maximum speed (minimum pressure) which occurs at a point on the upper surface of the airfoil and is then decelerated to the mean flow velocity at the trailing edge. An adverse pressure gradient is induced which decreases the momentum in the airflow until a point on the surface is reached where the momentum is zero and the flow separates from the airfoil. Providing sufficient lift is being generated by the attached flow near the leading edge, the airfoil will not stall. However, should the separation point move forward due to, for example, an increase in angle of attack, the flow rapidly separates from the airfoil. This results in a dramatic reduction in lift of up to 50% of the maximum value (*Prouty, 1990*). Stall thus induces a significant discontinuity in the blade loading distribution, which will become a contributor to the fuselage vibration levels and therefore the effects of stall must be included in the model.

The second phenomenon to effect the lift coefficient is the compressibility of the airflow at high speed. The combination of rotational and forward flight speed can induce very high Mach numbers on the advancing side of the rotor, especially near to the blade tip. Tip Mach numbers in the subsonic transition range ($\cong$ 0.7-1.0) can be obtained at low forward flight speed (the blade tip of the Puma in cruise reaches M$\approx$0.8). However, it is the asymmetry of dynamic pressure around the main rotor and the associated density distribution due to compressibility effects, which have the main impact upon accurate calculation of the blade aerodynamic loads. Simple techniques such as the Prandtl-Glauert conformal mapping method (*Keuthe & Chow, 1986*) can predict the effect of compressibility on the sectional lift coefficient. However, this mapping assumes a potential flow solution, invalidating such an approach for calculating the effect of compressibility on the sectional drag coefficient, which is strongly correlated to the size and shape of the airfoil wake. As no manageable analytical solution exists, the only recourse is to use experimental data.

Considering the complexity of the physics of stall and compressibility it is not surprising that a simple algorithmic solution cannot be found. However, for vibration analysis these effects must be included in the model while, at the same time, not significantly increasing the run-time of the simulation. The most expedient solution is to employ look-up tables derived from experimental wind tunnel test data. This is the

approach used in RASCAL. A 2-D look up table containing lift and drag coefficients at several operational angles of attack and mach numbers is interpolated to find the C_l and C_d appropriate to the angle of attack and Mach number of the element, as given by equations (2.3.17-18). Using this method, stall and compressibility effects are incorporated into the calculation of the blade aerodynamic loads, while still allowing the simulation to have a reasonable run-time.

2.3.6 Total Forces and Moments.

The total force acting on each blade element is the sum of the aerodynamic and inertial loads, which from Newton's 2nd law gives,

$$\underline{\boldsymbol{F}}_{elem} = \underline{\boldsymbol{F}}_{elem}^{aero} + \underline{\boldsymbol{F}}_{elem}^{inertial} \tag{2.3.24}$$

where,

$$\underline{\boldsymbol{F}}_{elem}^{inertial} = -m_{elem}\underline{\boldsymbol{a}}_{elem}^{bl}$$

The forces and moments acting on the airframe can now be calculated (*Houston, 1994*).

$$\boldsymbol{F}_{ext}^{rotor} = \mathrm{T}_1^{-1} \sum_{j=1}^{nbl} \left(\mathrm{T}_2^{-1}\mathrm{T}_3^{-1} \left\{ \sum_{i=1}^{nelem} \boldsymbol{F}_{elem} \right\} \right) \tag{2.3.25}$$

$$\underline{\boldsymbol{T}}_{ext}^{rotor} = \mathrm{T}_1^{-1} \sum_{j=1}^{nblades} \left(\mathrm{T}_2^{-1} \left(-\underline{\boldsymbol{r}}_{hg/hub} \times \left(\mathrm{T}_3^{-1} \left\{ \sum_{i=1}^{nelem} \underline{\boldsymbol{F}}_{elem} \right\} \right) \right) \right) + \underline{\boldsymbol{r}}_{hub/cg} \times \underline{\boldsymbol{F}}_{ext}^{rotor} \tag{2.3.26}$$

where $\underline{\boldsymbol{F}}_{ext}^{rotor}$ is the rotor force vector expressed in airframe axes, $\underline{\boldsymbol{T}}_{ext}^{rotor}$ is the rotor moment vector in airframe axes, n_{blades} is the number of blades on the rotor and n_{elem} is the number of elements on each blade.

2.4 *Blade Equations of Motion.*

In forward flight u_t varies with blade azimuth position, equation (2.3.5), giving cyclic variation of the local dynamic pressure and inducing a rolling moment across the rotor disc. The conventional method for alleviating this moment was pioneered by Juan de la Cierva among others (*Prouty, 1990*), who encountered adverse rolling moments when flight testing (and subsequently crashing) several early configurations of gyroplane. Cierva had successfully flown balsa wood gyroplane models without incident, validating the *concept* of rotary wing flight. The reason for the models success was finally attributed to the elasticity of the rotor blades with respect to motion out of the plane of rotation. What followed was the inception of the articulated hub assembly, a prodigious development in rotorcraft engineering.

Lift asymmetry in forward flight causes each blade to accelerate upwards on the advancing side of the rotor and downwards on the retreating side, changing the effective incidence of the mean airflow. As the blade accelerates upward, an additional component of inflow is generated which is proportional to the rate of change of the out-of-plane motion, $\dot{\beta}$. This reduces the local angle of attack and hence lift on the blade. On the retreating side, the downward acceleration - induced by an effective loss of dynamic pressure - reduces the inflow velocity and increases the angle of attack. Therefore, by using a hinge or elastomeric bearing as the blade - hub attachment, an equilibrium point is reached when the dynamic pressure asymmetry is balanced by flap induced changes in angle of attack, thus alleviating the roll moment observed by Cierva.

The inclusion of a hinge which allowed each blade to move out of the plane of rotation alleviated one blade root stress but another, equally severe remained. Flapping motion causes the radial position of the blade centre of gravity to move inboard, requiring that the in-plane angular velocity of the blade be increased to preserve the angular momentum of the system. This results in a 2/rev periodic in-plane oscillation of the blade, which will generate in-plane harmonic stresses at the blade root. This motion is known as lead-lag oscillation. As with the alleviation of the stress at the blade root induced by flapping, the simplest solution to the lead-lag problem was to use a hinge aligned with the rotor disc plane as the blade-hub attachment. It is assumed in

RASCAL that the flap and lead/lag hinges are co-located at a radial distance eR, where e is typically $O(0.03)$ and R is the blade radius.

Mathematically, the coupled blade equations of motion are derived directly from Newton's second law for angular motion,

$$\underline{\dot{H}}_{bl} + \left(\underline{\omega}_{hg}^{bl} \times \underline{H}_{bl}\right) = \underline{M}_{bl}^{aero} + \underline{M}_{bl}^{rest} \tag{2.4.1}$$

where $\underline{M}_{bl}^{aero}$ is the vector of aerodynamic torques and $\underline{M}_{bl}^{rest}$ is the vector of hinge restraints. It is practical and desirable to compute the motion of each blade with respect to the hinge axes. Equation (2.4.1) above refers to motion about the blade centre of mass, therefore to alter the equation such that blade motion is defined about the hinge, additional terms involving the hinge accelerations must be included.

$$\underline{\dot{H}}_{bl} + \left(\underline{\omega}_{hg}^{bl} \times \underline{H}_{bl}\right) - m_{blade}\left(\underline{r}_{blcg} \times \underline{a}_{hg}^{bl}\right) = \underline{M}_{bl}^{aero} + \underline{M}_{bl}^{rest} \tag{2.4.2}$$

Note that because $\underline{H}_{bl} = \mathrm{I}_{bl}\underline{\omega}_{hg}^{bl}$ and the blade equations of motion should give through integration the blade angles $\{\beta, \zeta, \theta\}$, equation (2.4.2) needs to be recast slightly in terms of $\{\ddot{\beta}, \ddot{\zeta}, \ddot{\theta}\}$. By inspection of equation (2.3.8) it is apparent that the blade angles are functions of $\underline{\omega}_{hg}^{bl}$, which can be obtained from section 2.3. In addition, it is a reasonable assumption that each blade can be represented as a thin lamina. This reduces I_{bl} to a diagonal matrix whose elements are all equal to the blade flap moment of inertia.

The equations of motion expressed in this form are functions of the complex kinematic transforms from body to blade discussed in section (2.3.2). A expanded model will be presented in Chapter VI and will form the basis of the design of an IBC controller . It is the authors intent to provide greater clarity as to the extent of the coupling between rotor and fuselage through the treatment of this model, yet to be presented.

2.4.1 *Multiblade Co-ordinate Transformation.*

The blade equations of motion described above are defined in a reference frame which rotates with the blade. For most helicopters, main rotor thrust and directional control is achieved through a conventional swashplate, *figure 2.10*. Rotor control is performed by the pilot by titling the swashplate in the non-rotating reference frame through cyclic and collective pitch inputs, the common representation of which is through a truncated Fourier series which contains only mean and first harmonic terms. For conventional flight mechanics analysis and high bandwidth control law design, where the crossover frequency is selected to be in the region of coupled rotor/fuselage modes (*Brinson, et.al., 1995., Low & Garrard, 1993*), it is desirable to be able to express the motion of the rotor disc in the non-rotating reference frame. To achieve this, a Fourier series transformation is applied to all the blades in the rotor simultaneously (*Johnson 1980*).

$$\beta_0 = \frac{1}{\mathrm{N}} \sum_{i=1}^{N} \beta^{(i)} ,$$

$$\beta_{nc} = \frac{2}{\mathrm{N}} \sum_{i=1}^{N} \beta^{(i)} \cos\left(n \psi_{(i)}\right), \qquad \beta_{ns} = \frac{2}{\mathrm{N}} \sum_{i=1}^{N} \beta^{(i)} \sin\left(n \psi_{(i)}\right) \tag{2.4.3}$$

For the rotor flapping motion, the non-rotating frame degrees of freedom which are calculated in RASCAL are β_0, the coning mode and β_{1c} and β_{1s} which are the tip-path-plane-tilt degrees of freedom. The remaining degrees of freedom, namely the higher order cyclic (n>1) and the reactionless modes, are not calculated as they involve no net force or moment transfer to the rotor hub. The extraction of the non-rotating frame lead/lag degrees of freedom is performed by the same transform. The corresponding general inverse transformations are,

$$\beta^{(i)} = \beta_0 + \sum_n \left(\beta_{nc} \cos\left(n\psi_{(i)}\right) + \beta_{ns} \sin\left(n\psi_{(i)}\right)\right)$$

$$\zeta^{(i)} = \zeta_0 + \sum_n \left(\zeta_{nc} \cos\left(n\psi_{(i)}\right) + \zeta_{ns} \sin\left(n\psi_{(i)}\right)\right) \tag{2.4.4}$$

which gives the motion of the individual blades again.

The multiblade transformations can be applied to the blade equations of motion as well (*Johnson, 1980*), the primary purpose of which is to enable linear theory analysis techniques to be applied to blade motion. This process allows the designer to characterise the stability and performance characteristics in terms of widely known and well-established linear metrics, eigenvalue analysis being but one example, which is a very important tool in the design of high-bandwidth control laws. Linear models which are valid over the rotor/fuselage coupling frequencies are necessary for designing high bandwidth flight control laws which will guarantee acceptable phase and gain margins, while maintaining good tracking and disturbance rejection qualities at low frequency (*Brinson et.al., 1995*).

2.5 Rotor Wake model.

Throughout the development of RASCAL's rotor model it was assumed that the perpendicular component of blade velocity due to the rotor wake, $\boldsymbol{u}_p^{wake}$, was known. Precise calculation of this variable is critical if accurate predictions of the aerodynamic forces and moments acting upon each blade element are to be attained (*Wheatley 1937, Chen 1989*). The importance of accurately determining aerodynamic forces and moments for a simulation intended for vibration prediction was introduced and explained within the literature review of Chapter I. Also, as will be shown in Chapter III, the rotor inflow distribution couples with external atmospheric disturbances to shape the frequency response of the helicopter vibration to progressive immersion into a sharp-edged gust. Therefore, it is appropriate that the type and development of the wake model be discussed in some detail.

During the course of the research, the RASCAL perturbation dynamic inflow model was replaced by the Peters-HaQuang (non-linear Pitt-Peters) dynamic inflow model (*Pitt & Peters, 1981., Peters & HaQuang 1988*). This update had to be performed for RASCAL to comply with the demands that all aspects of the model be

state-of -the-art, which for inflow prediction within a flight mechanics simulation is currently the Pitt-Peters' model. The earlier numerical experiments were repeated to ensure that gust-induced vibration with the same observed frequency distribution continued to be present, as was indeed the case. However, the discussions on dynamic inflow will continue to be performed through the derivation of the original perturbation model, although a brief summary of the Pitt-Peters model will be presented at the end of this section.

2.5.1 Static Inflow Models.

Momentum theory assumes that the rotor can be replaced by an actuator disc which induces a pressure discontinuity across the plane of the rotor (*Prouty, 1990*). In the simplest analysis, uniform distribution of the induced velocity and axial flow through the disc are assumed (conditions which are met in the hover). Invoking the conservation of mass and momentum delivers an expression for the induced velocity at the rotor.

$$v_{i0} = \sqrt{\left(\frac{T}{2\rho A}\right)} \tag{2.5.1}$$

Equation (2.5.1) demonstrates the close coupling which exists between thrust and inflow, evident in even a simple first order analysis. In forward flight the rotor wake geometry is altered both radially and in azimuth, leading to the general first harmonic cyclic expression for inflow distribution,

$$v_i = v_{i0} + \frac{r}{R}\left(v_{1s}\sin\psi + v_{1c}\cos\psi\right) \tag{2.5.2}$$

The uniform component is again determined by the rotor thrust. The harmonic components too are influenced by the rotor thrust, but are also functions of the rotor pitch and roll moments. Both the perturbation and Peters-HaQuang inflow models assume an inflow distribution of this form.

2.5.2 *Dynamic Inflow models.*

2.5.2.1 *Perturbation model.*

Central to the perturbation model is the assumption that the inflow states vary from the momentum-predicted values by only a small amount, i.e.,

$$\begin{aligned} v_{i0} &= (v_{i0})_{mom} + \delta v_{i0} \\ v_{1s} &= (v_{1s})_{mom} + \delta v_{1s} \\ v_{1c} &= (v_{1c})_{mom} + \delta v_{1c} \end{aligned} \qquad (2.5.3)$$

where, $(v_{1s})_{mom} = (v_{1c})_{mom} = 0$. Considering harmonic components first, with reference to *figure 2.11*, the elemental momentum aerodynamic rolling and pitching moments on the rotor are:

$$\begin{aligned} dL_a &= 2\rho V_t v_i r \sin\psi dA \\ dM_a &= -2\rho V_t v_i r \cos\psi dA \end{aligned} \qquad (2.5.4)$$

where, $dA = r\,dr\,d\psi$ and $V_t = \left(\sqrt{\left(V_f^2 + (v_{i0}/k_{mom})^2\right)} + 2/3R\dot{\beta}_0 \right)$, the velocity associated with the mass flow through the rotor. Note the term due to the rate of change of rotor coning angle, $\dot{\beta}_0$. This illustrates the coupling between blade motion and the aerodynamic forces surrounding the rotor, which in turn couple to the induced velocity. Substituting equation 2.5.2 for v_i and integrating between the radial and azimuth limits gives the quasi-steady harmonic inflow components. These expressions are rendered dynamic by adding an acceleration term, vis.

$$\begin{aligned} \tau_{1s}\dot{v}_{1s} &= -v_{1s} + 2L_a/\left(\rho V_t \pi R^3\right) \\ \tau_{1c}\dot{v}_{1c} &= -v_{1c} - 2M_a/\left(\rho V_t \pi R^3\right) \end{aligned}$$

and $$\tau_{1s} = \tau_{1c} = \frac{16R}{45\pi V_t} \qquad (2.5.5)$$

The uniform component is derived in a similar way. The rotor thrust is written

$$T = T_{mom} + T_{vi}\, dv_{i0} \tag{2.5.6}$$

where T_{vi} is a derivative relating the change in thrust from a change in induced flow. In general, an analytical closed loop form of this derivative is difficult to obtain. The solution is derived numerically from the blade element calculated thrust by a central differencing method. The uniform component of induced flow is then rendered dynamic by including an acceleration term, as with the moments.

$$\tau_0 \dot{v}_{i0} = - v_{i0} + k_{mom} T \left(1 - T_{vi} \left(\frac{dv_{i0}}{dT_{mom}} \right) \right) / \left(2 \rho A V_t \right)$$

where,

$$\tau_0 = \frac{4R}{3\pi V_t c_0} \tag{2.5.7}$$

The values for the time constants are given in Chen (*1989*). The factor k_{mom} in (2.5.7) and the expression for V_t consists of two terms, $k_{mom} = k_{power}/k_{ground}$. This factor is explicitly included in the momentum thrust equation to provide a simple mechanism for including real wake effects on power such as blade vortex interaction and tip loss through a simple induced velocity variation. Inclusion of both these effects has been validated at hover from flight test data by Houston & Tartellin(*1991a*). Johnson (*1980*), gives appropriate values of k_{power} for the effects of tip loss, root cut-out and non-uniform induced velocity distribution. The factor k_{ground} is calculated by the ground effect model in RASCAL and is included to reduce the induced velocity by an amount depending on the axial distance of the rotor from the ground. From Houston (*1991b*), the ground effect factor is given by,

$$k_{ground} = 0.5 + 0.95449\, h_{dist} - 0.45513\, h_{dist}^2 \quad \Leftrightarrow \quad 0.1 < h_{dist} < 1.2 \tag{2.5.8}$$

where h_{dist} is the non-dimensionalised (with respect to rotor radius) distance between the rotor disc and the ground. In RASCAL, the ground effect model is invoked if the

airspeed is less than 20kts. A full derivation of the inflow equations is contained in Houston (*1991b*).

2.5.2.2 *Peters HaQuang model.*

The Peters HaQuang dynamic inflow model (*Peters & HaQuang, 1988*) is a non-linear incarnation of the original Pitt - Peters model (*Pitt & Peters, 1981*). In addition, the effect of a transformation from wind to rotor axes on the derivatives (or gains) is incorporated explicitly in the derivation of the model. Although strictly developed for use as a dynamic inflow model, the roots of the Peters HaQuang model, like the perturbation model, are taken from a first-order representation of static inflow:

$$\begin{Bmatrix} \lambda_0 \\ \lambda_{1s} \\ \lambda_{1c} \end{Bmatrix}_{wind} = [L] \begin{Bmatrix} C_T \\ -C_L \\ -C_M \end{Bmatrix}_{wind}. \tag{2.5.9}$$

The standard derivation of the Peters HaQuang inflow model is presented throughout the literature in non-dimensionalised form. For consistency, the same convention shall be used here. The inflow states are rendered dynamic by introducing an apparent mass term containing the time constants of the system in a simple first order differential equation form.

$$[\mathbf{M}] \begin{Bmatrix} \dot{\lambda}_0 \\ \dot{\lambda}_{1s} \\ \dot{\lambda}_{1c} \end{Bmatrix} + [\mathbf{L}]_{nl}^{-1} \begin{Bmatrix} \lambda_0 \\ \lambda_{1s} \\ \lambda_{1c} \end{Bmatrix} = \begin{Bmatrix} C_T^{wind} \\ -C_L^{wind} \\ -C_M^{wind} \end{Bmatrix}_{aero.} \tag{2.5.10}$$

where,

$$[\mathbf{M}] = \begin{bmatrix} \frac{8}{3\pi} & 0 & 0 \\ 0 & -\frac{16}{45\pi} & 0 \\ 0 & 0 & -\frac{16}{45\pi} \end{bmatrix} \tag{2.5.11}$$

and,

$$[\mathbf{L}] = \begin{bmatrix} \frac{1}{2} & 0 & \frac{15\pi}{64}\sqrt{\frac{1-\sin\chi}{1+\sin\chi}} \\ 0 & \frac{-4}{1+\sin\chi} & 0 \\ \frac{15\pi}{64}\sqrt{\frac{1-\sin\chi}{1+\sin\chi}} & 0 & \frac{-4\sin\chi}{1+\sin\chi} \end{bmatrix} \tag{2.5.12}$$

The derivation of the gain [**L**] and apparent mass [**M**] matrices (*Peters & HaQuang, 1988*) is an involved and complex affair outside of the core remit of this thesis and will thus be omitted. The inflow model will be discussed again throughout the course of this dissertation.

2.6 Fuselage Aerodynamics.

The fuselage aerodynamic forces and moments are generally obtained using wind tunnel test data decomposed into one of four forms. Polynomials in angle of attack and sideslip where the function gives the forces and moments referred to a specific reference dynamic pressure or the force and moment coefficients. A look-up table of forces and moments or force and moment coefficients at measured angles of attack and sideslip. The fuselage angle of attack and sideslip are,

$$\alpha_{fus} = \tan^{-1}\left(\frac{w}{u}\right), \qquad \beta_{fus} = \sin^{-1}\left(\frac{v}{V_f}\right) \tag{2.6.1}$$

2.6.1 Polynomial expansion.

2.6.1.1 Absolute forces and moments.

In this incarnation of the test data, the absolute values of the forces and moments are predicted by the polynomial. The coefficients of the polynomial are extracted from the wind tunnel model operating at some reference dynamic pressure.

P_{rdp}. The results of the polynomial must therefore be scaled by the reference dynamic pressure. Denoting the actual dynamic pressure by,

$$dp = \frac{1}{2}\rho V_f^2 \tag{2.6.2}$$

then the fuselage aerodynamic forces and moments are given by,

$$\boldsymbol{X}_{fus} = \frac{dp}{P_{rdp}}\left(x_{fus0} + x_{fus1}\alpha_{fus} + x_{fus2}\alpha_{fus}^2 + x_{fus3}\alpha_{fus}^3 + x_{fus4}\alpha_{fus}^4 + x_{fus5}\alpha_{fus}^5\right) \tag{2.6.3}$$

$$\boldsymbol{Y}_{fus} = \frac{dp}{P_{rdp}}\left(y_{fus0} + y_{fus1}\beta_{fus} + y_{fus2}\beta_{fus}^2 + y_{fus3}\beta_{fus}^3 + y_{fus4}\beta_{fus}^4 + y_{fus5}\beta_{fus}^5\right) \tag{2.6.4}$$

$$\boldsymbol{Z}_{fus} = \frac{dp}{P_{rdp}}\left(z_{fus0} + z_{fus1}\alpha_{fus} + z_{fus2}\alpha_{fus}^2 + z_{fus3}\alpha_{fus}^3 + z_{fus4}\alpha_{fus}^4 + z_{fus5}\alpha_{fus}^5\right) \tag{2.6.5}$$

$$\boldsymbol{L}_{fus} = \frac{dp}{P_{rdp}}\left(l_{fus0} + l_{fus1}\beta_{fus} + l_{fus2}\beta_{fus}^2 + l_{fus3}\beta_{fus}^3 + l_{fus4}\beta_{fus}^4 + l_{fus5}\beta_{fus}^5\right) \tag{2.6.6}$$

$$\boldsymbol{M}_{fus} = \frac{dp}{P_{rdp}}\left(m_{fus0} + m_{fus1}\alpha_{fus} + m_{fus2}\alpha_{fus}^2 + m_{fus3}\alpha_{fus}^3 + m_{fus4}\alpha_{fus}^4 + m_{fus5}\alpha_{fus}^5\right) \tag{2.6.7}$$

$$\boldsymbol{N}_{fus} = \frac{dp}{P_{rdp}}\left(n_{fus0} + n_{fus1}\beta_{fus} + n_{fus2}\beta_{fus}^2 + n_{fus3}\beta_{fus}^3 + n_{fus4}\beta_{fus}^4 + n_{fus5}\beta_{fus}^5\right) \tag{2.6.8}$$

2.6.1.2 Aerodynamic coefficient expansion.

When the wind tunnel data has been reduced to non-dimensional coefficient form, there is no need to factor the result by the reference dynamic pressure. However, the wetted area of the fuselage, S_{fus} becomes included in the calculation, vis.

$$\boldsymbol{X}_{fus} = dpS_{fus}(Cx_{fus0} + Cx_{fus1}\alpha_{fus} + Cx_{fus2}\alpha_{fus}^2 + Cx_{fus3}\alpha_{fus}^3 + Cx_{fus4}\alpha_{fus}^4 + Cx_{fus5}\alpha_{fus}^5) \tag{2.6.9}$$

$$\boldsymbol{Y}_{fus} = dpS_{fus}(Cy_{fus0} + Cy_{fus1}\beta_{fus} + Cy_{fus2}\beta_{fus}^2 + Cy_{fus3}\beta_{fus}^3 + Cy_{fus4}\beta_{fus}^4 + Cy_{fus5}\beta_{fus}^5) \tag{2.6.10}$$

$$Z_{fus} = dpS_{fus}(Cz_{fus0} + Cz_{fus1}\alpha_{fus} + Cz_{fus2}\alpha_{fus}^2 + Cz_{fus3}\alpha_{fus}^3 + Cz_{fus4}\alpha_{fus}^4 + Cz_{fus5}\alpha_{fus}^5) \quad (2.6.11)$$

$$L_{fus} = dpS_{fus}(Cl_{fus0} + Cl_{fus1}\beta_{fus} + Cl_{fus2}\beta_{fus}^2 + Cl_{fus3}\beta_{fus}^3 + Cl_{fus4}\beta_{fus}^4 + Cl_{fus5}\beta_{fus}^5) \quad (2.6.12)$$

$$M_{fus} = dpS_{fus}(Cm_{fus0} + Cm_{fus1}\alpha_{fus} + Cm_{fus2}\alpha_{fus}^2 + Cm_{fus3}\alpha_{fus}^3 + Cm_{fus4}\alpha_{fus}^4 + Cm_{fus5}\alpha_{fus}^5) \quad (2.6.13)$$

$$N_{fus} = dpS_{fus}(Cn_{fus0} + Cn_{fus1}\beta_{fus} + Cn_{fus2}\beta_{fus}^2 + Cn_{fus3}\beta_{fus}^3 + Cn_{fus4}\beta_{fus}^4 + Cn_{fus5}\beta_{fus}^5) \quad (2.6.14)$$

where $x_{fus\#}$ and $Cx_{fus\#}$ are the coefficients of the polynomial in absolute and aerodynamic coefficient form.

2.6.2 Tabular approach.

Here, the forces and moments generated on the blade in the wind tunnel are stored over a range of angles of attack and sideslip.

2.6.2.1 Forces and moments.

$$X_{fus} = \frac{dp}{P_{rdp}} x_{fus}^{table} \quad (2.6.15)$$

$$Y_{fus} = \frac{dp}{P_{rdp}} y_{fus}^{table} \quad (2.6.16)$$

$$Z_{fus} = \frac{dp}{P_{rdp}} z_{fus}^{table} \quad (2.6.17)$$

$$L_{fus} = \frac{dp}{P_{rdp}} l_{fus}^{table} \quad (2.6.18)$$

$$M_{fus} = \frac{dp}{P_{rdp}} m_{fus}^{table} \quad (2.6.19)$$

$$N_{fus} = \frac{dp}{P_{rdp}} n_{fus}^{table} \quad (2.6.20)$$

2.6.2.2 *Coefficient abstraction.*

$$X_{fus} = dpS_{fus} Cx_{fus}^{table} \tag{2.6.21}$$

$$Y_{fus} = dpS_{fus} Cy_{fus}^{table} \tag{2.6.22}$$

$$Z_{fus} = dpS_{fus} Cz_{fus}^{table} \tag{2.6.23}$$

$$L_{fus} = dpS_{fus} Cl_{fus}^{table} \tag{2.6.24}$$

$$M_{fus} = dpS_{fus} Cm_{fus}^{table} \tag{2.6.25}$$

$$N_{fus} = dpS_{fus} Cn_{fus}^{table} \tag{2.6.26}$$

where, x_{fus}^{table} and Cx_{fus}^{table} are the values of force interpolated from the table in absolute and coefficient form.

2.7 Fin Aerodynamics

Like the fuselage aerodynamics the fin aerodynamics are generally available from wind tunnel tests, existing in form identical to that of the fuselage aerodynamics. It is assumed in the model that the aerodynamics are functions only of the fin sideslip angle, β_{fin}. Up to three fins can be modelled and the following equations are the general form for all three.

The sideslip angle of the fin is,

$$\beta_{fin} = \beta_s + \sin^{-1}\left(\frac{r(x_{fin} - x_{cg}) + v}{V_{ffin}}\right) \tag{2.7.1}$$

and the dynamic pressure across the fin is

$$dp_{fin} = \frac{1}{2}\rho V_{ffin}^2 \tag{2.7.2}$$

where,

$$V_{ffin} = \sqrt{\left(u^2 + \left(r\left(\underline{x}_{fin} - \underline{x}_{cg}\right) + v\right)^2 + w^2\right)} \tag{2.7.3}$$

The polynomial functions of the forces and moments are similar to those presented in the development of the fuselage aerodynamics. Consequently as the reproduction of equations (2.6.3-26) would yield no additional insight into the prediction of the fin aerodynamics, no such duplication will be made here.

2.8 Tailplane Aerodynamics

The calculation of the tailplane aerodynamics is performed in the same manner as the fuselage and fins. The effect of sideslip on the tailplane aerodynamics is minimal therefore it is assumed in the model that the aerodynamics are functions only of the tailplane angle of attack. Due to the pitching motion of the aircraft and the possible impingement of the rotor wake upon the tailplane, the dynamic pressure and angle of attack may differ considerably from the fuselage values. In addition, the tailplane may be rigged at some angle or indeed actively controlled. The tailplane angle of attack is,

$$\alpha_{tp} = \alpha_s + \tan^{-1}\left(\frac{w - q\left(x_{fin} - x_{cg}\right) - k_{tp}v_{i0}^b}{u}\right) \tag{2.8.1}$$

where α_s is the geometric incidence angle of the tailplane; k_{tp} is the tailplane induced velocity factor and v_{i0}^b is the uniform component of induced velocity in airframe body axes. The dynamic pressure across the tailplane is,

$$dp_{tp} = \frac{1}{2}\rho\left(u^2 + v^2 + \left(w - k_{tp}v_{i0}^b\right)^2\right) \tag{2.8.2}$$

Typically, the tailplane induced velocity factor, k_{tp} has a value of between 1.5 and 2 assuming the tailplane is immersed in the wake. When the tailplane is operating outwith the wake it's value is zero.

2.9 *Engine and Transmission Model*

In most rotorcraft an engine governor automatically adjusts engine torque to suit the required atmospheric or manoeuvre conditions. At least, this is the case with gas turbine powered rotorcraft, unlike piston powered helicopters which usually require the pilot to provide engine torque compensation. However, the presence of an engine governor means, in general, that the engine and transmission models cannot be treated separately. An engine governor arrangement is employed in RASCAL, although provision exist for accommodating the engine/transmission relationship found in piston powered helicopters.

The equation for the engine demanded torque is presented below.

$$q_d = k_e(\Omega_d - \Omega) + q_p \qquad (2.9.1)$$

It is apparent from equation (2.9.1) that both gas turbine and piston engine governor systems can be dealt with by neglecting either one of the terms on the right hand side. The engine governor demanded torque, q_d, for a gas turbine powered helicopter is equal to the engine/rotorspeed droop gain, k_e multiplied by the difference between the nominal governed rotorspeed, Ω_d and the actual rotorspeed, Ω for each rotor. The droop gain gives an indication of the reduction in steady state rotorspeed between autorotation and full power. This is to prevent any 'hunting' that may be initiated should the control system attempt to maintain constant rotorspeed (*Padfield, 1996*). For piston powered aircraft, the governor demanded torque is just that demanded by the pilot, q_p.

The transmission describing equation for a geared rotor system with primary rotor designated (1) and secondary rotor (2) is then,

$$\dot{\Omega} = \left(\underline{q_e} + N^r_{hub}(1) + \eta N^r_{hub}(2)\right) / I^{rotor} \tag{2.9.2}$$

where $N^r_{hub} = f^n\left(\dot{\Omega}, \dot{p}, \dot{q}, \dot{r}, \ddot{\beta}, \ddot{\zeta}\right)$. The engine describing equation is simply a first order lag with a specified time constant.

$$\dot{q}_e = \frac{q_e}{\tau_e} + \sum_{i=1}^{2}\left(\frac{\Omega(i)}{|\Omega_d(i)|}\right)\frac{q_d}{n_e \tau_e} \tag{2.9.3}$$

Modelling of counter clockwise rotating rotors is achieved by stipulating a negative rotorspeed. Consequently, the absolute value of the nominal rotorspeed is used to ensure that the engine torque is always positive during powered flight.

2.10 Atmosphere Model.

The atmosphere model is used to calculate the air density and local speed of sound from environmental information such as pressure setting, outside air temperature and altitude. A standard lapse rate approach is employed, Houston (*1991b*),

$$\left(\frac{\rho}{\rho_1}\right) = \left(\frac{T_2}{T_1}\right)^{\left(\frac{g-LR}{LR}\right)} \tag{2.10.1}$$

where subscript *1* denotes the reference point, L is the lapse rate and R is the gas constant. The air temperature at the aircraft altitude is then,

$$T_2 = T_1 - Lh \tag{2.10.2}$$

From Boyle's and Charles' laws,

$$\rho_1 = p_1 R T_1 \tag{2.10.3}$$

therefore,

$$\rho_1 = \frac{p_1}{R(T_2 + Lh)}\left(\frac{T_2}{T_2 + Lh}\right)^{\left(\frac{g - LR}{LR}\right)} \tag{2.10.4}$$

alternatively,

$$\rho_1 = \frac{100\,QNH}{R(273.15 + OAT + Lh)}\left(\frac{273.15 + OAT}{273.15 + OAT + Lh}\right)^{\left(\frac{g - LR}{LR}\right)} \tag{2.10.5}$$

where $OAT = T_1 - Lh$ and QNH is the pressure setting. The local speed of sound was presented in equation(2.3.17) but can be expressed alternatively as,

$$a = \sqrt{\gamma R T_2} = \sqrt{\gamma R(273.15 + OAT)} \tag{2.10.6}$$

2.11 Chapter Summary and Discussion.

A detailed description of the simulation model RASCAL has been presented. The full level of mathematical complexity required in the derivation of such a model has been omitted for reasons of brevity, although all of the key concepts in the simulation have been discussed.

It is clear that the intended purpose of RASCAL is that of a flight simulation tool and not conventional vibration analysis. In this respect, the two prime areas for concern are the omission of aeroelastic influences in the rotor blade loads calculations and the use of a momentum based inflow model (whether perturbation or Peters-HaQuang). It has been well documented throughout the literature (*Johnson, 1980; Padfield, 1996*) that a rotor model using a prescribed or free wake coupled with an aeroelastic model utilising several high order mode shapes is required for accurately predicting high frequency blade loading (*table 2.1*). However, these techniques are complex and computationally intensive and would require significant development time to assimilate them successfully within the architecture of RASCAL. The omission of these techniques would seem to prejudice RASCAL against vibration analysis, however normal vibration levels are *not* the primary subject of this investigation.

As will be explored in greater depth in the following chapter, the vibration which is generated by *discrete* gust-induced loading is very different in amplitude and frequency to that which is generated by conventional means.

CHAPTER III

Integration of a Gust Module within RASCAL.

It is the purpose of this chapter to present a method for integrating the effects of external atmospheric disturbances within the framework of a RASCAL simulation. The chapter will begin by detailing the algorithm used to assimilate gust effects within the simulation and the rationale behind the chosen approach. By flying the model through a simple gust shape, the algorithm is verified against previously published results. After successfully observing the defining characteristic of the vibratory gust response, a mathematical explanation is formulated and tested against RASCAL results.

3.1 What is Atmospheric Turbulence?

Atmospheric turbulence is characterised by a significant number of coupled parameter changes (pressure, velocity, density etc.), occurring in the airflow in a locally structured but globally random pattern. Such fluctuations in the airflow change the angle of attack and relative velocity of the airstream seen by the lifting surfaces of the aircraft. Consequently, the aerodynamic forces and moments generated by each surface deviate from trim in a dynamic, pseudo-random fashion. All of the degrees of freedom, (or states), of the helicopter (or simulation), are altered by the effects of turbulence, either directly or indirectly, as will become apparent later.

Incorporating such a highly complex phenomenon into a rotorcraft simulation model may seem daunting at first, but several assumptions can be invoked to simplify the process. The first assumption is that the helicopter does not significantly influence the structure of the turbulence field, locally preserving the stationarity of the random process. It is assumed that the helicopter, which generates a large, aerodynamically 'dirty' wake, imparts negligible changes in the structure, both locally and globally, of the turbulence field. Although this assumption is a substantial simplification of the interaction between helicopter and environment, it is perfectly valid for flight mechanics purposes, where the *cumulative* effect of the turbulence field on the trajectory of the aircraft is retained. This approach is also valid for the type of turbulence-induced vibration analysis which is to follow, as a statistically valid spatial and temporal structure is retained in the gust. Secondly, it is assumed that the patch of turbulence under inspection can be completely described at a single point in time by the velocity field associated with it. Consider the velocity seen by a component of the aircraft (blade, fuselage, tailplane etc.) when immersed in a patch of atmospheric turbulence. The local velocity perturbations modify the dynamic pressure (and hence the aerodynamic forces) of the nearest helicopter component as follows.

$$\underline{u} = \underline{u}_{component} - \underline{u}_{g} \tag{3.1.1}$$

where both velocities are defined with respect to the component axes set. The negative sign is necessary as $\underline{u}_g$ is an aerodynamic velocity, which is defined to act in the opposite direction to the motion of the body. For example, if a body is moving through air at a velocity u in the positive x-direction, then the airflow seen by the body is $-u$. Therefore, a headwind increases the effective local airspeed and a tailwind decreases it. *Figure 3.1* illustrates how a turbulence field, which has a spatial velocity vector, $\underline{u}_g = (u_g, v_g, w_g)^T$, at a position in space coincident with the aerodynamic centre of a blade element, influences the aerodynamic forces seen by that section. Inspection of *figure 3.1* shows that the gust vector (which has been transformed into blade axes) alters both the magnitude of the local air velocity and the angle of attack of the element. Generally for a vertical up-gust ($-w_g$), these effects combine to increase the magnitude and alter the inclination of the lift, drag and pitching moment forces (lift and drag only are shown in *figure 3.1*).

Rotorcraft turbulence modelling has evolved, in many respects, from the techniques applied to gust analysis of fixed-wing aircraft. Early investigations into helicopter gust response assumed the turbulence velocity vectors at all points on the rotor disc were identical to that sampled at the rotor hub (*Madhaven & Gaonkar, 1989*). However, to accurately predict the vibratory gust response, it is necessary to include the effects of the atmosphere in *every* aerodynamic force calculation, including the rotor blades on all rotors. Such an approach is called blade-fixed sampling (*Madhaven & Gaonkar, 1989; Riaz et.al., 1993*), the necessity of which is demonstrated in the following example. Consider the progressive immersion of the main lifting rotor into an infinitely repeating 1-COS discrete gust, *figure 3.2*, (*Costello et.al., 1992*). Sampling the turbulence at the hub gives the gust velocity distribution (shown here as a function of time) by,

$$u = \frac{1}{2} u_0 \left(1 - \cos \left(\frac{2\pi \left(V_f + V_{mw} \right) t}{2H_g} \right) \right) \tag{3.1.2}$$

By sampling at radial stations along each blade, the aerodynamic forces local to each blade element are modified by the component of the turbulence velocity field whose spatial location is coincident with that blade station. This introduces a rotational component to the gust distribution as follows,

$$u = \frac{1}{2} u_0 \left(1 - \cos \left(\frac{2\pi \left\{ \left(V_f + V_{mw} \right) t - R\cos \Omega t \right\}}{2H_g} \right) \right) \tag{3.1.3}$$

Figure 3.3 compares the two sampling techniques for flight speeds of 5, 30 & 100 knots. At lower airspeeds, a significant vibratory element is introduced to the rotor loads transmitted to the fuselage. Consequently, as this effect must be replicated in any realistic simulation of gust-induced vibration, it is imperative that a blade fixed sampling approach be adopted.

The gust velocity vector discussed above is defined in the atmospheric axes set which can be assumed, without any appreciable loss of accuracy, to be coincident with the North-East-Down (NED) earth-fixed inertial axes set, *figure 2.2*. This is the same

axes set upon which computation of the navigation equations within RASCAL are performed. Therefore, a series of axes transformations have to be applied to the gust vector, to place the elemental velocities (u_g, v_g, w_g) into an axes set which is coincident with the effected aircraft component. To illustrate this procedure, first consider the most complicated transformation, modification of the aerodynamic environment surrounding a blade element.

3.2 Transformation of the gust velocities to blade axes.

3.2.1 Blade element position.

Before it is possible to modify the aerodynamic properties of the airflow surrounding any helicopter component, the position of that component in inertial space has to be calculated. The conventional approach to this problem may perhaps be to start in the inertial frame of reference and work out to the desired component. However the reverse of this process, starting from the component position in native axes and working back to the position in inertial axes, is equally valid. Indeed, this is the preferred option for the proposed enhancement to RASCAL. The formalisation of the reversed method in the context of gust modelling was first proposed by Houston and Hamilton (*1993*). In the following development, it is worth noting that the subscripts refer to the position of the component and the superscripts to the current axes set.

The position of a co-located flap, lag and feather hinge with respect to a blade element ***i,*** is given in blade axes as

$$\underline{\boldsymbol{x}}_{hg}^{bl} = \left[0\ (R_i + \delta R_i/2)\ 0\right]^{\mathrm{T}} \tag{3.2.1}$$

The position of the hinge with respect to the blade element ***i*** in hinge axes is.

$$\underline{\boldsymbol{x}}_{hg}^{hg} = \boldsymbol{T}_3^{T}\ \underline{\boldsymbol{x}}_{hg}^{bl} \tag{3.2.2}$$

where T_3 transforms a vector from hinge to a set of blade axes. (Since the transformation is orthogonal, the inverse of the matrix is simply it's transpose). The transformation direction cosine is given by

$$T_3^T = \begin{bmatrix} cos\zeta & -cos\beta sin\zeta & sin\beta sin\zeta \\ sin\zeta & cos\beta cos\zeta & -cos\zeta sin\beta \\ 0 & sin\beta & cos\beta \end{bmatrix} \tag{3.2.3}$$

The position of the hub with respect to the blade element i in hinge axes is

$$\underline{x}_{hub}^{hg} = \underline{x}_{hg}^{hg} + [0\ eR\ 0]^T \tag{3.2.4}$$

The position of the hub with respect to the blade element i in hub (i.e. non-rotating axes) is

$$\underline{x}_{hub}^{hub} = T_2^T\ \underline{x}_{hub}^{hg} \tag{3.2.5}$$

where T_2^T is the transformation direction cosine from the non-rotating to rotating hub frame of reference and,

$$T_2^T = \begin{bmatrix} sin\psi & cos\psi & 0 \\ -cos\psi & sin\psi & 0 \\ 0 & 0 & 1 \end{bmatrix} \tag{3.2.6}$$

The position of the hub with respect to the blade element i in airframe axes is then

$$\underline{x}_{hub}^{a/c} = T_1^T\ \underline{x}_{hub}^{hub} \tag{3.2.7}$$

where T_1^T is the transformation direction cosine from non-rotating hub axes to airframe body axes through the shaft tilt angles and is given by

$$\boldsymbol{T}_I^T = \begin{bmatrix} cos\theta_s & sin\theta_s sin\phi_s & sin\theta_s cos\phi_s \\ 0 & cos\phi_s & -sin\phi_s \\ -sin\theta_s & cos\theta_s sin\phi_s & cos\theta_s cos\phi_s \end{bmatrix} \tag{3.2.8}$$

Now, the aircraft equations of motion are referred to an axes system that is aligned with the aircraft body axes but whose origin is at the aircraft centre of mass. The position of the centre of mass with respect to the blade element ***i*** in aircraft axes is

$$\underline{\boldsymbol{x}}_{cg}^{a/c} = \underline{\boldsymbol{x}}_{hub}^{a/c} - \underline{\boldsymbol{x}}_{hub} + \underline{\boldsymbol{x}}_{cg} \tag{3.2.9}$$

The position of blade element ***i*** with respect to the centre of mass in aircraft axes is then simply

$$\underline{\boldsymbol{x}}_{bl}^{a/c} = - \underline{\boldsymbol{x}}_{cg}^{a/c} \tag{3.2.10}$$

Finally the position of blade element ***i*** with respect to the Earth origin in earth axes is

$$\underline{\boldsymbol{x}}_{bl}^{E} = \boldsymbol{M}^T \underline{\boldsymbol{x}}_{bl}^{a/c} + \underline{\boldsymbol{x}}_E \tag{3.2.11}$$

and,

$$\boldsymbol{M}^T = \begin{bmatrix} cos\theta cos\psi & (sin\phi sin\theta cos\psi - cos\phi sin\psi) & (cos\phi sin\theta cos\psi + sin\phi sin\psi) \\ cos\theta sin\psi & (sin\phi sin\theta sin\psi + cos\phi cos\psi) & (cos\phi sin\theta sin\psi - sin\phi cos\psi) \\ -sin\theta & sin\phi cos\theta & cos\phi cos\theta \end{bmatrix} \tag{3.2.12}$$

Back-substitution then gives

$$\underline{\boldsymbol{x}}_{bl}^{E} = \boldsymbol{M}^T \left[\left(\underline{\boldsymbol{x}}_{hub} - \underline{\boldsymbol{x}}_{cg} \right) - \boldsymbol{T}_1^T \left[\boldsymbol{T}_2^T \left[\boldsymbol{T}_3^T \left[0 \left(R_i + \delta R_i \right) 0 \right]^T + \left[0 \, eR \, 0 \right]^T \right] \right] \right] + \underline{\boldsymbol{x}}_E \tag{3.2.13}$$

The set of experimental results against which the enhanced RASCAL simulation is to be tested (*Houston & Hamilton, 1993*), used a vertical sharp-edged gust as the

turbulence medium. It follows then that for the specific case of a sharp-edged gust, a blade element will be immersed in turbulence if

$$\underline{x}_{bl}^{E} \geq \underline{x}_{g}^{E} \tag{3.2.14}$$

where $\underline{x}_{g}^{E}$ is the location of the gust front in Earth axes. In the more general case, the position of the aerodynamic centre of blade element i, or indeed of any other component, can be compared with a known position / velocity relationship for the turbulence field. Now that the position of each blade element is known with respect to inertial space and a gust component can be assigned, the transformation of the gust velocity vector from inertial axes into blade axes (or the native axes set of any other component under investigation) remains.

3.2.2 Gust velocity in blade axes.

The elements of the gust vector are converted from atmospheric axes (assumed coincident with North-East-Down axes) to airframe axes through the following transformation.

$$\underline{u}_{g}^{a/c} = M\,\underline{u}_{g}^{E} \tag{3.2.15}$$

The transformation of the gust velocity components from aircraft to blade axes is then accomplished by series of similar operations; from aircraft to non-rotating hub axes; from non-rotating to rotating hub axes; from rotating hub axes to blade axes. The total transformation is then

$$\underline{u}_{g.}^{bl} = T_3 T_2 T_1 M\,\underline{u}_{g}^{E} \tag{3.2.16}$$

The transformation matrices T_3, T_2, T_1 & M were given in Chapter II.

3.2.3 *Non-rotating components.*

The corresponding equations for the fuselage, tailplane and fins are derived in a similar manner. For the special case of a sharp-edged gust, the fuselage will be immersed in the gust if

$$\underline{x}_E \geq \underline{x}_g^E \tag{3.2.17}$$

The fuselage aerodynamics are therefore augmented by the components of the gust vector collocated with the aircraft centre of gravity and expressed in body axes thus.

$$\underline{u}_g^{a/c} = M\,\underline{u}_g^E \tag{3.2.18}$$

The position of the tailplane in earth axes is given by,

$$\underline{x}_{tp}^E = M^T\left(\underline{x}_{tp} - \underline{x}_{cg}\right) + \underline{x}_E \tag{3.2.19}$$

and will have penetrated the gust front if

$$\underline{x}_{tp}^E \geq \underline{x}_g^E \tag{3.2.20}$$

Similarly, each fin will be augmented by the gust components occupying the inertial position given by,

$$\underline{x}_{fin}^E = M^T\left(\underline{x}_{fin} - \underline{x}_{cg}\right) + \underline{x}_E \tag{3.2.21}$$

if,

$$\underline{x}_{fin}^E \geq \underline{x}_g^E \tag{3.2.22}$$

The forces acting on the tailplane and fins are expressed in body axes. The gust velocities at these components are then transformed into the component axes by using equation (3.2.18). Having now provided a mechanism for integrating the effects of a changing aerodynamic environment within the core of the simulation, the response of a helicopter to a simple gust field will now be presented.

3.3 *The response of a single main and tailrotor helicopter to a sharp-edged gust.*

To test the performance of the encoded algorithm, it was decided to attempt to emulate the results published by Houston & Hamilton (*1993*) as an algorithm verification procedure. Azuma & Saito (*1982*) was the only other published work the author could find in the literature, from either computer simulation or experimental sources that documented the unexpected shape to the vibration PSD induced by a sharp-edged gust. Here progressive immersion in a sinusoidal gust was studied and the frequency split around N/rev was observed but attributed to the gust frequency. The lack of published experimental data is not altogether unexpected, as it is unlikely that the frequency split will be observed when applying conventional analysis techniques to flight test data. In most experiments, long segments of data are Fourier transformed to give an average response spectrum, (*Hoblit, 1988*). With this type of analysis, the ever-present N/rev vibration will typically contain more energy when averaged over the data record than the vibration induced by the gust. Indeed, this was shown in the results of Azuma & Saito (*1982*). Consequently, in many operational cases the gust-induced vibration signature will be engulfed by the bandwidth and leakage of the N/rev spike. However, by independently generating gust-induced vibration responses and by thoroughly analysing and interpreting the results, some degree of verification will have been obtained.

The Aerospatiale Super Puma, *figure(A.1)*, was used as the test aircraft in the simulations. It is a medium sized, twin engine helicopter with a conventional single main and tailrotor configuration. The four blades on the main rotor were each modelled by 8 blade elements and attached to the hub via collocated flap and lag hinges offset from the centre of rotation. The tailrotor has five blades and no lag hinges. The mass and inertia data is given in *table 3.1*.

A 2.5 ms^{-1} up-gust ($-w_g$) was positioned between 5 and 15 metres (depending on airspeed) ahead of the Puma. Four experiments were conducted with the aircraft flown at 5, 10, 15 and 20 knots into the gust. *Figure 3.4* shows the time histories of the body axes vertical acceleration as the helicopter progressively enters the gust. A significant vibratory component has been introduced to the helicopter response, which is a direct

result of employing blade-fixed sampling, as was discussed earlier in §3.1. The amplitude of the vibration is slightly less than that observed by Houston & Hamilton(*1993*), but the power spectral density plots of each time history, combined in *figure 3.5*, show the frequency split around N/rev. The split becomes more pronounced and the peak energy contained within the signal decreases as the relative airspeed between gust front and rotor disc increases. This distribution occurs because the length of time the velocity discontinuity (gust front) acts upon the rotor disc is inversely proportional to the helicopter velocity, i.e. the number of 'strikes' each blade has with the gust front during the immersion reduces with increasing relative velocity. From Parseval's theory of energy equivalence in the time and frequency domains (*Press et.al., 1992*), fewer 'strikes' will result in reduced amplitude in the PSD, as observed.

Application of Parseval's theory and a heuristic understanding of the physics involved has yielded a meaningful and mathematically correct explanation for the amplitude variations in the PSD distribution of *figure 3.5*. The next section will perform a similar rigorous analysis of the position of the frequency split.

3.4 Analysis of the Gust Vibration Signature.

Harmonic analysis of the progressive immersion of the Puma into a sharp-edged gust has shown an interesting and unexpected phenomenon in the characteristics of the predominant vibratory forcing frequency. The presence of a gust-induced split about N/rev could be significant for many design problems, such as the design of the passive vibration isolators or the active vibration control laws discussed in Chapter I. The energy analysis of the previous section has explained the amplitude distribution of *figure 3.5*. The remainder of this section will present a similar exercise designed to establish the extent of the deviation from N/rev.

Consider *figure 3.6*. Point 1 on the diagram represents the time at which an element of blade 1, a distance *r* from the hub, becomes immersed in the gust. Point 2 represents the instant in time in which an identical blade element on blade 2 (where

blade 2 lags blade 1 by $2\pi/N$ radians) encounters the gust. The time taken to go from point 1 to point 2 is given by $T - \Delta t$, where

$$T = \frac{2\pi}{N\Omega} \tag{3.4.1}$$

is the period associated with the fundamental blade passing frequency of the rotor. Δt is the amount of time by which the fundamental period is changed due to the relative velocity between the hub and the gust front. Heuristically, a positive relative velocity (defined as $V_{rel} = V_{hub,p} - V_{gust,p}$) causes the blades on the advancing side of the rotor to '*see*' the gust front faster than every T seconds, i.e. with frequency $1/(T-\Delta t)$ Hz. On the retreating side, each successive blade encounters the gust front discontinuity at a greater azimuth angle than the preceding blade, thus the time between successive encounters is increased, leading to a frequency of $1/(T+\Delta t)$ Hz. The key to finding the amount by which the vibratory forcing frequency has shifted from N/rev now reduces to the problem of establishing an expression for Δt.

3.4.1 Time Domain Calculation of the Phase Shift.

To derive an analytical expression for Δt consider the special case when $x_{g,1} = r$ and blade 1 has an azimuth angle of 180°. *Figure 3.7* illustrates this idea. From *figure 3.7*, it may be shown that

$$x_{g,2} = r - V_{rel}(T - \Delta t) \tag{3.4.2}$$

also,

$$x_{g,2} = r\cos(\Delta\psi) \tag{3.4.3}$$

$\Delta\psi$ is the non-dimensional time representation of Δt and is given as,

$$\Delta\psi = \left(\frac{2\pi}{N}\right) - \psi_2 \tag{3.4.4}$$

But, with $\psi_2 = \Omega(T - \Delta t)$, then by equating (3.4.2) and (3.4.3) and substituting for $\Delta\psi$ we get,

$$\Delta t = T - \frac{r}{V_{rel}}\left(1 - cos\left(\frac{2\pi}{N} - \Omega(T - \Delta t)\right)\right) \qquad (3.4.5)$$

Equation (3.4.5) can be solved for Δt using Newton-Rhapson iteration or some equivalent technique (*Press, et.al., 1992*). Upon establishing Δt, the vibratory forcing frequency is given by,

$$F_{/rev} = \frac{2\pi}{\Omega(T-\Delta t)} = \frac{N}{\left(1 - \frac{N\Omega}{2\pi}\Delta t\right)} \qquad (3.4.6)$$

The equations shown are those derived for the higher frequency lobe of the vibration split. For the estimation of the low frequency component, simply substitute $(T + \Delta t)$ for $(T - \Delta t)$ in equation (3.4.5). It is expected that the outboard blade elements (which have the highest dynamic pressure), will be the most severely effected by the gust front discontinuity. Therefore, to test the performance of the prediction algorithm, a nominal blade element radius, r, of 7m was chosen along with a rotorspeed (Ω) of 27 rad/s. *Figure 3.8* illustrates the predicted values of the frequency split for relative velocities of 5, 10, 15 and 20 knots.

By comparing the results in *figures 3.5 and 3.8*, the prediction based on equation (3.4.6) is accurate to within ±15% of the total deviation in frequency from 4/rev over the low speed range. This is an excellent correlation particularly considering the fidelity of the mathematics used to estimate the vibration response of the simulation. There are several possible reasons for the error, which include,

i. The changes in forward airspeed due to the effect of the gust. This will reduce the relative velocity between gust front and helicopter component and so change the value of Δt.

ii. The changes in pitch attitude induced by the gust, which in conjunction with an aft flap of the disc alters the distance between blade element and gust front.

iii. Changes in rotorspeed and/or lead-lag motion.

iv. Deviation in heading caused by the gyroscopic precession of the main rotor, which will generate lateral flap in response to the longitudinal flap induced by the gust. This will roll the helicopter in addition to the gust-induced pitching motion and will therefore yaw the aircraft, through the kinematic coupling of the orthogonal axes.

It is obvious then that the only way to improve the accuracy of the prediction is to radically increase the complexity of equation (3.4.5) to include rotor dynamics.

3.5 *Chapter summary and discussion.*

Deriving a mathematical basis for the vibration split has in part verified and most definitely strengthened the findings of Houston & Hamilton. As a result of this work there now exists a strong mathematical and heuristic hint that the low velocity frequency split about N/rev present in *figure 3.5* is a real, measurable, physical phenomenon. The lack of corroborating published work which could be unearthed in the literature review of the field was at first disappointing but expected. This is because the standard practice for analysing the frequency content of experimental or flight test data is to use data windows of several minutes duration, whereby any split present will be swamped by the underlying N/rev vibration in the averaging process. In addition, for flight test trials it would be necessary for the aircraft to encounter a sufficiently severe sharp-edged gust to correlate upon, which is highly unlikely without numerous flight trials, (which is an expensive process). Therefore, the logical next stage in the transformation of RASCAL to HISAT is to increase the fidelity of the turbulence model in the simulation and test whether the frequency split is still observed. This will be the topic of the next chapter.

CHAPTER IV

The Development of Advanced Turbulent Environments.

The previous chapter has illustrated the mechanism whereby changes in the aerodynamic environment surrounding the helicopter can be incorporated within a simulation. In this chapter, the next step is taken to generate and assimilate complex turbulence fields within RASCAL.

4.1 Atmospheric Turbulence Modelling.

The study of atmospheric turbulence for modelling purposes is a very complex area of research, attracting interest from research and development groups concerned with a variety of aeronautical applications, (*Judd & Newman, 1977; Hoblit, 1988; Jones et.al., 1993 and Hess, 1995*). The helicopter (and rotorcraft in general) presents a unique problem in accurately simulating response to turbulence. Not only does the statistical occurrence of turbulent velocity fluctuations have to be predicted, the physical structure of each gust has a profound impact on the aircraft response, particularly the response to higher frequency disturbances.

For any detailed simulation of an airborne vehicle encountering atmospheric disturbance, a crucial factor in the analysis is the accuracy with which the atmospheric turbulence model predicts spatial and temporal variations of gust velocity within the turbulence field. This is especially true for simulations tailored to investigate the

response of aircraft to disturbances across a large frequency range, typically 0-20Hz. Such a high required bandwidth enables the simultaneous development of coupled time responses of the fuselage rigid body dynamic modes, rotor blade flapping (and lagging) modes and main rotor vibration. Structuring a turbulence field that can be used to excite all of these dynamic modes simultaneously by conventional means is a very complex task (*Riaz, et.al., 1993*).

Traditional approaches to modelling atmospheric turbulence are largely dependent on the intended application of the model. For example, accurately determining the shape (gradient, intensity, maximum expected amplitude etc.) of high energy, discrete bursts of turbulence will be required for a limit load analysis. The analysis of a structured patch of turbulence as a singular event is known as *discrete* gust modelling. Alternatively, the frequency and corresponding amplitude at which the vehicle is subjected to continuous atmospheric load changes will be data required for determining the aeroelastic response of the aircraft. In particular, this technique is especially useful when estimating the likelihood of exciting resonance in one of the fuselage, blade or other structural modes. To perform this type of analysis effectively the atmosphere is generally modelled as a *continuous* stochastic process with *a priori* defined statistical properties. The requirements imposed on any candidate turbulence modelling scheme suitable for generating turbulence-induced vibration require facets of both the discrete and continuous approaches. Consequently, the simplifying assumptions, algorithms and techniques involved and the relative merits of both approaches will be presented and discussed in the following sections, before a novel method for achieving symbiosis of discrete and continuous turbulence is presented.

4.2 Techniques and Limitations of Existing Turbulence Models.

4.2.1 Modelling the Atmosphere Using Discrete gusts.

Physically, the variations of velocity in a turbulent flow, sampled at a fixed point in space, are due to the velocity distributions associated with discrete vortices (or smaller, turbulent eddies) convected past that point by the mean airflow. The

corresponding velocity component has both spatial and temporal co-ordinates represented in the inertial, or earth-fixed, co-ordinate system as $\underline{u}_g(x,y,z,t)$. There are three main types of gust shape used to emulate discrete eddies in the flow; the step, the ramp and the 1-COS discrete gusts (*figure 4.1*). The step gust (or sharp-edged gust) is modelled as a discontinuous change in gust velocity across a plane in 3-D space. For the particular case of the sharp-edged gust used in §3.3, the gust field can be described mathematically as follows,

$$\underline{u}_g(x) = \begin{cases} 0 & x < x_o \\ \underline{u}_{g_{max}} & x \geq x_o \end{cases} \quad . \qquad (4.2.1)$$

where x_o is the location of the gust front, measured longitudinally from the starting point of the simulation. Similarly, the ramp profile has a linear blending region between the plane of the gust front and the point of maximum amplitude at the gradient distance H_g. The ramp profile tends to the step profile in the limit $H_g \rightarrow 0$ thus.

$$\underline{u}_g(x) = \begin{cases} 0 & x < x_o \\ \dfrac{x}{H_g - x_0}\underline{u}_{g_{max}} & x_o \leq x \leq H_g \\ \underline{u}_{g_{max}} & H_g < x \end{cases} \qquad (4.2.2)$$

However, the most commonly used discrete gust representation is that of the 1-COS gust profile. The progression of the gust velocity as a function of distance travelled to the rear of the gust front, x, is given by,

$$\underline{u}_g(x) = \begin{cases} 0 & x < x_o \\ 0.5\,\underline{u}_{g_{max}}\left(1-\cos\left(2\pi x/2H_g\right)\right) & x \geq x_o \end{cases} \qquad (4.2.3)$$

The 1-COS gust is popular as it provides a gradual change in gust velocity, avoiding the sharp nonlinearities present in the piecewise linear step and ramp profiles. Such a description has been deemed to be more representative of an actual gust velocity profile (*Hoblit, 1988*). Discrete gust modelling is also particularly well suited to flight dynamics simulation because of the deterministic nature of the equations and

subsequent ease with which they can be incorporated into complex simulation codes. Only two parameters, the gradient distance H_g and the maximum amplitude $\underline{u}_{g_{max}}$, define the gust shape. By tuning these parameters, the 'tuned gust' can be found. This is the gust shape which provokes the maximum aircraft response, a necessary parameter for 'worst case' rigid body stability analysis.

The response of the Puma undergoing progressive immersion into a 1-COS gust at 10 knots is shown in *figure 4.2*. The gust was defined in the vertical plane with a magnitude of $-3ms^{-1}$ ($w_g = -3$), and a gradient length (H_g) of 10m. The gust-induced vibration can be clearly seen to act throughout the duration of the gust. Analysis of the signals frequency content shows that it also exhibits a split about 4/rev, *figure 4.3*. The amplitude of this vibration is less than the 10 knot progressive immersion into the sharp-edged gust of §3.3, as would be expected with a finite velocity gradient. However, the presence of the frequency split in response to a more realistic gust shape goes some way further to verifying the result.

4.2.2 Continuous turbulence models - PSD methods.

Discrete gust models represent the turbulence field through a highly localised model of the atmosphere. In general however, turbulence fields are composed of continuous, random velocity patterns containing irregular 'bursts' of ordered, high intensity activity (discrete gusts). It follows from this statement that a useful working definition of atmospheric turbulence can be stated as '*multi-directional velocity perturbations from the mean airflow*'. The magnitude and direction of the disturbance velocities are derived experimentally, usually measured in flight (for fixed wing aircraft) by a system of vanes coincident with the aircraft body axes. After filtering the aircraft rigid body response to the disturbance (and pilot inputs (*Hoblit, 1988*)), the gust velocity terms, ($u_g(x,y,z,t)$, $v_g(x,y,z,t)$ *and* $w_g(x,y,z,t)$) are obtained.

To begin the construction of a PSD model, the time domain statistical properties of the velocity terms in the turbulence field must first be extracted. The turbulence intensity, turbulence scale length and most importantly, the correlation matrix are generally sufficient to describe the statistical properties of the field. The correlation

matrix $R(t_1,t_2,r_1,r_2)$ contains the auto-correlations and cross-correlations of the gust velocities at two points in space and time,(*Costello et.al., 1992*).

$$R(t_1,t_2,r_1,r_2) = \begin{bmatrix} E[u(r_2,t_2)u(r_1,t_1)] & E[u(r_2,t_2)v(r_1,t_1)] & E[u(r_2,t_2)w(r_1,t_1)] \\ E[v(r_2,t_2)u(r_1,t_1)] & E[v(r_2,t_2)v(r_1,t_1)] & E[v(r_2,t_2)w(r_1,t_1)] \\ E[w(r_2,t_2)u(r_1,t_1)] & E[w(r_2,t_2)v(r_1,t_1)] & E[w(r_2,t_2)w(r_1,t_1)] \end{bmatrix} \quad (4.2.4)$$

where $E[]$ is the expectation operator. Analysis of flight test data (*Hoblit, 1988*), suggests that the differences in turbulence velocity sampled at a fixed spatial location but separated by time $\tau (= t_2\text{-}t_1)$ are small compared to the changes in the turbulence velocity field, valid at one point in time and sampled at two spatial locations. This leads to a simplification of the turbulence patch known as Taylor's '*frozen field*' Hypothesis. Taylor's Hypothesis roughly states that a patch of atmospheric turbulence can be assumed 'frozen in space' and convected past a point with the mean wind speed without any loss of statistical reliability. The temporal co-ordinates in the correlation matrix can then be neglected.

The Power Spectral Density (PSD) of a stationary signal may be estimated by a variety of means, one of which is the Fourier transform of the signal autocorrelation function.

$$\phi(\omega) = \frac{1}{2\pi}\int_{-\infty}^{\infty} cos(\omega\tau)R(\tau)\,d\tau \quad (4.2.5)$$

The PSD is a continuous function which represents the power contained within the signal corresponding to each of the signals' constituent frequencies, i.e. it contains the power between ω and $(\omega+\delta\omega)$: $\forall\,\omega$. Similarly, the cross-spectral density is obtained from the cross-correlation of two signals. There exists two PSD models that are most commonly used to emulate the frequency response of a given patch of turbulence. These are attributed to von Karman and Dryden respectively. These models are based on isotropic, homogeneous turbulence theory, but have empirically derived coefficients to match flight test data. To illustrate, a power spectral density curve for a typical patch

of atmospheric turbulence is shown in *figure 4.4*. The key to this type of modelling technique is to represent the Inertial Subrange (high frequency end of the spectrum) as accurately as possible, as it is turbulence in this region, which has the greatest impact on aircraft vibratory response.

The von Karman and Dryden PSD models for typical turbulent airflow are given below for vertical gusts.

$$\Phi(\Omega)=\sigma_w^2\,\frac{L}{\pi}\,\frac{1+\frac{8}{3}(1.339L\Omega)^2}{\left[1+(1.339L\Omega)^2\right]^{11/6}} \qquad \Phi(\Omega)=\sigma_w^2\,\frac{L}{\pi}\,\frac{1+3L\Omega^2}{\left[1+L^2\Omega^2\right]^2}.$$

von Karman *Dryden*

(4.2.6)

A comparison of the von Karman and Dryden vertical / lateral gust PSD's for a turbulence scale length (L) of 2500ft is shown in *figure 4.5*. From *figure 4.5*, the high frequency or inertial subrange area of the graph is more accurately predicted by the von Karman PSD, having the characteristic (-5/3) gradient predicted by Kolmolgorov's power law (*Komolgorov, 1941*). However, for practical implementations, the Dryden model is often used due to the simplicity in reconstructing a time series from the PSD. This is typically accomplished by passing a white noise signal through an appropriately shaped colouring filter (*Robinson & Reid , 1990(a&b); Pototzky, Zeiler & Perry, 1991*). A similar simple process for generating time domain data from a von Karman spectrum is not readily available (*Beal, 1993*).

Both the von Karman and Dryden models use the assumption that the sampled process (turbulence measurement) has a Gaussian (or normal) probability distribution (*Hoblit, 1988*). Gaussian probability theory is a relatively accurate model of most stationary, random processes. It is also easily extended to two or three dimensions, making it attractive for modelling purposes. The Gaussian probability distribution is given by,

$$p(y)=\frac{1}{\sqrt{2\pi}}\,\frac{1}{\sigma_y}\,e^{-\frac{1}{2}\left(\frac{y}{\sigma_y}\right)^2} \qquad (4.2.7)$$

In the probability equation, the measured variable $y(t)$ is the deviation of the process from the mean, i.e. $y(t)=(y(t)_{act} - y(t)_{mean})$. This restriction adds little complication to the calculations, as in most cases the atmospheric mean turbulence velocity, $y(t)_{mean}$ is assumed zero.

Using all of the above information the expected loads for a given flight mission can be estimated (using Rice's equation, (*Hoblit, 1998*)), if the process is stationary and Gaussian. Chen (*1972*) has shown that atmospheric turbulence is not strictly Gaussian, as shown by the leptokurtic kurtosis of the measured probability distribution in *figure 4.6*, which biases the distribution towards higher intensity activity. This should explain why pilots flying simulators using a Gaussian probability distribution report that the turbulence generated is 'too continuous', i.e. there are too few intermittent discrete events. Despite this, the Gaussian assumption is still widely used in many commercial flight simulators (*Robinson & Reid , 1990(a&b); Beal, 1993*).

4.2.3 Statistical Discrete Gust (SDG) Method.

The statistical Discrete Gust method was pioneered by Jones at the R.A.E. in the 1960's & 70's (*Jones, 1968; Jones, 1971*). It was developed "*primarily as a means of modelling the non-Gaussian characteristics of inertial range turbulence and the associated effects on the response of aircraft*", (*Jones, 1989*). The first key feature of the SDG model is the assumption that the turbulence has a pre-defined structure, a structure based on the vortex eddy velocity profile in *figure 4.7*. The vortex (ignoring the core) is characterised by two opposing smooth ramp velocity elements, the velocity varying with the distance from the vortex core. As a natural extension from this observation, the fundamental gust structure adopted by the SDG model is the ramp or smooth ramp velocity profile. As with the discrete gust case, the ramp is defined by the gradient distance H_{sdg} and the gust intensity, σ_{sdg} (H_{sdg} and σ_{sdg} are used to distinguish the parameters of the SDG model from the single discrete gust model).

A second concept used in the initial formulation of the SDG method is that of self-similarity. The property of self-similarity assumes that gusts of smaller wavelength are

scaled down versions of gusts of larger wavelength. By defining an additional intensity variable,

$$u_k = \sigma_{sdg} \Big/ H_{sdg}^{k} \tag{4.2.8}$$

the self-similar model is described for a range of σ_{sdg} and H_{sdg} ($H_{sdg} < L$), *figure 4.8*. For consistency with the classical Komolgorov similarity theory representation of high Reynolds number turbulence in the inertial subrange (*Komolgorov, 1941*), the similarity parameter in the SDG model is taken as $k = 1/3$. Another fundamental property, also from the assumption of self-similarity, is that all discrete gusts in one family ($u_k = const$) have equal probability of occurrence. The next step is then to formulate the probability of occurrence of each family of gusts in a given patch of turbulence. Let $N_{H,uk}.\, dH$ denote the average rate of occurrence per unit distance of smooth ramp elements with gradient distance in the range (H_{sdg}, $H_{sdg} + dH$) and intensity greater than u_k.

$$N_{H,uk} = (a/\ H_{sdg}^{2}\ )F(u_k/b) \tag{4.2.9}$$

where a and b are constants and $F(u_k/b)$ is a dimensionless function. The 'a' is known as the intermittency parameter and governs the spacing between fluctuations. The 'b' is the intensity parameter, the value of which governs the overall amplitude of the disturbances. $F(u_k/b)$ controls the distribution of smooth ramp elements. As high intensity velocity fluctuations tend to be non-Gaussian (*Chen, 1972*), to conform to the trends of measured data, the distribution often used is that of an exponential decay.

$$F(u_k/b) = exp[-(u_k/b)] \tag{4.2.10}$$

This model for isolated ramp gusts is easily extended to more complex patterns of discrete gusts (*Jones, 1989*). Calculation of the gust induced loads directly from SDG theory, as with the PSD approach, assumes a linear relationship between the gust pattern and aircraft response. This assumption is valid only for fixed wing aircraft and non-

rotating rotorcraft loads such as fuselage aerodynamics. The effects of turbulence on a main lifting rotor require additional consideration.

4.2.4 Limitations of Statistical Turbulence models.

The assumptions of stationarity, self-similarity and randomness implicit in the previous two methods are fundamental to their respective derivations. These conditions hold for most of the earth's atmosphere, even within the boundary layer (altitude ≤ 2500ft), where simple modification of parameters such as the turbulence length scale will maintain good coherence with flight test data. However, many modern aircraft, and especially rotorcraft, are expected to operate near to the surface of the earth in nap-of-the-earth (NOE) flight. Further demands of stealth and concealment during engagement for military rotorcraft require that flight in close proximity to large obstacles to the mean airflow is becoming commonplace. In this region of the flight envelope, atmospheric turbulence is highly structured, with the velocity fluctuations determined by the structure of the obstacle's wake, resulting in a non-stationary turbulence field through the localised, highly correlated statistical properties of the field. It is not therefore prudent to use a statistical-based turbulence model that relies on the ambiguous assumption of stationarity in this region. On a practical level, the PSD method offers no control over the desired structure of turbulence, a critical parameter for this study. The SDG approach appears to be much more promising in this regard as structure can be built into a gust family. The problem with this method is that flight test data of the scenario under investigation is required for an SDG probability distribution to be extracted. This is an impracticable and indeed prohibitively expensive solution if, as would be the case here, a number of operating environments are to be tested.

The random nature of both approaches also makes repeatability of experiments difficult to guarantee. To gain insight into the performance of the controllers yet to be designed, performance against a fixed field will enable better comparison of controller performance and stability. Finally, one of the primary aims of the study is to investigate dynamic vibratory behaviour at low speed in a realistic environment, which will almost certainly be in the neighbourhood of some obstacle or obstruction to the flow. Therefore, a method is required which will generate a turbulence field $u_{gust}(x,y,z)$ which is representative of the turbulent environment of the MTE chosen for testing, is not founded on a mathematical uncertainty and allows repeatability of experiments. All of

the above conditions can be satisfied by using a CFD package to generate the flowfield.

4.3 Generating a Turbulent Environment Using CFD.

Computational Fluid Dynamics is a numerical technique for modelling the dynamics of a fluid around and within complex shapes. The flowfield is separated into a number of small, adjacent control volumes or cells, which combine to form a grid encompassing the field. In each cell, the fluid dynamic equations of motion, the Navier-Stokes equations (or simplifications thereof) are solved for the fluid states in that cell, such as pressure, velocity etc. This process is repeated for each cell in the grid. However, the boundary conditions on the walls of each cell (mass flux, velocity, pressure, effective viscosity etc) are determined in part by the states of the other cells in the grid. In fact, to a greater or lesser extent, each cell influences the states of every other cell in the grid. This represents a classic implicit function problem, the solution to which is achieved through one of several iterative minimisation techniques (*Press, et.al., 1992*).

As with many iterative minimisation problems, global convergence is difficult to ensure and numerical instabilities sometimes occur. Consequently, a good, well-defined, well-conditioned grid becomes essential for acceptable convergence. A well-conditioned grid will have many core features, for example, close to the obstruction the grid should be densely packed with cells to enable the boundary layer and other viscous effects to be included. For a rectangular, standard, structured grid (as used in this study) the angles in each cell should be as close to 90° as possible. Skewed grids, especially in the boundary layer, may lead to erroneous results, *figure 4.9*. However, the number of cells available in the grid is finite, so it is not always possible to maintain a desirable structure in all areas of the grid. For the current application, the choice of grid topology was determined as much by the suitability of the grid shape for integration with a rotorcraft model (RASCAL), as it was in ensuring a well-converged solution.

4.3.1 Merging with a Rotorcraft Simulation.

From the perspective of a rotorcraft simulation, the most useful function of CFD is as a mechanism for generating a look-up table containing turbulence field velocity data. The structured grid, with its rectangular matrix arrangement, is similar to the

structure of a traditional Cartesian co-ordinate system, removing the need for any additional post-processing or interpolation of the flowfield. Using a structured grid topology, look-up table generation is a relatively straightforward procedure. Once the grid is established, and a solution found, the CFD engine generates an output file containing the inertial (x,y) Cartesian co-ordinates and corresponding (u,v) velocities for the $(i,j)^{th}$ point on the grid ((i,j) represents the intersection of the i^{th} row and j^{th} column of the grid). After some format adjustment, RASCAL reads in a 2-D matrix containing the inertial positions of the grid points. Two further matrices, containing the u and v inertial velocity terms of the turbulence field are read. RASCAL calculates the inertial positions of the various helicopter components (position of the blade-elements, position of the fuselage aerodynamic centre, position of the fin aerodynamic centre, etc) using the equations described in §3.2. By comparing each component position with the inertial position matrix, the corresponding turbulence field velocities modify the component local aerodynamics accordingly.

The density of the inertial position matrix is determined by the grid topology, which is in turn governed by the choice of the flow solution algorithm within the CFD package. Most of the available solution algorithms operate on the premise that any continuous nonlinear function can be approximated to arbitrary accuracy by a succession of linear segments of infinitesimal length. Therefore, if a converged solution is obtained it can be reasonably inferred that an approximately linear relationship exists between corresponding parameters in adjacent cells. Using this information, the velocity and position look-up tables can be addressed with a bilinear interpolation scheme without introducing significant additional errors.

4.3.2 Bilinear Interpolation.

The bilinear interpolation scheme adopted was that described by Press et.al. (*1992*). Consider the 2-D table shown by *figure 4.10*. Points 1, 2, 3 & 4 correspond to the inertial positions of the grid points that bound the desired inertial location of the helicopter component. Subscripts u and l denote upper and lower respectively. Associated with each grid point is a gust velocity vector pair u_g^{table} & v_g^{table}, which for

conciseness will be combined under the general heading λ_g (where it is understood that λ_g can mean either u_g^{table} or v_g^{table} and λ_{g1} is λ_g at point 1). The gradient information along each axis is given by,

$$\nabla x = \left(\frac{x - x_l}{x_u - x_l} \right) \qquad \nabla y = \left(\frac{y - y_l}{y_u - y_l} \right) \tag{4.3.1}$$

(so that ∇x and ∇y each lie between 0 and 1). Then, the velocities at component location (x,y) are given by,

$$\lambda_g(x,y) = (1-\nabla x)(1-\nabla y)\lambda_{g1} + \nabla x(1-\nabla y)\lambda_{g2} + \nabla x \nabla y \lambda_{g3} + (1-\nabla x)\lambda_{g4} \tag{4.3.2}$$

This operation is performed for both inertial gust velocities at each component on the helicopter.

4.4 Examples of CFD Generated Obstruction-Induced Turbulence.

The Computational Fluid Dynamics software used throughout this study was a commercially available package called FLUENT™. FLUENT is a highly versatile CFD package that can model internal and external flows, temperature variations, multiple flow interactions and flow through porous materials. In addition, the solver comes packaged with a compatible CAD tool, called PRE-BFC, for generating the grids. After the grid has been imported into FLUENT and accepted, the user is presented with a menu system for customising the solution, such as defining inlet and outlet zones, flow parameters (velocity, density, temperature etc.), wall roughness and solver method. FLUENT then calculates the flow parameters in each cell and sums the residual error to generate a cost function for the implicit optimisation routine. Once the residual error has been reduced below a tolerance on each cell parameter (set by the user) the flow can be viewed using the built-in graphical post-processing tools. It is at this stage that the user must decide whether the solution is acceptable, usually by checking the boundary

layer shape, overall flow shape etc. Each of the following flowfields were repeatedly tested (through multiple solution runs) and thoroughly scrutinised before being accepted as accurate representations of the flow.

4.4.1 Flow around a tower block.

The first flowfield to be developed and integrated within RASCAL was the flow around a rectangular obstruction with dimensions comparable to those of a small urban tower block. This flowfield was designed to provide a lateral/directional addition to the existing suite of (predominantly longitudinal) turbulence environments (the discrete gust models). The tower block has dimensions (10m x 40m) and is surrounded by a grid of (450m x 270m), *figure 4.11*. The nominal freestream velocity of the flow is $5ms^{-1}$ and enters the grid from the left-hand side. The velocity magnitude (*figure 4.12*) ranges from $0ms^{-1}$ at the surface of the tower block (dark blue) to a maximum of $8.5\ ms^{-1}$ (dark red). Examination of the pressure contours and streamlines of the flow (*figures 4.13 & 4.14*), show the existence of two separation bubbles and the drop in dynamic pressure to the rear of the tower block inferred by the velocity distribution. The overall shape of the flow appears to be correct as, from Bernoulli's equation (*Munson, Young & Okiishi, 1990*), the flow accelerates around the upper and lower sides of the block to conserve mass flow and linear momentum, as expected.

These results represent a snapshot of the flowfield in time. The dynamic motion of the wake is implied by the elongation of the bottom separation bubble, which is due to periodic vortex shedding in the wake (known as a Karman vortex trail). Although the wake is now shown to have a time-varying component, invoking Taylor's Hypothesis means that this snapshot picture of the flow can be an adequate representation of the mean turbulence for simulation purposes.

4.4.2 Flow over a cliff.

For the second turbulence field the classic example of flow over a backwards step was used to model the wake induced by flow over a cliff-edge. Again a large area grid

was used, *figure 4.15*, covering 400m in length and 200m in height. The flow is intended to operate in the x-z plane of the helicopter body axes. In addition to generating a naturally-occurring, vertical, sharp-edged gust (*figure 4.16*), it can also be used to estimate the optimal hovering and/or approach patterns for air ambulance and air/sea rescue missions in turbulence. The apex of the cliff is located at grid co-ordinate position (*100m, 50m*). The flow is from left to right, enters via the left-hand vertical plane on the grid at a velocity of 5ms-1 and is accelerated to a maximum velocity of $10.6ms^{-1}$.

The up-gust at the cliff edge (*figure 4.16*), is generated by the acceleration of the flow as it moves around the apex of the cliff (from Bernoulli's equation), combined with the energy released by a clockwise rotating vortex that exists on the cliff plateau (*figures 4.17 & 4.18*). The cumulative effect is a gradual, smooth ramp shaped increase in velocity in the vicinity of the cliff apex. This flow then exhibits characteristics which are strikingly similar to the 1-COS and SDG models and will therefore be an ideal candidate for extending the vibration analysis to continuous turbulence.

4.4.3 Flow across a valley.

The third turbulence field generated was that of flow across a valley. This flow pattern is typical of that which will be encountered during NOE flight through a canyon or glacier cut valley. The grid dimensions are 400m x 200m, with the valley dimensions 100m x 50m, *figure 4.19*. The velocity magnitude contour plot (*figure 4.20*) shows a reasonably benign vortex pattern that is confirmed by the pressure and streamline contour plots of *figures 4.21 & 4.22*. A shear layer covers the opening to the valley, which should excite an interesting response in the helicopter upon exit.

4.4.4 Flow around an offshore oil platform.

The final turbulence field generated for this study was that of the flow around an offshore oil platform. The geometry of the model (*figure 4.23*) was inspired by the Brent Charlie oil rig deployed in the North Sea. Two variants of the flow around this

platform were constructed based on the assumptions used to model the influence of the support pillars on the flow pattern. In the first variant, it was assumed that the supports have a negligible effect on the flow pattern, i.e. they provide minimal obstruction to the flow, *figure 4.24*. The velocity magnitude distribution for this 'unsupported' rig is shown in *figure 4.25*. Most of the turbulent energy is convected downstream in a narrow channel behind the platform, *figures 4.26 & 4.27*.

In the second description of the flow it is assumed that the supporting pillars do make a significant contribution to the pattern of the flow, *figure 4.28*. As a first order, 2-D approximation to what is primarily a 3-D effect, the supporting pillars are modelled as a porous medium that reduces the momentum of the flow beneath the platform. This has a dramatic effect upon the flow pattern as can be seen in *figure 4.29*. Probably the most worrying development, from a flight safety perspective, is the generation of a large vortex immediately above the helideck, *figures 4.30 & 31*. Both grids were included in HISAT because the geometry of the platform is too complex to analyse heuristically and the author did not have access to any corroborating flow information. It is intended that the less realistic flow will be discarded when other external flow information becomes available.

All of the grids were modelled with a 120x120 point lattice that was scaled to fit each individual geometry. This results in a 14400 cell grid that approaches the maximum grid size (16000 cells), which FLUENT can accommodate. The limitation in available grid size was the main obstacle to generating full 3-D environments. It proved to be impossible to accommodate both the resolution of the cells necessary to obtain meaningful results and the required grid volume for a useful simulation with the number of cells available. There is no theoretical barrier which will prohibit future versions of HISAT from incorporating full 3-D environments.

4.5 *Analysis of the response to longitudinal and lateral/directional turbulence.*

4.5.1 Uncontrolled flight past a tower block

To test the validity of the results and the performance of the simulation it was decided to run two test cases, one which would excite lateral/directional motion and one which would excite purely longitudinal motion. Of course, the kinematic transformation of the gust components into native axes results in non-zero elements of the local velocity vector in all three dimensions. The first test to be performed was that of the flight past an urban tower block, *figure 4.11*, again using the Puma as the test aircraft. The Puma was trimmed at 10 knots forward flight, heading due north, in the field at the position shown in *figure 4.32*. As the aircraft flies into the wake it first encounters the peak lateral velocity (dark red zone in *figure 4.12*), which results in a small, positive lateral deviation from track shown in *figures 4.34 & 4.35*. It then progresses further into the 'reversed flow' region of the wake, in which the small, negative lateral gust velocity and the unbalanced controls (which had to balance a mean side-wind in trim), combine to cause a rapid lateral translation towards the tower block. Significant changes in attitude also occur at this stage, predominantly roll and heading, *figure 4.36*. The Puma then encounters the fast airflow pushing round the top of the tower and begins to rapidly 'weathercock' into the flow, now heading due east. The velocity position and heading graphs begin to diverge at this point indicating that without corrective action by the pilot, the helicopter will transition into a slow unstable mode. The accelerations, *figure 4.37*, do not undergo any significant vibratory motion during this time.

The trends in the response predicted by RASCAL are intuitively correct and in the absence of corroborating empirical data, indicate that the turbulence model is working correctly.

4.5.2 Uncontrolled flight over a cliff top.

In the second test case, the flow over a cliff top scenario was used. Again the

Puma was used as the test aircraft and was trimmed in the flow at the position shown in *figure 4.33*, this time at 30 knots forward speed. The starting position is 40m downstream of the cliff face and 20m above the cliff top. The upwash over the cliff edge provides a natural extension to the 1-COS gust, which in turn is a progression from the sharp-edged gust of Chapter III. The upwash rapidly destabilises the aircraft sending it into a spiral type of lateral mode as can be seen from the large roll & heading angles (*figure 4.40*) and associated lateral deviation and velocity profiles, *figures 4.38 & 4.39*. This is probably due to the gyroscopic precession of the main rotor in conjunction with the destabilising action of the turbulence field. However, it is the acceleration time histories, *figure 4.41*, which are of most interest.

A significant vibratory component can be clearly seen in the body axis vertical acceleration, $\dot{w}$, in *figure 4.41*. The harmonic analysis of this response is shown in *figure 4.42,* where there is an obvious split around the fundamental vibration frequency at 4/rev. This is a very important result as it demonstrates, for the first time, a split around the fundamental vibration frequency of the helicopter induced by a complex turbulence environment. To this end, one of the fundamental aims of this thesis has been achieved, as this result lends further weight to the existence of this phenomenon.

4.6 Chapter summary and Discussion.

Throughout the discussion of the traditional methods for modelling atmospheric turbulence, and by relating this to the vibration induced by a sharp-edged gust presented in Chapter III, a good understanding of the requirements for turbulence induced vibration modelling has been gained. Put simply, a suitable turbulence field must exhibit defined structure and sharp velocity gradients. To further impose an additional constraint, that the turbulence field created must be representative of that likely to be encountered during operation, the limitations of the traditional discrete gust, PSD and SDG methods quickly become apparent. However, the novel technique of using CFD generated flowfields as the turbulence generator, provides an effective solution which satisfies the criteria outlined above. In the authors opinion, this development creates a modelling framework capable of being used for the prediction of rotorcraft/turbulence interaction.

As an example of the usefulness of the embryonic HISAT, a frequency domain analysis of the vibration induced by flight through a continuous, CFD generated turbulence field has shown the same split about N/rev as the sharp-edged model. This is an important result, as it shows that the vibratory response first observed by Houston & Hamilton is not confined to abstract, mathematical gust fields, but is present in more complex turbulence environments. This suggests that the vibration split may be a real phenomenon that affects all rotorcraft during their operational lifespan, which has a direct impact on the (nominally tuned) techniques and devices for vibration alleviation. The impact this phenomenon would have on active vibration control laws will be the main topic for discussion in Chapter VI.

The integration of an effective and realistic turbulence generator into RASCAL means that the transition from RASCAL to HISAT is now 50% complete. The next chapter will complete the transformation by adding an inverse simulation algorithm.

CHAPTER V

The Inverse Simulation of RASCAL

This chapter will begin by introducing the concept of inverse simulation, illustrating the benefits of the approach over explicit control law design. After discussion of two inverse methods, a detailed derivation of the GENISA algorithm (the inverse algorithm chosen for this research) will be presented. Numerical and physical problems associated with the implementation of the algorithm with RASCAL are identified and possible solutions proposed.

5.1 Continuing Development of HISAT.

One of the primary project objectives introduced in Chapter I was the development of HISAT (*Helicopter Inverse Simulation through Atmospheric Turbulence*) to be achieved through a series of enhancements to RASCAL, (*Houston, 1991b*). The modifications of the previous chapter now enable RASCAL to calculate the response of the helicopter induced by atmospheric turbulence. The remainder of this chapter will discuss inverse techniques and develop the inverse simulation algorithm, GENISA, which will complete the transition from RASCAL to HISAT.

5.1.1 *Advantages of Inverse Simulation.*

Conventional simulation, or forward simulation, is a numerical process for calculating the response of a dynamic system to known inputs. Inverse simulation, as the name suggests, is the inverse of this process, i.e. given the outputs of a dynamic system, find the inputs which were required to generate them. Inverse simulation has found applications in the fields of piloting strategies (*Thomson, Talbot et.al., 1995*), handling qualities requirements (*Thomson & Bradley, 1994*) and conceptual design (*Thomson & Bradley, 1990b*). Considerable experience (*Thomson & Bradley, 1997*) has been gained at the University of Glasgow on the use of inverse simulation for handling qualities and workload assessment of aircraft performing ADS-33D (*Anon, 1994*) manoeuvres (denoted for future reference as Mission Task Elements or MTE's). To aid in the understanding of the conceptual differences between conventional and inverse simulation, consider the following two examples.

A mathematical model, which calculates the roll response of a helicopter to a step input of lateral cyclic pitch (through a transfer function or some equivalent mechanism), is an example of simulation in the conventional sense. Transient and steady state response characteristics will be evident in the resulting time histories, which may then be classified in terms of natural frequency, damping, gain and phase margins etc. An example of inverse simulation is the calculation of the control inputs required to translate a helicopter over a prescribed distance in a set time. The resulting control time histories can then be examined to

i) determine the magnitude and rate of change of control deflection (pilot workload) and

ii) establish whether the aircraft can perform the manoeuvre without exceeding the control position and rate limits (performance evaluation).

Inputs to a model of this type would typically take the form of desired ground track as a function of time.

The traditional approach to the simulation of helicopters executing manoeuvres would require the design of several flight controllers about many operating points

scattered throughout the flight envelope. Conceptually, there are no theoretical barriers to using a flight controller, or pilot model, to drive RASCAL. A standard tracking or servodesign feedback loop would be sufficient for most problems with the manoeuvre definition used as the reference input to the loop. The feedback / feedforward gains of the controller would be interpolated or 'scheduled' between operating points. However optimal (or near optimal) performance could only be guaranteed if the helicopter is simulated at or near one of these points. In addition, a separate set of gains would be required for each aircraft type simulated, classifying this approach as aircraft specific rather than generic. This impinges directly on the robustness requirement of Chapter I, which demands a generic (with respect to helicopter type and configuration) flight control algorithm.

In crude terms, inverse simulation -and in particular the integration method- can be thought of as a technique which automates the entire process of controller design. System identification of reduced order, linear models and control selection algorithms invoked at discrete intervals ensure the manoeuvre is flown in a piecewise-optimal fashion, irrespective of helicopter type or configuration. Unlike traditional control design the approach satisfies the algorithm robustness and optimality requirements presented in Chapter I. The relative simplicity of the algorithms is an additional and welcome alternative to the trend for increasingly complex ideologies, endemic to many sectors of the control community at present.

5.1.2 Methods of Inverse Simulation.

Inverse simulation algorithms generally adhere to either of two forms, the differentiation method or the integration method. Here, a general description of the inverse problem is used as the base for the subsequent development of both approaches. Mathematically, the inverse problem can be defined from the following input-output relationship for a non-linear dynamic system.

$$\dot{\underline{x}} = f(\underline{x}, \underline{u}); \qquad \underline{x}(0) = \underline{x}_0 \tag{5.1.1}$$

$$\underline{y} = g(\underline{x}) \tag{5.1.2}$$

Where, $\underline{x}$ is the state vector of the system;

$\underline{u}$ is the control vector and

$\underline{y}$ is the output vector.

Equations (5.1.1-2) display the general non-linear state space representation of a dynamic system, using standard notation, which is applied extensively in conventional simulation. The inputs to the system are contained within the control vector, $\underline{u}$ and generally are, in the case of helicopter simulation, the main and tailrotor collective pitch and the main rotor longitudinal and lateral cyclic pitch. For the inverse problem, equations (5.1.1) & (5.1.2) have to be rewritten in a form which allows the pre-defined output vector, $\underline{y}_{dem}$, to drive the simulation. The output of the inverse system has to be the control time history required to produce $\underline{y}_{dem}$. This may be illustrated more clearly by differentiating equation (5.1.2), (*Thomson, 1997).*

$$\dot{\underline{y}} = \frac{dg}{dx}\dot{\underline{x}} = \frac{dg}{dx} f(\underline{x}, \underline{u}) \tag{5.1.3}$$

Assuming (5.1.3) can be inverted with respect to $\underline{u}$ it is possible to write,

$$\underline{u} = h(\underline{x}, \dot{\underline{y}}) \tag{5.1.4}$$

which, when substituted into equation (5.1.1) gives,

$$\dot{\underline{x}} = f(\underline{x}, h(\underline{x}, \dot{\underline{y}})) = F(\underline{x}, \dot{\underline{y}}) \tag{5.1.5}$$

Equations (5.1.4) and (5.1.5) present a complete description of the inverse problem. The system is driven by the rate of change of the output vector and produces, once

integrated between two points in time, a time history of control displacements required to generate the desired output vector. It should be noted, however, that the dynamics of the inverse system are not the same as the dynamics of the original system, which infers that the stability properties of (5.1.1) and (5.1.5) are dissimilar. This is a direct result of imposing the constraint that only observable states can be used to drive the inverse system. This is similar in concept to the stability problems associated with the design of an output feedback controller using modern state space methods. No definitive statements of stability can be guaranteed from the outset of the design (unlike a full state feedback LQR design, which should have infinite gain margin and 60° phase margin). The stability characteristics of inverse helicopter simulations have undergone considerable research (*Thomson & Bradley, 1990b*), some of the results of which will be used later in this chapter.

The key to conventional and inverse simulation is finding a series of ordinary differential equations that best approximates the mapping function f. RASCAL (Chapter II) was used throughout this body of research for calculating the mapping in the conventional, i.e. forward simulation sense. Although possible, the explicit algorithmic inversion of RASCAL to calculate the inverse mapping f^{-1} would be an extremely complex procedure. Therefore, a reduced order, invertible, linear approximation, derived numerically from RASCAL, is needed to perform the input-output mapping function in the inverse simulation algorithm GENISA. GENISA (GENeric Inverse Simulation Algorithm)- which is an integration method algorithm- will be presented and discussed in greater depth later in this chapter. Although not performed explicitly during the course of this research, it is prudent to discuss the various numerical techniques employed in inverse simulation, to illustrate the novelty of the preferred approach.

5.1.3 Inverse Simulation by Differentiation.

The differentiation method of inverse simulation, with respect to helicopter flight, is best exemplified by the HELINV algorithm developed by Thomson (*1988*) at the University of Glasgow. Like most complex inverse simulation models, Helinv is

composed of two intertwined entities, the helicopter model and the inverse algorithm. It is not within the remit of this work to reproduce a detailed description of Helinv, rather to present a summary of the algorithm and note the most significant features contained within. In so doing, it is hoped that some conclusions can be drawn about differentiation algorithms in general.

The inverse algorithm which forms the core of a helinv simulation begins by applying a simple first order implicit scheme to equation (5.1.1), (*Thomson, 1997*).

$$\frac{\underline{x}(t_k) - \underline{x}(t_{k-1})}{t_k - t_{k-1}} = f\left(\underline{x}(t_k), \underline{u}(t_k)\right) \tag{5.1.6}$$

$$\underline{y}(t_k) = g\left(\underline{x}(t_k)\right) \tag{5.1.7}$$

where $\Delta t = t_k - t_{k-1}$ is the differentiation time step. The algorithm unfolds as follows. Given the state of the system at the previous time point t_{k-1}, $\underline{x}(t_{k-1})$ and the desired output at the current time point, $\underline{y}(t_k)$ the above equations can be solved for $\underline{x}(t_k)$ and by applying the Newton-Rhapson scheme, $\underline{u}(t_k)$. The Newton-Rhapson iterative multidimensional optimisation algorithm (to be discussed in detail later in this chapter) finds the control vector, which minimises the error function,

$$\underline{e}(t_k) = \frac{\underline{x}(t_k) - \underline{x}(t_{k-1})}{t_k - t_{k-1}} - f\left(\underline{x}(t_k), \underline{u}(t_k)\right) \tag{5.1.8}$$

at time t_k. The algorithm produces a control time history through instantaneous rather than differential solution of the vehicle equations of motion.

5.1.4 Inverse Simulation in the Forward Sense using Integration.

The integration method of inverse simulation has been exhaustively investigated by, among others, *Hess et.al. (1991), Hess & Gao (1993), Haverdings (1983)* and *Rutherford & Thomson (1994)*, for various applications and manoeuvres. The integration method has demonstrated considerable flexibility in flying demanding manoeuvres, while keeping the performance metrics at a premium and achieving higher

numerical stability than the differentiation method, *(Lin, Lu & Smith, 1993)*. Such results are an important indicator of the competency of the algorithm, but another facet of the technique renders this approach particularly attractive. Unlike differentiation algorithms such as HELINV, *integration-based inverse simulation algorithms operate independently of the helicopter model used.* Using a differentiation algorithm similar to HELINV would require a massive redevelopment of RASCAL that is not accounted for in the project budget. Indeed, the required modifications to RASCAL would be so severe that a complete rewrite of the model would probably become necessary. Obviously any method that circumvents this problem would have a significant advantage over the differentiation method for our purposes.

Unlike the differentiation method, which resolves the equations of motion into algebraic form, the integration method uses conventional simulation to integrate between time points. Assuming all initial conditions have been correctly assigned, the output vector can be approximated by,

$$\underline{\boldsymbol{y}}(t_{k+1}) = \boldsymbol{H}(\underline{\boldsymbol{x}}(t_k), \underline{\boldsymbol{u}}(t_k)) \tag{5.1.9}$$

Where the mapping function $\boldsymbol{H}()$ is approximated by RASCAL. As the desired output vector, $\underline{\boldsymbol{y}}_{des}(t_{k+1})$ is known, an error function can be constructed of the type,

$$\underline{\boldsymbol{e}}(t_{k+1}) = \underline{\boldsymbol{y}}_{des}(t_{k+1}) - \underline{\boldsymbol{y}}(t_{k+1}) \tag{5.1.10}$$

Using an initial guess for $\underline{\boldsymbol{u}}(t_k)$ (usually $\underline{\boldsymbol{u}}(t_{k-1})$) $\underline{\boldsymbol{e}}(t_{k+1})$ can be minimised using Newton-Rhapson iteration or some equivalent technique. Repeated application $\forall t_k$ in the manoeuvre solves the inverse problem.

5.2 *Description of the GENISA Algorithm.*

The GENISA algorithm is a specific implementation of the integration inverse algorithm of *Hess et.al. (1991)*. The algorithm was refined by *Rutherford (1997)* for assessment of compound helicopter configurations performing complex manoeuvres. Rutherford used an individual blade / blade element main and tail rotor in his helicopter model to test the performance of the algorithm and it handled most manoeuvres very

well. The rotor model was not as complex as that in RASCAL, lead-lag and rotorspeed dynamics the most notable omissions. However, it was advanced enough to suggest that GENISA could fulfil the inverse simulation requirements of HISAT detailed in Chapter I. The development of the algorithm proceeds as follows.

Consider the general integration input-output relation presented at the beginning of this chapter.

$$\underline{\dot{x}}(t_k) = f\left(\underline{x}(t_k), \underline{u}(t_k), \underline{w}(t_k)\right) \tag{5.2.1}$$

$$\underline{y}(t_k) = g\left(\underline{x}(t_k)\right) \tag{5.2.2}$$

The expression for the state derivative has been made discrete and augmented by the vector $\underline{w}(t_k)$, a concise description of the influence of atmospheric disturbances on the motion of the system. For most situations, the disturbance vector acts independently of the control inputs, i.e.,

$$\frac{\partial \underline{w}}{\partial \underline{u}} \cong \frac{\partial \underline{u}}{\partial \underline{w}} \cong \underline{0} \tag{5.2.3}$$

These derivatives are approximately, not exactly zero because some situations do arise when the control and disturbance inputs influence each other. $\partial \underline{w} / \partial \underline{u}$ is non-zero when distortion of the disturbance flowfield due to the presence of the vehicle is modelled. $\partial \underline{u} / \partial \underline{w}$ can be non-zero if the blade models are adjusted to include aeroelastic torsional deformation of the blades. Neither of these effects is modelled in the current version of HISAT and it is not envisaged that they would cause any significant problems were they to be included in future issues of the model.

The states, and therefore the outputs at the $(k+1)^{th}$ time point can be found by integrating $\underline{\dot{x}}(t_k)$ over the interval $t_k \rightarrow t_{k+1}$, i.e.,

$$\underline{x}(t_{k+1}) = \underline{x}(t_k) + \int_{t_k}^{t_{k+1}} f(\underline{x}(t_k), \underline{u}(t_k), \underline{w}(t_k))dt \qquad (5.2.4)$$

The fourth order Runge-Kutta integration algorithm used by RASCAL is widely regarded as the standard integration routine for complicated differential models using fixed time steps. The integration interval of the Runge-Kutta algorithm $\Delta\tau$ is always at least 1 order of magnitude smaller that the discretisation interval of GENISA. This ensures that the probability of any numerical instability emanating from the integration algorithm is minimal.

The manoeuvre is specified in terms of the desired output vector at the next time point, $\underline{y}_{des}(t_{k+1})$. Defining an error function thus,

$$\underline{e}(t_{k+1}) = \underline{y}_{des}(t_{k+1}) - \underline{y}(t_{k+1}) = \underline{y}_{des}(t_{k+1}) - \boldsymbol{g}(\underline{x}(t_{k+1})) \qquad (5.2.5)$$

Minimising the error function with respect to the available controls at time t_k will ensure that the manoeuvre constraints are met by the inverse algorithm. Continued application of this procedure during the entire duration of the manoeuvre will yield a time history of the required control inputs. Newton-Rhapson iteration is used in GENISA to minimise the error function using the following equation,

$$\underline{u}(t_k)_{n+1} = \underline{u}(t_k)_n - [\boldsymbol{J}]_n^{-1}\underline{e}(t_{k+1})_n \qquad (5.2.6)$$

The iteration loop is terminated when $\underline{e}(t_{k+1})_n \leq \boldsymbol{tol}$, where ***tol*** is a pre-set tolerance, which reflects the demanded accuracy of the simulation. It will be seen later that the tolerance limits have a significant bearing on the stability of HISAT, a feature not observed by Rutherford (*1997*). Equation (5.2.6) requires the inversion of the system Jacobian (***J***), which has the potential to inject numerical instability into the simulation. To remove this possibility, the Newton-Rhapson algorithm is recast as,

$$\underline{u}(t_k)_{n+1} = \underline{u}(t_k)_n - \underline{u}_{err}(t_k)_n \qquad (5.2.7)$$

Where, $\underline{\boldsymbol{u}}_{err}(t_k)_n$ is the solution of

$$[\boldsymbol{J}]_n \underline{\boldsymbol{u}}_{err}(t_k)_n = \underline{\boldsymbol{e}}(t_{k+1})_n \tag{5.2.8}$$

Which is, in turn solved by using Crout's method or some equivalent decomposition algorithm (*Rutherford, 1994*).

5.2.1 Estimation of the System Jacobian.

It is impossible to extract from RASCAL the elements of the Jacobian matrix in a closed form, analytical manner. The complexity of the non-linear equations of motion solved by RASCAL demands that the Jacobian has to be evaluated numerically if it is to be truly representative of the helicopter system. Several techniques exist in both the time and frequency domains for estimating the Jacobian elements, (*Press, et., al., 1992*), (*Cheney & Kincaid, 1985)* but as the manoeuvres are to begin from trim, a differencing method appears the most viable option. In the case of GENISA, the central differencing method was used. The elements of the system Jacobian are given by,

$$\boldsymbol{J}_{ij} = \frac{\partial \boldsymbol{e}_i(t_{k+1})_n}{\partial \boldsymbol{u}_j(t_k)_n} = \frac{\boldsymbol{e}_i\left(\boldsymbol{u}_j(t_k) + \delta \boldsymbol{u}_j(t_k)\right)_n - \boldsymbol{e}_i\left(\boldsymbol{u}_j(t_k) - \delta \boldsymbol{u}_j(t_k)\right)_n}{2\delta \boldsymbol{u}_j(t_k)_n} \tag{5.2.9}$$

The first step of the algorithm is to calculate $\underline{\boldsymbol{e}}(t_{k+1})_n$ using the controls from the previous time point. This gives a baseline value of the error function. Each of the controls are then separately perturbed by $\pm \delta \boldsymbol{u}_j$ in turn and the associated error functions stored. The control perturbations must be small to be consistent with linear theory, but they also must be large enough to stimulate body response. Iterative adjustment of the perturbation size over several manoeuvres suggests using a fixed step size of 2mrad for all controls to be the near optimal configuration.

5.3 *Polynomial Method of Flight Path Generation.*

A necessary requirement for the successful implementation of any inverse simulation algorithm is an accurate mathematical abstraction of the desired manoeuvre (*Thomson & Bradley, 1990a*). Ideally, the manoeuvre should be continuous in position, velocity, acceleration and at the very least linear in jerk. Imposing these constraints removes the possibility of any sharp nonlinearities or discontinuities appearing in the manoeuvre. Manoeuvre validity is not degraded by this action; in fact, the reverse is true. For example, if the pilot violently displaces the control inceptors, his actions will not immediately invoke an equally violent change in acceleration. Electro-mechanical or electro-hydraulic lag associated with the transfer function of the control actuators, coupled with the natural transient response of the helicopter damp the motion. The cumulative effect of these and other factors is a 'smoothing' of the flight path contour, although aerodynamic rotor vibration is still present.

Standard manoeuvre profiles suitable for our purpose are defined in ADS-33C/D, (*Anon., 1994*). This document discusses in detail a collection of standard military manoeuvres, which are assessed to determine operational suitability, severity (quickness parameters) and difficulty (handling qualities rating on the Cooper-Harper scale). Typical manoeuvres include the hurdle-hop, side-step, slalom and pirouette, all of which are common civilian and military helicopter MTE's. Boundary conditions (such as the lateral displacement of a side-step), define the severity and general shape of the MTE's and can further be used to construct polynomial expressions of each manoeuvre variable as a function of time.

5.3.1 *Boundary Value Polynomials.*

Before the manoeuvre profiles can be generated as polynomial functions of time, the boundary conditions on each constraint must be specified. The boundary conditions are generally defined at the ends and at any maxima or minima of the function. To illustrate, consider the boundary conditions of a simple manoeuvre designed to accelerate from hover to a final inertial velocity, $\dot{x}_f = \dot{x}(t_f)$ in t_f seconds.

$$\begin{aligned} t = 0: &\qquad \dot{x}(t) = \ddot{x}(t) = 0 \\ t = t_f: &\qquad \dot{x}(t) = \dot{x}_f, \qquad \ddot{x}(t) = 0 \end{aligned} \tag{5.3.1}$$

As there are 4 boundary conditions, a 3rd order polynomial should adequately describe the manoeuvre,

$$\dot{x}(t) = a_0 + a_1 t + a_2 t^2 + a_3 t^3 \qquad (5.3.2)$$

Application of the first boundary condition removes the first two coefficients (a_0, a_1) of equation (5.3.2). The remaining coefficients are found by solving a set of simultaneous equations in t_f, which gives the manoeuvre polynomial defined by,

$$\dot{x}(t) = \dot{x}_f \left(3\left(\frac{t}{t_f}\right)^2 - 2\left(\frac{t}{t_f}\right)^3 \right) \qquad (5.3.3)$$

The manoeuvre profile is shown in *figures 5.1 & 5.2*. In the following simple example, polynomial expressions for the manoeuvre profile are not required, as the manoeuvre is the simplest of all, maintaining trim. However, the technique has been used to generate the profiles of all the non-trivial manoeuvres that were included in HISAT, namely the side-step, inverse hurdle-hop and flare to hover manoeuvres, (*figures 5.3, 5.4, 5.5* and in Appendix I). The precision flare-to-hover manoeuvre will be used in §5.7 to test HISAT and demonstrate that it meets the design objectives defined in Chapter I.

5.4 Simple Example – Maintaining Trim.

The simplest possible manoeuvre with which to test the GENISA algorithm embedded within RASCAL is maintaining rectilinear, steady flight or trim. The desired manoeuvre is simply described by the time integral of the inertial rates at trim and heading,

$$\underline{y}_{des}(t_k) = \left(x_E(t_k), y_E(t_k), z_E(t_k), \psi(t_k)\right) \qquad (5.4.1)$$

where, $x_E(t_k) = \dot{x}_{E,trim} * t_k$ etc. The reasons for choosing such a simple manoeuvre to

test the performance of GENISA are two fold. Firstly, the simplicity of the manoeuvre definition helps to prevent manoeuvre specific issues from intruding into the results. Secondly, as the motion is longitudinal by definition, conclusions regarding the off-axis response of the helicopter simulation can be drawn. Finally, as will be borne out by the results, further modification of GENISA is required before it can readily be used in conjunction with RASCAL. The simulations will be performed using data gathered for an Aerospatialé Super Puma, *figure A.1*. The Puma will be flown under ISA standard atmospheric conditions, at an altitude of 1000ft above sea level. Altitude above ground is also 1000ft thus removing the influence of ground effect from the simulation.

5.4.1 Analysis of Simulation Time Histories.

Figures (*5.6*) through (*5.9*) contain plots of the aircraft constraints, controls, accelerations and attitudes of a Puma trim simulation using the GENISA algorithm. It is obvious that the algorithm maintains the trim extremely well with lateral and vertical deviations confined to less than 20mm and heading error of less than 8mm, *figure 5.6*. However, there is considerable and very possibly divergent oscillation present in the off-axis roll and pitch responses, *figure 5.9*. These may be constraint oscillations (*Thomson & Bradley, 1990b*), which are an unfortunate side effect of inverse simulation that may be damped but never removed. An analysis of the helicopter angular response will be undertaken in §5.6 to determine the exact cause of these oscillations.

The convergence rate of GENISA is extremely poor, often taking 5 or 6 iterations of the Newton-Rhaphson algorithm to arrive at a solution. This significantly increases the simulation run time while simultaneously reducing the numerical stability of the algorithm by repeated recalculation of the system Jacobian. Because numerical differentiation is employed on an untrimmed system, there is a significant risk that an ill-conditioned Jacobian will result, which will generate erroneous control inputs and drive the simulation unstable. Therefore, any modification of the algorithm, which reduces the number of iterations per control interval, is to be welcomed. A novel modification to GENISA, which improves both the convergence rate and internal stability, will be presented in §5.5.

5.4.2 *The importance of the control application interval to stability.*

The numerical experiments that were performed during the course of this research showed an unfortunate sensitivity in the algorithm to the chosen control application interval, given by $t_{k+1} - t_k$ in equation 5.2.4. To quantize this sensitivity into a meaningful index, first define a reduced system state vector,

$$\underline{x}_r = [y_E, z_E, \theta, \phi, \psi, u, v, w, p, q, r, \dot{u}, \dot{v}, \dot{w}, \theta_0, \theta_{1s}, \theta_{1c}, \theta_{tr}] \qquad (5.4.2)$$

The state variables chosen offer a complete definition of the rigid body dynamic motion of the helicopter. The control terms were included to penalise the control energy used in the inverse algorithm. It has been shown that the errors are typically oscillations about a mean value, therefore the standard deviation (*Press et.al., 1992*) is a good measure of the error. To group these terms into a single index, define the cumulative standard deviation coefficient thus,

$$\Pi = \sum_{i=1}^{Np} \sigma_i \qquad (5.4.3)$$

where, σ_i is the standard deviation of the time history of the i^{th} state and

Np is the number of states.

The discretisation interval was defined in terms of an integer number of complete tail rotor turns (the tail rotor to main rotor gear ratio of the Puma is approximately 29 : 6, i.e. 29 turns of the tail rotor equals 6 turns of the main rotor). Cumulative standard deviation coefficients were obtained for a simple trim using control intervals of 4, 6, 8, 10 & 12 tail rotor turns, *figure 5.10*. The minimum error is achieved using 8 tail rotor turns, which corresponds to approximately 1.65 turns of the main rotor. One possible reason for this value is given by considering the transient response of blade flapping motion. Once disturbed, the settling time for blade flap motion is approximately ½ of a main rotor turn. Using 8 tail rotor turns, this leaves approximately 1 complete revolution of the rotor for the 'steady' main rotor thrust vector to minimise the flight path errors. In other words, it appears that for stability it is necessary to match rotor periodicity *after* the flap transients have dissipated. The extremities of *figure 5.10*

represent regions where the rotor periodicity matching is approaching anti-phase, leading to instabilities.

5.4.3 *Other numerical sensitivities.*

The control application interval is not the only numerical parameter to which the GENISA algorithm is sensitive. Both the tolerance limit on each constraint and the control perturbation size must be carefully chosen from the outset to ensure convergence throughout the simulation. As has been previously stated in §5.2.1, a perturbation size of 2mrad applied to all controls appears to be the most robust configuration. To establish the tolerance limits, consider the observation (from classical control theory), that in general, tracking error is proportional to control activity, i.e. small error demands require large control inputs. Thus, the tolerance limit effectively sets the bandwidth of the inverse algorithm. If the tolerance is set too small, the algorithm will not converge and if it is too large, the helicopter will not fly the manoeuvre properly. From a series of experiments, a tolerance of 0.0001(*m* or *rad*) was selected.

5.5 *Enhancement of the Newton Step.*

The analysis of the previous section has provided compelling evidence pointing to the existence of numerical instabilities in the results generated by GENISA. Such dynamics are an unacceptable feature that could quite easily jeopardise the robustness and functionality properties of HISAT. It has been suggested by Rutherford & Thomson (*1996*), that stability can be improved by tracking higher order derivatives of the constraint variables, i.e. inertial velocities and accelerations rather than positions. Unfortunately, because HISAT has inherited the complex rotor arrangement of RASCAL, which includes variable rotorspeed and lead-lag motion, the inverse algorithm quickly destabilises to inertial rate commands. This is yet another indication that the numerical stability of GENISA has to be improved. Ideally, a mechanism for

tracking rotor periodicity is required, so reducing the numerical errors inherent in the construction of the Jacobian (5.3.1). However, a simpler and more expedient solution to ensuring global convergence of HISAT is to enhance the Newton-Rhapson algorithm.

In the book *Numerical Recipes*, (*Press, et.al.,1992*) it is stated that '*Newton's method has an unfortunate tendency to wander off into the wild blue yonder if the initial guess is not sufficiently close to the root*'. The solution they propose for ensuring global convergence is a modification of the Newton step, $\underline{u}_{err}$. Essentially, the Newton step is a *descent direction* parameter which determines the direction of the function minimum with respect to the current position. It is not always necessary to take the full Newton step to converge on the minimum, sometimes only a fraction of the step is required, as illustrated by *figure 5.11*. On a highly nonlinear problem space, using the full Newton step may result in many iterations before global convergence is reached, if at all.

5.5.1 Enhancement of the Newton Step Using the Bisection Algorithm.

The bisection method is a simple root finding algorithm '*which cannot fail*', (*Press et.al., 1992*). It was chosen for this research because it provides a good mechanism for searching the subspace of the global solution (the Newton step) with few function calls and does not require any gradient information. The algorithm proceeds as follows. The first step is to alter the Newton-Rhapson equation (5.2.6) by multiplying each change of controls by an additional scale factor, γ_m (where m is the iteration number of the bisection algorithm).

$$\underline{u}(t_k)_{n+1} = \underline{u}(t_k)_n - \gamma_m \underline{u}_{err}(t_k)_n \tag{5.5.1}$$

Where $\gamma_1 = 1$

$\gamma_2 = 0.5$

$\gamma_3 = 0.75$ if $\underline{e}(t_{k+1})_n^{\gamma_1} < \underline{e}(t_{k+1})_n^{\gamma_2}$

$\gamma_3 = 0.25$ if $\underline{e}(t_{k+1})_n^{\gamma_1} > \underline{e}(t_{k+1})_n^{\gamma_2}$

Thus, the bisection algorithm truncated to the first 3 iterations, enhances the accuracy of the Newton step. Obviously, the absolute optimum cannot be guaranteed as only three further function calls are made. However, this simple technique works surprisingly well, sometimes reducing the value of the error function by up to two orders of magnitude. The maximum number of iterations per time step rarely exceeds two, a substantial improvement over the original algorithm, which averaged three to four iterations per time step. This reduces the number of function calls and Jacobian calculations per time step. The effect on the amplitude of the off-axis oscillations is illustrated by the following simulation results.

5.5.2 Applying the Modified Newton Step Technique to Preserving Trim.

Validation of the improvements to GENISA can be best shown by returning to the example of §5.4. The results of an identical helicopter flying an identical manoeuvre are given in *figures 5.12* through *5.15*. Looking at the constraint plots of *figure 5.12* shows that the tracking error has been reduced by approximately one order of magnitude. The control deflections required to maintain this flight path (*figure 5.13*) are considerably less than those predicted by the original GENISA algorithm. This is primarily due to the massive reduction in amplitude of the oscillations in the roll and pitch attitude channels, *figure 5.15*. As these oscillations have reduced, so too has the total control effort, which in turn reduces the amplitude of the body axes accelerations to the point where main rotor vibration can be observed, *figure 5.14*.

The improvement in stability caused by the enhancement of GENISA is significantly better than was hoped for from the outset. Indeed it is now possible to track inertial velocities as well as positions without incurring any stability penalties whatsoever. This will be demonstrated in the verification procedure to be presented in §5.7, whereby a flare to hover manoeuvre (defined with respect to inertial velocities) is flown.

5.5.3 *Tracking Flight Path Accelerations.*

The stability gains afforded by the bisection algorithm have enabled the tracking of flight path velocities to be performed without error. The next logical step is to extend the technique to tracking flight path accelerations. However, tracking accelerations requires matching periodicity caused by the asymmetric, periodic loading of the main rotor, i.e. matching rotor vibration. This is relatively straightforward in rotorcraft simulations with no lag or rotorspeed degrees of freedom modelled, however, when these are introduced, as in HISAT, matching the periodicity of the rotor becomes very difficult to achieve.

Some initial experiments were conducted using an adapted form of the filter algorithm to be presented in the next chapter. The error function was fed through a low-pass Butterworth filter before being used in GENISA. However, the filter destabilised GENISA to the extent that even the simplest or most benign manoeuvres could not be successfully completed. As a result, inertial rates are the highest order derivatives to be tracked in HISAT at present.

5.6 *Constraint Oscillations.*

To determine whether the oscillations in the off-axis responses are due in part to the flight path constraints placed on the manoeuvre, an analysis of the aircraft dynamics is required. The first stage in this process is to linearise the model and recast the rigid body equations of motion in state-space form.

$$\dot{\underline{x}} = A\underline{x} + B\underline{u} \tag{5.6.1}$$

where $\underline{x} = (u\ v\ w\ p\ q\ r\ \phi\ \theta\ \psi)^{T}$ and $\underline{u} = (\theta_0\ \theta_{1s}\ \theta_{1c}\ \theta_{tr})^{T}$. The system ($A$) and control ($B$) matrices were calculated from RASCAL trims by invoking the linearisation option (perturbation model), mentioned in Chapter II. Equation (5.6.1) can chart the unconstrained response of the helicopter to a time history of control inputs. Stability

analysis is performed by examining the position in the complex plane of the eigenvalues of the A matrix. Attached to each eigenvalue is a corresponding eigenvector which defines the associated mode of motion (short-period, phugoid, dutch roll etc.). Eigenvalues that have positive real parts define unstable modes, while those with non-zero imaginary parts will exhibit oscillatory behaviour. However, this type of analysis will not yield a true picture of the underlying physics governing the dynamic response of the *inverse* system, as the inverse system is driven by flight path and heading constraints *not* control inputs. Thomson & Bradley (*1990b*) devised a technique for transforming the linear representation of the unconstrained helicopter to a linear representation of the inverse dynamics. As this technique was used to analyse the trims of §5.4, a short description of the method, followed by the results will now be given. A complete discussion of this transformation is contained in Appendix II.

The first step is to partition the state vector into constraint influenced and unconstrained states (as heading forms one of the constraints it is removed from the state vector), thus,

$$\underline{x}_1 = (u\ v\ w\ r)^{\mathrm{T}} \qquad \underline{x}_2 = (p\ q\ \theta\ \phi)^{\mathrm{T}} \tag{5.6.2}$$

The system and control matrices can then be partitioned,

$$\begin{bmatrix} \dot{\underline{x}}_1 \\ \dot{\underline{x}}_2 \end{bmatrix} = \begin{bmatrix} A_{11} & A_{12} \\ A_{21} & A_{22} \end{bmatrix} \begin{bmatrix} \underline{x}_1 \\ \underline{x}_2 \end{bmatrix} + \begin{bmatrix} B_1 \\ B_2 \end{bmatrix} [\underline{u}] \tag{5.6.3}$$

The unconstrained states can then be expressed in terms of the constraint influenced states.

$$\dot{\underline{x}}_2 = \left[A_{22} - \left(B_2 B_1^{-1}\right) A_{12}\right] \underline{x}_2 + \left[A_{21} - \left(B_2 B_1^{-1}\right) A_{11}\right] \underline{x}_1 + \left(B_2 B_1^{-1}\right) \dot{\underline{x}}_1 \tag{5.6.4}$$

After some extensive algebraic manipulation, the linearised statement of the inverse problem can be simplified to,

$$\dot{\underline{x}}_2 = A_c \underline{x}_2 + B_c \underline{u}_c \tag{5.6.5}$$

The matrices A_c, B_c and the vector of applied constraints, $\underline{u}_c$, are expanded in Appendix II. A simple, linear dynamic relationship now exists between the unconstrained states and the applied constraints within the framework of a classical state-space model. Therefore, extraction of the stability characteristics of the constrained model is performed by examining the eigenvalues of A_c.

The system and control matrices for a Puma in trim at 10 knots are presented in *figure 5.16*. Also shown is the 'system matrix' for the constrained system, Ac. The eigenvalues of this matrix are given in *table 5.17* and for clarity, the damping and natural frequency of each eigenvalue has been included in this table. The power spectral density for the roll angle time history generated by the original incarnation of GENISA is given in *figure 5.18*. Unfortunately, the dominant frequency does not correspond to either of the eigenvalues predicted by the constraint oscillation analysis. Performing the same operation on the roll angle time history obtained using the modified version of GENISA yields a spike in the PSD (*figure 5.19*), at 2.295 rad/s. This correlates well with the natural frequency (2.28 rad/s) of one of the predicted constraint oscillation modes, confirming that the oscillations generated by the modified version of GENISA are indeed constraint oscillations. The oscillations observed in the body attitude time histories using the original version of GENISA are probably due to a process akin to pilot-induced oscillations. The original algorithm (which only has the full Newton step to work with), uses larger control effort spread amongst the primary and off-axis control inputs to achieve the prescribed tracking accuracy. This causes a large degree of overshoot, which will tend to destabilise the inverse algorithm as time progresses. The same effect is observed in deadbeat controllers when the bandwidth is incorrectly assigned.

The analysis of the constraint oscillations suggests that enhancing the Newton step stabilises GENISA to the obtainable limit of an inverse solution. This is an important result as it demonstrates that it is possible to use a high fidelity individual blade rotor model in the context of inverse simulation, yet still obtain results that possess the numerical stability of disc models. However, the model also predicts the high frequency transient and modal response of each blade throughout the manoeuvre. HISAT therefore represents the current state-of -the-art in helicopter inverse simulation

alone, but coupled with the atmospheric turbulence response capabilities, results in a powerful and unique analysis and design tool.

5.7 *Helicopter Inverse Simulation Through Atmospheric Turbulence - HISAT.*

Assimilating GENISA within the RASCAL-CFD hybrid model completes the modifications to RASCAL which were necessary to fulfil the large scale simulation requirements of the project. In the penultimate section of this chapter, the functionality of HISAT is tested with a flare-to-hover manoeuvre in an approach to the oil rig platform with porous support, *figure 5.20*.

5.7.1 Precision Flare-to-Hover Manoeuvre.

The precision flare-to-hover manoeuvre is employed by the military for rapid troop deployment/extraction and, in a less severe role, in civilian offshore oil platform operations. The manoeuvre can be decomposed into three distinct (though connected) sections,

i) the transition into a suitable glide path from the starting manoeuvre,
ii) the deceleration of the helicopter along the glide path and finally,
iii) the transition to hover at the target point.

Figure *5.21* shows how the demanded flight path angle varies with time. Unlike standard MTE's which have been documented extensively (*Thomson & Bradley, 1990a*), the flare to hover manoeuvre is not constructed from a single polynomial but rather from three piecewise constant polynomials. The manoeuvre profile is given in *figure 5.5*. Polynomial expressions defining the manoeuvre are derived in Appendix I.

The time histories for this manoeuvre are presented in *figures* 5.22 through 5.25. The Puma was again chosen as the test aircraft, trimmed at 30 knots with the turbulence field switched on. This is to prohibit excessive transient behaviour at the beginning of the manoeuvre. The transition period from trim onto the glide slope takes 1 second to complete (*figure 5.25*). The deceleration phase forms the remainder of the manoeuvre, which the Puma follows well, as can be seen from the plot of $\dot{x}_E$ in *figure 5.22*. The vertical deceleration observed in $\dot{z}_E$ is necessary to maintain a constant flight path angle of 9°. For the transition to hover, the flight path angle is changed back to 0° through the reverse polynomial of phase 1. This stage is triggered when $\dot{x}_E$ is equal to 2.5ms^{-1} (or the nearest equivalent time step). The aircraft is brought to hover 10m above the centre of the helideck 15 seconds after the manoeuvre was begun.

It is apparent from the plots of the constrained state time histories (*figure 5.22*) that the Puma performs the manoeuvre well, even in the presence of the turbulence field. The controls (*figure 5.23*), generally follow the expected trends, such as a steady increase in collective pitch needed to balance the reduction in main rotor thrust because of reduced dynamic pressure. An increase in thrust leads to an increase in aerodynamic torque that is balanced by the increase in tail rotor collective pitch. The longitudinal and lateral cyclic control inputs are unfortunately swamped by the need to control the constraint oscillations, but the expected forward then aft motion of θ_{1s} is present. The constraint oscillations themselves are very severe (*figure 5.25*), most probably a consequence of the destabilising action of the turbulence field. A combination of large step changes in the controls (necessary to allow blade transients to settle as rotor periodicity is not matched – variable rotorspeed and lead/lag dynamics modelled) and destabilisation of the wake by this and the atmospheric conditions, both contribute to accentuating the amplitude of the constraint oscillations. The numerical stability could be improved by designing a control filter to mimic the analogue actions of the pilot. Such a filter will be incorporated in future versions of HISAT, as time limitations placed upon the research contract made the investigation impossible at this time. However, it should be stressed again that HISAT in its current configuration, represents the state-of-the-art for inverse simulation in terms of fidelity of rotorcraft model used and applicability of the tool. No other simulation has the capability to investigate gust loading on rotor blades during arbitrary manoeuvres, therefore its development alone

represents a significant achievement. The development of this model is the beginning of a process which should ultimately enhance the understanding of the changes in response characteristics for helicopters under severe operational conditions.

5.8 *Chapter Summary.*

By merging the modified version of the GENISA algorithm with the version of RASCAL with turbulence modelling capabilities, the transformation from RASCAL to HISAT has been completed. This action fulfils the first major objective of this research program, i.e. to construct a mathematical model capable of predicting helicopter response to atmospheric turbulence in a realistic operational environment. In addition, a novel enhancement of GENISA has been presented that resolves many of the numerical stability issues which arose during development, primarily due to the high fidelity of the rotor model in RASCAL. Indeed, an individual blade rotor model with flap, lag and rotorspeed degrees of freedom has never before been implemented in inverse simulation. Thus, the development of HISAT alone makes an important and in many respects, original contribution to the understanding of the effects of high frequency rotor dynamics on helicopter inverse simulation.

The development of a mathematical simulation tool that is compliant with the requirements specified in Chapter I has been accomplished. The next step is to use this tool for assessing the performance of active vibration control laws when presented with gust-induced vibration. This will be the topic of the next chapter.

CHAPTER VI

Strategies for Implementing Active Vibration Control.

In this chapter, the development of the vibration control laws employed in the study will be reported. Of the many active vibration control techniques discussed in the introduction to this thesis, Higher Harmonic Control (HHC) and Individual Blade Control (IBC) are the two concepts that will be examined in detail. Several modified control algorithms will be presented

6.1 Active Vibration Control Techniques.

It has been demonstrated in the previous chapters that HISAT is capable of predicting the vibratory response of rotary wing aircraft to various simulations of atmospheric disturbance. The next logical stage of development is to use the model in the design of control laws for regulating turbulence-induced vibration in the fuselage. The opening chapter of this document discussed four state-of-the-art active vibration ideologies currently favoured in the literature (*Reichert, 1981; Pearson, Goodall & Lyndon, 1994; Friedman & Millot, 1995*). To recap, the techniques reviewed were Higher Harmonic Control (HHC), Individual Blade Control (IBC), Active Control of Trailing-edge Flaps (ACTF) and Active Control of Structural Response (ACSR), an approach pioneered by Westland Helicopters (*Pearson, Goodall & Lyndon, 1994; Venkatesan & Udayasankar, 1997*). A preliminary feasibility study aimed at identifying the techniques most suitable for the problem at hand, favoured HHC and

IBC designs. ACSR and ACTF were discarded, as they require either modified aircraft geometry (for trailing-edge flap control) or a modal structural analysis (to identify fuselage node points for ACSR). (The additional development time required for designing and coding a Finite Element structural analysis model of each helicopter and assimilating the results within RASCAL far exceeded that allocated for the study. Therefore, although by reviewing the published results, the technique appears promising, it is outwith the scope of this study to fully investigate the potential of ACSR). The design of active control laws will begin by considering the Higher Harmonic Control family of algorithms.

6.2 Higher Harmonic Control.

The concept of Higher Harmonic Control to suppress helicopter vibration is a simple one derived from the principle of superposition. Assume for example that there exists a system whereby a vibrating load is applied to the fixed plane through the reaction forces from a piece of rotating machinery. The principle of superposition can be stated as follows (*Thompson, 1989*). If control inputs can be applied to rotating machinery to induce a response which exactly matches the amplitude and frequency of the vibration but in anti-phase, then the vibration transmitted to the fixed plane will be completely nulled. This principle presents an extremely attractive option to the control engineer. If the correct signal can be applied to the rotating plant, 100% attenuation of the vibration amplitude is theoretically obtainable. However, as with all control law designs, the usefulness of the theory is limited by the hardware used to implement it. For helicopter vibration control, the hardware limitations are primarily attributable to the bandwidth of the swashplate actuation system.

Helicopter vibration acts on the fuselage at a fundamental frequency of N/rev. For small to medium aircraft, where the rotorspeed typically falls within a 25-35 rad/s range, this gives a vibration frequency of approximately 16-20 Hz or 100-140 rad/s. From the principle of superposition, the controlling signal has to be applied at the same frequency as the vibration it is to regulate, in this case between 16 and 20Hz.

Therefore, to ensure that non-linear actuator effects, specifically rate saturation, are not included in the feedback loop, the actuator bandwidth must be at least 40-50Hz. In addition, the actuators must be stiff enough to provide the swashplate control force demanded by the control law; otherwise, the controller will be operating in a sub-optimal (or even unstable) region. Finally, as the actuators are airborne devices, a significant weight penalty is imposed upon their design. Over the past decade (*Achache&Polychroniadis, 1987; Lehmann, 1985; Richter et.al., 1990*) swashplate actuation systems have become available which can conform to the requirements above and meet CAA / FAA safety compliance demands.

Assuming for the moment that a suitable actuator servo system is available, the problem of designing the control law remains. Although HHC had been discussed theoretically for many years, one of the first helicopter vibration control laws was proposed by Shaw (*1967*). He postulated that the frequency response function between the Fourier coefficients of the harmonic input and the Fourier coefficients of the measured vibration could be exploited for the purposes of control. This relationship can be summarised as follows,

$$\underline{Z}(t_{k+1}) = \underline{Z}(t_0) + \boldsymbol{T}\,\underline{\theta}(t_k) \qquad (6.2.1)$$

Where, $\underline{Z}(t_{k+1})$ is the vector of Fourier coefficients at the $(k+1)^{th}$ rotor turn,

$\underline{Z}(t_0)$ is the baseline vector of Fourier coefficients,

$\underline{\theta}(t_k)$ is the vector of Fourier coefficients of the control inputs to the k^{th} rotor turn and

$\boldsymbol{T}$ is the Jacobian of the rotor system, identified on-line.

Application of this subtle method succeeds in replacing the relationship between vibration control and response, from a complex, non-linear, periodic problem in the rotating frame, to a simple linear association in the frequency domain. More importantly, HHC can be applied to the rotor through the conventional swashplate arrangement, which meant that the controllers could be tested on existing aircraft and experimental apparatus.

A variety of multicyclic or higher harmonic control algorithms were proposed in the early eighties, (*McCloud, 1980*), (*Shaw & Albion, 1981*), (*Shaw et.al., 1989*), (*O'Leary & Miao, 1982*), (*Du Val et.al, 1984*) and (*Molusis et.al., 1983*), when the theory was promoted by some as the control panacea for active vibration alleviation. However, the main limitations of the theory soon became apparent. Of greatest concern was the excitation of rotor modes in the neighbourhood of N/rev by the application of N/rev higher harmonic control. In some cases, the blade root stresses were amplified at certain frequencies (*McCloud, 1980*), although, overall, multicyclic control methods proved successful in simultaneously attenuating vibration and blade root stresses.

6.3 Harmonic Analysis of Vibration data.

6.3.1 Fourier Analysis.

Central to the operation of all multicyclic controllers is an efficient and accurate harmonic analysis technique, capable of extracting the Fourier series coefficients from a short, noise-corrupted sample of data. The Fourier coefficients are defined in the frequency domain and describe the amplitude and phase content of a signal corresponding to a discrete frequency ω. Transformation between the frequency and time domains is performed through the Fourier transform equation.

$$X(\omega) = \int_{-\infty}^{\infty} x(t)\, e^{-i\omega t}\ dt \qquad (6.3.1)$$

For a periodic signal of arbitrary shape, signal $x(t)$ can be reconstructed in the time domain by combining the Fourier coefficients $X(\omega)$ at integer harmonics of the fundamental period of the signal. For a helicopter rotor the fundamental period is one complete revolution of the rotor, which is more conveniently measured with respect to azimuth angle (ψ) rather than time.

$$\psi = \Omega t \qquad (6.3.2)$$

$$X(\psi) = \tfrac{1}{2} a_0 + \sum_{n=1}^{\infty} a_{nc} \cos n\psi + b_{ns} \sin n\psi \qquad (6.3.3)$$

Replacing the dependant variable does not alter the mathematical validity of the approach, (*Murphy, 1989*). The reconstructed time domain signal consists of a mean component a_0 and an infinite sum of harmonics each of an amplitude determined by the Fourier coefficients a_{nc}, b_{ns} where,

$$a_{nc} = \frac{1}{\pi} \int_0^{2\pi} X(\psi) \cos n\psi \, d\psi \qquad (6.3.4)$$

$$b_{ns} = \frac{1}{\pi} \int_0^{2\pi} X(\psi) \sin n\psi \, d\psi \qquad (6.3.5)$$

For the purposes of this study, the time series in each integral $X(\psi)$ is the measured body axes vertical acceleration, $\dot{w}$. This fuselage parameter is the most sensitive to changes in rotor vibration and as such is the primary state to control. However, as $X(\psi)$ is a measured quantity, no mathematically closed form solution to the Fourier integral is possible and so numerical methods must be used. Often the Fast Fourier Transform (FFT) of the signal would be calculated and the element, or bin, of the FFT output vector corresponding to the desired frequency, ω, would be inspected. Although many standard forms exist for computing the FFT (*Press et.al., 1992*), it is inherently a complex procedure, which for analysis at only one discrete frequency constitutes a significant and unnecessary software development overhead. Therefore a simpler and relatively inexpensive (in terms of software development time), algorithm for approximating the Fourier integral was used.

6.3.2 *Trapezoidal Approximation to the Fourier Integral.*

The trapezoidal rule is a low-order numerical integration technique, which does not require knowledge of the time derivative of the function to be integrated. The trapezoid algorithm approximates the integral,

$$\int_a^b f(x)\,dx \tag{6.3.6}$$

by first dividing the interval $[a,b]$ into a finite number of sub-intervals. Assuming the function varies linearly across each sub-interval, the area under the curve subtended by each sub-interval can be approximated by a trapezoid. The total integral is then evaluated by summing all of the trapezoids under the curve. The trapezoid approximation to the integral (6.3.6) calculated with uniform spacing between division points, is given by the equation (*Cheney & Kincaid, 1985*),

$$\int f(x) \approx \frac{h}{2}\sum_{i=1}^{n-1}\left[f(x_i)+f(x_{i+1})\right] \tag{6.3.7}$$

where, h is the length of each subinterval,

n is the total number of points in the data stream and

$$\frac{h}{2}\sum_{i=1}^{n-1}\left[f(x_i)+f(x_{i+1})\right] \quad \rightarrow \quad \int_a^b f(x) \qquad as \quad h \rightarrow 0 \tag{6.3.8}$$

This simple integration scheme worked satisfactorily, with the additional benefit of helping to keep the overall complexity of the controller down. This would facilitate the process of debugging the simulation and so reduce development time overall. Naturally, the algorithm was thoroughly tested to ensure that sufficient complexity was retained in the harmonic analysis routine. The algorithm was tested by reconstructing the input signal generated by a 45° tail rotor azimuth integration step (corresponding to the smallest sampling rate) using only the 4/rev harmonic coefficients extracted by equations (6.3.4 - 6.3.7). The signal reconstructed using equation (6.3.3) and the original vibration data are shown for comparison in *figure 6.1*. The predicted and

measured vibration data match reasonably well, as expected. The phase between signal and estimate is negligible and the amplitudes of the N/rev sinusoids are practically identical. The overshoots of the peaks in the measured signal are generated by the second vibration harmonic at 8/rev.

6.3.3 High pass filter algorithm.

Progressive immersion into a sharp-edged gust does not only result in a dramatic increase in vibration amplitude, but also induces a significant rigid body response. This introduces large amplitude motion at frequencies below 0.5Hz into the vibration signal. Now, the harmonic analysis is performed every rotor turn, which corresponds to a data stream buffer length of approximately 0.25 seconds, which in turn leads to a minimum detectable frequency of 4Hz. This means that the rigid body motion associated with the gust will be alaised into the bandwidth of the harmonic analysis routine (4-175Hz, for 350Hz sampling frequency ≈ 22.5° tail rotor azimuth in Puma). Therefore, it is necessary to remove the rigid body response from the signal prior to extracting the Fourier coefficients.

A conventional Butterworth high-pass filter was used for this operation. However, the phase change problems associated with direct filtering introduced phase errors in the calculation of the Fourier coefficients (*Press et.al. 1992*), which in turn invalidated the controller (control inputs will no longer be in anti-phase with the vibration). To overcome this problem, an unusual filtering approach was used.

The Butterworth filter coefficients were calculated in MATLAB™ using the HISAT integration interval as the data time-step. The filter is implemented via the discrete convolution of the vibration data with the impulse response function of the filter. The data is convolved with the filter four times, with the signal reversed after each pass. End effects and transient behaviour are removed by extrapolating the signal at each end prior to convolution with the filter. The net result is that the measurements and filter outputs have exactly the same phase, as required.

6.4 The Design of an Optimal Multicyclic Controller.

From the authors' review of the published work on active vibration control in the public domain, and multicyclic methods in particular, it is obvious that a vast array of control law structures have been investigated. It would be foolish to ignore such techniques in the blind pursuit of fashionable control ideologies, especially as the performance of existing control technologies has yet to be evaluated against a structured disturbance induced vibration signature (*Houston & Hamilton, 1993*). Many of the algorithms reported in the literature were designed for applications defined within the remit of a specific project, (*O'Leary & Miao, 1982; Lehmann, 1985*). However, in keeping with the fundamental aims of this study, any existing technique considered a suitable candidate for further exploration should ideally have a generic structure. Identification of the aircraft dynamics should be performed on-line. The controller must have sufficient stiffness and bandwidth to attenuate *any* disturbances and the control law must be robust to parameter uncertainties and system nonlinearities, while continually sustaining near optimum performance. From the literature review, three variants of the standard HHC algorithm published in the paper by Achache and Polychroniadis entitled '*Development of an experimental system for active control of vibration on helicopters - development methodology for an airborne system*', (*1987*) matched all of the requirements outlined above. Two of the HHC variants, the *variational* and *stochastic* models will be explained below.

The purpose of any higher harmonic controller is to provide compensatory control inputs intended to attenuate transmitted main rotor vibration at a specific frequency (N/rev). The goal is to find the control inputs that will minimise the left-hand side of equation (6.2.1), i.e.

$$\underline{Z}(t_{k+1}) = \underline{Z}(t_0) + \boldsymbol{T}\,\underline{\theta}(t_k)$$

$$\boldsymbol{T}\,\underline{\dot{\theta}}(t_k) = -\underline{Z}(t_0) \qquad (6.4.1)$$

This is the result predicted by the superposition theory, i.e. $\underline{Z}(t_0)$, the baseline rotor vibration, will be completely attenuated if the sinusoid generated by $\boldsymbol{T}\,\underline{\theta}(t_k)$ is in anti-phase with $\underline{Z}(t_0)$. In (*Achache & Polychroniadis, 1987*), such a description of the

multicyclic, vibration dynamics is referred to as a '*global*' model. Two other types of model, the '*variational*' and '*stochastic*' are used to improve the computational efficiency of the global model.

6.4.1 Optimal control methods.

Borrowing heavily from modern, multivariable optimal control techniques (LQR, LQG/LTR), the first step in designing an optimal HH controller is the definition of a cost function. This is a positive semi-definite function of the states to be regulated (Fourier coefficients of measured vibration) and the control inputs (Fourier coefficients of HHC inputs). A good cost function will asymptotically tend to zero as its elements approach their desired values (regulator action). The simplest cost function (used in LQR and/or H_2 designs) is the quadratic form, which if tailored to the HHC problem could be expressed as,

$$\boldsymbol{J} = \underline{\boldsymbol{Z}}(t_{k+1})^T \underline{\boldsymbol{Z}}(t_{k+1}) + \Delta\underline{\theta}(t_k)^T \boldsymbol{W} \Delta\underline{\theta}(t_k) \tag{6.4.2}$$

where,

$$\Delta\underline{\theta}(t_k) = \underline{\theta}(t_k) - \underline{\theta}(t_{k-1}) \tag{6.4.3}$$

Minimisation of this cost function will ensure that the vibration levels over the next rotor turn, $\underline{\boldsymbol{Z}}(t_{k+1})$, tend to zero asymptotically. A term is included which is proportional to the control action provided to the rotor $\Delta\underline{\theta}(t_k)^T \boldsymbol{W} \Delta\underline{\theta}(t_k)$, completing the requirements for control in the optimal sense, i.e. maximum attenuation with minimum control effort. A weighting matrix, $\boldsymbol{W}$, is included to enable direct manipulation of the penalties placed on available control energy. This cost function can be minimised with respect to higher harmonic control inputs if the first derivative is set to zero. However, direct substitution of (6.4.2) into (6.4.1) results in terms of $\underline{\boldsymbol{Z}}(t_0)$ in the equation that computes the optimal change in controls, requiring on-line identification of baseline vibration, $\underline{\boldsymbol{Z}}(t_0)$. This can be avoided by utilising the *variational* form of (6.4.2) thus,

$$\Delta\underline{\boldsymbol{Z}}(t_{k+1}) = \boldsymbol{S}\Delta\underline{\theta}(t_k),$$

$$\underline{\boldsymbol{Z}}(t_{k+1}) = \underline{\boldsymbol{Z}}(t_k) + \Delta\underline{\boldsymbol{Z}}(t_{k+1}) = \underline{\boldsymbol{Z}}(t_k) + \boldsymbol{S}\Delta\underline{\theta}(t_k) \tag{6.4.4}$$

Substituting equation (6.4.4) into (6.4.1),

$$\boldsymbol{J} = \left(\underline{\boldsymbol{Z}}(t_k) + \boldsymbol{S}\Delta\underline{\theta}(t_k)\right)^{\mathrm{T}}\left(\underline{\boldsymbol{Z}}(t_k) + \boldsymbol{S}\Delta\underline{\theta}(t_k)\right) + \Delta\underline{\theta}(t_k)^{T}\boldsymbol{W}\Delta\underline{\theta}(t_k) \tag{6.4.5}$$

This cost function can be minimised with respect to the change in controls, $\Delta\underline{\theta}(t_k)$, by equating the first partial derivative to zero.

$$\frac{\partial \boldsymbol{J}(t_k)}{\partial\Delta\underline{\theta}(t_k)} = \boldsymbol{S}^{\mathrm{T}}\underline{\boldsymbol{Z}}(t_k) + \left(\boldsymbol{W} + \boldsymbol{S}^{\mathrm{T}}\boldsymbol{S}\right)\Delta\underline{\theta}(t_k) = \underline{0} \tag{6.4.6}$$

giving,

$$\Delta\underline{\theta}^{*}(t_k) = -\left(\boldsymbol{W} + \boldsymbol{S}^{\mathrm{T}}\boldsymbol{S}\right)^{-1}\boldsymbol{S}^{\mathrm{T}}\underline{\boldsymbol{Z}}(t_k) \tag{6.4.7}$$

The optimal control input at time t_k is given by the sum of the optimal control deviation, $\Delta\underline{\theta}^{*}(t_k)$ and the previous control inputs $\underline{\theta}(t_{k-1})$,

$$\underline{\theta}(t_k) = \underline{\theta}(t_{k\text{-}1}) + \Delta\underline{\theta}^{*}(t_k) \tag{6.4.8}$$

The control sensitivity matrix in the variational model, *figure 6.2*, has been denoted $\boldsymbol{S}$ as opposed to $\boldsymbol{T}$ for the global model, to enhance the distinction between each matrix. The global sensitivity matrix, $\boldsymbol{T}$, is a matrix of first derivatives - a *Jacobian* – between the vibration and control vectors directly. On the other hand, the variational sensitivity matrix, $\boldsymbol{S}$, maps the *change* in controls to the *change* in vibration over a single rotor turn, essentially a matrix of second derivatives or *Hessian*. The extraction of each type of sensitivity matrix is discussed in the next section.

6.4.2 *Calculation of the Sensitivity Matrix.*

As with GENISA, numerical differentiation was used to calculate the individual elements of the sensitivity matrices of the global and variation models. The starting

point for both algorithms is a baseline measurement of the vibration levels with no harmonic control applied. The harmonic controls are then perturbed; the simulation is flown for another rotor turn and the vibration levels measured. For global control, the elements of the sensitivity matrix can be calculated by,

$$\boldsymbol{T}_{i,j} = \frac{\partial \underline{Z}_i}{\partial \underline{\theta}_j} = \frac{\left(\underline{Z}_{pert} - \underline{Z}_0\right)}{\underline{\theta}_{pert}} \tag{6.4.9}$$

If the variational control scheme is employed, then the harmonic controls are set to zero again and the simulation flown for another rotor turn. This action resets the simulation to the baseline state. The controls are then perturbed again by twice the initial perturbation size and the simulation flown over a fourth rotor turn. The sensitivity matrix for the variational model is then,

$$\boldsymbol{S}_{i,j} = \frac{\partial(\Delta \underline{Z}_i)}{\partial(\Delta \underline{\theta}_j)} = \frac{\left(\underline{Z}_{pert,2} - \underline{Z}_0\right) - \left(\underline{Z}_{pert,1} - \underline{Z}_0\right)}{\underline{\theta}_{pert,2} - \underline{\theta}_{pert,1}} \tag{6.4.10}$$

where subscripts 1 & 2 denote the first and second perturbations respectively.

6.5 Performance of the HHC algorithm.

6.5.1 Baseline Performance of the Variational HHC Algorithm.

Before progressing onto the control of gust-induced vibration, it is prudent to examine the performance of the control law for the still-air case. Of the four test flight speeds, 20 knots was chosen for this test, as the largest amplitude still-air vibration is generated at this velocity. The results of the test are presented in *figures (6.3)* through *(6.5)*. Figure *6.3* shows the time history of w produced by HISAT. The initial vibration amplitude can be clearly seen at the beginning of the response, followed immediately by a transient region as the HHC inputs are initialised. The vibration peak-to-peak amplitude is reduced by over 50%, but this does not give a clear picture of the

effectiveness of the controller. Figure *6.4* shows the PSD of w for an uncontrolled simulation. The spike at 4/rev can be clearly seen. Comparing this with *figure 6.5* shows that the vibration energy at 4/rev has effectively been nulled by the action of the controller. This result proves that the HHC algorithm is working as predicted.

6.5.2 Attenuation of Step-Gust-Induced Vibration.

The performance of the optimal HH controller when pit against baseline helicopter vibration was most impressive. Having demonstrated the validity of the algorithm and functional competency of each constituent component (harmonic analysis, matrix inverse, etc.) the next logical step is to test the controller under worst-case conditions. Progressive immersion into a vertical step gust inducing a high split about the fundamental frequency shall provide a severe test of the robustness of the controller.

The test parameters are as follows. The aircraft type is again the Aérospatiale Super Puma with the same mass and inertia parameters as in previous experiments. The amplitude of the gust was again 2.5 ms^{-1} and 4 experiments were performed, at 5, 10, 15, and 20 knots relative airspeed. Figures *6.6* through *6.9* show the PSD`s of the uncontrolled and controlled responses for each of the experiments. The attenuation of vibration energy at 5 knots (*figure 6.6*) is reasonable, approximately 80%. At 10 knots, the controller really begins to struggle, achieving only about 20% attenuation, *figure 6.7*. At 15 and 20 knots (*figures 6.8 & 6.9*), the controller actually begins to contribute vibration energy, rather than control it.

It is apparent from these results that optimal HHC algorithms quickly degrade in performance when introduced to large gradient gust induced vibration. It can also be inferred that passive devices tuned to N/rev would suffer similar performance degradation. This may be a direct consequence of applying control at a single frequency, or it may be that the linear model is invalid during the gust. Both of these concerns will be addressed in the subsequent sections.

6.5.3 *Stochastic Model (Kalman Filter Implementation).*

The variational controller has successfully attenuated still-air vibration, proving that the controller has been implemented correctly. However, it performs poorly when confronted with the vibration associated with a sharp-edged gust. This poor performance may be due to controlling the vibration at the 'wrong' frequency (N/rev *not* N±δ/rev), a topic to be discussed in the next section. Another reason may be that the control sensitivity matrix of the linear model is invalid inside the gust. To try to eliminate this possibility, an extended Kalman Filter was used to identify the dynamics of the system on-line.

Crudely speaking, the Kalman Filter (*Kalman-Bucy* filter in the continuous case) is an optimal observer used to identify system states in the presence of external disturbances and noise (*Stefani et. al., 1994*). The filter is optimal in the sense that given *á priori* information of the statistical properties of the disturbance and measurement noise affecting the plant, the Kalman filter will attempt to minimise the size of the estimation error intensity, giving an optimal (in the stochastic sense) estimate of the state (*Stevens & Lewis, 1992*). The Kalman filter arrangement investigated was originally published by Molusis, Hammond and Cline (*1983*) and is shown below.

$$\underline{\hat{x}}_j(i+1) = \underline{\hat{x}}_j(i) + \boldsymbol{K}(i+1)[\underline{Z}_j(i+1) - \Delta\underline{\theta}^T(i)\underline{\hat{x}}_j(i)],$$

$$\boldsymbol{K}(i+1) = \frac{\boldsymbol{P}_j(i)\Delta\underline{\theta}(i)}{\boldsymbol{V} + \Delta\underline{\theta}^T(i)\boldsymbol{P}_j(i)\Delta\underline{\theta}(i)},$$

$$\boldsymbol{P}(i+1) = \boldsymbol{P}(i) + \boldsymbol{W} - \boldsymbol{K}(i+1)\Delta\underline{\theta}^T(i)\boldsymbol{P}_j(i) \qquad (6.5.1)$$

where,

$\underline{\hat{x}}_j(i+1)$ is the $(i+1)^{th}$ estimate of the j^{th} row of the sensitivity matrix,

$\boldsymbol{K}(i+1)$ is the $(i+1)^{th}$ estimate of the Kalman gain matrix,

$\boldsymbol{P}(i+1)$ is the $(i+1)^{th}$ estimate of the filter covariance matrix and

$\boldsymbol{W}, \boldsymbol{V}$ are the system process and measurement noise covariance matrices

respectively.

The Kalman filter estimates the elements of the control sensitivity matrix in a recursive fashion using the output error as an indicator of the error in the sensitivity matrix. For the undisturbed case (no gust), the Kalman filter made tiny adjustments to the system matrix elements, driven mostly by numerical error in the harmonic analysis routine[1]. However, when the gust was introduced, HISAT became unstable in the majority of runs. The controller was very sensitive to the shape and magnitude of the initial disturbance noise covariance matrix, even during on-line estimation of this matrix. It is likely that the slow sampling rate (1 rotor turn) was insufficient to allow the internal covariance observer to settle on a good estimate while being subjected to the rapidly-varying gust.

Upon reflection, it is not surprising that the Kalman filter failed and the reasons for this are two-fold. First, a reliable estimate of the statistical properties of the gust-induced disturbance is necessary to drive the filter accurately. The disturbance is highly structured and therefore a stationary statistical model is extremely difficult to extract, if not impossible. Secondly, the discretisation interval of the controller (1 rotor turn) is slow in comparison to the dynamics of the disturbance. It is well known from observer theory that the bandwidth of the estimator should exceed that of the plant to be estimated by some margin, whereas here the reverse is in fact the case. As there appeared to be no apparent benefit to be gained, the stochastic controller incorporating a Kalman filter was not pursued any further.

6.5.3 Multi-Harmonic control.

The attenuation of gust-induced vibration using an N/rev HHC algorithm is substantially poorer than expected from the outset. This result also infers that both active multicyclic controllers and passive, dynamically tuned absorbers will suffer rapidly degraded performance in turbulent operating environments. This is because the bandwidth over which control is effective for a single N/rev control signal applied to the rotor is too small to control disturbances in the neighbourhood of N/rev, a direct

---

[1] It is generally accepted that for a Kalman filter to operate well, a degree of noise must be present in the system.

consequence of tuning the controller/device to a specific frequency. In an attempt to increase the effective bandwidth surrounding N/rev; (N-1)/rev and (N+1)/rev inputs were added to the rotor.

The motivation for superimposing 3 and 5/rev inputs onto the HHC law comes from looking at the frequency response characteristics of cascaded harmonic oscillators, *figure 6.14*. The transfer functions used to create *figure 6.14* are simple undamped, second order poles, located at frequencies corresponding to 3,4 & 5 per rev. This is of course an abstraction of the actual bode plot of a harmonic controller. The most fundamental difference is the phase at each tuned frequency: the HHC algorithm delivers a control signal which is in anti-phase (-180°) to the input signal (the vibration), whereas a second-order pole has only a 90° phase lag. However, this representation of the controller is sufficient to illustrate the intent driving the application of multi-harmonic control.

Essentially, the cascade arrangement gives the HHC is an increase in gain in the neighbourhood of the tuned frequency at N/rev. The variational HHC algorithm demonstrated in *figures 6.6* and *6.7* its capability for partially attenuating gust-induced vibration transmitted at N±δ /rev (for small δ). By increasing the control gain in the neighbourhood of N/rev, better suppression was expected. However, when the control law was augmented with 3/rev and 5/rev inputs, the results were almost identical to those obtained with the standard control configuration, *figures 6.10 to 6.13*. This is because there is effectively an addition, not multiplication, of each control input transfer function when the sub- and super-harmonic inputs are added to the N/rev input. Again, using the resonant second-order abstractions of the control laws, summing together gives the gain plot shown in *figure 6.15*. It is clear that two zeros have been introduced into the overall transfer function, causing the actual increase in gain near N/rev to be negligible.

The only way to regain the properties of cascade control implementation is to switch from the signal summation arrangement illustrated in *figure 6.16*, to a multiplicative scheme shown in *figure 6.17*. However, another problem develops here, as the overall controller becomes highly nonlinear, as shown below.

additive scheme : $\underline{\theta} = (\Gamma_3 + \Gamma_4 + \Gamma_5)\dot{w}$

multiplicative scheme: $\underline{\theta} = (\Gamma_3 \Gamma_4 \Gamma_5)\dot{w}^3$

The applied control would then be proportional to the cube of the measured body axis vertical acceleration, $\dot{w}$. The multiplicative scheme was attempted out of curiosity but, as expected, the closed-loop response was highly unstable.

6.6 Disturbance Feed-Forward Higher Harmonic Control.

The results of the investigations conducted in the past two sections imply that poor attenuation of the variational HHC algorithm to gust inputs can be neither attributed to an inaccurate sensitivity matrix, nor can it be improved by the addition of further integer harmonics of rotorspeed to the control signal. The final modification to the HHC algorithm was inspired by well known fact (*Skogestad & Postlethwaite, 1996; Stefani, et.al., 1994*) that complete disturbance attenuation is theoretically possible if a precise model of the disturbance is made available. This will be the topic for discussion in this section.

6.6.1 Description of the Controller.

The disturbance feedforward higher harmonic control (DHHC) algorithm is a novel extension of the variational control scheme described in §6.4.1 above. In this new algorithm, the cost function of equation (6.4.2) is augmented with an estimate of the N/rev Fourier coefficients of the disturbance acting over the next rotor turn.

$$\boldsymbol{J} = \underline{\boldsymbol{Z}}(t_{k+1})^T \underline{\boldsymbol{Z}}(t_{k+1}) + \Delta\underline{\theta}(t_k)^T \boldsymbol{W} \Delta\underline{\theta}(t_k) + \underline{\boldsymbol{d}}(t_{k-1}) \qquad (6.6.1)$$

The disturbance acts at a frequency of N±δ/rev. However, sampled over 1 rotor turn, the energy contained at frequencies N±δ can be approximated by N/rev coefficients, which have been phase-shifted to give a 'best-fit' estimate to the disturbance energy. By following the same procedures of §6.4.1, the optimal higher harmonic collective input is given by,

$$\Delta\underline{\theta}^{*}(t_k) = -\left(\boldsymbol{W} + \boldsymbol{S}^{\mathrm{T}}\boldsymbol{S}\right)^{-1}\boldsymbol{S}^{\mathrm{T}}\left(\underline{\boldsymbol{Z}}(t_k) + \underline{\boldsymbol{d}}(t_k)\right) \tag{6.6.2}$$

The disturbance estimate is obtained by performing two identical simulation runs, one in still air, the other through a gust, with the N/rev signal content recorded. The disturbance estimate is then given by the difference of the harmonic coefficients at each rotor turn. This information is stored in a separate data file, which is accessed by the DHHC algorithm as required.

6.6.2 Performance of the Controller.

The performance of the DHHC algorithm (under the same conditions as the variational and multi-harmonic schemes) is shown in *figures 6.18* through *6.21*. This control law demonstrates a significant improvement over the standard HHC scheme, attenuating disturbance-induced vibration throughout the entire speed range of interest. The decrease of percentage attenuation with forward airspeed is most probably due to the N/rev approximation of the harmonic content in the disturbance. As the frequency shift δ increases, the approximations in $\underline{\boldsymbol{d}}(t_{k+1})$ become cruder and errors begin to intrude into the control loop.

The DHHC control law fulfils the fourth aim of this thesis, as an improvement to current active vibration control algorithms has been designed and tested by simulation and shows that attenuation of worst-case gust-induced vibration is possible. However, some severe implementation issues remain, most prominently the estimation of the disturbance Fourier coefficients over the next rotor turn. Intuitively, this would lead to the design of a predictor-corrector estimator. Such a model would use previous control inputs, measured vibration and past estimates of the disturbance term to estimate the

expected disturbance over the next rotor turn. Considering the failure of the Kalman Filter in the stochastic HHC algorithm, it was felt that nonlinear estimation techniques would stand a better chance of success. To this end, Artificial Neural Networks (ANN's) were used to construct the disturbance estimator. The results of this investigation will be presented in the next chapter.

6.7 Individual Blade Control.

As the name suggests, Individual Blade Control is the control of the pitch of each blade individually in the rotating frame of reference. A significant body of work in this area has been published by Ham (*Ham et.al., 1958; Zvara & Ham, 1960; Ham, 1975; Ham, 1980; Ham et.al. 1983; Ham 1987; Ham 1995*) encompassing theoretical and experimental results obtained at MIT over the past two decades. The effect of IBC on suppressing lag motion (*Ham, Behal & McKillip, 1983; Kessler & Reichert, 1996*), minimising ground resonance (*Tettenborn, Kessler & Reichert, 1997*) and vibration suppression (*Belo & Marques, 1996; McKillip, 1985*) has been well documented. The control of blade flap motion has also been used as the test vehicle for investigations into time-periodic control laws (*Calico & Weisel, 1984, 1986 and Webb, Calico & Weisel, 1991*). More recent applications of the technique have witnessed a shift towards Aeroelastic/ACSR methods, (*Belo & Marques, 1996*) and symbiosis with harmonic ideas (*Arnold, Müller & Richter, 1997*).

6.7.1 Defining the IBC Strategy.

The first step in designing an IBC controller is selecting an appropriate blade state to control. For the gust alleviation task, it is imperative that the chosen state is observable, controllable and sensitive to the gust. Figure *6.22* shows the flap angle time history for a single blade as the rotor immerses into a 2.5ms^{-1} step gust at 10 knots forward speed. It is quite clear from this plot that the gust front interacts with the blade from around 1½ seconds to 6½ seconds, where it stimulates transient behaviour before

finally settling at a new equilibrium position. The disturbance significantly influences the mean amplitude of flap motion (as expected), without altering the frequency of the response (1/rev). The impact on blade lag is much less severe, most of the periodic motion coming from the coriolis coupling between the modes. Therefore, as flap motion appears to be the more sensitive of the two rigid blade states available, this will be used as the output for feedback in the subsequent IBC control law designs.

6.8 Derivation of the Blade Equations of Motion.

The reduction of the blade equations of motion to a useful form is a complex affair which is simplified significantly by using the general kinematic expansions of blade velocity and acceleration developed in § 2.3.3-4. Assuming an idealised hinge, i.e. one unable to withstand any external moment and assuming at this point that no restoring moment (through a flap spring or lag damper) is present, an equality must exist between the aerodynamic and inertial moments acting about the hinge.

$$\int_0^{R-eR} \underline{r}_{section/hg} \times \underline{F}^{aero}_{section}\, dr = \int_0^{R-eR} \underline{r}_{section/hg} \times \overline{m}\,\underline{a}^{bl}_{section}\, dr \qquad (6.8.1)$$

where, $\underline{F}^{aero}_{section}$ is the vector of blade sectional aerodynamic forces,

$\underline{r}_{section/hg}$ is the distance from the hinge to the blade section and

$\overline{m}$ is the blade mass per unit length.

6.8.1 Inertial Terms.

Consider first the RHS of equation (6.8.1). Recall the acceleration of a blade element as defined in equation (2.3.14) as,

$$\underline{a}^{bl}_{section} = \underline{a}^{bl}_{hg} + \underline{\alpha}^{bl}_{hg} \times \underline{r}_{section/hg} + \underline{\omega}^{bl}_{hg} \times \left(\underline{\omega}^{bl}_{hg} \times \underline{r}_{section/hg}\right) \qquad (6.8.2)$$

To predict the motion of the blade with respect to the hinges it is necessary to express (2.3.14) with respect to hinge axes, (see *figure 2.7*). It is reasonable to assume that the flap and lag hinges are co-located without any appreciable loss of accuracy.

$$\underline{\boldsymbol{a}}^{bl}_{section} = \mathrm{T}_3 \underline{\boldsymbol{a}}^{hg}_{hg} + \left(\mathrm{T}_3 \underline{\boldsymbol{\alpha}}^{hg}_{hg} + \left[\ddot{\beta}\ 0\ \ddot{\zeta}\right]^{\mathrm{T}}\right) \times \underline{\boldsymbol{r}}_{section/hg} + \left(\mathrm{T}_3 \underline{\boldsymbol{\omega}}^{hg}_{hg} + \left[\dot{\beta}\ 0\ \dot{\zeta}\right]^{\mathrm{T}}\right) \times \left(\left(\mathrm{T}_3 \underline{\boldsymbol{\omega}}^{hg}_{hg} + \left[\dot{\beta}\ 0\ \dot{\zeta}\right]^{\mathrm{T}}\right) \times \underline{\boldsymbol{r}}_{section/hg}\right) \tag{6.8.3}$$

By deriving the equation of motion with respect to the hinge axes, which are in the rotating reference frame of the rotor, the complexity of the algebra is greatly reduced. Further simplifications are obtained by explicit definition of the hinge velocity and acceleration vectors and by noting that the flap and lag angles will be small, i.e.

$$\mathrm{T}_3 = \begin{bmatrix} 1 & \zeta & 0 \\ -\zeta & 1 & \beta \\ 0 & -\beta & 1 \end{bmatrix}$$

and

$$\underline{\boldsymbol{a}}^{hg}_{hg} = \left[a^{hg}_{hg,x}\ a^{hg}_{hg,y}\ a^{hg}_{hg,z}\right]^{\mathrm{T}} \qquad \underline{\boldsymbol{\alpha}}^{hg}_{hg} = \left[\alpha^{hg}_{hg,x}\ \alpha^{hg}_{hg,y}\ \alpha^{hg}_{hg,z}\right]^{\mathrm{T}} \qquad \underline{\boldsymbol{\omega}}^{hg}_{hg} = \left[p^{hg}\ q^{hg}\ r^{hg}\right]^{\mathrm{T}}$$

where, $\underline{\boldsymbol{a}}^{hg}_{hg}$ is the linear acceleration of the hinge in hinge axes,

$\underline{\boldsymbol{\alpha}}^{hg}_{hg}$ is the angular acceleration of the hinge in hinge axes and

$\underline{\boldsymbol{\omega}}^{hg}_{hg}$ is the angular velocity of the hinge in hinge axes.

then (2.3.14) becomes, after some manipulation,

$$\underline{\boldsymbol{a}}^{bl}_{elem} = \begin{bmatrix} a^{hg}_{hg,x} + \zeta a^{hg}_{hg,y} \\ -\zeta a^{hg}_{hg,x} + a^{hg}_{hg,y} + \beta a^{hg}_{hg,z} \\ -\beta a^{hg}_{hg,y} + a^{hg}_{hg,z} \end{bmatrix} + \begin{bmatrix} r_{section}\left(\alpha^{hg}_{hg,z} - \beta\alpha^{hg}_{hg,y} + \ddot{\zeta}\right) \\ 0 \\ -r_{section}\left(\alpha^{hg}_{hg,x} + \zeta\alpha^{hg}_{hg,y} + \ddot{\beta}\right) \end{bmatrix} + \begin{bmatrix} -r_{section}\left(p^{hg} + \zeta q^{hg} + \dot{\beta}\right)\left(-\zeta p^{hg} + q^{hg} + \beta r^{hg}\right) \\ r_{section}\left(\left(r^{hg} - \beta q^{hg} + \dot{\zeta}\right)^2 \left(p^{hg} + \zeta q^{hg} + \dot{\beta}\right)^2\right) \\ -r_{section}\left(r^{hg} - \beta q^{hg} + \dot{\zeta}\right)\left(-\zeta p^{hg} + q^{hg} + \beta r^{hg}\right) \end{bmatrix} \tag{6.8.4}$$

Substituting equation (6.8.4) into equation (6.8.1) and integrating along the blade span gives the equations of motion for the flap and lag degrees of freedom. As flap is defined as rotation about the blade x-axis and lag about the blade z-axis, only rows 1 and 3 need to be evaluated. The equation of motion for the flap degree of freedom becomes,

$$\begin{aligned}\ddot{\beta} &= q^{hg} r^{hg} \beta^2 - \left(p^{hg} q^{hg} \zeta + r^{hg} \dot{\zeta} + r^{hg^2} - q^{hg^2} - \frac{M_\beta}{I_\beta} a^{hg}_{hg,y} \right) \beta \\ &+ (p^{hg} r^{hg} + p^{hg} \dot{\zeta} - \alpha^{hg}_{hg,y}) \zeta - \left(q^{hg} \dot{\zeta} + q^{hg} r^{hg} - \alpha^{hg}_{hg,x} + \frac{M_\beta}{I_\beta} a^{hg}_{hg,z} \right) + \frac{\boldsymbol{L}_{aero}}{I_\beta}\end{aligned} \tag{6.8.5}$$

and similarly, for the lag,

$$\begin{aligned}\ddot{\zeta} &= -q^{hg} p^{hg} \zeta^2 - \left(p^{hg} \dot{\beta} - r^{hg} q^{hg} \beta + p^{hg^2} - q^{hg^2} + \frac{M_\beta}{I_\beta} a^{hg}_{hg,y} \right) \zeta \\ &+ (p^{hg} r^{hg} + r^{hg} \dot{\beta} + \alpha^{hg}_{hg,y}) \beta + \left(q^{hg} \dot{\beta} + q^{hg} p^{hg} - \alpha^{hg}_{hg,z} + \frac{M_\beta}{I_\beta} a^{hg}_{hg,x} \right) - \frac{\boldsymbol{N}_{aero}}{I_\beta}\end{aligned} \tag{6.8.6}$$

These equations illustrate the strong coupling that exists between the rotor blade states and fuselage rigid body modes. However, simulating the blade dynamics to this fidelity within MATLAB/SIMULINK would be a significant task. Of greater interest at this stage is the coupling between the rotor states themselves and the impact that coupling may have on the resulting IBC strategy. Therefore, although the above equations may be used in future programs, they shall be considered here only for the simplest case when the fuselage dynamics are either uncoupled from the rotor, or the aircraft is in a perfect linear trim. The equations then reduce to the more workable form (with respect to control law design) of,

$$\ddot{\beta} + \left(\Omega \dot{\zeta} + \left(\frac{2+e}{2(1-e)} \right) \Omega^2 \right) \beta = \frac{\boldsymbol{L}_{aero}}{I_\beta} \tag{6.8.7}$$

and

$$\ddot{\zeta} - \Omega \beta \dot{\beta} + \frac{M_\beta}{I_\beta} \Omega^2 e R \zeta = \frac{-\boldsymbol{N}_{aero}}{I_\beta} \tag{6.8.8}$$

The aerodynamic moments $\boldsymbol{L_{aero}}$ and $\boldsymbol{N_{aero}}$ will now be derived.

6.8.2 *Aerodynamic Terms.*

In calculating the aerodynamic moments acting about the hinge arrangement, it is necessary to evaluate the sectional aerodynamic forces at each radial station along the blade. These forces, sectional lift and drag, were depicted graphically in *figure 2.4*. Consider first, the equation for sectional lift.

$$\overline{L} = \frac{\rho \bar{c} a_0}{2}\left(u_t^2 + u_p^2\right)(\theta + \phi) \tag{6.8.9}$$

and make the following assumptions,

i) $\theta = (\theta + r_{section}\theta_{tw})$

ii) $\phi = \tan^{-1}\left(\frac{u_p}{u_t}\right) \approx \frac{u_p}{u_t}$

iii) $u_t^2 + u_p^2 \approx u_t^2$

iv) $u_p \approx v_{in} - r_{section}\dot{\beta}$

Under these assumptions, the out-of-plane moment about the hinge (flap moment) may be expressed as,

$$\overline{L} = \frac{\rho \bar{c} a_0}{2} u_t^2\left(\theta + r_{section}\theta_{tw} + \frac{v_{in} - r_{section}\dot{\beta}}{u_t}\right) \tag{6.8.10}$$

Expansion of equation (6.8.10) above yields an expression which is linear in terms of θ, θ_{tw}, $\dot{\beta}$ and v_{in}, therefore the aerodynamic flap moment is,

$$\boldsymbol{L_{aero}} = M_{\theta}\theta + M_{\theta_{tw}}\theta_{tw} + M_{\dot{\beta}}\dot{\beta} + M_{v_{in}}v_{in} \tag{6.8.11}$$

where,

$$M_{\theta} = \frac{\rho \bar{c} a_0}{2} \frac{\Omega^2 R^4}{12} (3 + 8\mu \sin(\psi) + 6\mu^2 \sin^2(\psi)) \quad (6.8.12)$$

$$M_{\theta_w} = \frac{\rho \bar{c} a_0}{2} \frac{\Omega^2 R^5}{30} (6 + 15\mu \sin(\psi) + 10\mu^2 \sin^2(\psi)) \quad (6.8.13)$$

$$M_{\beta} = -\frac{\rho c a_0}{2} \frac{\Omega R^4}{12} (3 + 4\mu \sin(\psi)) \quad (6.8.14)$$

$$M_{v_{in}} = -\frac{\rho \bar{c} a_0}{2} \frac{\Omega R^3}{12} (4 + 6\mu \sin(\psi)) \quad (6.8.15)$$

The aerodynamic lag moment can be derived in a similar vain, however, the authors attempts to estimate the drag coefficient resulted in a highly nonlinear expression for N_{aero}. Noticing however, that the typical lift-drag ratio of a slender wing is approximately 10-1, it was decided to approximate the aerodynamic lag moment by $1/10^{th}$ the magnitude of the flap moment. Indeed, after constructing a SIMULINK model of equations (6.8.7)-(6.8.11), *figures 6.23 - 6.24*, it was found that a gain of 0.12 gave lag time histories very close to those obtained from RASCAL.

6.8.3 SIMULINK Model of Coupled Flap-Lag Motion.

As mentioned in the previous section, a mathematical model of the blade equations of motion has been written within the MATLAB environment using SIMULINK. The model uses equations (6.8.7)-(6.8.11) as the basic engine of the simulation, but also includes a model of the gust disturbance as well. The top-level block diagram is shown in *figure 6.23*. The standard SISO negative feedback loop convention is used, with the signal flow commencing at the reference (or command) signal to the left of the diagram and moving along the principal path from left to right thereafter. The pilot commands augment those calculated by the controller, modelling a conventional swashplate actuation system with an IBC servo replacing the rigid pitch link. Inside the block entitled 'blade motion' (*figure 6.24*), the aerodynamic and inertial moment balance is computed to yield the flap and lag angles (and rates) about the hinge. Returning to the

top-level, the flap angle (β) is then combined with the signal from the gust disturbance generator. The feedback loop is then closed on this signal.

Only the hover case was simulated in this exercise (to remove periodic damping from the control model), as may be seen from the constant terms used to estimate the aerodynamic moments in *figure 6.24*. However, the model has been constructed in such a way as to allow for easy integration of nonlinear modules in the future. The dynamic response characteristics for the Puma are very close to those published in Padfield (*1996*) and the time-histories are very similar to those obtained by RASCAL. For example, using a hinge offset of 3.87% (Appendix III), the flapping frequency is 1.06/rev, compared with 1.052 reported in Padfield. Using the collective, longitudinal and lateral cyclic pitch positions obtained from a RASCAL trim at hover, the SIMULINK model predicts the flap and lag motion to within ± 11% of the figures returned by RASCAL (Appendix IV). These tests suggest the model is accurate enough for control law design purposes. It was felt that to reproduce the fidelity of non-linearity in RASCAL in a model intended solely for control design purposes would be a futile exercise.

6.9 IBC Controller Design for Disturbance Rejection.

The controller strategy chosen for this work uses a standard tracker (or servo) negative feedback loop with the command signals generated from the coning and first-order cyclic flap coefficients obtained from a RASCAL trim. The controller is fed with the error signal between measured flap angle (including disturbance) and command. In general, the tracker problem precludes the use of optimal design control techniques such as LQR and LQG/LTR, which are fundamentally derived to provide regulator action. Optimal tracker algorithms do exist, (*Stevens & Lewis, 1992*) but are only optimal to a known, simple input. To avoid clouding the design with algorithmic peculiarities at this early stage, a PID controller structure was chosen. This is the most general form of the classical loop-shaping compensator design methods, enabling assessment of the

controller *structure*, not necessarily the control law. At this stage the *principle* of vibration suppression by IBC methods was being tested, not the specific control law.

Working on the assumption that closed-loop gain at a specific frequency is proportional to the phase lag of the closed loop transfer function at that frequency, it was decided to require that the phase lag should be less than 1° at 1/rev. Consulting the Nichols chart shows that a proportional gain (K_P) of approximately 50 is needed. Using such a high gain dramatically reduces the phase margin (from 93.1° to 8.8°), so the response is woefully underdamped. However, the open-loop (cascade arrangement) has a gain of 34dB at 1/rev, more than enough to reject the disturbance (verified through simulation of the SIMULINK model). Next, an integrator term was added to reduce the tracking error. In selecting the integrator gain, the breakpoint of the PI transfer function had to be less than 27rad/s, to reduce the impact of the integrator lag (90°) on the phase margin. Selecting a breakpoint at 10rad/s gives an integrator gain (K_I) of 500. The design is completed by setting the derivative gain (K_D) to 0.5 (obtained from simulation). The transfer function of the compensator is given below.

$$C(s) = \frac{K_D s^2 + K_P s + K_I}{s} \tag{6.9.1}$$

The bode plot is shown in *figure 6.25*.

Before combining the controller with RASCAL, it was necessary to freeze the integration of the fuselage states, effectively decoupling the rotor, prior to running the simulation. The reasons for this are given in the next section. To test the control law, the Puma helicopter was trimmed at hover and subjected to a sharp-edged gust of $2.5ms^{-1}$ intensity with a closing velocity of 10 knots. For the first run, no IBC control inputs were applied. On the second run, the PID controller of equation (6.9.1) was activated. The results of the PSD's of each time history are shown in *figure 6.26*. It is obvious from this plot that the gust-induced vibration levels have been attenuated extremely well, comparable in fact to the DHHC algorithm. This result alone indicates that the IBC of blade flap motion can be used as an active vibration alleviation algorithm.

6.10 Controller Assessment Under Operational Conditions.

Disturbance-rejection controllers capable of significantly attenuating the effects of gust-induced vibration have been derived and results presented. However, the step gust is a worst-case mathematical abstraction of a realistic, turbulent aerodynamic environment. The next step in assessing the performance of the HHC and IBC schemes, such that useful, realistic conclusions could be drawn on their performance, was to evaluate the vibration rejection capabilities from within HISAT.

Unfortunately, it has proved impossible to harmonise the control laws with HISAT without destroying the numerical stability of the simulation. Consider first the operation of the HHC algorithm during the most benign manoeuvre possible – maintaining rectilinear trim. Several variations of control application interval were tried from within the inverse simulation framework, but none resulted in a successful, numerically stable simulation. It is felt by the author this is primarily due to the manner in which the inverse simulation algorithm operates, in particular, the way the Jacobian is constructed. Step changes in control deflection calculated by the inverse algorithm induce a vertical acceleration profile governed by the reaction of the blades to the hub (*Houston & Tartellin, 1991*). This profile contains a sharp step (caused by the instantaneous change in lift) which is difficult to filter from the data passed to the HHC algorithm. Numerical errors are introduced which, when coupled with the inherent numerical instability of the inverse algorithm (from the numerical differentiation step), inevitably lead to failure of the simulation before completion. Actuator lag was introduced to smooth out the control steps, but was found to have a negligible impact on the numerical stability of the simulation. It is obvious that a control-blending filter should encase the GENISA algorithm to mimic the analogue demands of the pilot. Time constraints on this project have meant the filter could not be designed and implemented, however, such a design should be a prime consideration in any future work.

Full integration of the IBC scheme proved to be difficult on two counts. First, the controller designs are based on linear, constant coefficient models of the blade dynamics. These assumptions become more inaccurate with increasing forward airspeed as the periodic terms in the flap damping coefficient gain importance. The PID

controller has sufficient margins to ensure some degree of robustness but this was not an explicit design constraint. In addition, the bandwidth of the controller is too high to allow fully coupled nonlinear flight to be performed. Although the combined control inputs from pilot and servo are well within normal operating limits for most of the simulation, a large control spike, typical of compensators with phase-advance characteristics, is seen at the start. This input interacts with the wake model to quickly destabilise the simulation – most runs ending after less than ½ second. Therefore, without more precise loop-shaping in the controller design stage, it is impossible to simulate a HISAT / IBC combination. By extrapolation, it is reasonable to assume a similar situation will exist for control of actual aircraft.

6.11 Chapter Summary.

Several important results have been presented during this chapter. First, it was shown that the existing HHC algorithms perform extremely poorly when subjected to gust-induced vibration. Indeed, under certain conditions, the controllers actually seem to generate vibration, rather than attenuate it. The inclusion of stochastic estimators and multi-harmonic control inputs failed to yield any improvement. However, as N±δ/rev can be approximated by phase-shifted N/rev Fourier coefficients over a finite interval (1 rotor turn), a novel algorithm has been developed which augments the HHC algorithm explicitly with a disturbance feedforward term and significantly improves performance. Some severe implementation issues remain with this algorithm however, to be discussed in the next chapter.

An accurate model of coupled flap & lag blade motion has been developed within the MATLAB and SIMULINK environment. Results from this model, and numerical experiments with RASCAL, have shown that gust-induced vibration suppression is achievable through simple PID control of flap motion. However, to ensure there is enough gain at 1/rev to attenuate the disturbance, the bandwidth of the PID scheme becomes unacceptably large. Advanced techniques offering precise loop shaping are needed. Potential problems have also been identified with respect to extending IBC to the forward flight case. Research in this area (time-periodic control) is embryonic at best – definite avenue for future research.

Successful simulation of any of the HHC algorithms for an aircraft performing manoeuvres from within HISAT has proved to be impossible. Numerical instabilities generated by the discrete nature of the GENISA algorithm destabilise the harmonic analysis routine, leading to eventual failure of the controller. Including actuator lag into the algorithm yielded little benefit, which suggests that a more sophisticated blending algorithm is needed. This should be a primary aim of any follow-on study resulting from this work.

CHAPTER VII

ACTIVE VIBRATION CONTROL LAW DESIGN USING ADVANCED CONTROL TECHNIQUES.

In this chapter, the successes and limitations of the HHC and IBC control strategies are reviewed to suggest the optimal avenues for controller enhancement. After a short investigation of modern control design procedures, precision loop shaping via mixed-sensitivity H_∞ control and disturbance estimation using neural networks are investigated in some detail.

7.1 Review of HHC & IBC Controllers.

In the previous chapter, two of the most promising state of the art active techniques for vibration alleviation were tested using HISAT. They demonstrated conclusively that it is at least theoretically possible to design active controllers which will suppress not only mean aerodynamic vibration levels but also the sudden high intensity levels induced by sharp-edged gusts. With the Higher Harmonic Control algorithm it was found necessary to explicitly include a direct feedforward term of the expected vibration levels over the forthcoming rotor turn. Such information is unavailable, in the sense that the gust over the next rotor turn cannot be measured as it has yet to occur! In a practical system it will be necessary to use a prediction of the

expected vibration levels at each rotor turn, constructed from the measured data of the previous turns. The conventional approach to state estimation and prediction practised by most control engineers is to employ a Kalman Filter in some guise. However, as demonstrated in §6.5.3, the Kalman Filter performs poorly when stimulated by the type of gust-induced vibration discussed throughout this report. Another estimation algorithm is required, one which has the theoretical capability to cope with large signal magnitude changes and system nonlinearities. After conducting a preliminary review of several techniques based upon published results and theoretical limitations, it was decided to continue the investigation using a Neural Network as the disturbance predictor/estimator. The results of this exercise will be presented in §7.5.

From a practical standpoint, the IBC scheme may be viewed as the more attractive option, as the demands on the control servos are much less acute (the IBC scheme attenuates 1/rev disturbances, whereas the HHC actuators have to attenuate N/rev, demanding stiffer, higher bandwidth servos). However, the classical PID individual blade controller design has shown rotor/body coupling problems because of the high bandwidth control gain produced (resulted in instability when fuselage states were integrated). An optimal balance needs to be struck between controller bandwidth and closed-loop gain at 1/rev. Classical frequency domain loop-shaping techniques could be employed here, but it would require an exceptionally skilled control engineer to arrive at *the* optimal solution meeting the performance requirements without undergoing an extensive process of design iteration. To avoid this scenario, several of the many modern, optimal control techniques were investigated and assessed with respect to their suitability for implementation within an IBC strategy.

7.2 Modern Optimal Control Law Design Techniques.

7.2.1 State-Space Optimal Control Methods.

State space methods of optimal control are time domain techniques developed in the 1960's for multivariable applications. The motivation behind the development of

these techniques was the increasing demands on the control of complex, multivariable systems. The classical approach was to close each feedback loop sequentially, which is a laborious process littered with opportunities for making errors. By expressing the plant in state-space form, all of the dynamics are encapsulated within the matrices and so by using matrix methods, all of the feedback loops are closed in a single step. Several techniques were borne out of this era, the most noticeable being eigenstructure assignment, Linear Quadratic Regulator (LQR) and Linear Quadratic Gaussian with Loop Transfer Recovery (LQG/LTR).

The most common implementation of these techniques is when they are used as *regulator* loops, i.e. the system states are driven asymptotically to zero by the controller. Recall that the IBC strategy as defined in §6.7.1 is a *servodesign* or tracker loop. As touched upon in §6.9, the LQR method and its extensions can be recast into a tracker formulation by replacing the regulator cost function,

$$J = \frac{1}{2}\int_0^\infty \underline{x}^T A\underline{x} + \underline{u}^T B\underline{u}\ dt \tag{7.2.1}$$

with a cost function based on tracking error,

$$J = \frac{1}{2}\int_0^\infty (\underline{r} - C\underline{x})^T A(\underline{r} - C\underline{x}) + \underline{u}^T B\underline{u}\ \ dt \tag{7.2.2}$$

However, when this cost function is expanded using the Hamilton-Jacobi-Bellman equations and the method of dynamic programming, the cost becomes a function of the command and command derivative. Stevens & Lewis (*1992*) suggest a procedure for solving this problem based upon assumptions imposed on the structure of the command signal. This is a neat, but far from optimal solution. The second and most important problem with modern control law designs is that it is difficult to directly shape the frequency response of the closed-loop plant. In the early eighties, frequency shaped cost functionals appeared in the LQG scheme and were applied to the problem of helicopter

vibration (*Gupta, 1980; Gupta & DuVal, 1982*). However, by this time a potentially more powerful control technique was gaining prominence.

7.2.2 H_∞ Synthesis.

Originally conceived by George Zames (*1979*), H-infinity theory (H_∞) was developed in the early eighties to bridge the gap between optimal, multivariable, time domain techniques such as LQG and classical, frequency domain-based designs. The research was largely motivated by the poor robustness properties of multiple input-multiple output (MIMO) optimal time-domain designs in the presence of model uncertainty. Indeed, poor robustness to plant uncertainty has been the main reason for the continued support of classical design techniques by the industrial community. The H_∞ approach as it now stands provides a framework for designing an optimal controller in the frequency domain, which is not only robust to plant uncertainties and external disturbances, but does so in a formal, sequential and structured manner.

In the context of individual blade control, the most obvious benefits that H_∞ synthesis can afford is the capability of precise loop shaping of the closed-loop performance parameters (*Kwakernaak, 1993; Doyle et.al., 1989*). In addition, H_∞ synthesis is not constrained to provide regulator action (*Stefani, et.al., 1994*). As a further incentive, very little appears in the IBC literature pertaining to H_∞ synthesis, contrary to general control publications. The technique has been used to design fixed-wing and helicopter flight control laws (*Kaminer et.al., 1990; Ingle & Celi, 1994*), however, the closest example to IBC that could be found is using rotor state feedback (multicyclic) in the design of high bandwidth flight control laws, (*Brinson, et.al., 1995*: *Howitt, et.al., 1997*). The opportunity is thus presented for this work to make a significant contribution to understanding the benefits and difficulties of designing IBC control laws using H_∞ procedures.

There now follows a brief description of the most salient points required to perform an H_∞ design. Where prudent, particular emphasis is placed upon features of

the technique of particular relevance to blade flap control, namely those properties of the controller which lead to a precisely shaped closed loop response.

7.3 *Individual Blade Control via Mixed-Sensitivity H_∞ Synthesis.*

Prior to commencing on a description of the mechanics of mixed sensitivity H_∞ synthesis (*Doyle et.al., 1989*), (and to avoid confusion in later sections) there will now follow a short description of the sensitivity function and its variants, as well as the physical manifestation of the H_∞ norm. After this, the concepts and significance of weighting functions and plant augmentation will be detailed, before finally discussing the benefits of γ-iteration.

7.3.1 *Closed-Loop Performance Parameters.*

Classical frequency domain designs provide control by shaping the open loop characteristics of the plant. H_∞ designs on the other hand, calculate the control laws by explicitly shaping the parameters of the closed loop response. Consider the general description of a feedback system given by the block diagram of *figure 7.1*. The closed loop response is given by,

$$\underline{y} = \frac{1}{1+C(s)G(s)}\, G_d(s)\underline{d} \;+\; \frac{C(s)G(s)}{1+C(s)G(s)}\;\underline{r} \;-\; \frac{C(s)G(s)}{1+C(s)G(s)}\;\underline{n} \qquad (7.3.1)$$

using the closed-loop parameters,

i). the loop gain, $\boldsymbol{L}(s) = \boldsymbol{C}(s)\boldsymbol{G}(s)$,

ii). the sensitivity, $\boldsymbol{S}(s) = \frac{1}{1+\boldsymbol{L}(s)}$ and

iii). the complementary sensitivity, $\boldsymbol{T}(s) = \frac{\boldsymbol{L}(s)}{1+\boldsymbol{L}(s)}$.

It is obvious from (*i-iii*) above that for good disturbance rejection it is desirable to have $\boldsymbol{S}(s)\rightarrow 0$ and for good sensor noise attenuation to have $\boldsymbol{T}(s)\rightarrow 0$. However, for good tracking performance, $\boldsymbol{T}(s)\rightarrow 1$ is desirable. These are conflicting requirements which are further complicated by noting that $\boldsymbol{S}(s)+\boldsymbol{T}(s) = 1$ at all times over the entire frequency range. Closed loop control then becomes a trade-off between the sensitivity and the complementary sensitivity functions over frequency. For IBC active vibration control, it is desirable to have $\boldsymbol{S}(s)$ as small as possible in the neighbourhood of 1/rev. This demand will manifest as large control gain in the region, analogous to the requirements of classical compensator design. $\boldsymbol{T}(s)$ small at high frequencies will help limit the bandwidth and reduce the significance of blade structural resonance in the loop.

7.3.2 H_∞ norm.

The 'H' in the term H_∞ describes one member of the family of spaces introduced by the mathematician Hardy. It is the space of functions on the complex plane that are analytic and bounded in the right half plane. The norm is a scalar value that represents the 'size' of a mathematical expression such as a vector, matrix or transfer function. The infinity norm is defined as the *supremum* of the transfer function over all frequencies, ω.

$$\left\|\boldsymbol{T}(s)\right\|_\infty = \sup_\omega \left\{\left|\boldsymbol{T}(j\omega)\right|\right\} \tag{7.3.2}$$

From equation (7.3.2) it is obvious that the H_∞ norm is defined within the frequency domain. However, for a multivariable system, a conventional Bode plot is ill defined. To overcome this problem, Singular Value Decomposition (SVD) of the system model has been universally adopted within the H_∞ control community (*Kwakernaak, 1993; Grimble & Johnson, 1991*). The infinity norm is then the maximum singular value of the transfer function over all positive frequencies.

$$\left\|\boldsymbol{T}(s)\right\|_\infty = \sup_\omega \bar{\sigma}\left(\boldsymbol{T}(j\omega)\right) \tag{7.3.3}$$

A very coarse explanation of the effect minimising the H_∞ norm of the closed-loop transfer function has on a feedback system, is that it increases the damping (and correspondingly the phase margin) of the system for the most likely (largest σ) mode. Graphically, this corresponds to minimising the 'hump' seen in the singular value plot of the closed-loop transfer function in the vicinity of the crossover frequency.

7.3.3 Weighting functions and the Mixed Sensitivity Algorithm.

One of the most popular H_∞ control design algorithms is the *Mixed Sensitivity* approach of Verma and Jonckheer (*1984*), popularised by Doyle et.al. (*1989*), which has found favour in many engineering CAD packages, most notably the Robust Control Toolbox for MATLAB. In a Mixed Sensitivity design, the control engineer assigns frequency dependant weightings to each of the closed-loop performance parameters and during the course of the optimisation procedure, the H_∞ solution algorithm will attempt to ensure,

$$\begin{aligned} |\boldsymbol{W}_S(j\omega)\boldsymbol{S}(j\omega)| &\le 1 \qquad 0 \le \omega \le \infty \\ |\boldsymbol{W}_R(j\omega)\boldsymbol{R}(j\omega)| &\le 1 \qquad 0 \le \omega \le \infty \\ |\boldsymbol{W}_T(j\omega)\boldsymbol{T}(j\omega)| &\le 1 \qquad 0 \le \omega \le \infty \end{aligned} \tag{7.3.4}$$

or alternatively,

$$\left\| \begin{matrix} \boldsymbol{W}_S(j\omega)\boldsymbol{S}(j\omega) \\ \boldsymbol{W}_R(j\omega)\boldsymbol{R}(j\omega) \\ \boldsymbol{W}_T(j\omega)\boldsymbol{T}(j\omega) \end{matrix} \right\|_\infty \le 1 \tag{7.3.5}$$

That is, the Mixed Sensitivity algorithm minimises the H_∞ norm of the *weighted* sensitivity, control sensitivity and complementary sensitivity of the closed-loop system. The shape and magnitude of the weights have to be selected extremely carefully, as they are the primary mechanism for the designer to influence the performance and robustness of the controller. For example, as it is a requirement that the sensitivity be small in the frequency range over which $G_d(s)$ acts (nominally close to 1/rev for the gust alleviation

problem), $|\boldsymbol{W}_S(j\omega)|$ should be large in this region. The control sensitivity, $\boldsymbol{R}(s)=C(s)S(s)$ determines the available control energy at a given frequency. It is often demanded to have low-pass filter characteristics, reducing the gain at high frequencies and so improving stability and noise rejection. Typically, the complementary sensitivity weighting $\boldsymbol{W}_T(j\omega)$, is used to control the high frequency roll-off characteristics of the loop, maximising robustness to sensor noise and high-frequency unmodelled dynamics (aeroelastic blade resonances).

7.3.4 Plant Augmentation and the H_∞ Small Gain Problem.

Before the H_∞ optimisation procedure can proceed, the plant must be augmented by the weighting matrices in some fashion. The first step in the augmentation of the plant is to transform *figure 7.1* into the generic block diagram representation of control systems shown in *figure 7.2*. The exogenous inputs to the plant such as the disturbance, noise and reference commands are combined into vector w. The output z contains the signals which are to be regulated or controlled. For the current problem, the output z will comprise outputs of the weighted sensitivity functions. The signals measured for feedback into the controller are held in y and the plant control inputs in u. Assuming the control loop is in the form of *figure 7.1*, and the weighting functions have been defined, automatic procedures for constructing the augmented plant $\boldsymbol{P}(s)$ are packaged with the Robust Control Toolbox for MATLAB.

The mixed sensitivity problem is probably the most popular derivative of the standard H_∞ small gain problem. The standard H_∞ small gain problem can be stated that given the augmented plant transfer function matrix $\boldsymbol{P}(s)$, find a stabilising controller $\boldsymbol{C}(s)$ such that the closed loop transfer function $\boldsymbol{P}_{wz}$ between w and z is internally stable and its H_∞ norm is less than one, i.e.,

$$\left\|\boldsymbol{P}_{wz}\right\|_\infty \leq 1 \tag{7.3.6}$$

If the plant is augmented by appropriate weighting matrices, the infinity norm of the system transfer function can be given by,

$$\|P_{wz}\|_\infty \le 1 \quad \Leftrightarrow \quad \left\| \begin{bmatrix} W_S S(j\omega) \\ W_R R(j\omega) \\ W_T T(j\omega) \end{bmatrix} \right\|_\infty \le 1, \quad 0 \le \omega \le \infty \tag{7.3.7}$$

The algorithm of Doyle et.al., (*1989*) provides a state-space solution to the minimisation (equation 7.3.7) above.

7.3.5 γ– iteration.

It is not always possible, or desirable, to achieve the mathematically optimal solution to the H_∞ control problem. Instead, the standard H_∞ control problem is often solved.

$$\underset{C(s)\,stabilising}{Find} \quad \|P_{wz}\|_\infty \le \gamma \tag{7.3.8}$$

In the solution to the standard problem, the value of γ becomes intertwined with the Ricatti equations that result from the solution of the H_∞ problem. This introduces another tuning parameter directly into the solution procedure, i.e. to find the 'best' controller, start with a value of γ and reduce it until the problem fails to have a solution. The value of γ is lowered via a search algorithm, in a procedure called γ-iteration. All of the H_∞ controllers presented in this chapter are sub-optimal, i.e. they satisfy equation(7.3.8).

There has been no mention of model uncertainty in the discussion above, principally because for the hover case the flap transfer function is well known in the frequency region of interest (excluding structural modes). However, for the forward flight case the damping changes considerably with azimuth. Such changes are easily modelled by a multiplicative uncertainty (*Skogenstad & Postlethwaite, 1996*) and assimilated into the complementary sensitivity function. However, this is not central to

the current investigation, although it will provide an excellent research topic for a future study.

7.4 Individual Blade Control via Mixed-Sensitivity H_∞ Synthesis.

7.4.1 Design 1: Sensitivity-Only Weighting.

In the first attempted design, only the sensitivity function was assigned a dynamic weighting term. The control sensitivity weighting function was set at a constant value of 0.0001, primarily to ensure the rank conditions imposed upon the augmented plant matrix, $\boldsymbol{P}$ were met. This also places very limited penalties on the control energy within the H_∞ algorithm. The fundamental sensitivity weighting function was defined using a second-order transfer function thus,

$$\boldsymbol{W}_S(s) = \frac{\beta\left(\alpha s^2 + 2\zeta_1\omega_c\sqrt{\alpha}s + \omega_c^2\right)}{\beta s^2 + 2\zeta_2\omega_c\sqrt{\beta}s + \omega_c^2} \tag{7.4.1}$$

where,
- β is the DC gain of the weighting,
- α defines the high frequency gain,
- ω_c is the crossover frequency and
- ζ_1, ζ_2 are the damping ratios at the corner frequencies.

This weighting function is particularly popular as it imposes a roll-on rate of 30dB/decade on the sensitivity, which gives a good balance between phase margin and robustness to high-frequency uncertainty. The fundamental weighting is then augmented by a term included to further minimise the sensitivity in the neighbourhood of 1/rev, $\boldsymbol{W}_{S.2}$.

$$\boldsymbol{W}_{S.2}(s) = \frac{s^2 + 1.4\omega_n s + \omega_n^2}{s^2 + 0.6\omega_d s + \omega_d^2} \tag{7.4.2}$$

where, $\omega_n = 55$; $\omega_d = 35$rad/s. The SVD plot of the final sensitivity weighting function with the performance parameters defined as $\beta = 500$, $\alpha = 0.9$, $\omega_c = 80$ rad/s and $\zeta_1 = \zeta_2 = 0.7$, is given in *figure 7.3*. The H_∞ controller computed by the mixed-sensitivity algorithm is a 6th order transfer function,

$$H_\infty = \frac{52985472(s+50.05)(s^2+31.69s+773)(s^2+55.14s+2513)}{(s+2.49e4)(s+1.09e4)(s^2+5s+12.8)(s^2+21s+1255)} \qquad (7.4.3)$$

One curious point to note is that the controller is performing direct pole-zero cancellation, evident by the first, 2nd-order term in the numerator of (7.4.3), which is the denominator of the flap transfer function. The SVD plot of the open-loop compensated plant is given in *figure 7.4*, alongside the uncontrolled blade flap transfer function and the open-loop PID compensated plant. It is evident that the bandwidth has been reduced considerably from approximately 460 rad/s to 170 rad/s. The gain in the vicinity of 1/rev is very close to the PID gain, only 1½ dB's of loss. However, the bandwidth is still too high and the roll-off rate is woefully inadequate. For implementation in any practical system, the roll-off rate has to be increased or there will be very little gain margin in the presence of even a moderately damped structural resonance.

7.4.2 Design 2: Sensitivity and Complementary Sensitivity Weighting.

To force the roll-off rate to be at least -40dB/decade and to reduce the bandwidth still further, dynamic weighting of the complementary sensitivity function was added to the H_∞ algorithm. Several weighting functions were examined, but

$$W_T(s) = \frac{s^2}{\omega_T^2} \qquad (7.4.4)$$

yielded the best controller,

$$H_\infty = \frac{126856.8(s+26.13)(s^2+31.69s+773)(s^2+35.87s+1514)}{(s+7401)(s+189.2)(s^2+3.13s+5)(s^2+21s+1255)} \qquad (7.4.5)$$

when ω_T = 80 rad/s and ω_c = 50 rad/s. The open-loop SVD plot for *design 2* is shown in *figure 7.5*, again alongside the uncompensated and PID compensated plants. The bandwidth has now been reduced to 75 rad/s and the roll-off rate increased to -40dB/decade. This has come at the expense of a drop in gain at 1/rev of approximately 16dBs. This represents quite a significant drop in available disturbance rejection power. In examining the impact of this gain reduction, the non-linear SIMULINK model was used to test the disturbance-rejection capabilities of the H_∞ design. The performance of the PID controller (*figure 7.6*) has been shown to enable direct comparison with the H_∞ controller of *figure 7.7*. The closed-loop response is plotted next to the uncompensated, open-loop response of the flap angle to a sharp-edged gust. It is apparent that both controllers reject the disturbance well, particularly in regards to the steady-state offset. However, the H_∞ controlled model is more affected by the disturbance, evident by the drop in cyclic flap amplitude in the centre of the disturbance. This is actually caused by the phase lead characteristics of the controller, which can be seen to be leading the reference signal by approximately 30° inside the transient portion of the gust.

It is somewhat unfair to degrade the disturbance rejection performance of the H_∞ controller in comparison to the PID scheme, as the H_∞ scheme does not have the added benefit of rate feedback. Employing rate feedback would significantly ease the phase burdens on the controller and enable much higher gain in the vicinity of 1/rev. The results from numerical experiments conducted with the SIMULINK model suggest that there is considerable mileage in the application of H_∞ synthesis to the IBC problem, and should be expanded further to include multiple input-multiple output models. MIMO H_∞ control for IBC schemes would provide an excellent topic for further research.

7.5 DHHC Disturbance Estimation: - Neural Networks.

One of the main conclusions of Chapter VI was that a reliable, nonlinear prediction/estimation algorithm would be needed to provide the feedforward information necessary to drive the DHHC algorithm. Ideally, the algorithm should be

able to generalise, or *learn* the gust patterns from a minimal number of samples. One of the most popular nonlinear prediction and estimation algorithms is the highly parallel *Neural Network.*

The neural network (NN) is attractive for the disturbance predictor/estimator role principally because of the guarantee from the outset that no *theoretical* barriers exist to prohibit the design of a useful predictor. Behind this statement is the mathematical proof that neural networks can learn *any* input-output mapping to an arbitrary degree of accuracy, due to the Universal Approximation Theorem (*Haykin, 1994*). In addition, they have been used successfully in several aerospace control designs, (*Haas, et.al., 1995; Napolitano & Kincheloe, 1995; Sadhukhan & Feteih, 1996*), and consequently present a relatively mature technology for control applications.

7.5.1 What are Neural Networks?

Neural networks are mathematical abstractions designed to emulate the human decision making process by modelling the physical, biological processes in the brain. The human brain is essentially an electrical device with massively parallel processing capabilities. Billions of interconnected nodes, or *neurons*, perform low-level, logical processing that, when completely integrated with all other neighbouring neurons, enable memory, reasoning and motor functions to be controlled. The architecture of a neural network (NN) is generally copied from the synaptic interconnection network of the brain.

Two types of network architecture have proved popular for control and estimation tasks: the feedforward multilayer perceptron network and the recurrent Hopfield network (*Narendra & Parthasarthy, 1990; Nguyen & Widrow, 1990; Hunt et.al., 1992; Lightbody, Wu and Irwin, 1992*). In the multilayer perceptron network, *figure 7.8* the signal flows from the input nodes on the left, through (perhaps several) layers of 'hidden' neurons to emerge from the layer of 'output' neurons on the far right. The output of each neuron can only be connected to the inputs of the neurons in the next layer. The Hopfield network on the other hand has feedback interconnections between

nodes. After completing a literature review of the topic and consulting the excellent text by Haykin (*1994*), the multilayer feedforward neural network scheme was adopted, primarily because algorithms were in place (*Haykin, 1994*) for extending to time-varying weighting if this proved to be necessary.

7.5.2 Neuron Models.

The earliest models of a *neuron*, or *perceptron*, were developed in the 1960's, most notably being the *Adaline* (adaptive linear element) by Widrow and Hoff (*1960*). The learning and pattern classification properties of the perceptron were apparent even then, although a stable method for training an interconnected network of perceptrons was not available until 1986. The development of the *Backpropogation* algorithm by Rumelhart et.al. (*1986*) opened the floodgates on neural network research activity, as it offered a straightforward process for designing and training a complete network. Many advanced techniques are now available for designing network architectures (simulated annealing, evolutionary programming) and for pruning and tuning a network to the given application.

The model of a neuron is relatively simple, *figure 7.9*. The neuron takes as input the weighted output of each connected node in the previous layer. These weights are summed and the result is passed through an activation function. The activation function can be either a linear or, more commonly, non-linear function. For a network with a two-state output (such as a switch control in an electronic circuit) the activation function can simply be *sgn(v)*. For a scaled normalised output the two most common activation functions are the *sigmoid* and *hyperbolic tangent* functions defined by,

$$\varphi(v) = \frac{1}{1+\exp(-av)} \qquad \text{and} \qquad \varphi(v) = \frac{1-\exp(-v)}{1+\exp(-v)} \tag{7.5.1}$$

Following the recommendations of the tutorials in MATLAB, the hyperbolic tangent activation function was used in the hidden layers and a linear activation function in the output layer.

7.5.3 *Training the Network – The Backpropogation Algorithm.*

An interconnected series of neurons forms the basic architecture of a neural net and for most useful networks, training is performed by application of the backpropogation algorithm. The backpropogation algorithm is a multi-layer extension to the Widrow-Hoff delta rule (*1960*), which is essentially a gradient descent optimisation algorithm. The weights on each neuron are updated using the following rule,

$$w_{i,j}(n+1) = w_{i,j}(n) + \eta \Delta w_{i,j}(n) \tag{7.5.2}$$

where $w_{i,j}$ is the weight at the i^{th} neuron from the j^{th} neuron in the previous layer at the n^{th} iteration (a function of the total error in the network) and η is a learning rate parameter. Varying the value of η through (0,1] alters stability and rate of convergence. For supervised learning (common to most multilayer feedforward networks) the error is usually taken to be the difference between the actual and desired values of each neuron in the output layer. The backpropogation algorithm then feeds back, layer by layer, the network error, using the error to calculate $\Delta w_{i,j}$. Derivation of the backpropogation algorithm is involved and will not be replicated here, see (*Haykin, 1994*) for a complete proof. The update equations are,

$$\begin{aligned} \delta_j^{(l)}(n) &= e_j^{(L)}(n) o_j(n)[1 - o_j(n)] && \text{for neuron } j \text{ in output layer } L \\ \delta_j^{(l)}(n) &= y_j^{(l)}(n)[1 - y_j^{(l)}(n)] \sum_k \delta_k^{(l+1)}(n) w_{kj}^{(l+1)}(n) && \text{for neuron } j \text{ in hidden layer } l \end{aligned} \tag{7.5.3}$$

where,

$o_j(n)$ is the output of the j^{th} neuron in the output layer at the n^{th} iteration

$e_j^{(L)}(n)$ is the output error of the j^{th} neuron in the output layer at the n^{th} iteration,

$\delta_j^{(l)}(n)$ is the local gradient of the j^{th} neuron in the l^{th} layer at the n^{th}

iteration and,

$y_j^{(l)}(n)$ is the input signal of neuron j in the l^{th} layer at the n^{th} iteration.

The delta rule then becomes,

$$w_{ji}^{(l)}(n+1) = w_{ji}^{(l)}(n) + \eta\delta_j^{(l)}(n)y_i^{(l-1)}(n) \qquad (7.5.4)$$

This procedure is iterated until the global error is reduced to an acceptable value.

7.5.4 Improving Convergence by Adding a Momentum Term.

It is reported in Haykin (*1994*) that "a simple method of increasing the rate of learning and yet avoiding the danger of instability is to modify the delta rule of" (7.5.4) "by including a *momentum* term".

$$w_{ji}^{(l)}(n+1) = w_{ji}^{(l)}(n) + \alpha[w_{ji}^{(l)}(n) - w_{ji}^{(l)}(n-1)] + \eta\delta_j^{(l)}(n)y_i^{(l-1)}(n) \qquad (7.5.5)$$

α is usually a positive number called the momentum constant. Essentially the momentum term penalises large changes of the weights in the backpropogation algorithm. This is a minor modification to the weight update, yet it can have highly beneficial effects on the learning behaviour of the algorithm (*Haykin, 1994*). The momentum term should also help to reduce the probability of the learning process terminating in a shallow local minima.

7.6 Design and Training of a Neural Network for Gust Parameter Prediction.

7.6.1 Network Architecture.

To ensure some degree of forward compatibility (if the need arose), the chosen architecture was that of a multilayer feedforward neural network (*figure 7.8*). To benefit from the Universal Approximation Theory, the network must have a minimum of 1 hidden layer. It is good design practise to make the network as sparse and simple as possible. This helps to prevent overfitting of the training data and paves the way for good network generalisation. After several iterations, the chosen network architecture consisted of six input nodes, twelve neurons in the hidden layer, each using hyperbolic tangent activation functions and two neurons in the output layer, one dispensing the sine harmonic of the N/rev Fourier coefficient and the other the cosine harmonic. The network is fed with three input pairs of harmonic coefficients. The first pair are the Fourier coefficients of the higher harmonic control signal (null for the uncontrolled case). The other two pairs are the n^{th} and $(n\text{-}1)^{th}$ estimates of the disturbance coefficients, i.e. the last two entries of a finite memory tapped delay line filter storing the estimated disturbance signal. A schematic of the network architecture is shown in *figure 7.10.*

7.6.2 Network Performance.

The network was simulated and trained within the MATLAB environment using functions supplied with the Neural Network Toolbox. The learning rate parameter was assigned an initial value of 0.01 to ensure conservative updating of the weights, but was allowed to increment by a factor of 1.05 and decrease by a factor of 0.7 every epoch. One epoch corresponds to the presentation of the entire training data set to the network. The number of epochs allowed in the training cycle was limited to 2000. The *batch* mode of backpropogation learning was used throughout, where weight updating is performed *after* the presentation of all the training samples in the epoch. An attempt was made at training the network using *pattern* mode learning (weight updating after each training sample) but this method resulted in substantially poorer performance.

The training data itself was the response of the same Puma aircraft as used in previous experiments (Appendix III) to progressive immersion into a 2.5ms^{-1} sharp-edged up-gust at a relative airspeed of 10 knots, as predicted by HISAT.

Figures *7.11* and *7.12* show a comparison of the actual and predicted Fourier coefficients from the network. At first glance it would seem that the results were not too encouraging, however upon closer inspection some important trends begin to emerge. Looking first at the cosine harmonic time history (*figure 7.11*), the trends are predicted well, particularly in the central region where most of the vibration energy is located. This is most evident in the sharp change in both magnitude and direction between 7 & 9 turns and 10 & 11 turns. For most of the response, the neural network is conservative, i.e., the magnitude of the predicted disturbance is less than the actual disturbance. Such conservatism would tend to suggest that the DHHC algorithm would remain stable if driven by this network. Further weight can be assigned to this statement by noting that the correct sign is predicted throughout. This is one of the most important aspects, as at least then there is a chance that the (linear) DHHC algorithm will calculate controls in the right direction.

One interesting discovery is that the cosine and sine predictions have almost exactly the same shape, different only through a scaling factor. Recalling that linear activation functions were used in the output layer, this suggests that there were either too few neurons or too few hidden layers to allow the network to differentiate between the harmonics. A larger network may have better success, but will probably lose a degree of generality. In any event, there is an infinite number of possible architectures to test, so any redesign of the architecture should be encased inside an optimisation algorithm such as simulated annealing or genetic programming.

It should be emphasised at this point, that the problem at hand presents a very difficult system identification scenario, because the data is highly non-linear and sparsely sampled. In this respect, and considering the accuracy of the predictions and the suggested avenues for improvement, there could be considerable mileage in pursuing neural network algorithms, not only to drive the DHHC algorithm but also as a

replacement for the linear sensitivity matrix in a fully integrated nonlinear higher harmonic controller. Of course, this drastic step would require that the network learns the dynamics of the helicopter rotor in the frequency domain, and not necessarily just in the neighbourhood of N/rev. It would also be necessary to train the network with a large number of data sets or embody the controller with adaptive capabilities, either through direct plant inversion or a neural emulator (*Narendra & Parthasarthy, 1990; Hunt et.al., 1992*). Whichever avenue is chosen however, this topic would provide an excellent focus for a future study.

7.7 *Chapter Summary.*

A substantial body of novel work was presented in this chapter, and the results of the research conducted were largely successful. To recap, the two main areas of concern discovered in Chapter VI were the practicalities of implementing the DHHC algorithm in a stand-alone simulation and reducing the bandwidth of the IBC controller while still maintaining high gain at 1/rev. Concentrating first on the IBC problem, after a short review of modern, linear control theory, precise loop shaping via H_∞ synthesis was adopted as the preferred solution. Two controllers were designed and were shown to meet the bandwidth and gain requirements, a first in IBC control. Multiple input single output, in particular rate feedback, was suggested as a possible vehicle for controller improvement.

The prediction capabilities of a multilayer feedforward artificial neural network were used to create a nonlinear disturbance prediction/estimation model. The network predicted the trends in the disturbance data fairly well, although the absolute values were somewhat erroneous. However, the task as set was an incredibly demanding system identification problem and with this in mind, the network performed extremely well. Possible improvement could be gained by optimising the network architecture, a good topic of study for future work.

The research documented within this chapter has fulfilled the final research aim of this project, and in so doing, has unearthed several potentially fruitful avenues for future research.

CHAPTER VIII.

Conclusions and Recommendations for Future Work.

In this final chapter, the research presented in this dissertation will be assessed against the aims detailed in Chapter I. Novel areas of development, achievement, design and observation will be highlighted. As it is hoped that this work will prove to be a catalyst for future research endeavours, recommendations of the most promising avenues will be reported.

8.1 Review of the Research Aims.

Before embarking on the conclusions of this dissertation, it is worthwhile to restate the aims of the research described in Chapter I. The first aim was to develop a mathematical model suitable for turbulence-induced vibration analysis. Using this model, the response of a helicopter to flight through a realistic atmospheric environment was to be investigated, to determine whether the curious vibration signature of the sharp-edged gust was present. The model was then to be upgraded with an inverse simulation algorithm to enable the simulation of exacting operational conditions, also the performance of higher harmonic and individual blade control algorithms to sharp-edged gust disturbance was to be examined. Finally, if the vibration controllers proved to be inadequate, novel improvements and/or enhancements were to be suggested. In the subsequent sections of this chapter, it will be shown that the research aims were met and will highlight the importance of the model development and research observations to the wider fields of rotorcraft flight mechanics and control.

8.2 *Development of HISAT.*

Several stages of development were involved in the modification of RASCAL to form HISAT, expanding upon the previous level of understanding of the physics and processes involved. Each of these stages will now be discussed, with the research conclusions and important achievements highlighted throughout the text.

The first achievement to note was the successful integration of a blade-sampling based gust module within the RASCAL framework. The vibration induced by progressive immersion of the main rotor into a sharp-edged gust exhibited the same frequency distribution in the neighbourhood of N/rev as the experiments of Houston & Hamilton (*1993*) suggested. In addition, experiments using a standard 1-COS discrete gust indicate a strong coupling between gust gradient and vibratory response as would intuitively be expected.

The explanations for the frequency split offered by Houston & Hamilton were largely heuristic, based on the lead authors considerable expertise in the field. The novel, rigorous mathematically-formulated description of the physical processes generating this phenomenon, presented in this thesis, add considerable weight to the *potential* for existence of this event in actual flight conditions. The standard practice for frequency analysis of flight test data (averaging process) and the low probability of encountering sufficiently severe sharp-edged gust to correlate upon without numerous flight trials helps to explain the lack of corroborating published work. Incidentally, the predictions of the frequency split correlated well with results obtained via numerical experiments performed with RASCAL. This gave further weight to the probable existence of a previously unmeasured response.

Conceding that the sharp-edged gust is a highly idealised mathematical abstraction of atmospheric turbulence, the next step was to assimilate typical operational flowfields into the simulation. The chosen method – CFD modelling of the flowfield surrounding a typical obstruction – is a completely novel approach which was shown to be extremely successful. This original method enables exact repeatability of experiments and coherence between the force changes of each aerodynamic surface in a consistent and correlated manner. The framework now exists within HISAT to

accommodate any size of 2D turbulence field and predict the dynamic response of the aircraft at any point within that field.

Of most relevance to the current theme of interest however, was the observation of the frequency split about N/rev in the vibration signature for rectilinear flight over a cliff-top, one of the CFD-generated turbulence fields. This was a significant result as it demonstrated that under certain operational conditions, main rotor vibration could be transmitted to the fuselage at a frequency other than N/rev. Another interesting point was that this phenomena occurred during flight at 30 knots, giving further proof to the theory proposed in Chapter IV, that it is a combination of relative velocity and gust gradient that causes a split in the vibration frequency response. This finding could have severe implications for the design requirements of passive vibration isolators and AV mounts, in addition to raising questions about the robustness of active vibration control laws, a concern which proved to be justified under later investigation.

Extension of the model to incorporate an inverse simulation algorithm, GENISA, was the next task. The GENISA algorithm had been used with great success on simpler rotorcraft models, but the fidelity of rotor dynamics modelled in RASCAL (principally variable rotorspeed and lead/lag dynamics) presented a much greater challenge. Indeed, the algorithm initially struggled to cope, predicting large oscillations in the off-axis responses, but some massaging of the principal parameters (tolerance, perturbation size and discretisation interval) in the numerical differentiation scheme helped to stabilise the simulation. Fundamentally, it is expected that numerical errors are introduced into the algorithm because rotor periodicity is not matched. Matching of periodicity is possible in trim but extremely difficult to ensure during an aggressive manoeuvre where rotorspeed and lead/lag modes are persistently excited. Ideally, the GENISA algorithm should be overhauled and the fixed discretisation interval replaced with a variable one attached to the main rotor marker blade azimuth angle, particularly if the benefits of tracking accelerations are to be enjoyed. (*It is understood that research is being conducted at the University of Glasgow into such a modification at this time*). Instead, the algorithm was modified by adjusting the change in control deflections calculated from GENISA by optimising the length of the Newton step. This proved to be an extremely valuable modification, significantly reducing the numerical

instabilities of the algorithm to levels comparable with traditional inverse simulations. In the final incarnation of HISAT, the numerical instabilities are reduced below the level of the constraint oscillations (verified by analysis).

HISAT now represents the current state-of-the-art for rotorcraft inverse simulation in terms of model fidelity, applicability, versatility and robustness. The potential applications for any tool as powerful and diverse as HISAT are numerous, and include covert urban warfare and stand-off engagement tactical analysis, assessing approach patterns for air/sea and mountain rescue teams, and computing optimal approach vectors for offshore oil-platform heli-deck landings. It is expected that HISAT will also be used as a test bed for high fidelity, advanced control laws and will give insight into the merits and deficiencies of the algorithms in a manner never before possible.

8.3 Active Vibration Control.

For the remainder of the project, HISAT was used for the specific application of assessing and designing gust-induced vibration control laws, specifically the higher harmonic and individual blade control schemes.

The optimal HHC algorithm chosen as the baseline design achieved approximately 99% reduction of N/rev vibration amplitude in trim. However, the degradation in performance for flight through a sharp-edged gust was significantly more acute than expected. In fact, the gust completely destabilises the controller for relative velocities above 15 knots! It was obvious that modifications to the algorithm were required. Borrowing ideas from classical control theory, a parallel arrangement of multi-harmonic inputs was tried, to increase the control gain in the neighbourhood of N/rev. This was completely unsuccessful, making very little change to the controller performance. Attempts to improve the controller by including a Kalman filter for updating the harmonic control sensitivity matrix yielded no significant control enhancement either, and in fact lead to numerical instability. At this point, all of the

current HHC technologies and algorithms had been tested and had failed. This alone is an important result.

Explicit inclusion of the disturbance vector (in Fourier space) into a new variant of the HHC control law significantly improved controller performance. However, severe implementation issues were recognised and addressed by designing a nonlinear predictor/estimator using an artificial neural network. The output of the neural network was not ideal, but recommendations were made for possible improvement. This approach is entirely innovative and the initial exploratory results are encouraging.

A necessary pre-requisite in the design of the IBC controller is a representative reduced order model of the blade dynamics. To this end, a fully coupled flap-lag degree of freedom simulation was derived from first principles and written using SIMULINK. As the blade states $\{\beta,\zeta\}$ are periodic around the rotor azimuth, a tracking loop was the only viable control scheme available. Using the flap angle as the controlled variable, a PID controller was designed to track the flap deflection in the hover. Successful implementation within HISAT was only achieved when the fuselage dynamics were de-coupled from the rotor dynamics, full model flight proving to be completely unstable. However, successful attenuation of the gust-induced vibration was observed.

Recognising that the controller bandwidth was almost certainly too high, H_∞ synthesis was applied to the flap control problem. As a result, two H∞ controllers were successfully tested within the SIMULINK model and demonstrated performance comparable with the PID controller. As with the DHHC algorithm, this research was completely novel in both concept and application.

It is unfortunate that the full manoeuvring flight through realistic turbulence potential of HISAT could not be exploited in testing the performance of the controllers designed. However, the results obtained for the worst case scenario provides a solid bedrock from which to launch future investigations.

8.4 *Recommendations for Future Work.*

The areas of particular significance or interest unearthed by this project which could benefit from further investigation are as follows.

1. Either re-design the GENISA algorithm with a variable discretisation interval or construct a smoothing filter through which the control angles are passed and converted into 'analogue' pilot-like commands. This would take a significant step towards improving integration inverse simulation algorithms in general and would provide a hook into neuro-physiological pilot modelling.

2. Enhance the HISAT rotor model still further to incorporate a free wake model. This should settle the debate, once and for all, of whether the frequency split is an observable characteristic of helicopter flight or is swamped by the underlying N/rev vibration.

3. The successful application of H_∞ synthesis to an individual blade control strategy certainly merits further investigation. Multiple signal feedback, in particular rate feedback, could significantly improve performance. In addition, IBC control forward flight could be possible by treating the changes in blade damping as a parametric uncertainty and incorporating this directly into the weighting functions.

4. The architecture of the neural estimator of Chapter VII could be optimised to provide better prediction and generalisation. However, the network's capacity to handle nonlinear prediction in the Fourier domain could be exploited to design adaptive nonlinear harmonic controllers.

The problems, solutions, algorithms, techniques and discoveries reported in this thesis have perhaps raised as many new questions as they have answered. However, it is hoped that in so doing, this work may in some small way help stimulate rotorcraft flight mechanics and control research in these areas for many years to come.

APPENDIX I

Derivation of the Manoeuvre Profiles Available in HISAT

There are currently four manoeuvres available in HISAT, three of which are complicated enough to merit description by polynomial functions. The fourth manoeuvre is a simple longitudinal trim, in which the only non-zero inertial position, $x_{E,dem}$, is the time integral of $\dot{x}_{E,trim}$. The other manoeuvres are the side-step, inverse hurdle hop and flare to hover, illustrated in *figures 5.3 - 5.5.*

i). The Side-Step.

The side step is used to move laterally between two areas of concealment while maintaining constant heading (i.e., weapons trained on target). There is an initial acceleration from hover to a maximum lateral inertial velocity, $\dot{y}_{E,max}$, followed by a deceleration back to hover. The boundary conditions of the velocity profile are therefore,

$$\begin{aligned} t = 0 : &\qquad \dot{y}_{E,dem}(t) = \ddot{y}_{E,dem}(t) = 0 \\ t = \tfrac{1}{2} t_f : &\qquad \dot{y}_{E,dem}(t) = \dot{y}_{E,max} \\ t = t_f : &\qquad \dot{y}_{E,dem}(t) = \ddot{y}_{E,dem}(t) = 0 \end{aligned} \tag{A1.1}$$

With 5 boundary conditions, a fourth order polynomial should be sufficient to describe the manoeuvre, (*Thompson & Bradley, 1988*).

$$\dot{y}_{E,dem}(t) = a_0 + a_1 t + a_2 t^2 + a_3 t^3 + a_4 t^4 \tag{A1.2}$$

From the velocity and acceleration initial conditions,

$$\begin{aligned} \dot{y}_{E,dem}(t)\big|_{t=0} &= 0 = a_0 \\ \ddot{y}_{E,dem}(t)\big|_{t=0} &= 0 = a_1 \end{aligned} \tag{A1.3}$$

The remaining coefficients are the solutions to the three simultaneous equations.

$$\begin{aligned} a_2 t_f^2 + a_3 t_f^3 + a_4 t_f^4 &= 0 \\ \frac{a_2}{4} t_f^2 + \frac{a_3}{8} t_f^3 + \frac{a_4}{16} t_f^4 &= \dot{y}_{E,max} \\ 2a_2 t_f + 3a_3 t_f^2 + 4a_4 t_f^3 &= 0 \end{aligned} \qquad \text{(A1.4)}$$

giving,

$$\dot{y}_{E,dem}(t) = \dot{y}_{E,max}\left(16\left(\frac{t}{t_f}\right)^2 - 32\left(\frac{t}{t_f}\right)^3 + 16\left(\frac{t}{t_f}\right)^4\right) \qquad \text{(A1.5)}$$

The time to complete the manoeuvre can be specified in terms of the total lateral translation (s) and the maximum lateral velocity,

$$t_f = \frac{15s}{8\dot{y}_{E,max}} \qquad \text{(A1.6)}$$

ii). The Inverse Hurdle-Hop.

The inverse hurdle-hop is the mirror of a conventional hurdle hop defined in ADS33C/D, (*Anon, 1994*). This is a longitudinal manoeuvre tailored for use in conjunction with the flow across a valley turbulence scenario. The helicopter begins and ends the manoeuvre in trim and it is assumed that the manoeuvre is performed at a constant flight speed. The manoeuvre is defined by motion in the vertical plane and by the boundary conditions,

$$\begin{aligned} t = 0 : &\quad z_{E,dem}(t) = \dot{z}_{E,dem}(t) = \ddot{z}_{E,dem}(t) = 0 \\ t = \tfrac{1}{2} t_f : &\quad z_{E,dem}(t) = h, \quad \dot{z}_{E,dem}(t) = 0 \\ t = t_f : &\quad z_{E,dem}(t) = \dot{z}_{E,dem}(t) = \ddot{z}_{E,dem}(t) = 0 \end{aligned} \qquad \text{(A1.7)}$$

where h is the maximum loss of altitude attained during the manoeuvre. With 8 boundary conditions, a 7th order polynomial will be sufficient to define the manoeuvre.

$$z_{E,dem}(t) = a_0 + a_1 t + a_2 t^2 + a_3 t^3 + a_4 t^4 + a_5 t^5 + a_6 t^6 + a_7 t^7 \qquad \text{(A1.8)}$$

The coefficients are found in an analogous fashion to the side-step manoeuvre.

$$z_{E,dem}(t) = 64\,h\left(\left(\frac{t}{t_f}\right)^3 - 3\left(\frac{t}{t_f}\right)^4 + 2\left(\frac{t}{t_f}\right)^5 - \left(\frac{t}{t_f}\right)^6\right) \qquad \text{(A1.9)}$$

As the manoeuvre is flown at a constant flight speed, the longitudinal inertial velocity is then given by,

$$\dot{x}_{E,dem}(t) = \sqrt{V_f^2(t) - \dot{z}_{E,dem}^2(t)} \qquad \text{(A1.10)}$$

where,

$$\dot{z}_{E,dem}(t) = 64\,h\left(\frac{3t^2}{t_f^3} - \frac{12t^3}{t_f^4} + \frac{15t^4}{t_f^5} - \frac{6t^5}{t_f^6}\right) \qquad \text{(A1.11)}$$

iii). The Flare-to-Hover Manoeuvre.

The final manoeuvre available to HISAT is the flare to hover manoeuvre along a fixed glide slope. This manoeuvre definition was created by the author primarily with an approach and landing on an offshore oil platform in mind. The manoeuvre, defined with respect to a desired flight path angle, is split into three sections:

i). transition onto the desired glide slope,

ii). deceleration along a constant glide slope and

iii). final transition to hover.

The aircraft is assumed to begin the manoeuvre from trim with an initial flight path angle of 0°. The boundary conditions governing the change in flight path angle are,

$$\begin{aligned} t = 0 : &\qquad \gamma_{dem}(t) = \dot{\gamma}_{dem}(t) = 0 \\ t = t_1 : &\qquad \gamma_{dem}(t) = \gamma_{max}, \quad \dot{\gamma}_{dem}(t) = 0 \end{aligned} \tag{A1.12}$$

which gives the polynomial,

$$\gamma_{dem}(t) = \gamma_{max}\left(3\left(\frac{t}{t_1}\right)^2 - 2\left(\frac{t}{t_1}\right)^3\right) \tag{A1.13}$$

This initial phase lasts for 1 second (t_1), during which time $\dot{x}_{E,dem}(t)$ is kept at the trim value and,

$$\dot{z}_{E,dem}(t) = \dot{x}_{E,dem}(t)\, tan(\gamma_{dem}(t)) \tag{A1.14}$$

In the second stage, $\gamma_{dem}(t)$ is kept constant while $\dot{x}_{E,dem}(t)$ follows the deceleration profile,

$$\dot{x}_{E,dem}(t) = \dot{x}_{E,trim}\left(1 - 3\left(\frac{t-t_1}{t_f - t_1}\right)^2 + 2\left(\frac{t-t_1}{t_f - t_1}\right)^3\right) \tag{A1.15}$$

Again, $\dot{z}_{E,dem}(t)$ is given by (A2.14). The third stage is triggered when $\dot{x}_{E,dem}(t) = 2.5 ms^{-1}$, corresponding to $t = t_2$ in *figure 5.21*. In the final transition to hover, the flight path angle changes back to 0°,

$$\gamma_{dem}(t) = \gamma_{max}\left(1 - 3\left(\frac{t-t_2}{t_f - t_2}\right)^2 + 2\left(\frac{t-t_2}{t_f - t_2}\right)^3\right) \tag{A1.16}$$

and $\dot{x}_{E,dem}(t) = \dot{z}_{E,dem}(t) = 0 ms^{-1}$ at $t = t_f$.

APPENDIX II

Constraint Oscillation Predictor Model

This procedure is initiated by assuming a standard linear state space description of the helicopter rigid body dynamics is available,

$$\dot{\underline{x}} = A\underline{x} + B\underline{u} \tag{A2.1}$$

The state vector may then be partitioned into constraint influenced and unconstrained states (as heading forms one of the constraints it is removed from the state vector). Recall from equation (5.6.2),

$$\underline{x}_1 = (u\ v\ w\ r)^T \qquad \underline{x}_2 = (p\ q\ \theta\ \phi)^T \tag{A2.2}$$

The system and control matrices can then be partitioned,

$$\begin{bmatrix} \dot{\underline{x}}_1 \\ \dot{\underline{x}}_2 \end{bmatrix} = \begin{bmatrix} A_{11} & A_{12} \\ A_{21} & A_{22} \end{bmatrix} \begin{bmatrix} \underline{x}_1 \\ \underline{x}_2 \end{bmatrix} + \begin{bmatrix} B_1 \\ B_2 \end{bmatrix} [\underline{u}] \tag{A2.3}$$

The unconstrained states can then be expressed in terms of the constraint influenced states.

$$\dot{\underline{x}}_2 = \left[A_{22} - \left(B_2 B_1^{-1}\right)A_{12}\right]\underline{x}_2 + \left[A_{21} - \left(B_2 B_1^{-1}\right)A_{11}\right]\underline{x}_1 + \left(B_2 B_1^{-1}\right)\dot{\underline{x}}_1 \tag{A2.4}$$

The constraint influenced states can be given by (*Thompson & Bradley, 1990*).

$$\underline{\boldsymbol{x}}_1 = T_1 \underline{\dot{\boldsymbol{f}}}_c + T_2 \underline{\boldsymbol{f}}_c + T_3 \underline{\boldsymbol{x}}_2 \tag{A2.5}$$

where,

$$T_1 = \begin{bmatrix} l_{1_0} & l_{2_0} & l_{3_0} & 0 \\ m_{1_0} & m_{2_0} & m_{3_0} & 0 \\ n_{1_0} & n_{2_0} & n_{3_0} & 0 \\ 0 & 0 & 0 & \cos\theta_e \sec\phi_e \end{bmatrix} \qquad T_2 = \begin{bmatrix} 0 & 0 & 0 & l_3 \\ 0 & 0 & 0 & m_3 \\ 0 & 0 & 0 & n_3 \\ 0 & 0 & 0 & 0 \end{bmatrix}$$

$$T_3 = \begin{bmatrix} 0 & 0 & l_1 & l_2 \\ 0 & 0 & m_1 & m_2 \\ 0 & 0 & n_1 & n_2 \\ 0 & -\tan\phi_e & 0 & 0 \end{bmatrix} \tag{A2.6}$$

The derivative of the constraint states is given by,

$$\dot{\underline{\boldsymbol{x}}}_1 = T_1 \ddot{\underline{\boldsymbol{f}}}_c + T_4 \dot{\underline{\boldsymbol{x}}}_2 + T_5 \underline{\boldsymbol{x}}_2 + T_6 \underline{\boldsymbol{x}}_1 \tag{A2.7}$$

where,

$$T_4 = \begin{bmatrix} 0 & 0 & 0 & 0 \\ 0 & 0 & 0 & 0 \\ 0 & 0 & 0 & 0 \\ 0 & -\tan\phi_e & 0 & 0 \end{bmatrix} \qquad T_5 = \begin{bmatrix} 0 & -w_e & 0 & 0 \\ w_e & 0 & 0 & 0 \\ -v_e & u_e & 0 & 0 \\ 0 & 0 & 0 & 0 \end{bmatrix}$$

$$T_6 = \begin{bmatrix} 0 & 0 & 0 & v_e \\ 0 & 0 & 0 & -u_e \\ 0 & 0 & 0 & 0 \\ 0 & 0 & 0 & 0 \end{bmatrix} \tag{A2.8}$$

Combining equations 22 and 29 gives,

$$\dot{\underline{\boldsymbol{x}}}_1 = T_1 \ddot{\underline{\boldsymbol{f}}}_c + T_4 \dot{\underline{\boldsymbol{x}}}_2 + \left[T_5 + T_6 T_3\right] \underline{\boldsymbol{x}}_2 + T_6 T_1 \dot{\underline{\boldsymbol{f}}}_c + T_6 T_2 \underline{\boldsymbol{f}}_c \tag{A2.9}$$

This then results in,

$$\dot{\underline{\boldsymbol{x}}}_2 = A_c \underline{\boldsymbol{x}}_2 + B_c \underline{\boldsymbol{u}}_c \tag{A2.10}$$

where,

$$A_c = \left[I - B_2 B_1^{-1} T_4\right]^{-1} \left\{A_{22} - B_2 B_1^{-1}\left(A_{12} - T_5\right) + \left[A_{21} - B_2 B_1^{-1}\left(A_{11} - T_6\right)\right] T_3\right\}$$

$$B_c = \begin{bmatrix} \left[I - B_2 B_1^{-1} T_4\right]^{-1} B_2 B_1^{-1} T_1 \\ \left[I - B_2 B_1^{-1} T_4\right]^{-1} \left(A_{21} - B_2 B_1^{-1}\left(A_{11} - T_6\right)\right) T_1 \\ \left[I - B_2 B_1^{-1} T_4\right]^{-1} \left(A_{21} - B_2 B_1^{-1}\left(A_{11} - T_6\right)\right) T_2 \end{bmatrix}$$

$$\underline{u}_c = \begin{bmatrix} \underline{\ddot{f}}_c \\ \underline{\dot{f}}_c \\ \underline{f}_c \end{bmatrix} \qquad \underline{f}_c = \begin{bmatrix} x \\ y \\ z \\ \psi \end{bmatrix} \qquad \underline{x}_2 = \begin{bmatrix} p \\ q \\ \theta \\ \phi \end{bmatrix} \tag{A2.11}$$

The elements of the transitional matrices T_i result from a linearisation of the Euler transformation,

$$\begin{bmatrix} u \\ v \\ w \end{bmatrix} = \begin{bmatrix} l_{1_0} & l_{2_0} & l_{3_0} \\ m_{1_0} & m_{2_0} & m_{3_0} \\ n_{1_0} & n_{2_0} & n_{3_0} \end{bmatrix} \begin{bmatrix} \dot{x} \\ \dot{y} \\ \dot{z} \end{bmatrix} + \begin{bmatrix} l_1^{\cdot} & l_2^{\cdot} & l_3^{\cdot} \\ m_1^{\cdot} & m_2^{\cdot} & m_3^{\cdot} \\ n_1^{\cdot} & n_2^{\cdot} & n_3^{\cdot} \end{bmatrix} \begin{bmatrix} \theta \\ \phi \\ \psi \end{bmatrix} \tag{A2.12}$$

where,

$$\begin{aligned} l_{1_0} &= \cos\theta_e \cos\psi_e \\ l_{2_0} &= \cos\theta_e \sin\psi_e \\ l_{3_0} &= -\sin\theta_e \\ m_{1_0} &= \sin\phi_e \sin\theta_e \cos\psi_e - \cos\phi_e \sin\psi_e \\ m_{2_0} &= \sin\phi_e \sin\theta_e \sin\psi_e + \cos\phi_e \cos\psi_e \\ m_{3_0} &= \sin\phi_e \cos\theta_e \\ n_{1_0} &= \cos\phi_e \sin\theta_e \cos\psi_e + \sin\phi_e \sin\psi_e \\ n_{2_0} &= \cos\phi_e \sin\theta_e \sin\psi_e - \sin\phi_e \cos\psi_e \\ n_{3_0} &= \cos\phi_e \cos\theta_e \end{aligned}$$

and,

$$\begin{aligned} l_1^{\cdot} &= l_{3_0}\left(\dot{x}_e \cos\psi_e + \dot{y}_e \sin\psi_e\right) - \dot{z}_e \cos\theta_e \\ l_2^{\cdot} &= 0 \\ l_3^{\cdot} &= -\dot{x}_e l_{2_0} + \dot{y}_e l_{1_0} \end{aligned}$$

$$
\begin{aligned}
m_1' &= m_{3_0}\left(\dot{x}_e \cos\psi_e + \dot{y}_e \sin\psi_e\right) - \dot{z}_e l_{3_0} \sin\phi_e \\
m_2' &= \dot{x}_e n_{1_0} + \dot{y}_e n_{2_0} + \dot{z}_e n_{3_0} \\
m_3' &= -\dot{x}_e m_{2_0} + \dot{y}_e m_{1_0} \\
n_1' &= n_{3_0}\left(\dot{x}_e \cos\psi_e + \dot{y}_e \sin\psi_e\right) + \dot{z}_e cos\phi_e \\
n_2' &= -\left(\dot{x}_e m_{1_0} + \dot{y}_e m_{2_0} + \dot{z}_e m_{3_0}\right) \\
n_3' &= -\dot{x}_e n_{2_0} + \dot{y}_e n_{1_0}
\end{aligned}
$$

The subscript '*e*' denotes states at the reference trim condition.

APPENDIX III

Puma Data File.

Puma airframe mass/inertia information

Aircraft mass,	m	5805	kg
Moments of Inertia,	I_{xx}	9638	kgm^2
	I_{yy}	33240	kgm^2
	I_{zz}	25889	kgm^2
	I_{xz}	-2226	kgm^2
Centre of gravity location,	x_{cg}	-0.2	m
	y_{cg}	0	m
	z_{cg}	-0.675	m

Rotor data : main rotor

Number of blades,	N	4	
Elements per blade,		8	
Blade radius	R	7.489	m
Hinge offset	e	3.87	%
Lag Damper		14.15	Nm/rad/s
Nominal rotorspeed	W	27 rad/s	

Rotor data : tail rotor

Number of blades,	N	5	
Elements per blade,		9	
Blade radius	R	1.518	m
Hinge offset	e	7.2	%
Lag Damper		50	Nm/rad/s
Nominal rotorspeed	W	137	rad/s

APPENDIX IV

RASCAL Trim Output at Hover.

Aircraft type selected was : Puma

Airspeed is 0.0000 knots, rate of descent is 0.0000 feet per minute

Heading is 0.0000 degs , turn rate is 0.0000 deg/s

QNH is 1013.2500 mb , surface temp. is 15.0000 deg

Altitude is 1000.0000 feet , ground height is 0.0000 feet

Trim calculated, as follows: function value = 0.000000 IFAIL = 0

Trim state for this flight condition as follows -

****

Rotor no. 1 multiblade pitch angles are ;
theta0 ; 13.50556738 degrees
theta1s ; -0.30132912 degrees
theta1c ; -0.17852183 degrees

Rotor no. 1 inflow components are ;
vi0 ; 11.59515801 m/s
v1s ; 0.01100927 m/s
v1c ; -0.03103503 m/s

Rotor no. 1 multiblade flap angles are ;
beta0 ; 4.46650813 degrees
beta1s ; 0.03887882 degrees
beta1c ; 0.53789925 degrees

Rotor no. 1 multiblade lag angles are ;
zeta0 ; -10.63765863 degrees
zeta1s ; -0.03987515 degrees
zeta1c ; 0.09223039 degrees

Rotor no. 1 rotorspeed is ; 27.43876395 rad/s
Rotor no. 1 power is ; 1322.70269233 kW

****

Rotor no. 2 multiblade pitch angles are ;
theta0 ; 12.63411302 degrees
theta1s ; 0.00000000 degrees
theta1c ; 0.00000000 degrees

Rotor no. 2 inflow components are ;
vi0 ; 17.24195298 m/s
v1s ; -0.00006176 m/s
v1c ; 0.00005786 m/s

Rotor no. 2 multiblade flap angles are ;
beta0 ; 5.96241763 degrees
beta1s ; -0.00006462 degrees
beta1c ; -0.00010355 degrees

Rotor no. 2 multiblade lag angles are ;
zeta0 ; 0.00000000 degrees
zeta1s ; 0.00000000 degrees
zeta1c ; 0.00000000 degrees

Rotor no. 2 rotorspeed is ; 132.62069253 rad/s
Rotor no. 2 power is ; 50.72094776 kW

****

Aircraft attitude angles are ;
roll angle = 6.54175347 degrees
pitch angle = 5.78028647 degrees
yaw angle = 0.00705928 degrees

****

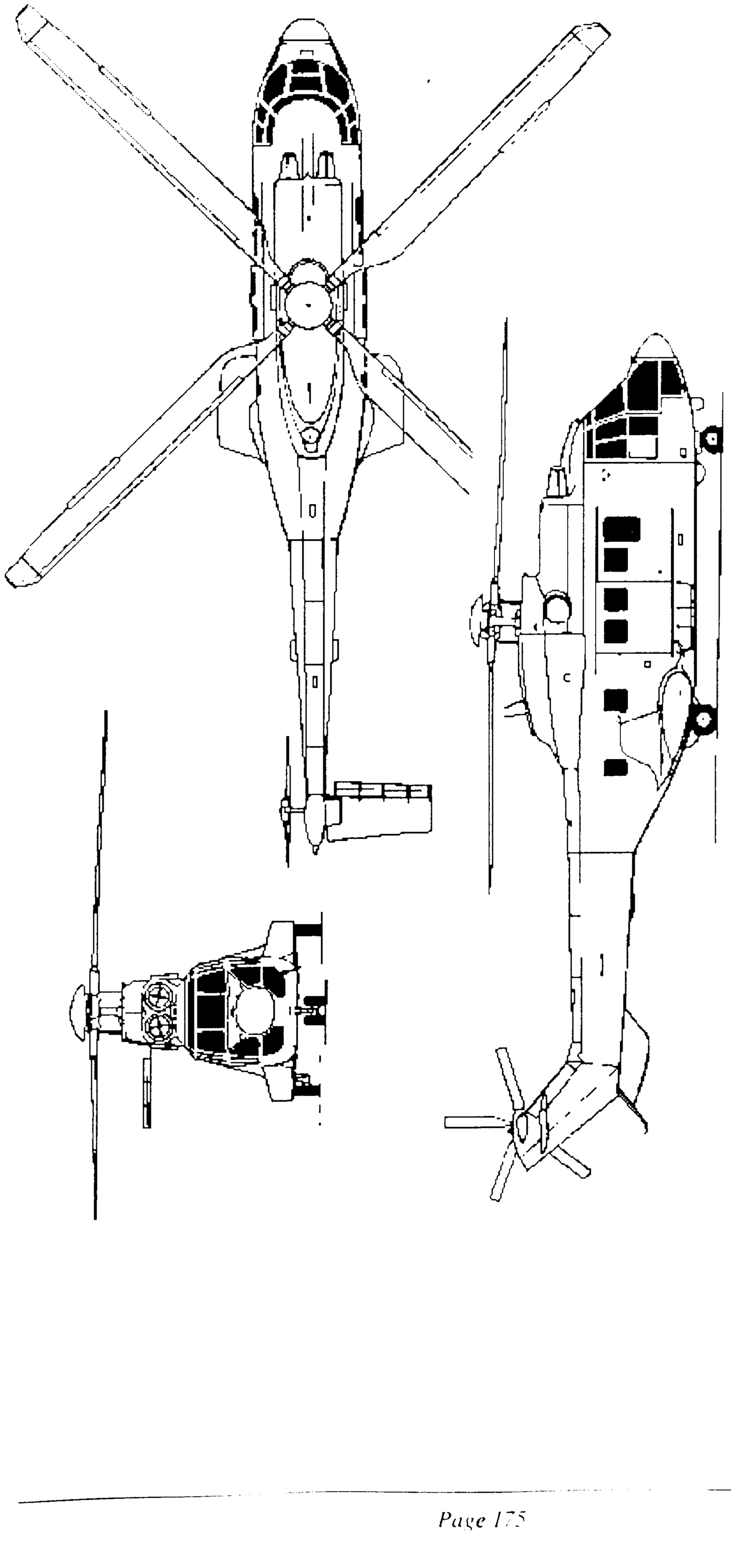

Figure A.1 : Schematic diagram of the Aerospatiale AS 332L Super Puma modelled in RASCAL/HISAT.

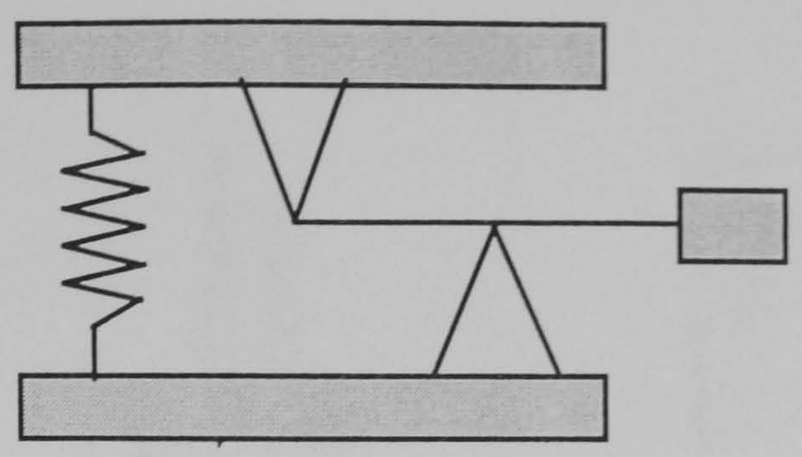

Figure 1.1 : **Schematic of the Dynamic Anti-resonant Vibration Isolator (DAVI).**

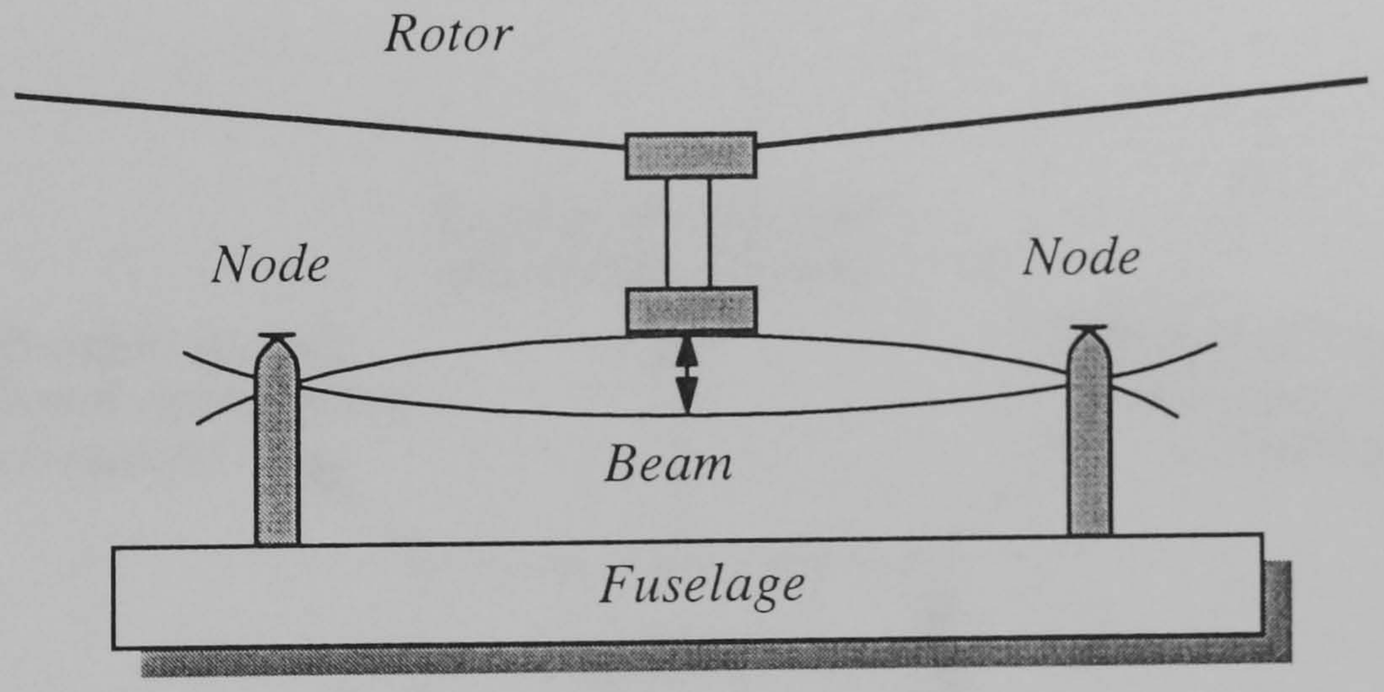

Figure 1.2 : **Anti-resonant node point locations for a fixed beam vibration absorber.**

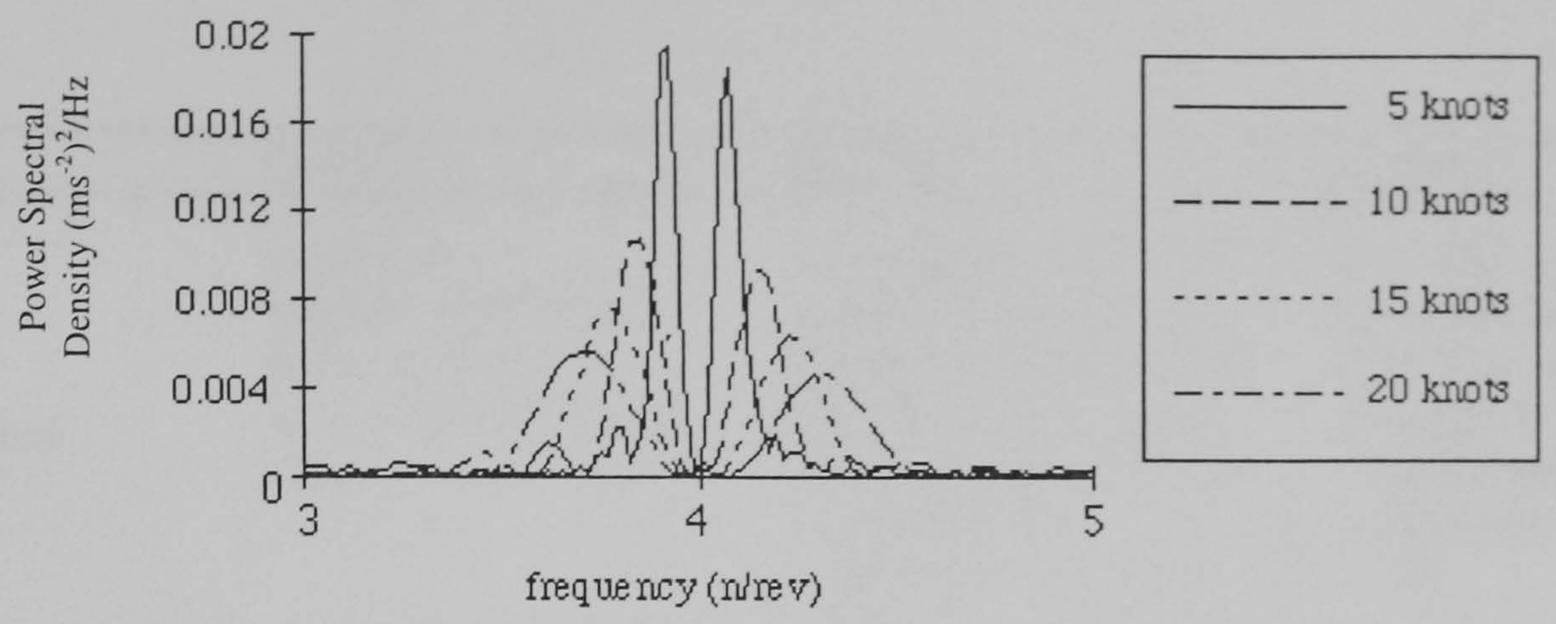

Figure 1.3 : **Vibration spectra showing the effects of progressive immersion into a sharp-edged gust.**

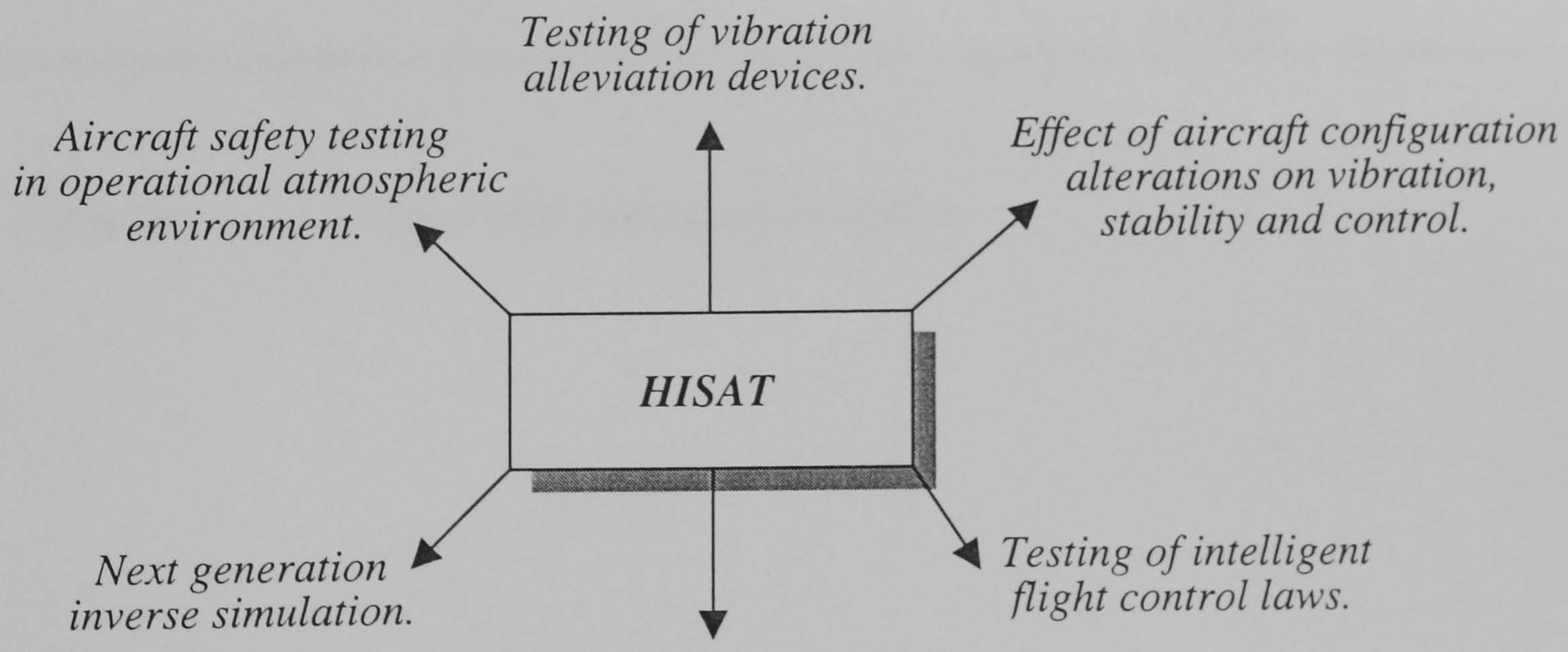

Figure 1.4 : **Possible implementations for the HISAT simulation tool.**

	Level 1	Level 2	Level3
Aerodynamics	linear 2-D dynamic inflow/local momentum theory analytically integrated loads.	nonlinear (limited 3-D) dynamic inflow/local momentum theory local effects of blade vortex interaction unsteady 2-D compressibility numerically integrated loads	nonlinear 3-D full wake analysis (free or prescribed) unsteady 2-D compressibility numerically integrated loads
Dynamics	rigid blades (1) quasi-steady motion (2) 3 DoF flap (3) 6 DoF flap + lag (4) 6 DoF flap + lag + quasi-steady torsion	(1) rigid blades with options as in Level 1 (2) limited number of blade elastic modes	detailed structural representation as elastic modes or finite elements
Applications	parametric trends for flying qualities and performance studies well within operational flight envelope low bandwidth control	parametric trends for flying qualities and performance studies up to OFE medium bandwidth appropriate to high gain active flight control	rotor design rotor limit loads prediction vibration analysis rotor stability analysis up to safe flight envelope

Table 2.1 : Levels of rotor mathematical modelling

Model item	Characteristics
Rotor dynamics (both rotors)	- up to 10 individually-modelled rigid blades - fully-coupled flap, lag and feather motion - blade attachment by offset hinges & springs - lag damper
Rotor loads	- aerodynamic and inertial loads represented by up to 10 elements per blade
Blade aerodynamics	- lookup tables for lift and drag as function of angle-of-attack and Mach number
Wake model	- momentum-derived dynamic wake model - uniform and harmonic components of inflow - rudimentary interaction with tail surfaces - ground effect
Transmission	- coupled rotorspeed and engine dynamics - up to 3 engines - geared or independently-controlled rotor torque
Airframe	- fuselage, tailplane and fin aerodynamics by lookup tables or polynomial functions
Atmosphere	- International Standard Atmosphere - provision for variation of sea-level temperature and pressure

Table 2.2 : Summary of the key modelling and functional aspects of RASCAL.

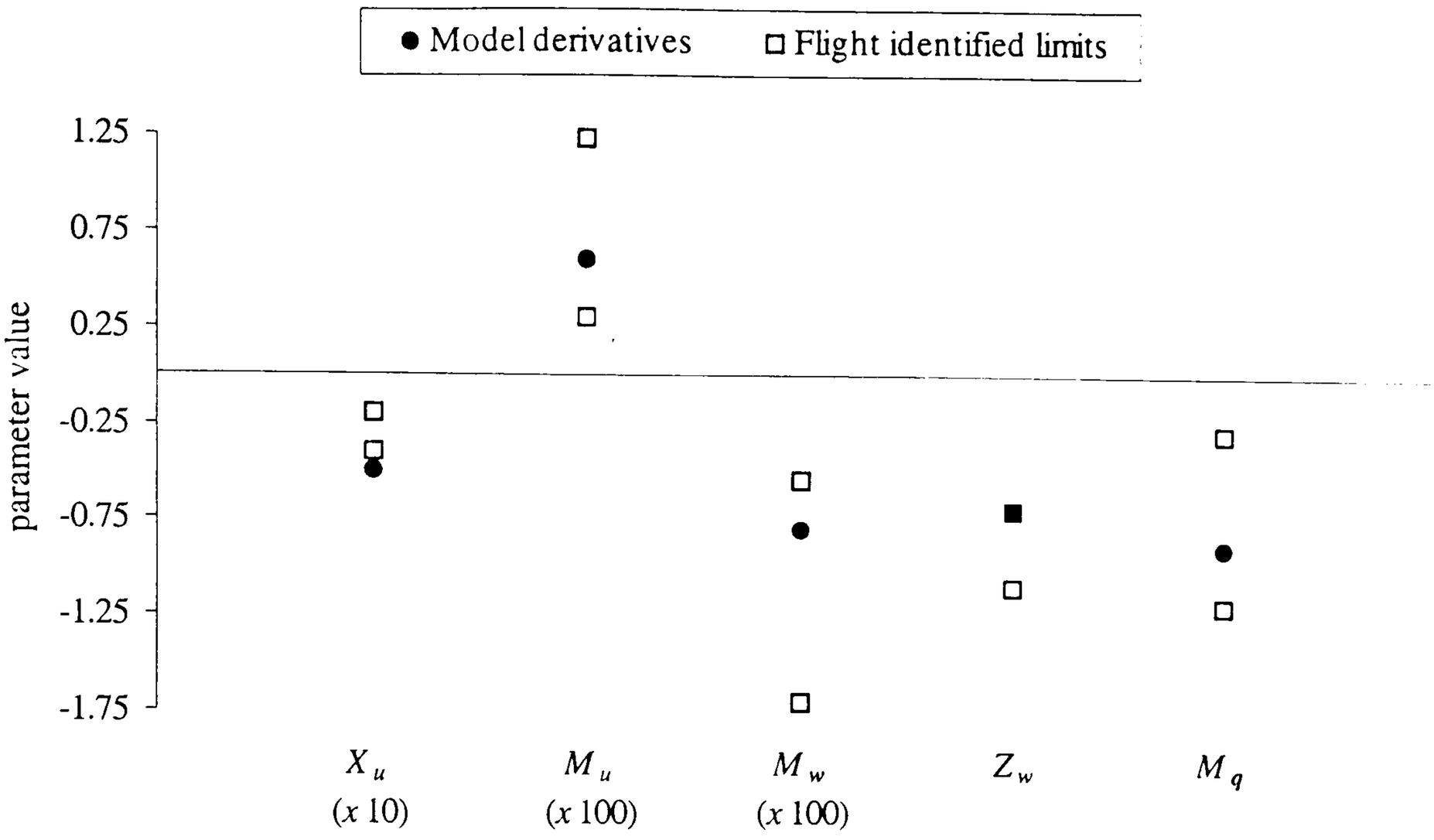

Figure 2.1 : **Comparison of RASCAL – predicted longitudinal stability derivatives with flight test data. (Reproduced from Houston, 1994).**

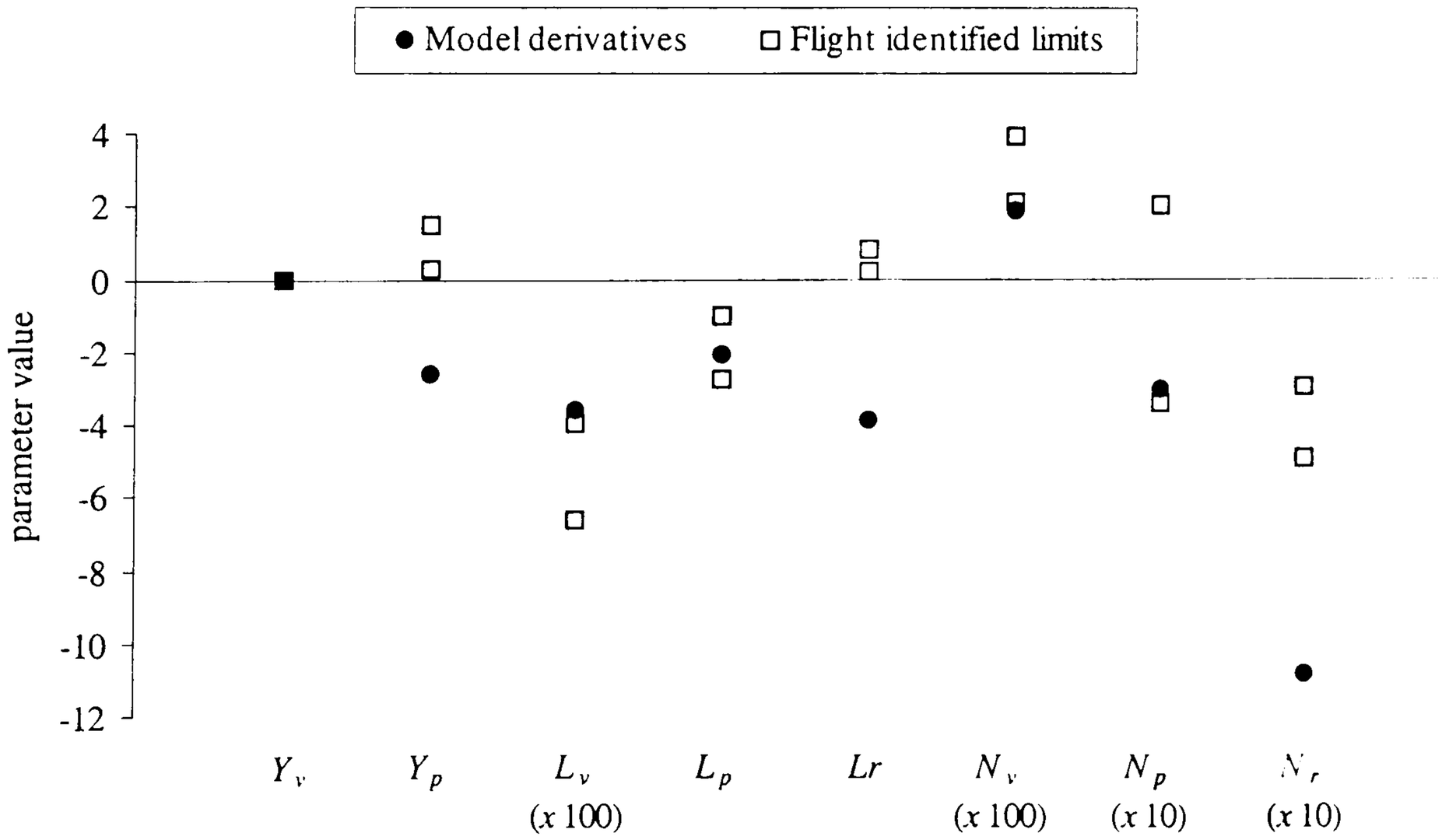

Figure 2.2 : **Comparison of RASCAL – predicted lateral/directional stability derivatives with flight test data. (Reproduced from Houston, 1994).**

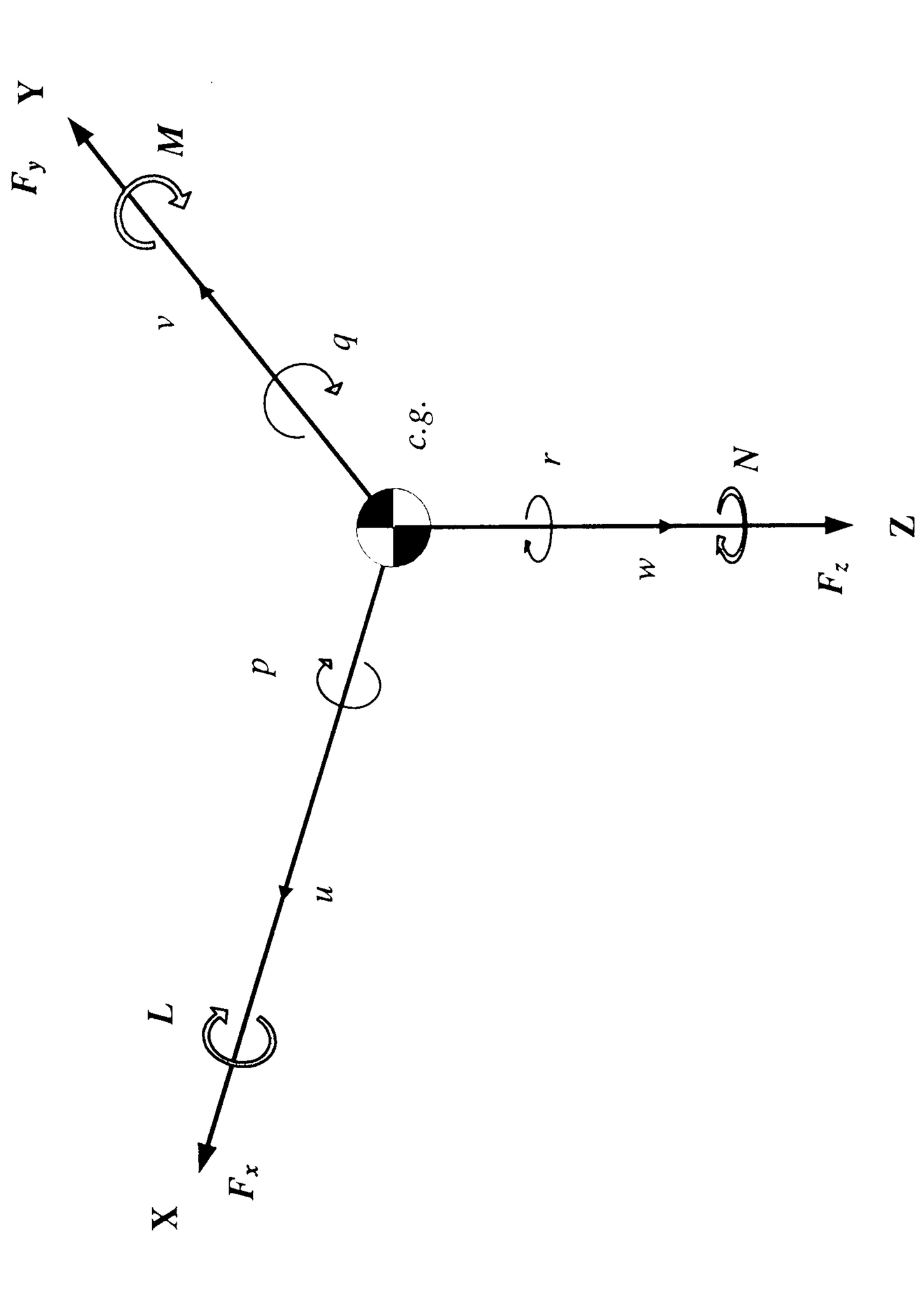

Figure 2.3 : Forces, moments, rates and velocities defined around an orthogonal right-handed set.

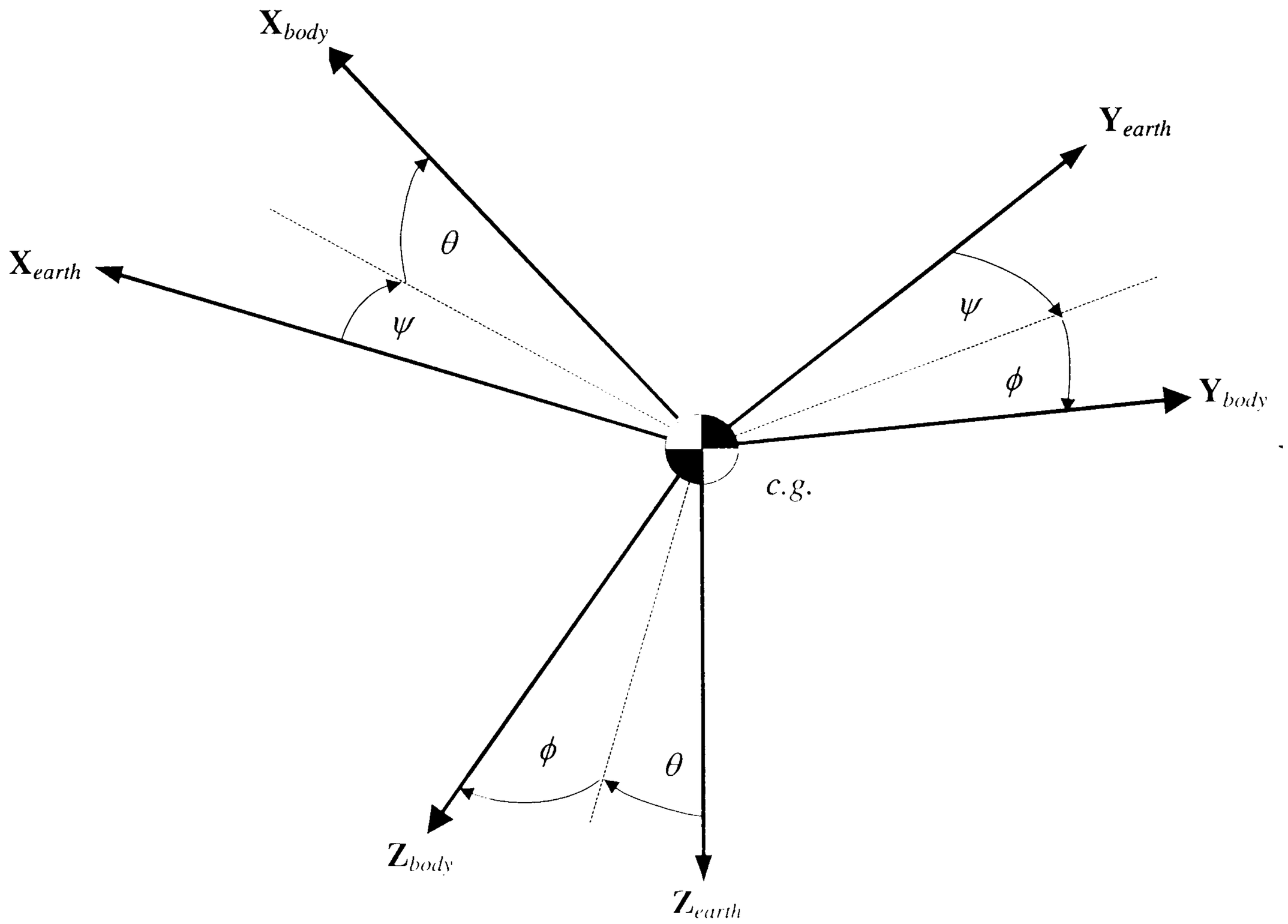

Figure 2.4 : Euler angles transformation from earth to body axes.

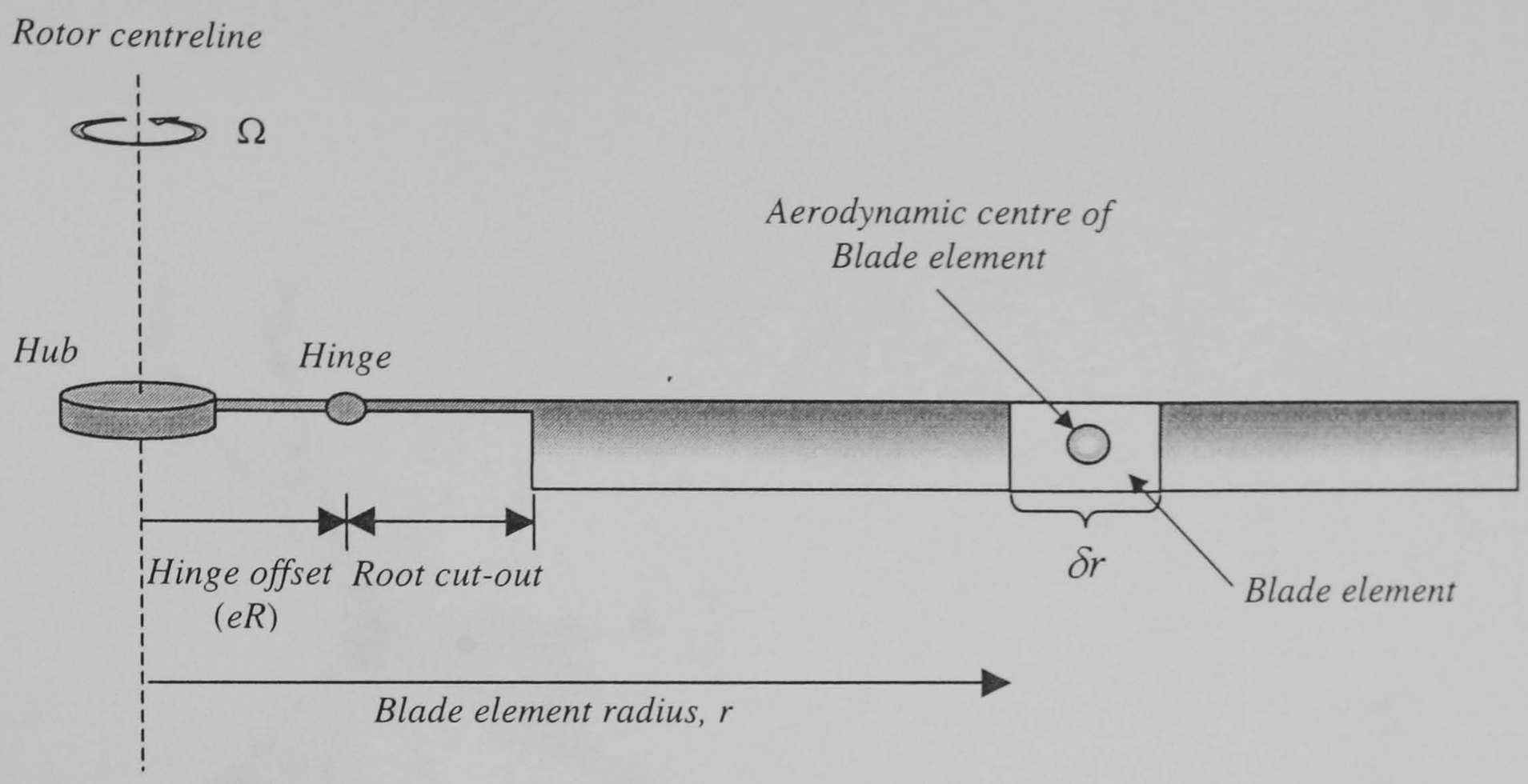

Figure 2.5 : **Standard notation for the location of a blade element at a distance, r along the blade.**

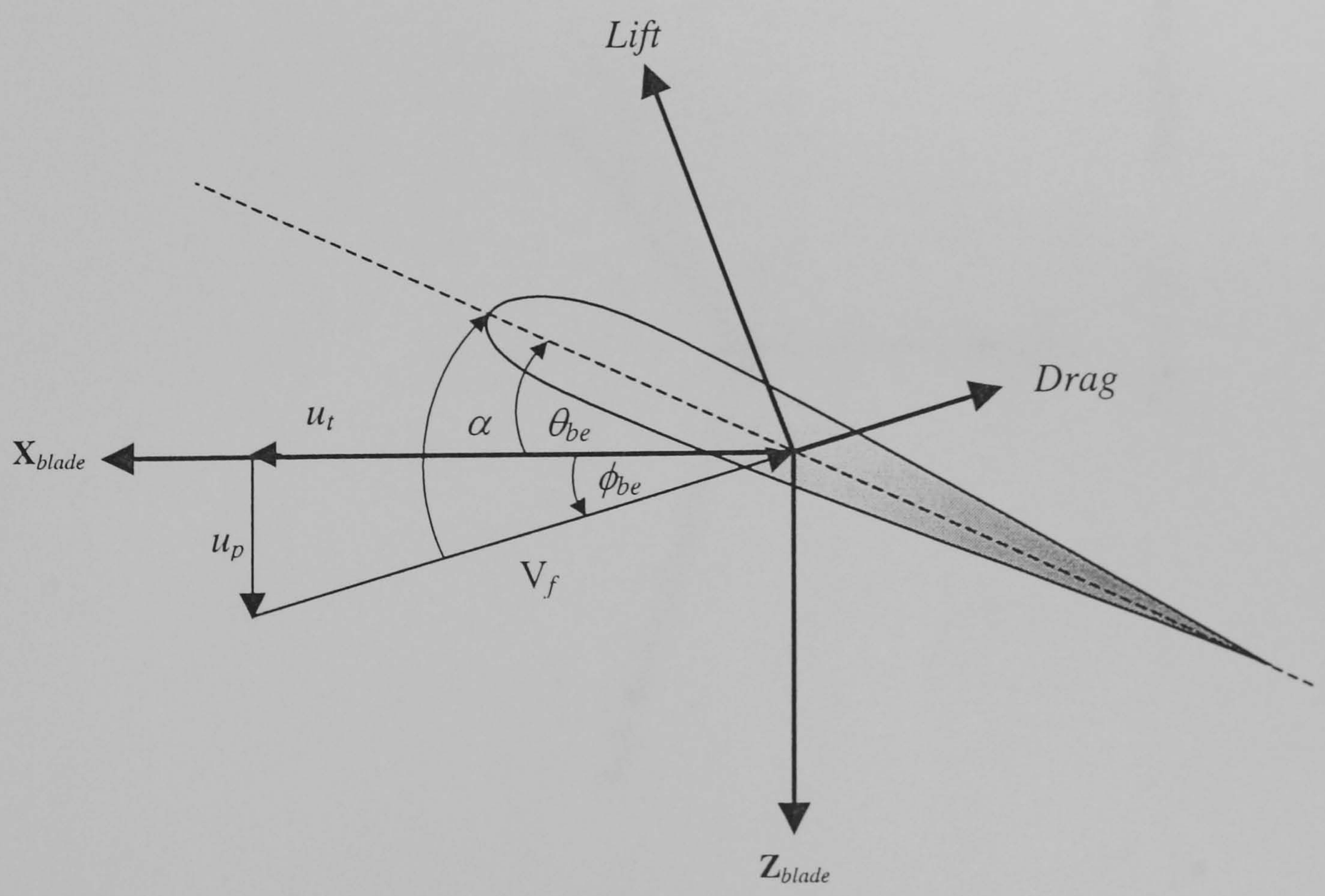

Figure 2.6 : **The aerodynamic forces experienced by a blade element.**

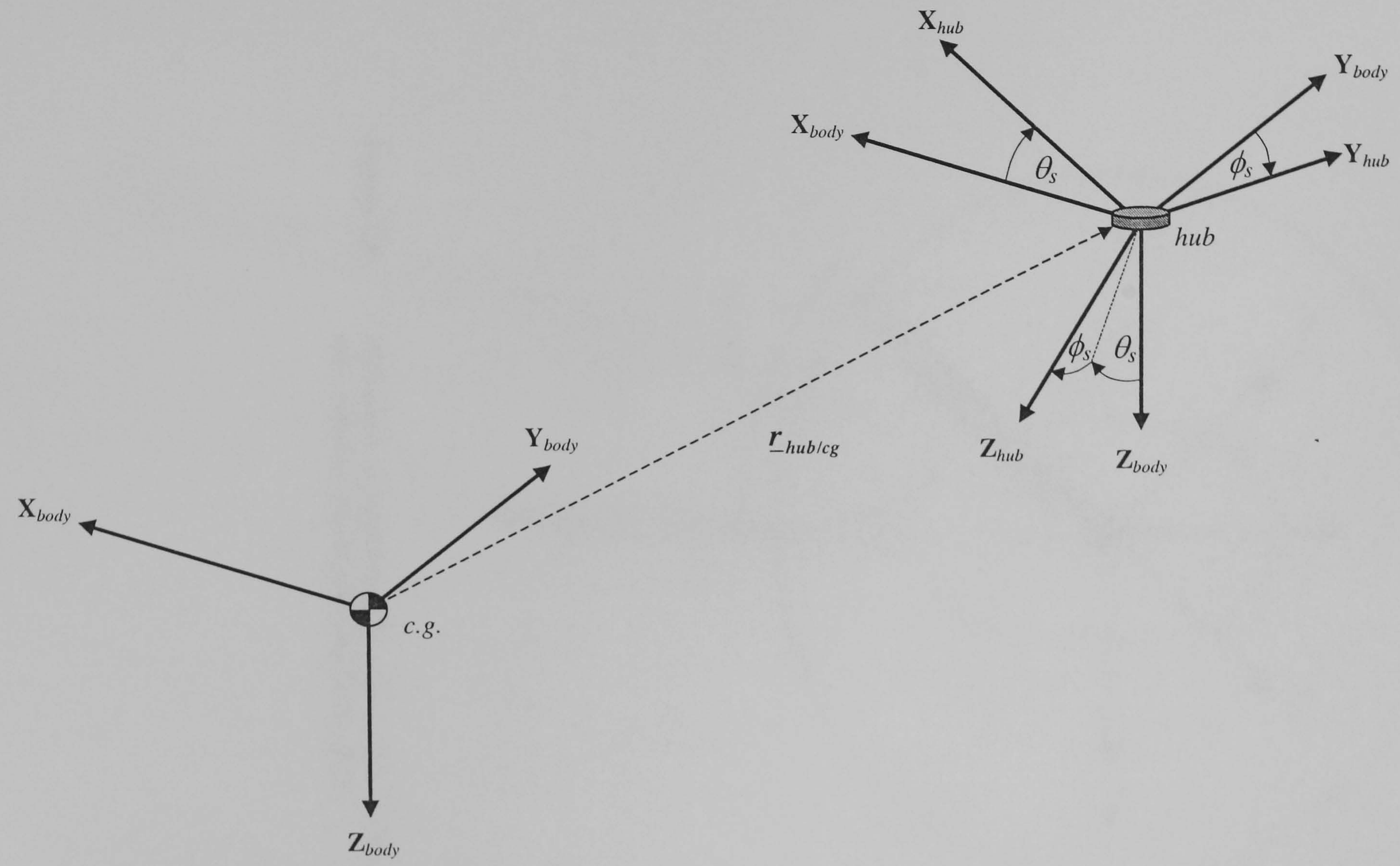

Figure 2.7 : **Transformation from body axes to native hub axes.**

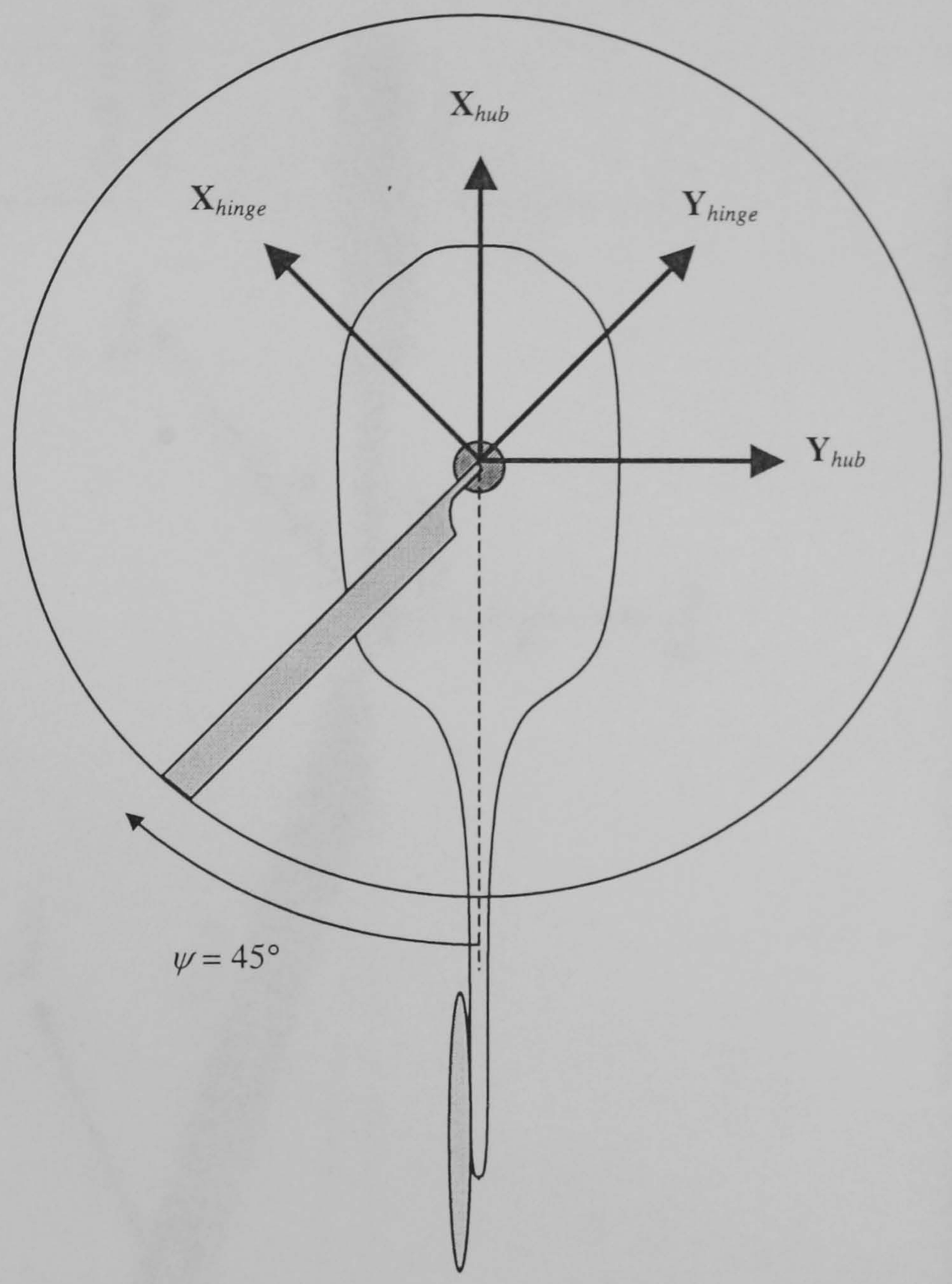

Figure 2.8 : **Definition of azimuth angle and transformation from non-rotating hub to rotating hinge axes.**

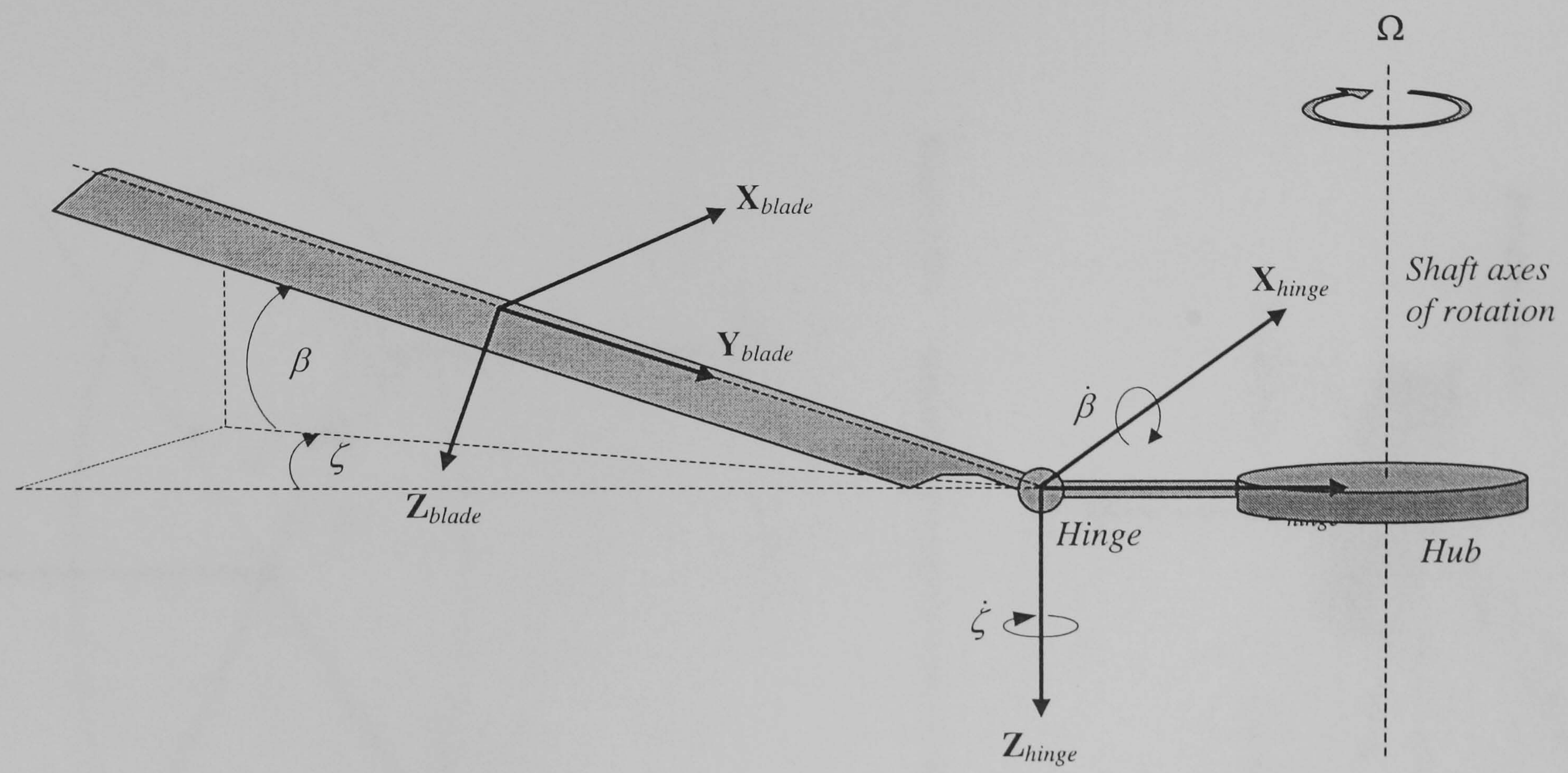

Figure 2.9 : **Transformation from hinge to blade axes through the blade flap and lag degrees of freedom.**

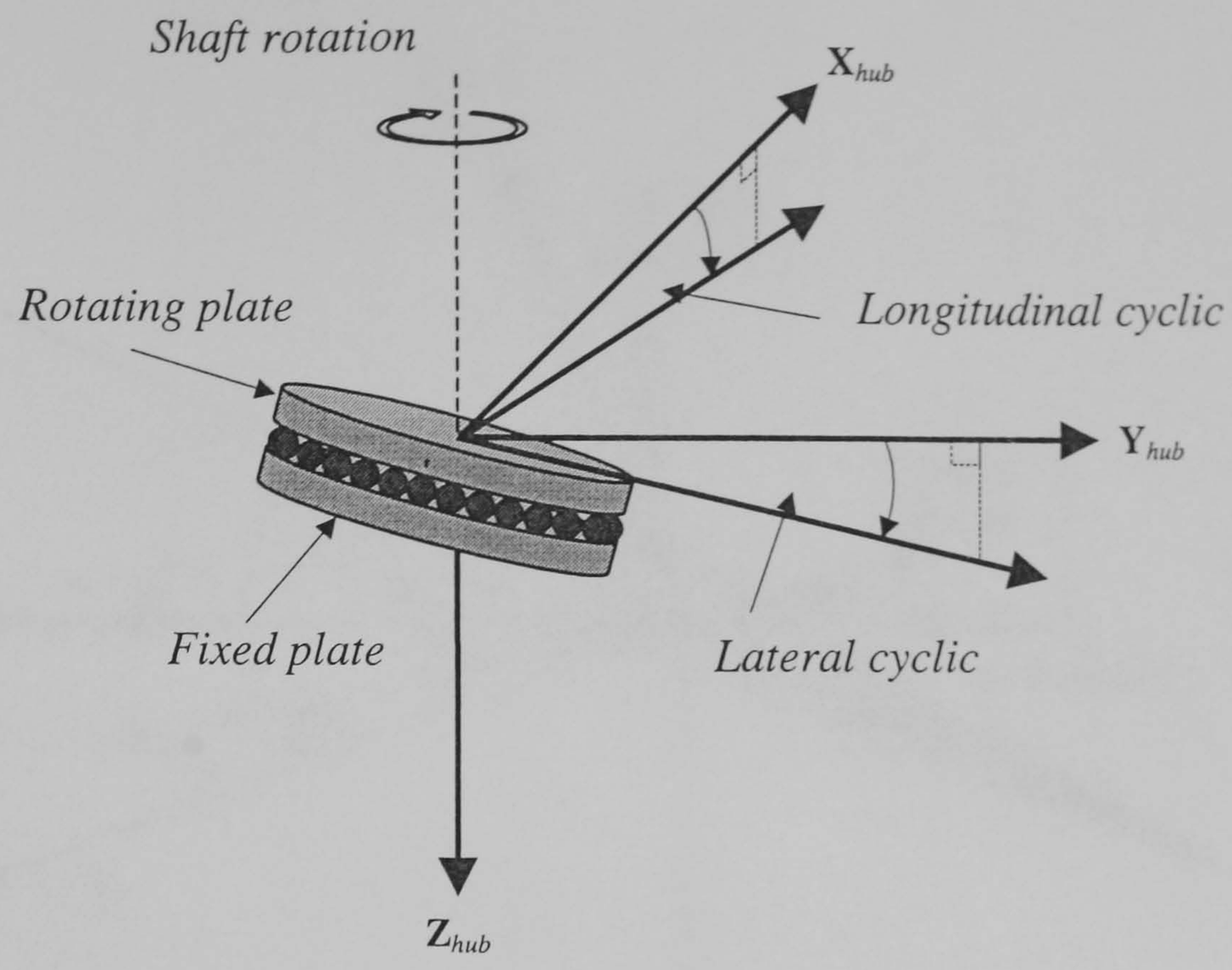

Figure 2.10 : Geometry of a conventional swashplate arrangement.

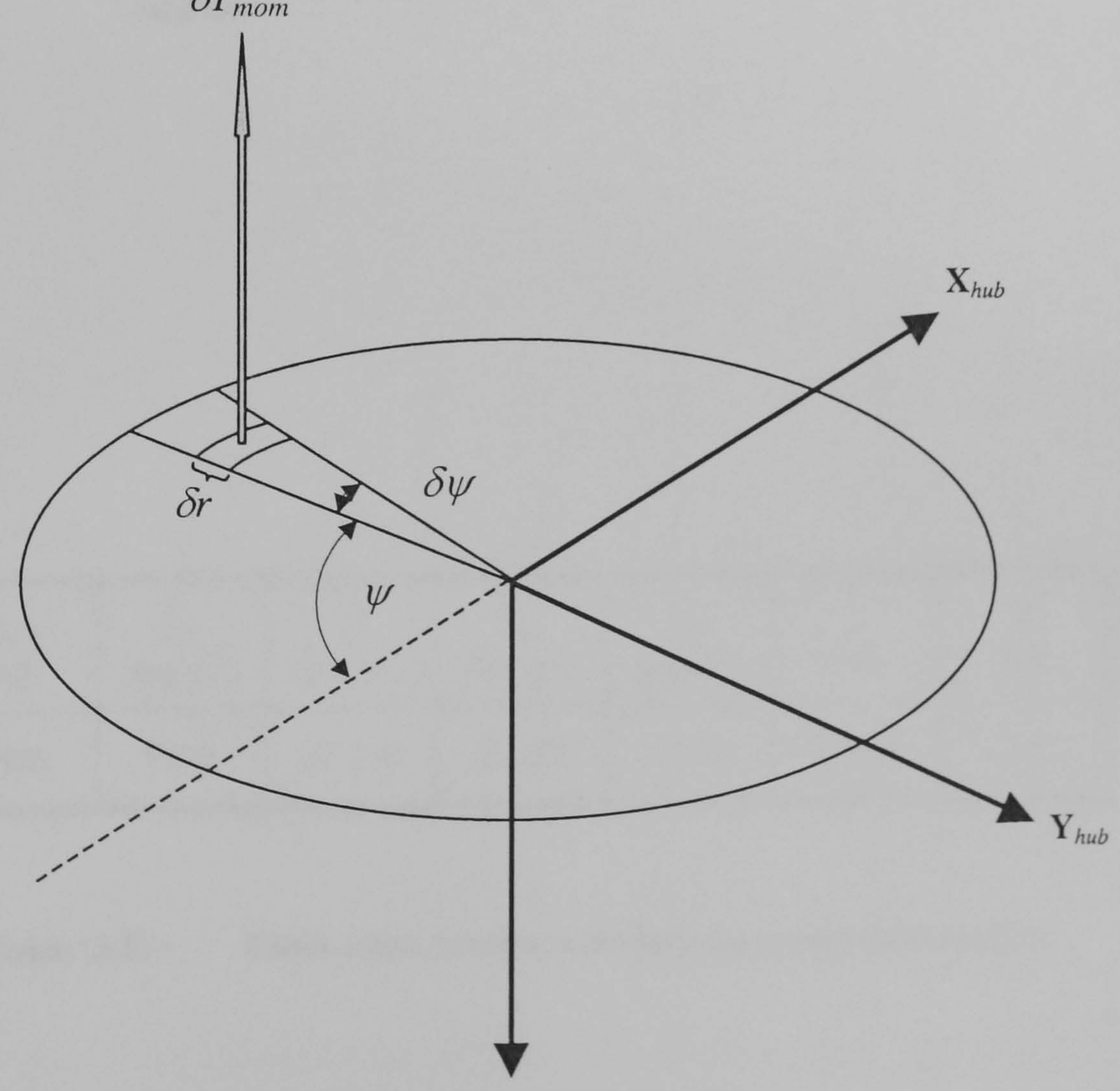

Figure 2.11 : Incremental disc area showing aerodynamic moments.

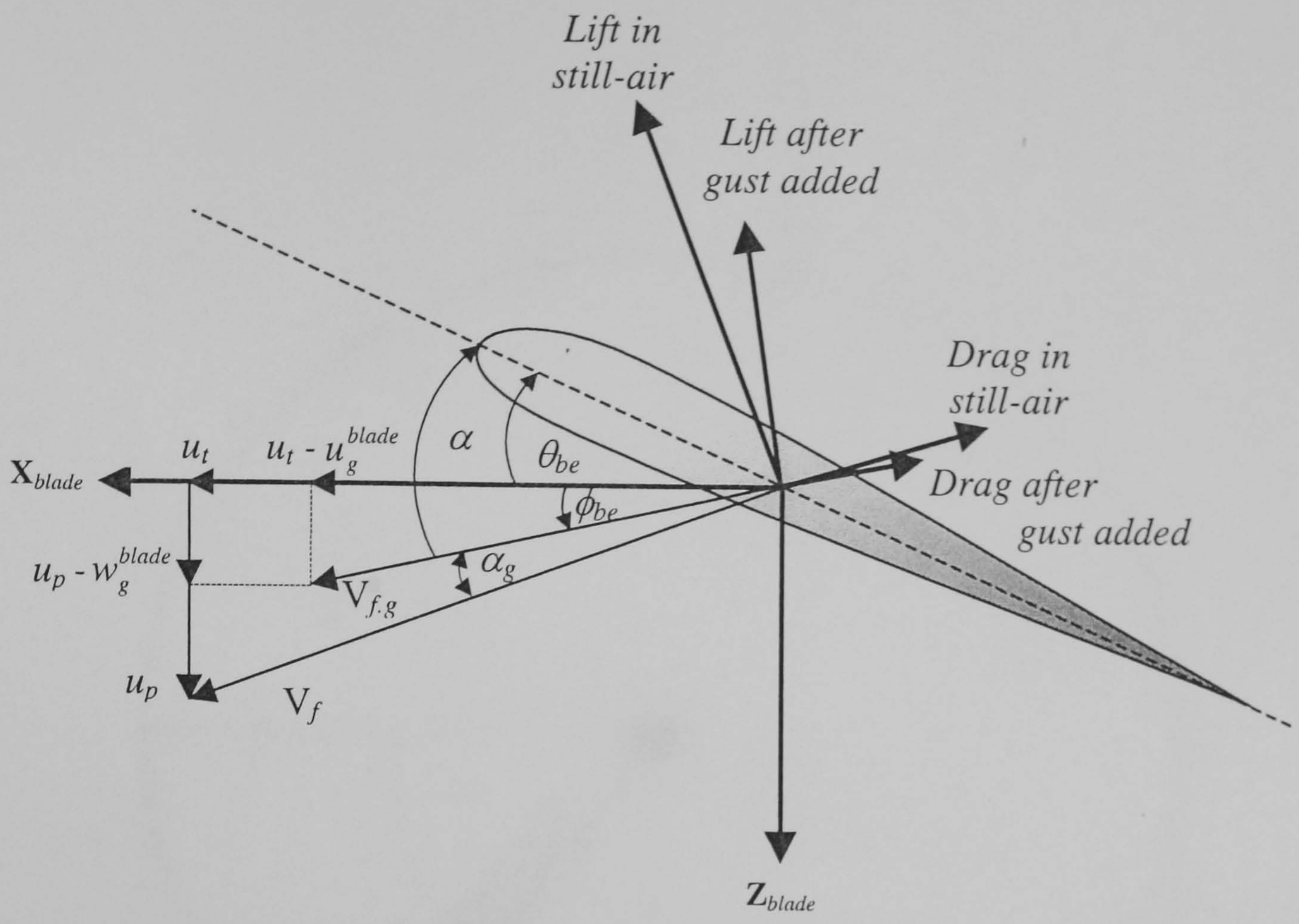

Figure 3.1 : **The effect of turbulence on the local aerodynamics of a blade element.**

mass (kg)	I_{xx} (kg m^2)	I_{yy} (kg m^2)	I_{zz} (kg m^2)	I_{xz} (kg m^2)	c (m)	R (m)
5805	9638	33 240	25 889	2226	0.5401	7.5

Table (3.1) : **Puma mass, inertia and blade geometry information.**

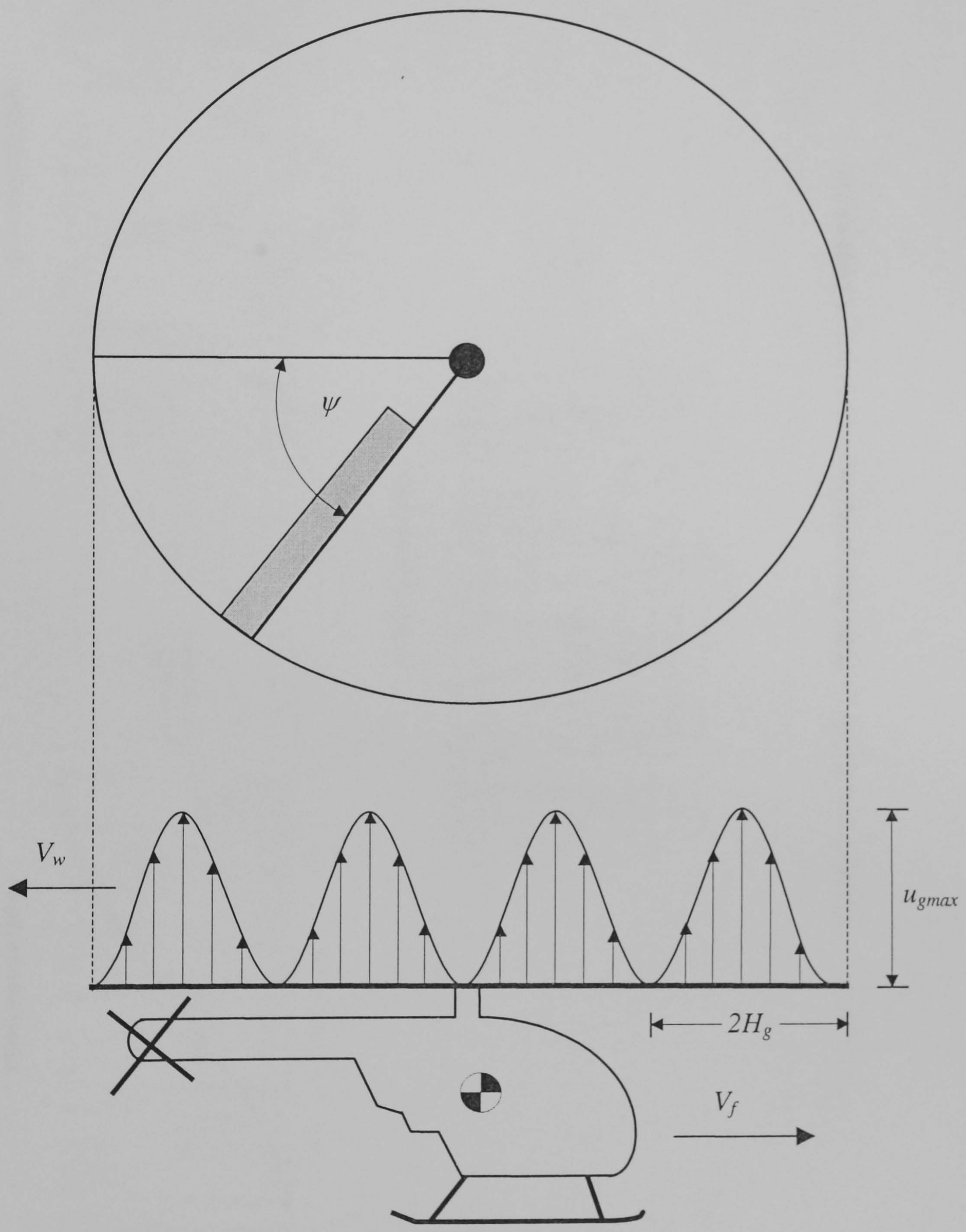

Figure 3.2 : **Schematic of a helicopter encountering a sinusoidal gust field.**

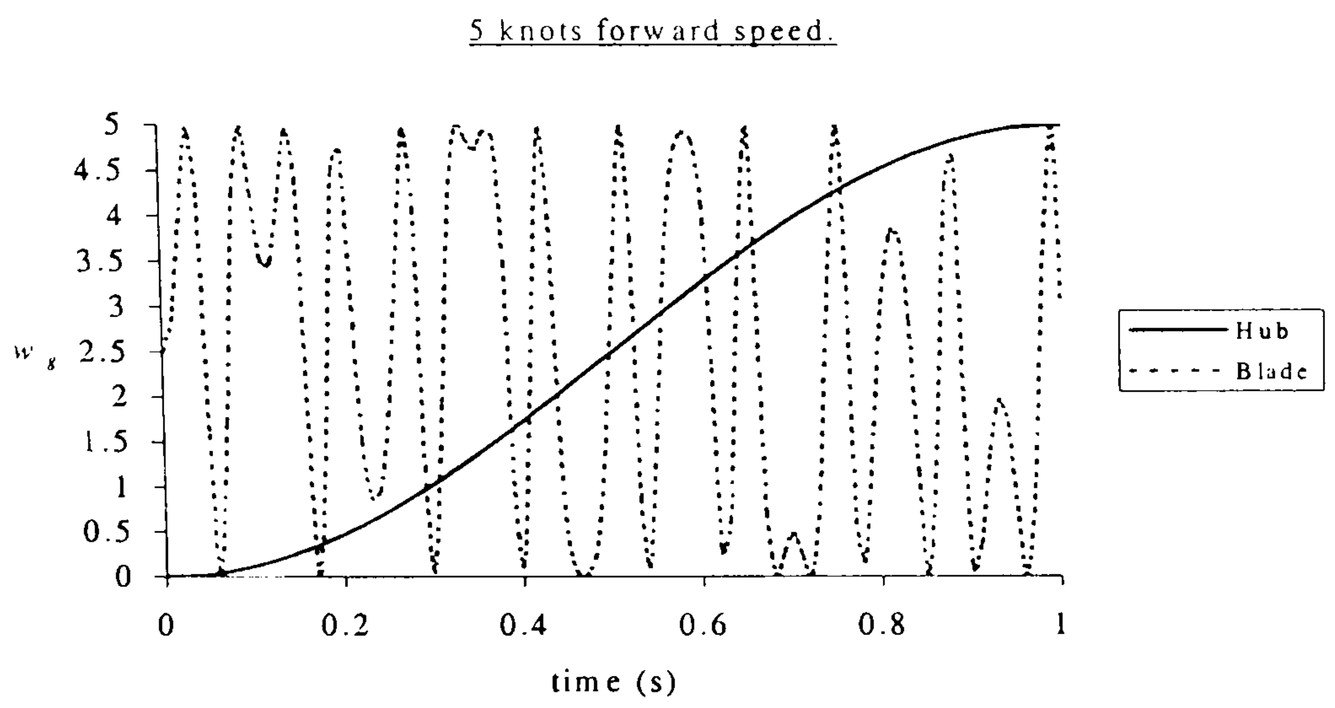

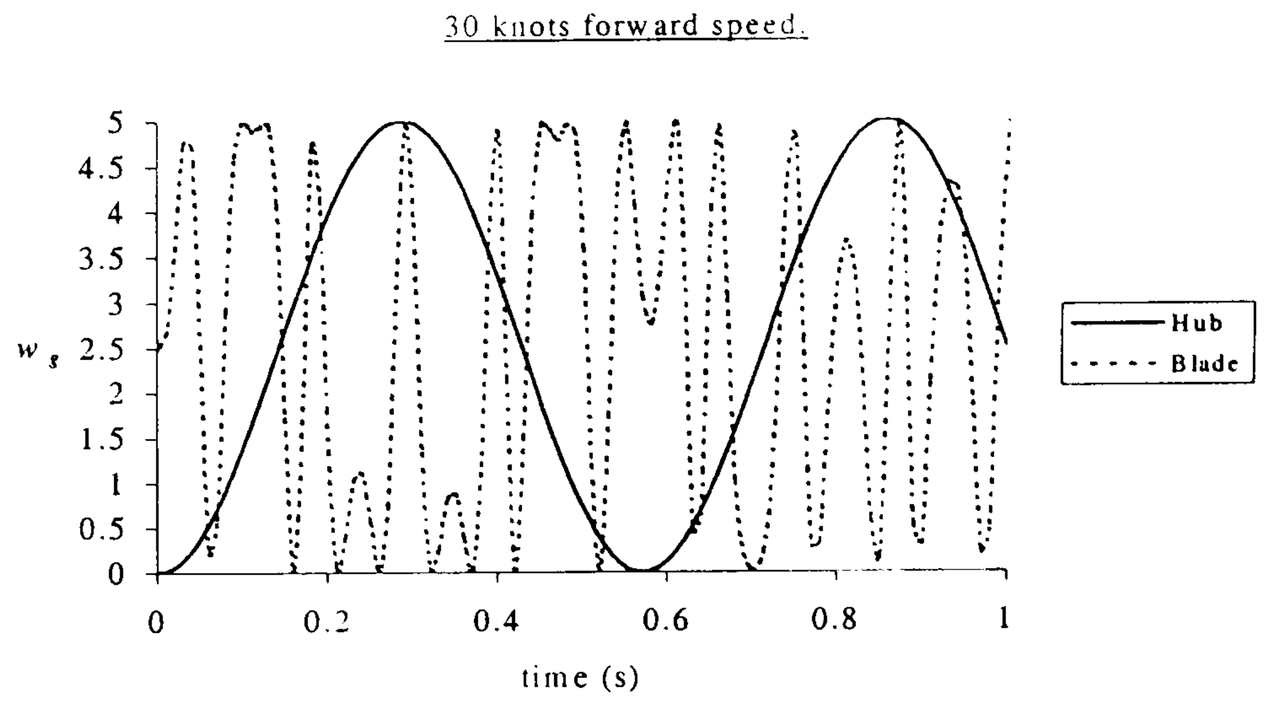

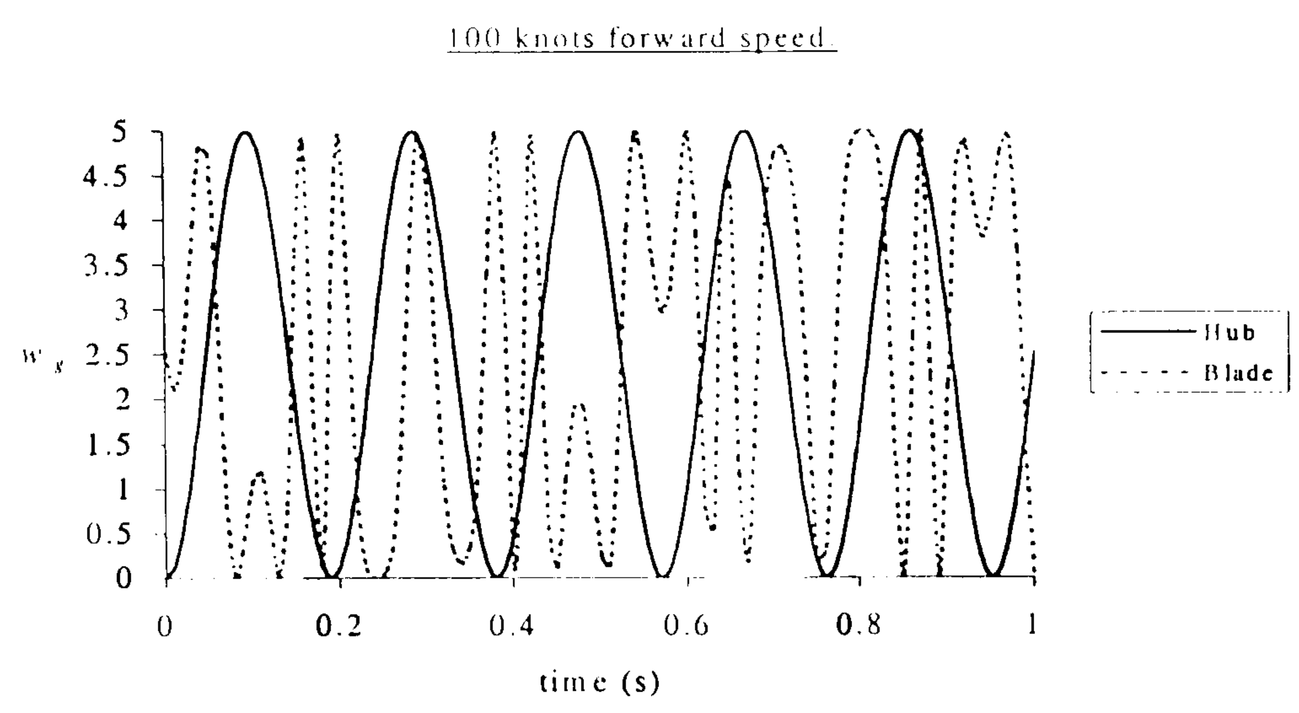

Figure 3.3 : **A comparison of hub vs. blade-fixed sampling for a variety of flight speeds.**

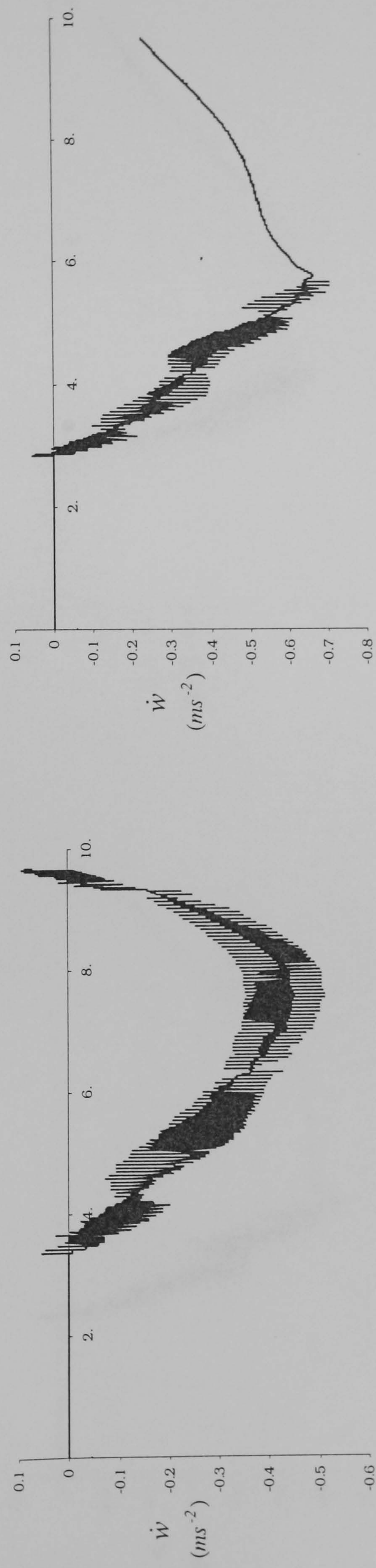

Figure 3.4 : Response of a Puma to progressive immersion into a 2.5ms^{-1} sharp-edged vertical gust.

15 knots

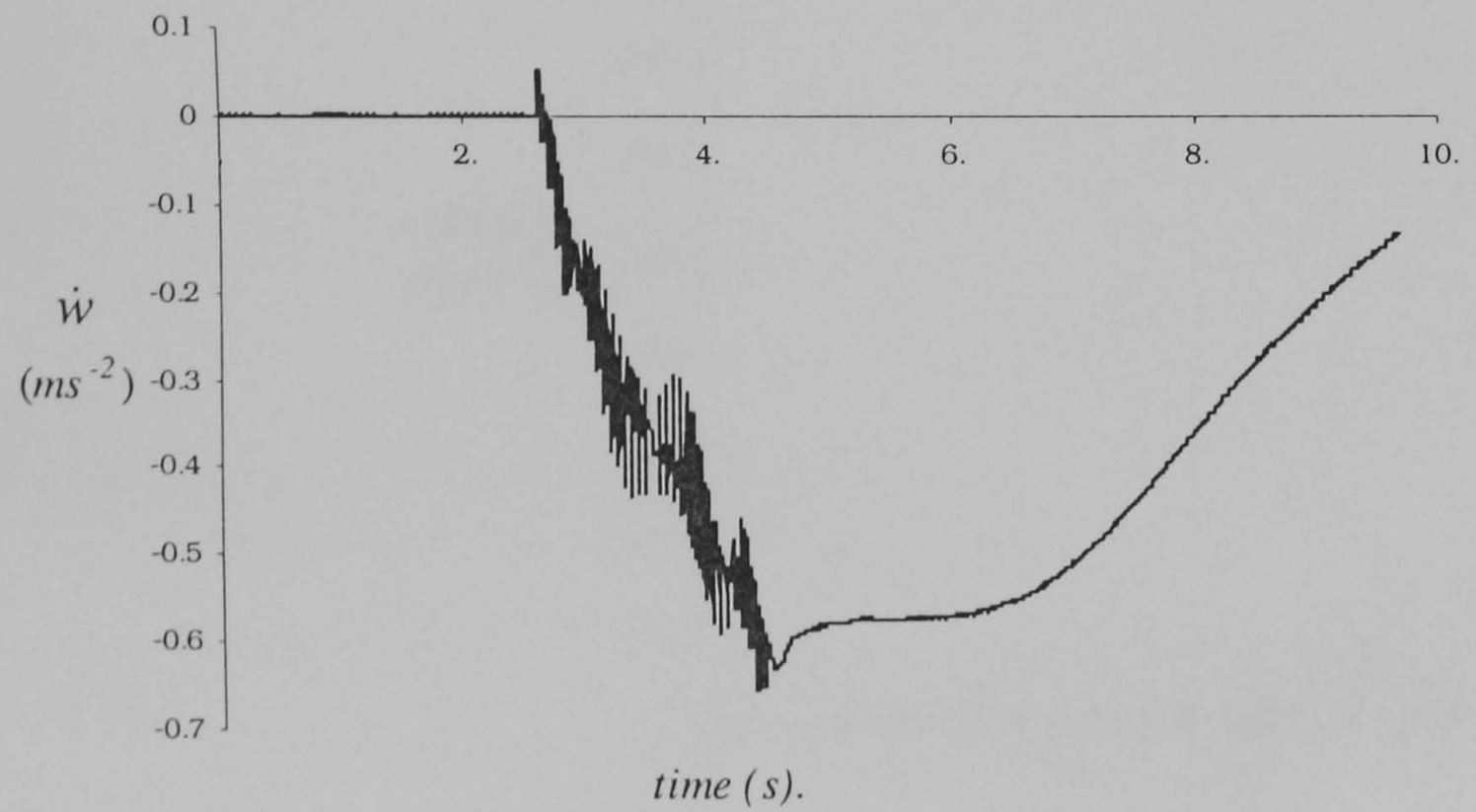

20 knots

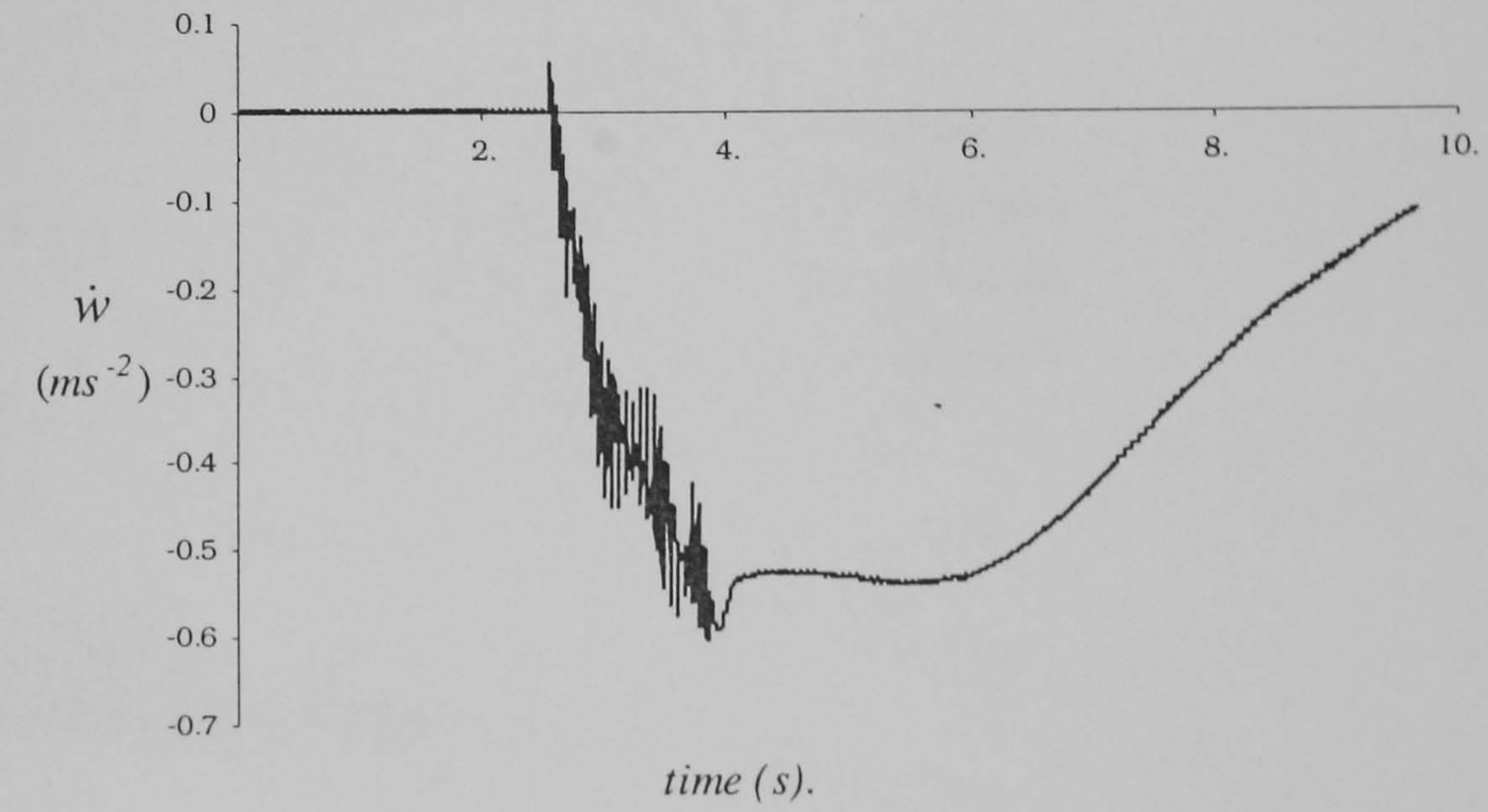

Figure 3.4 : Continued.

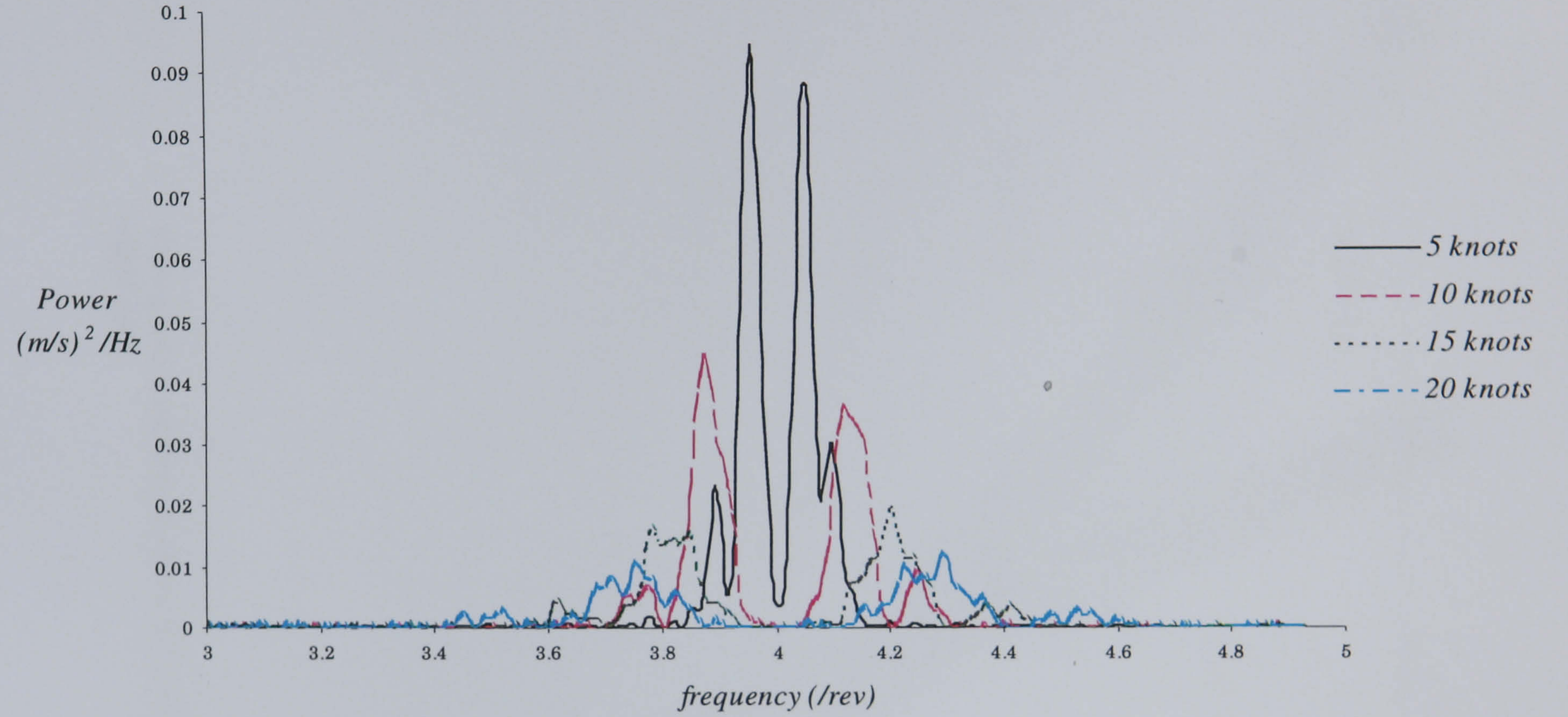

Figure 3.5 : **Power Spectral Density distributions for progressive immersion into a 2.5ms^{-1} vertical sharp-edged gust.**

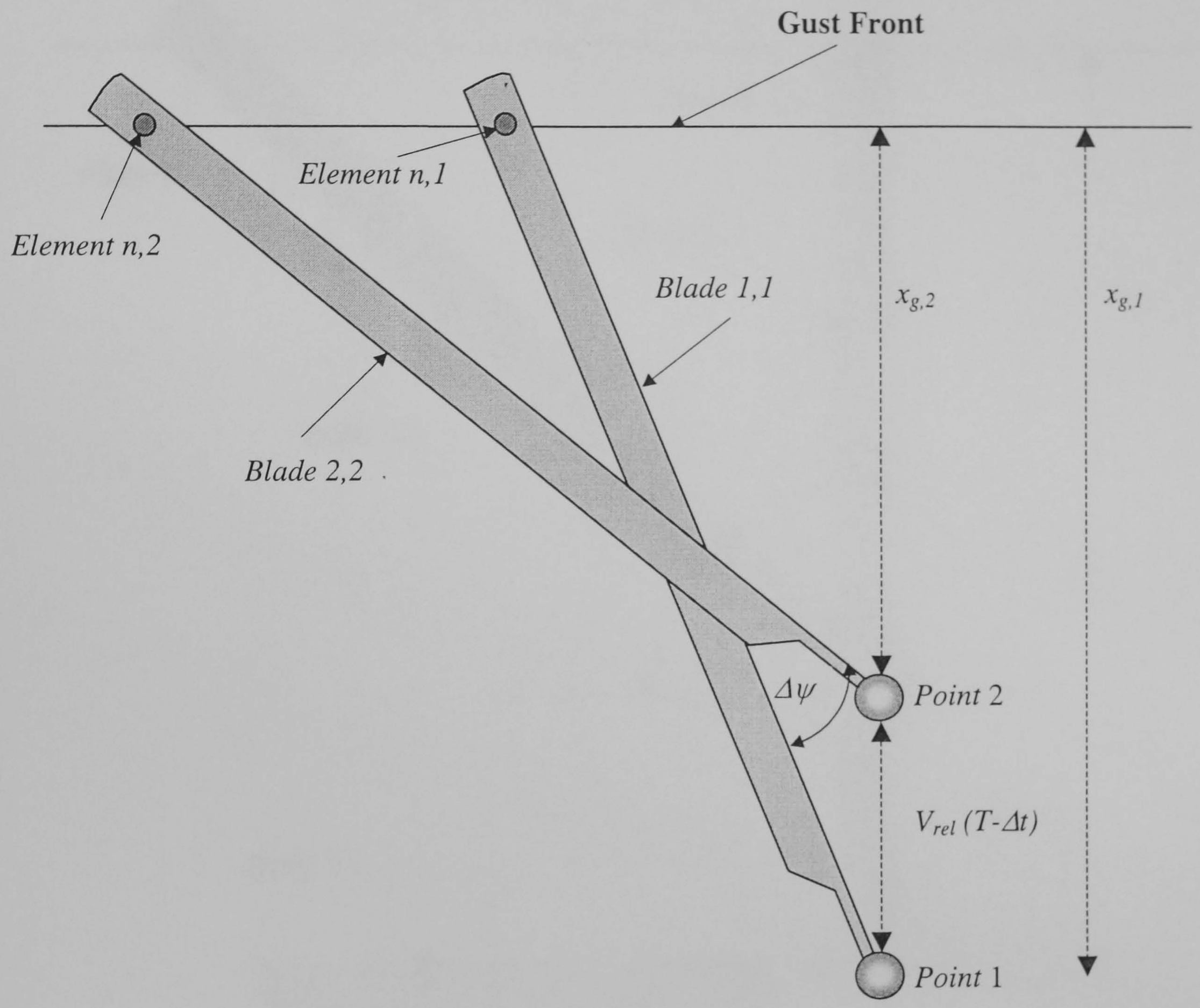

Figure 3.6 : Timing and geometry diagram for a rotor encountering a sharp-edged gust.

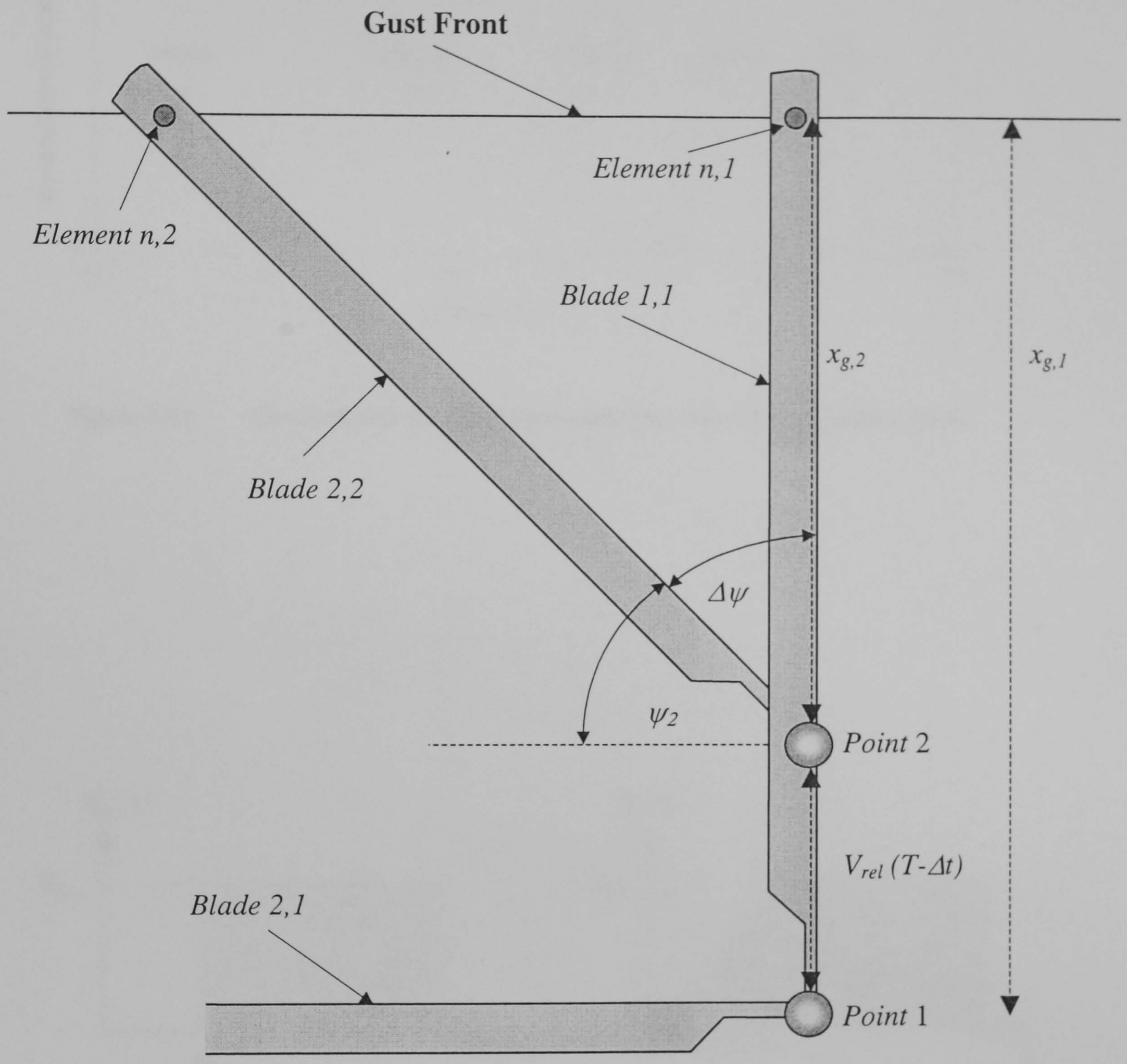

Figure 3.7 : **The special case when the perpendicular distance of the gust front is exactly one blade element length from the hub.**

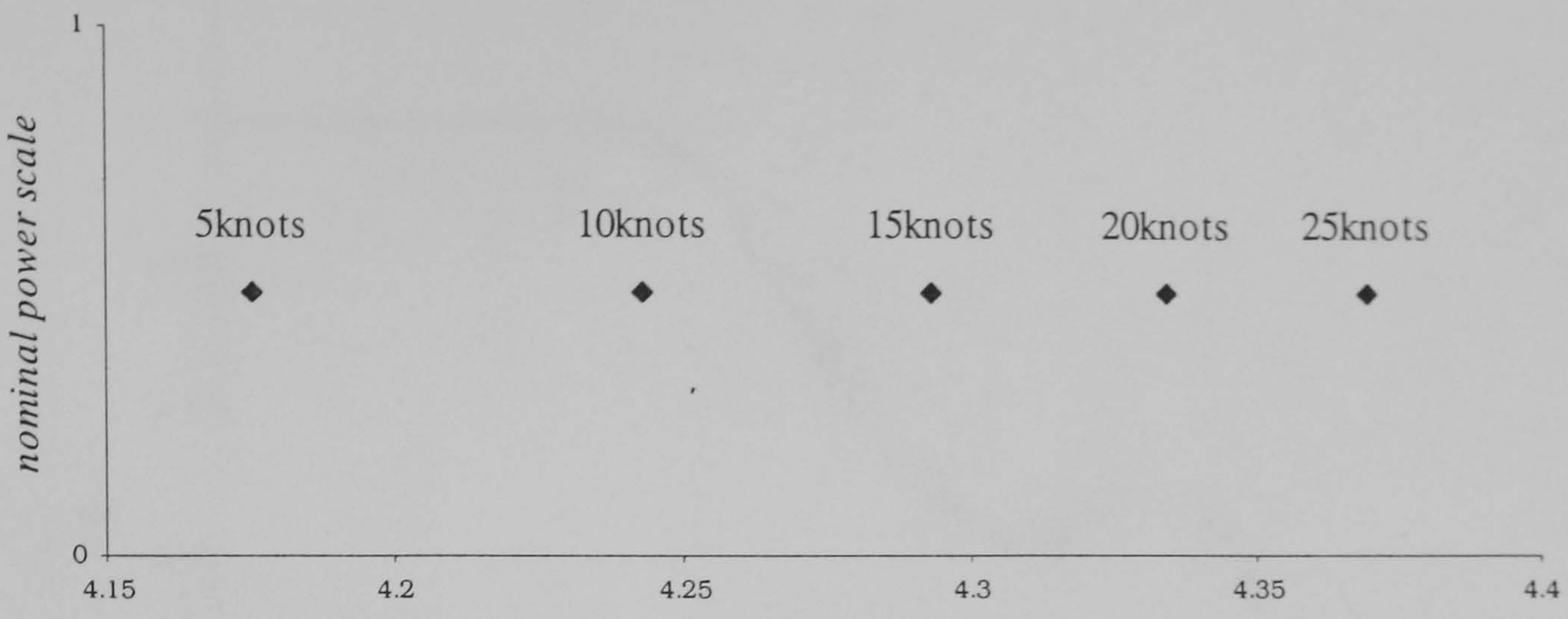

Figure 3.8 : Gust-induced vibration phase shift as predicted by equation (3.4.6).

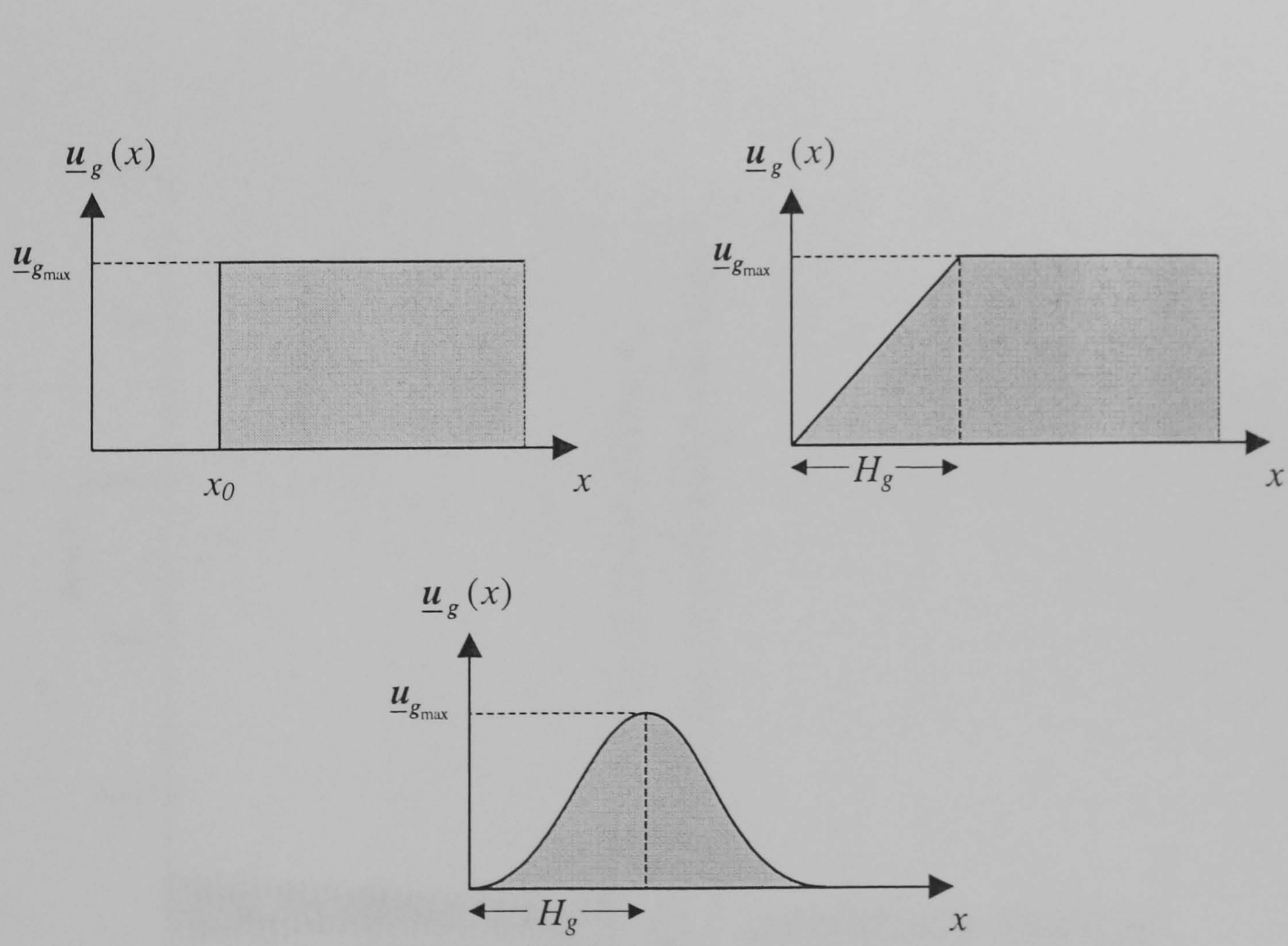

Figure 4.1 : The 1-COS, step and ramp-step discrete gust shapes.

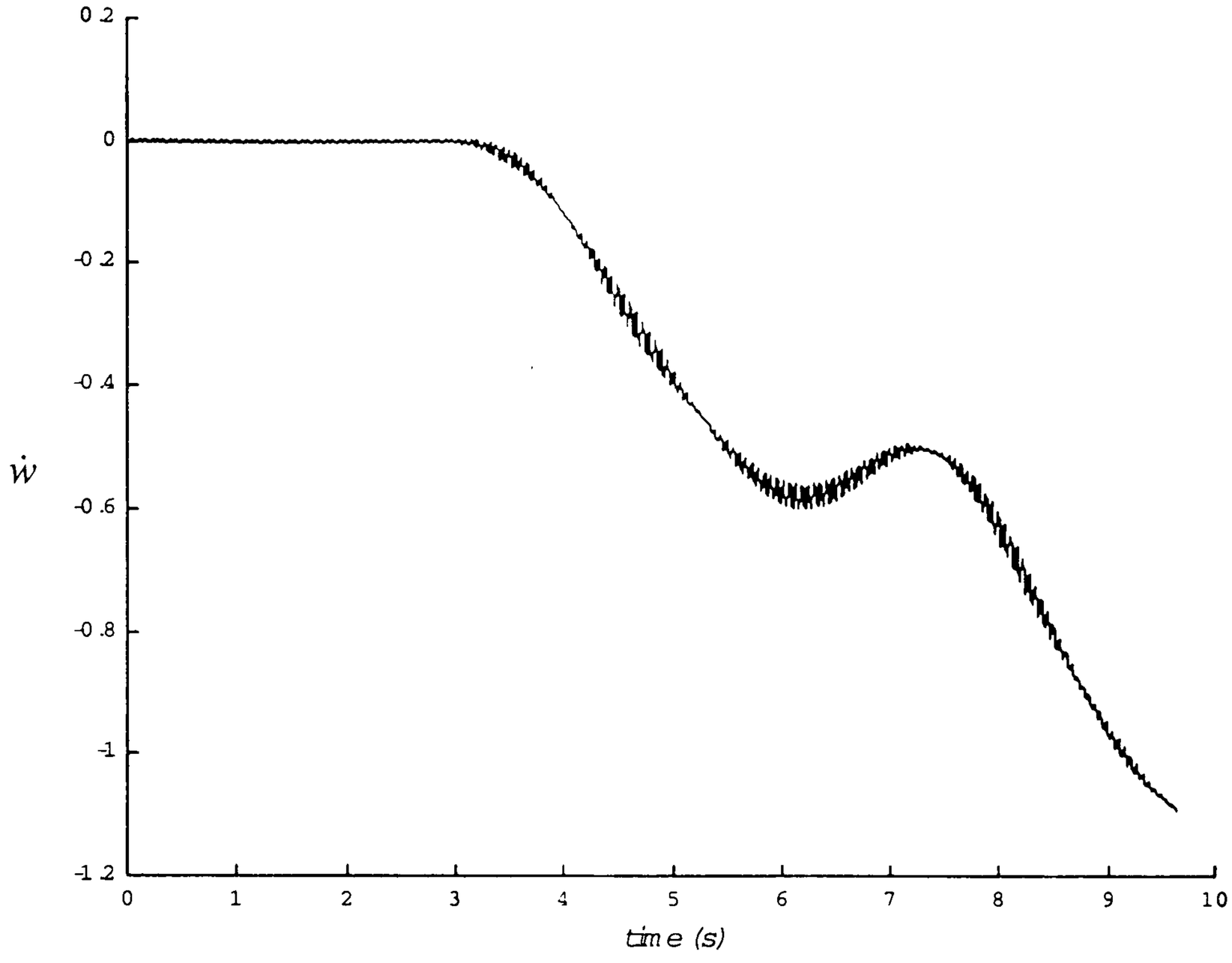

Figure 4.2 : **Vibration response of progressive immersion into a 1-cos gust.**

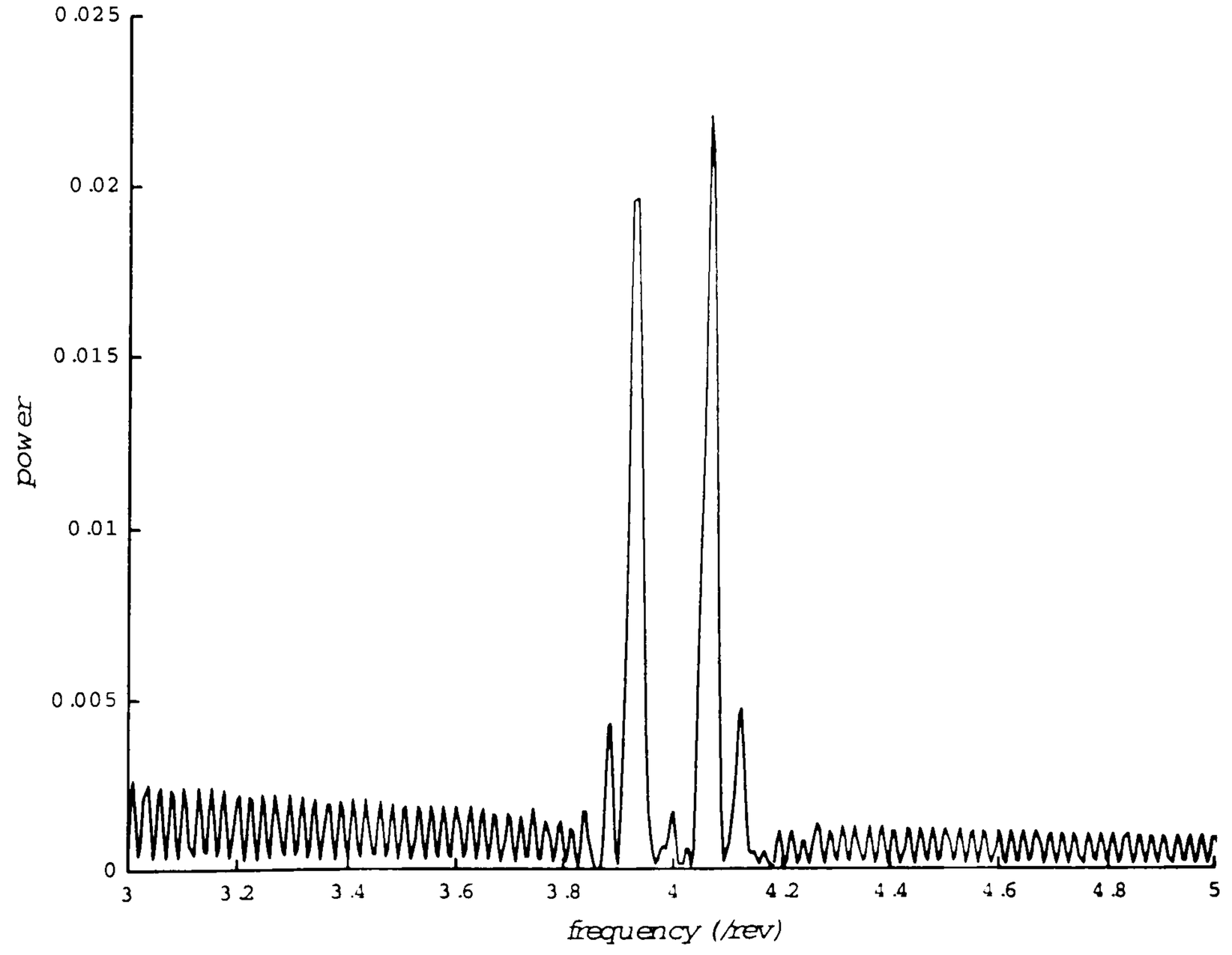

Figure 4.3 : **PSD of the vibration response of progressive immersion into 1-cos gust.**

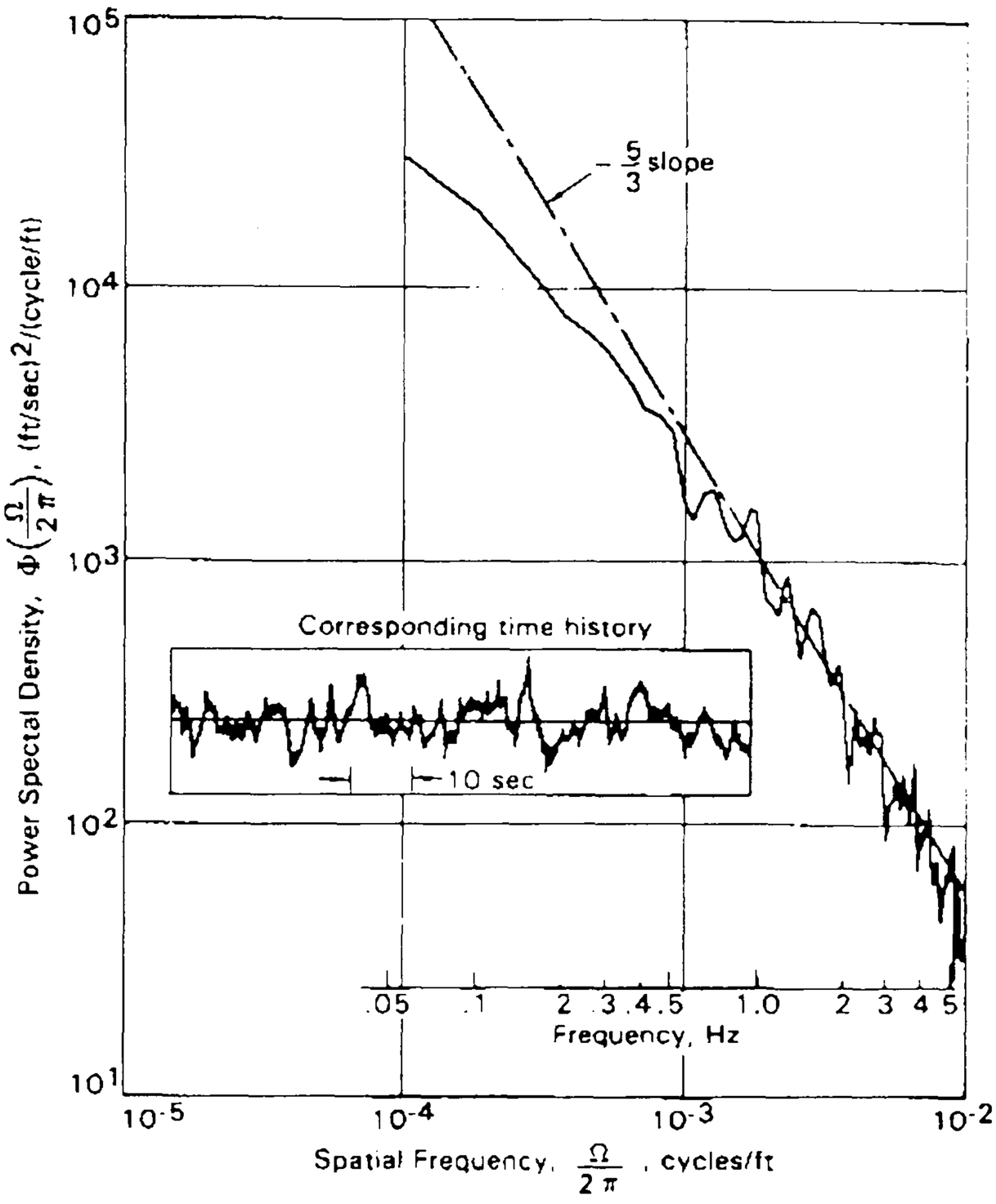

Figure 4.4 : **Typical gust velocity PSD extracted from flight test data (picture reproduced from Hoblit (1988)).**

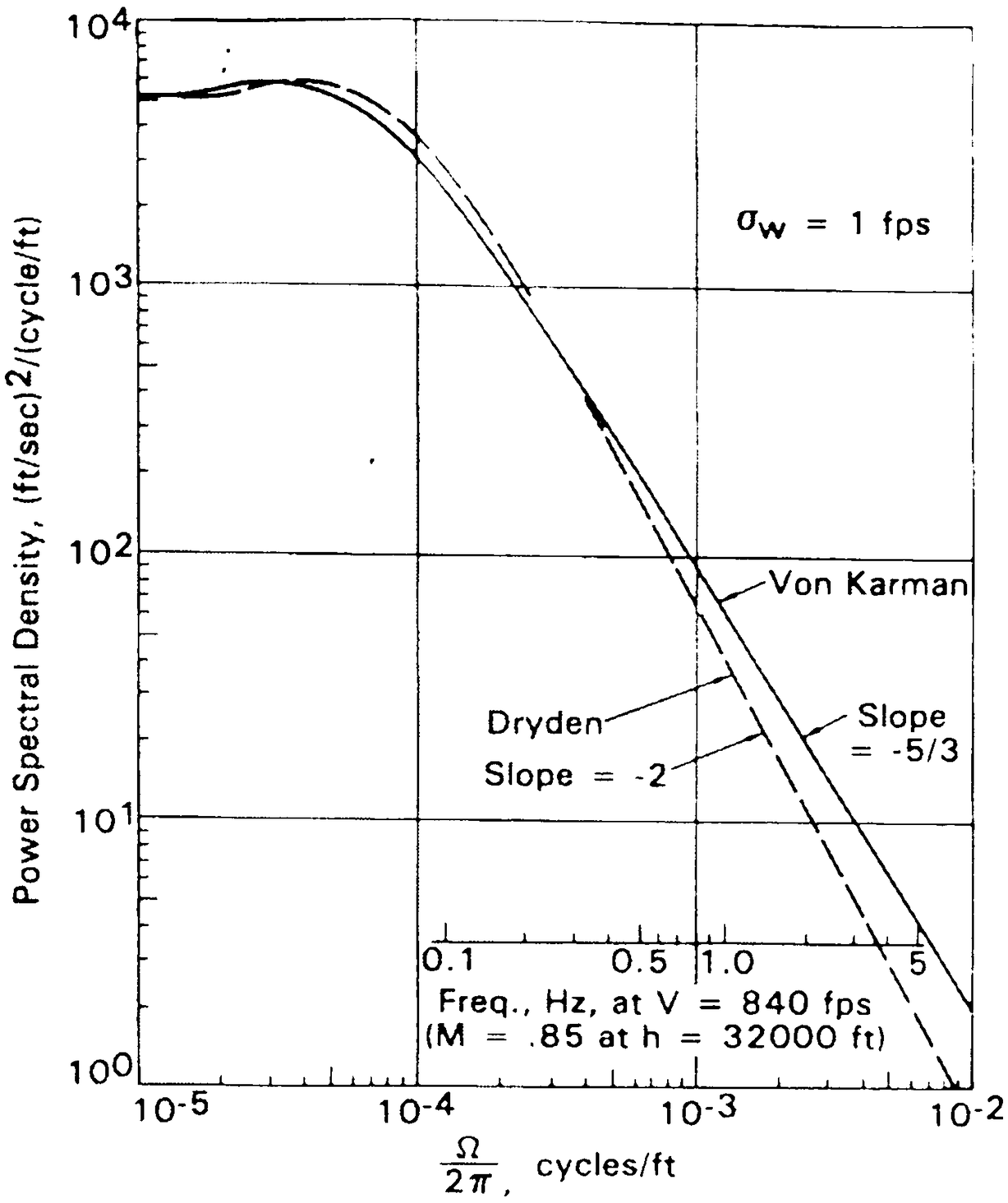

Figure 4.5 : **A comparison of the shape of the Dryden and von Karman PSD's in the inertial subrange (picture reproduced from Hoblit (1988)).**

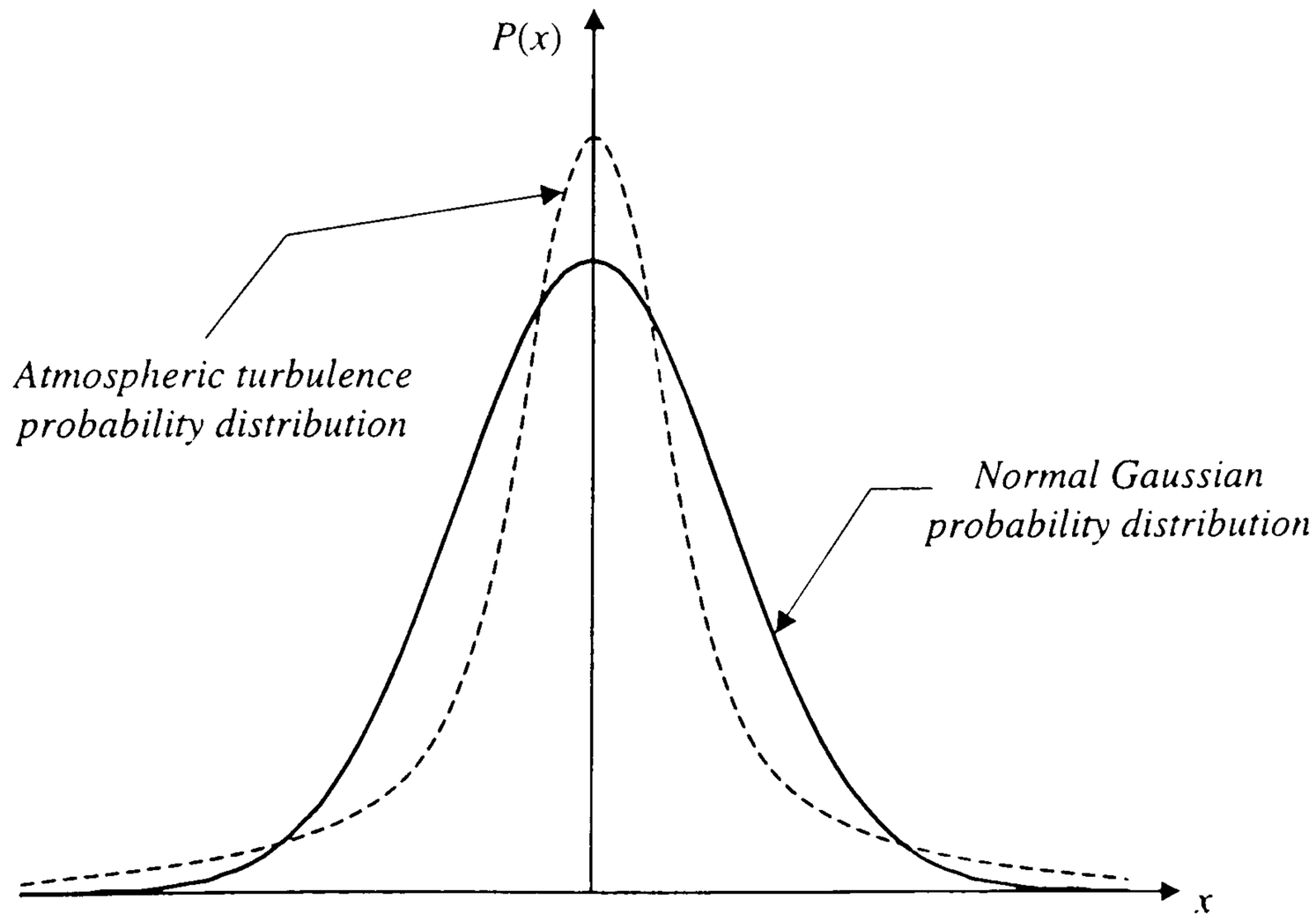

Figure 4.6 : **A comparison of the probability distributions of measured atmospheric turbulence and normal Gaussian, illustrating the kurtosis of the measured distribution.**

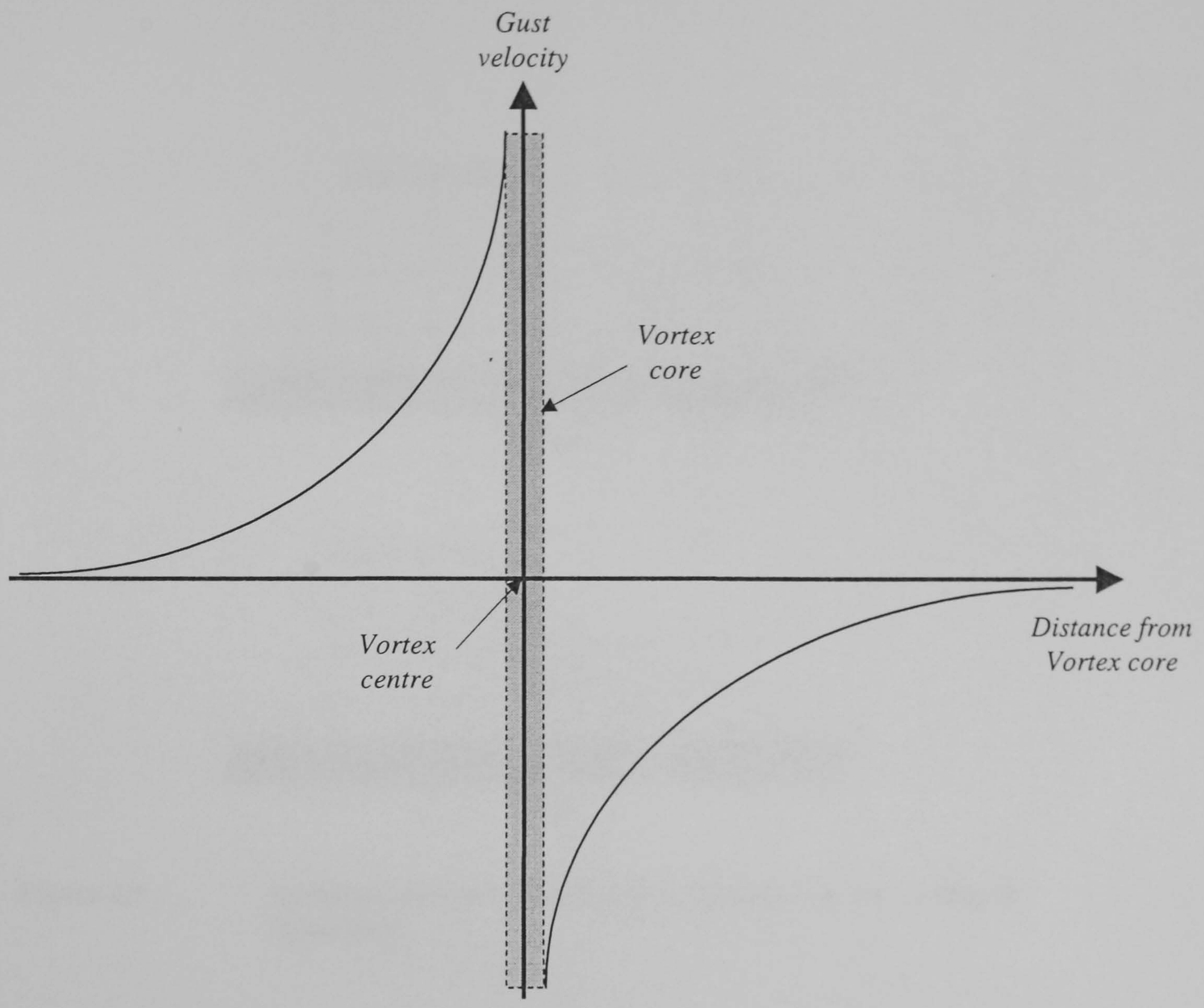

Figure 4.7 : **The velocity distribution through a discrete vortex.**

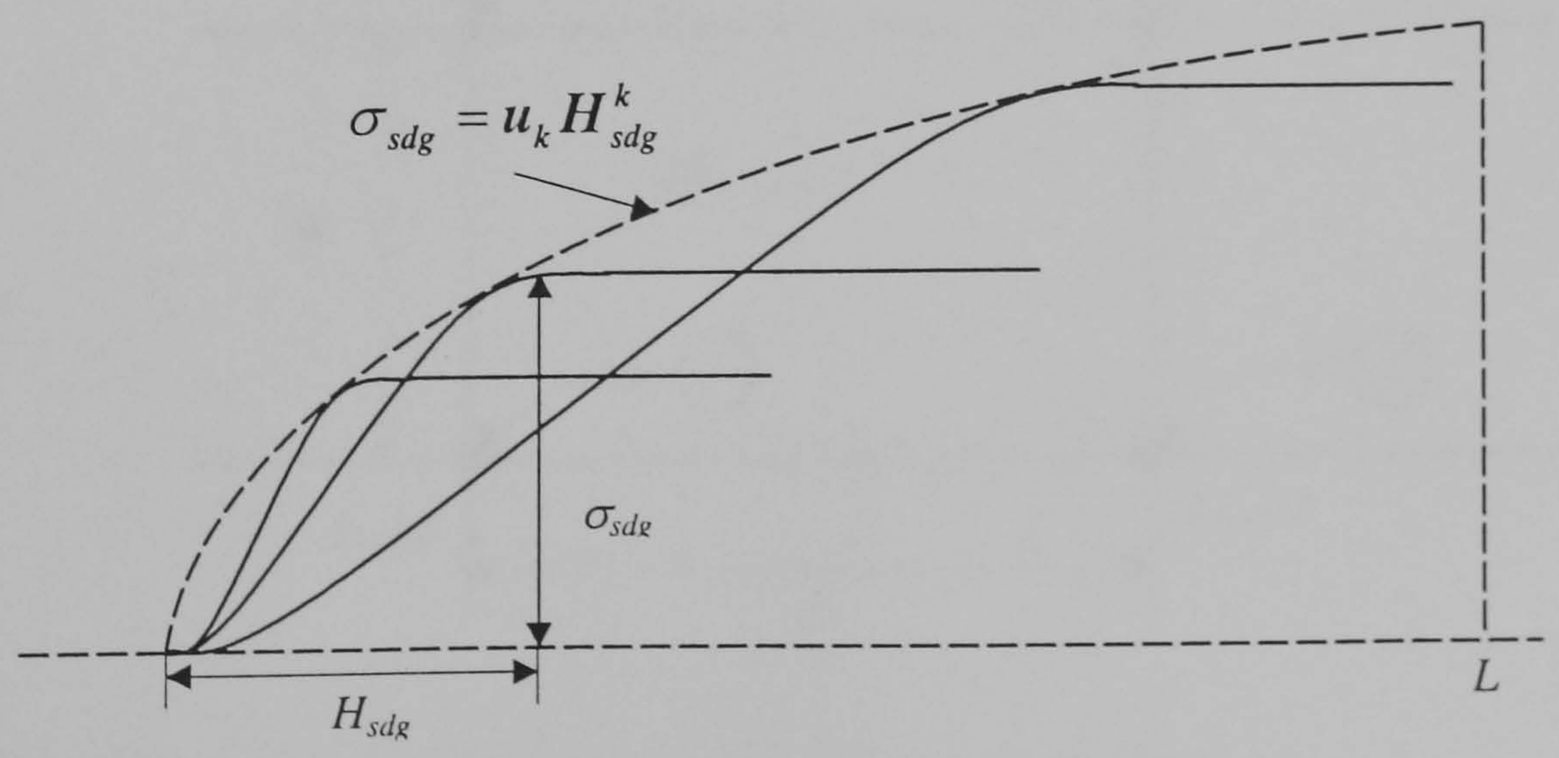

Figure 4.8 : **Family of ramp gusts defined for $H_{sdg}<L$ by u^k.**

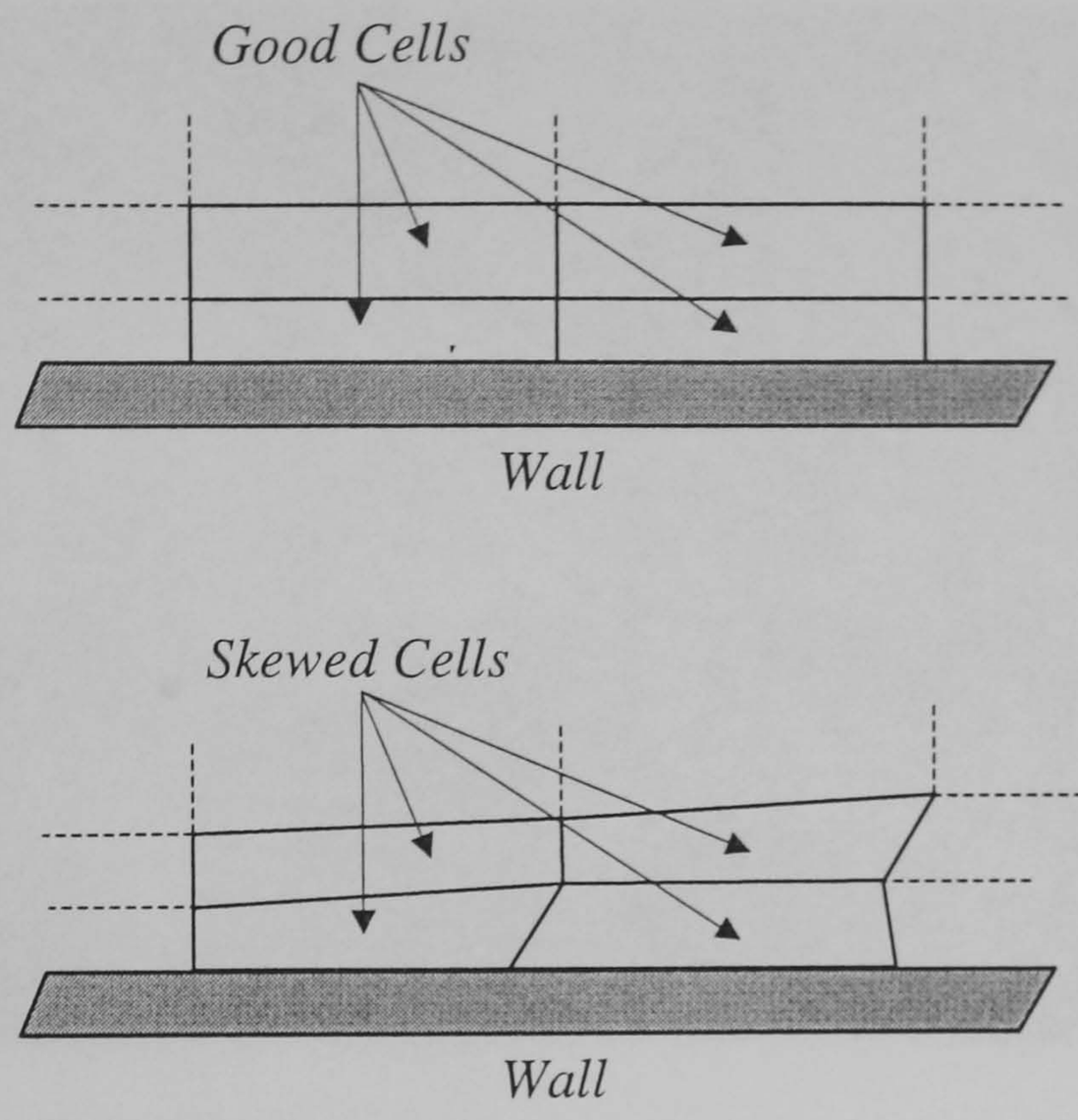

Figure 4.9 : **An illustration of well and poorly constructed near wall grid topologies.**

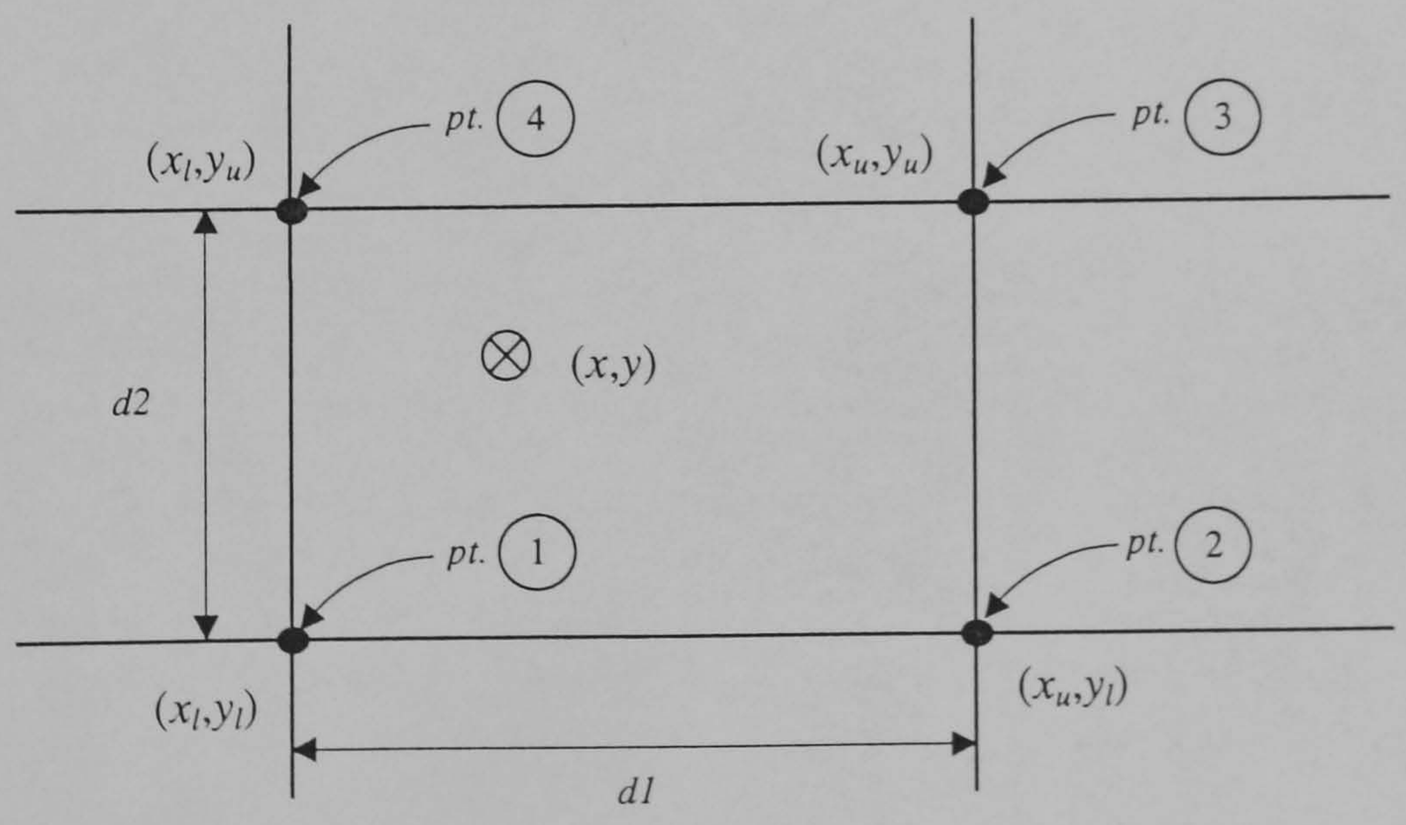

Figure 4.10 : **Labelling of points scheme used in the bilinear interpolation routine.**

(400m,195m)

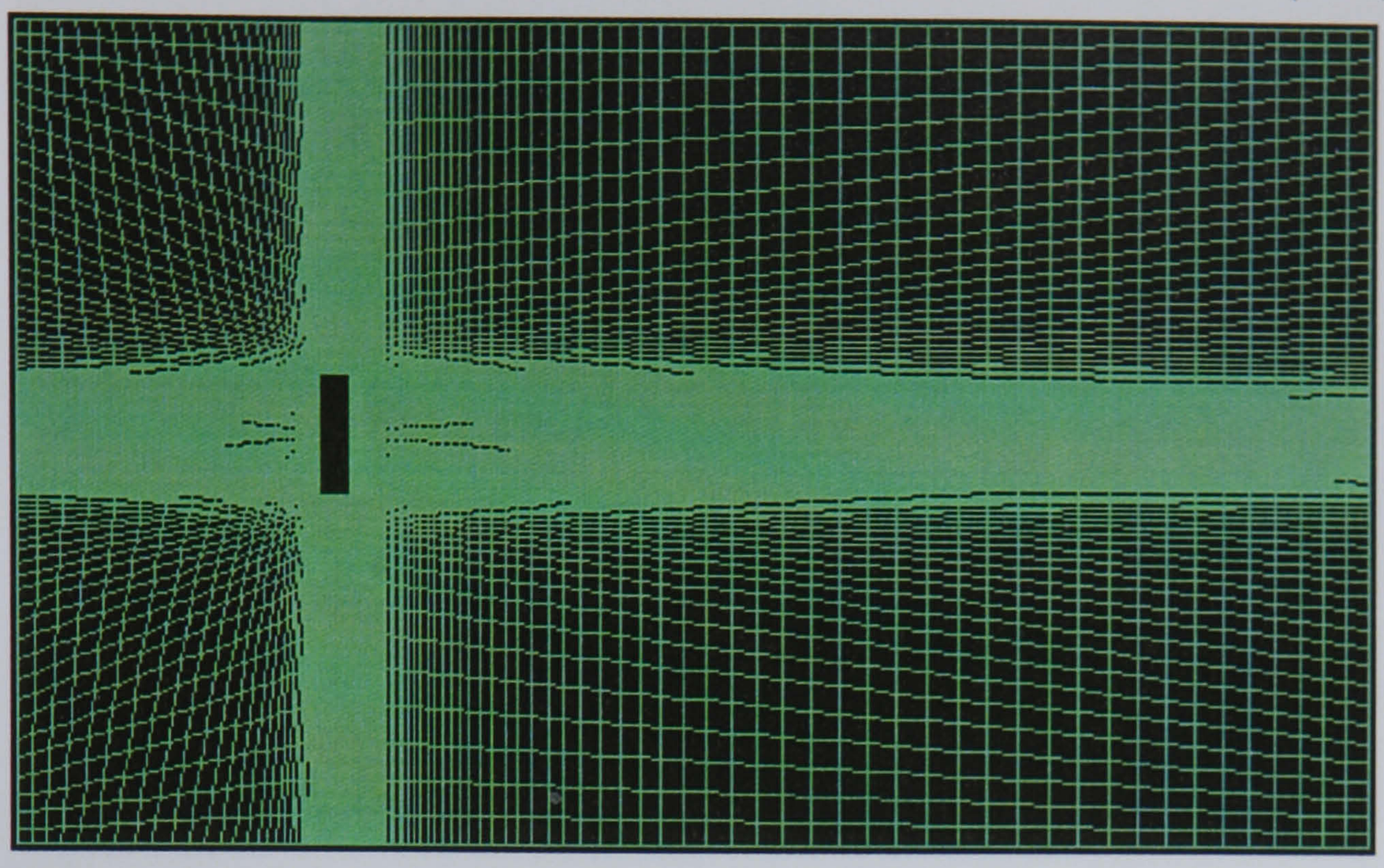

(-50m,-75m)

Figure 4.11 : **The CFD grid used to model flow around a rectangular block. The bottom left corner of the rectangle is located at position (50m, 40m) in the grid.**

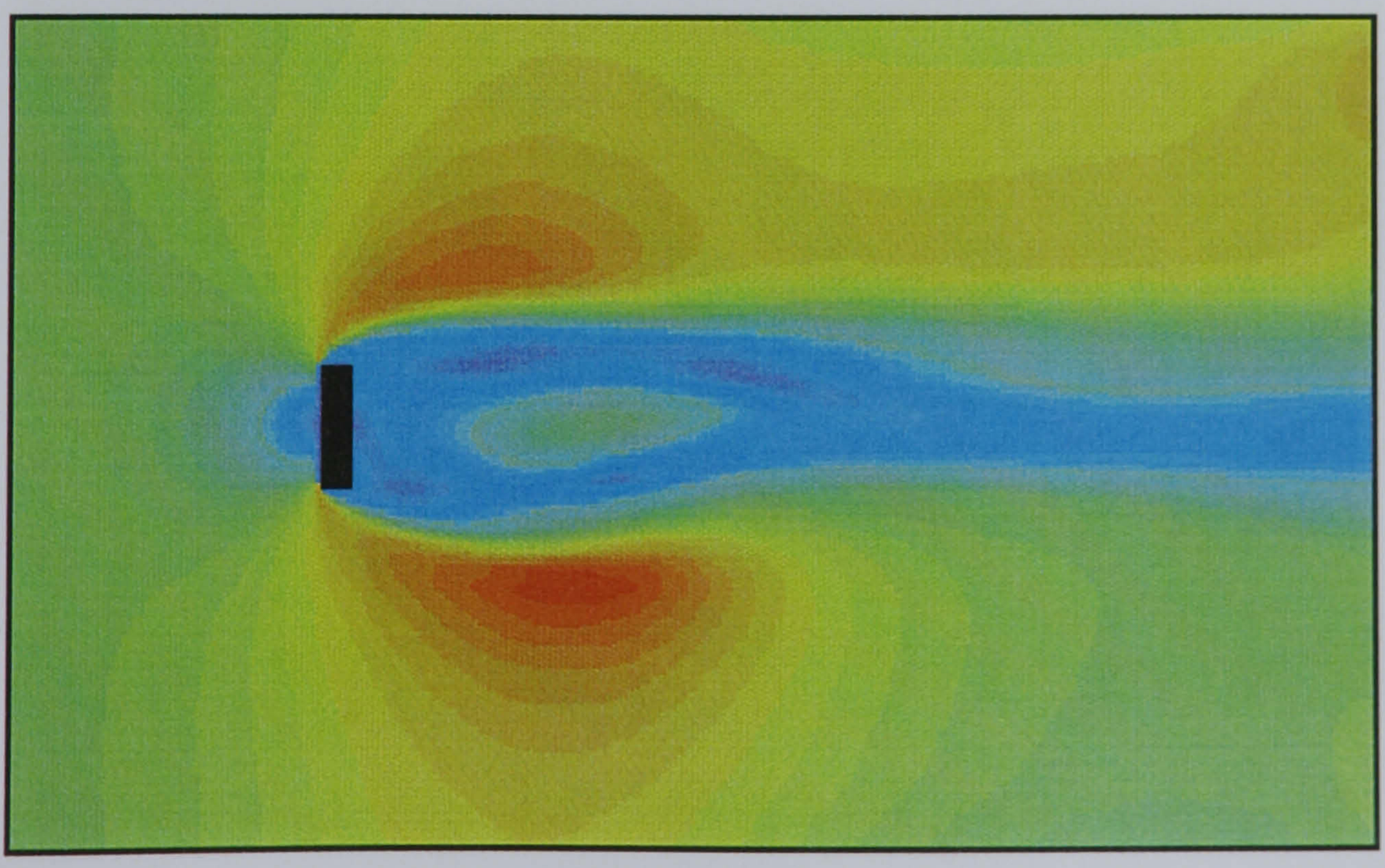

Figure 4.12 : **A contour plot of the velocity magnitude of the flow around a rectangular block.**

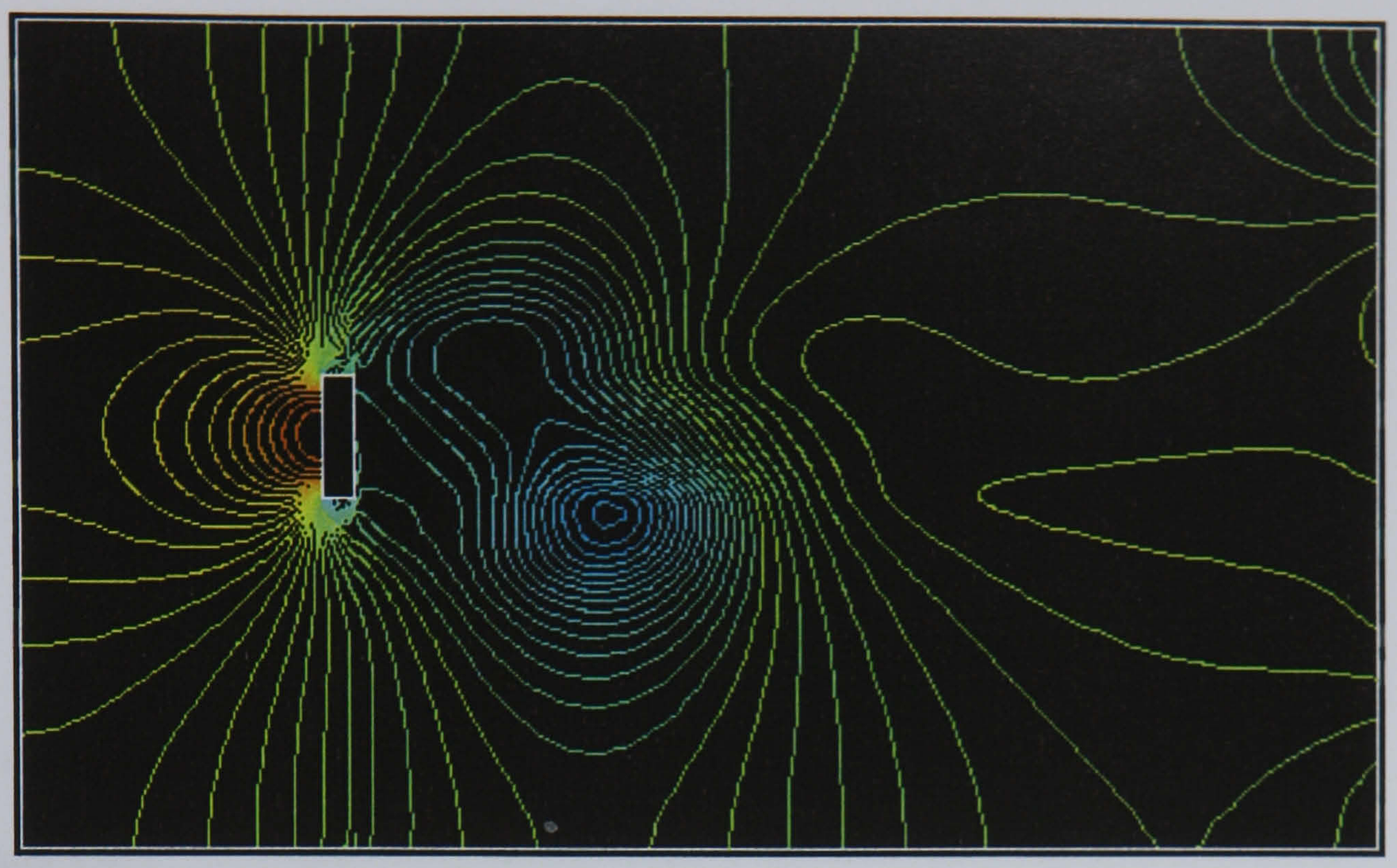

Figure 4.13 : **Pressure distribution contours of the flow around a rectangular tower block (red-high pressure, blue-low pressure).**

Figure 4.14 : **A streamline plot of the flow around a rectangular tower block.**

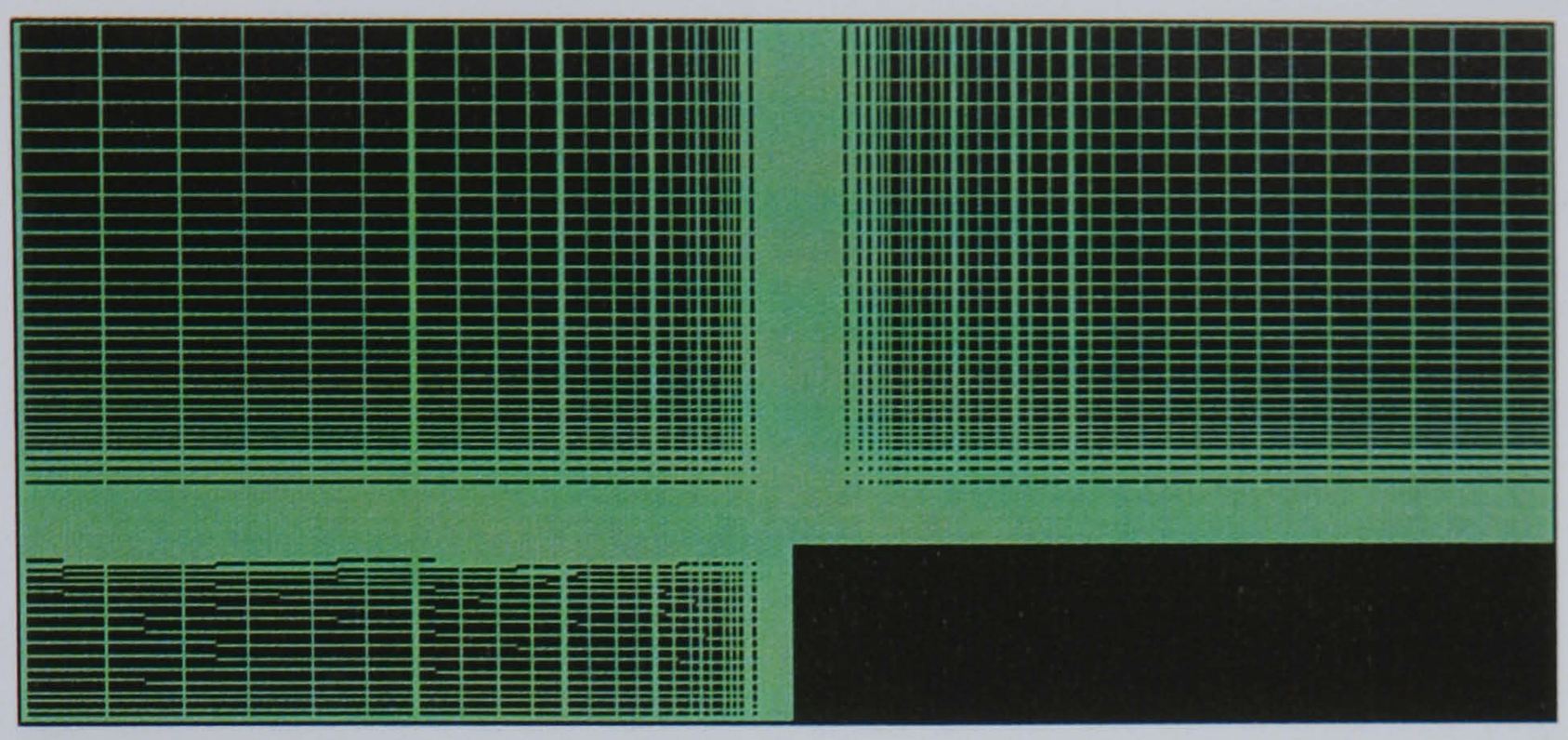

Figure 4.15 : **The CFD grid used to model the flow over a cliff top. The corner of the cliff top is at position (*100m, 50m*) in the grid.**

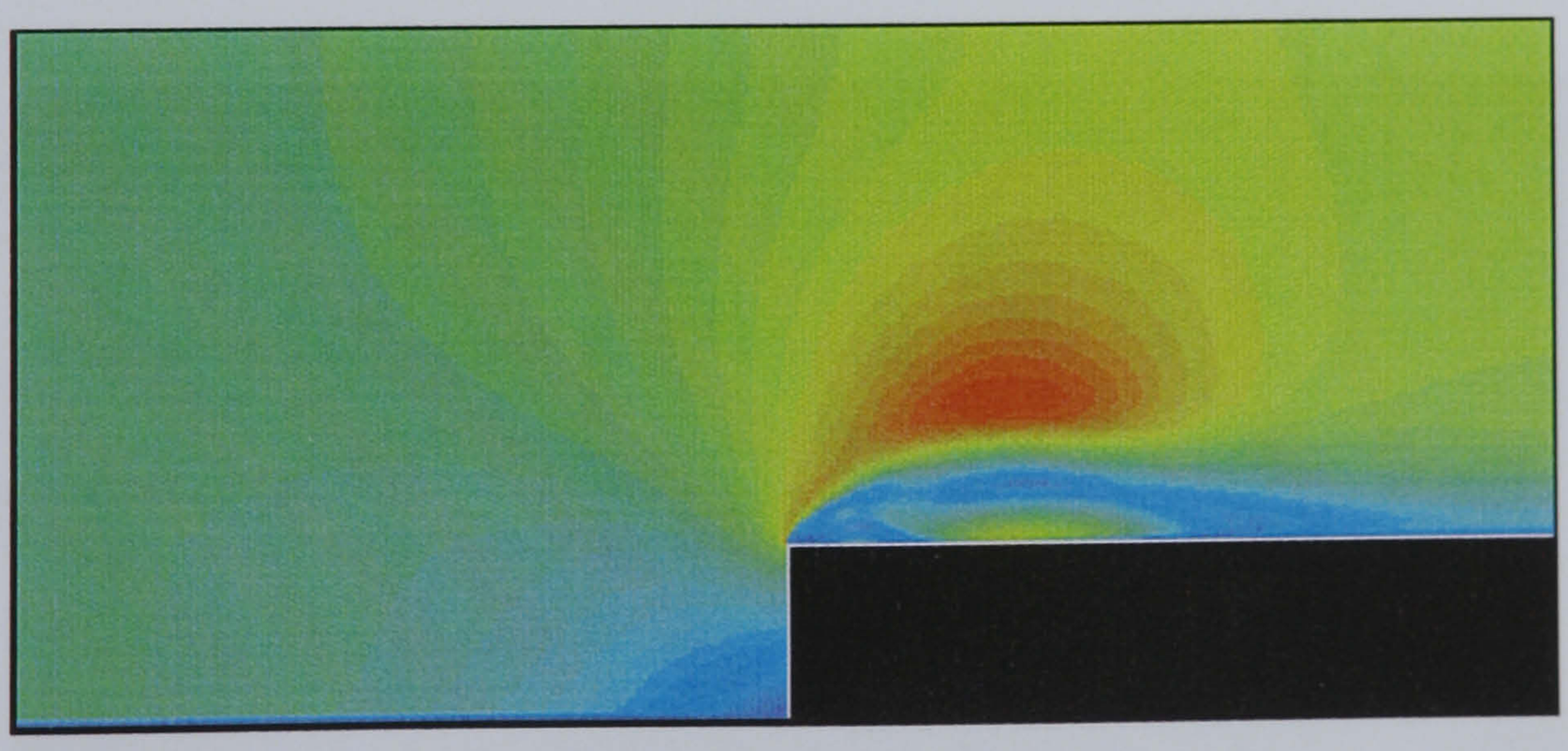

Figure 4.16 : **Velocity magnitude controur plot for the flow over a clifftop Red-high velocity (max 10.6 ms^{-1}) to dark blue-low velocity (min 0ms^{-1}) .**

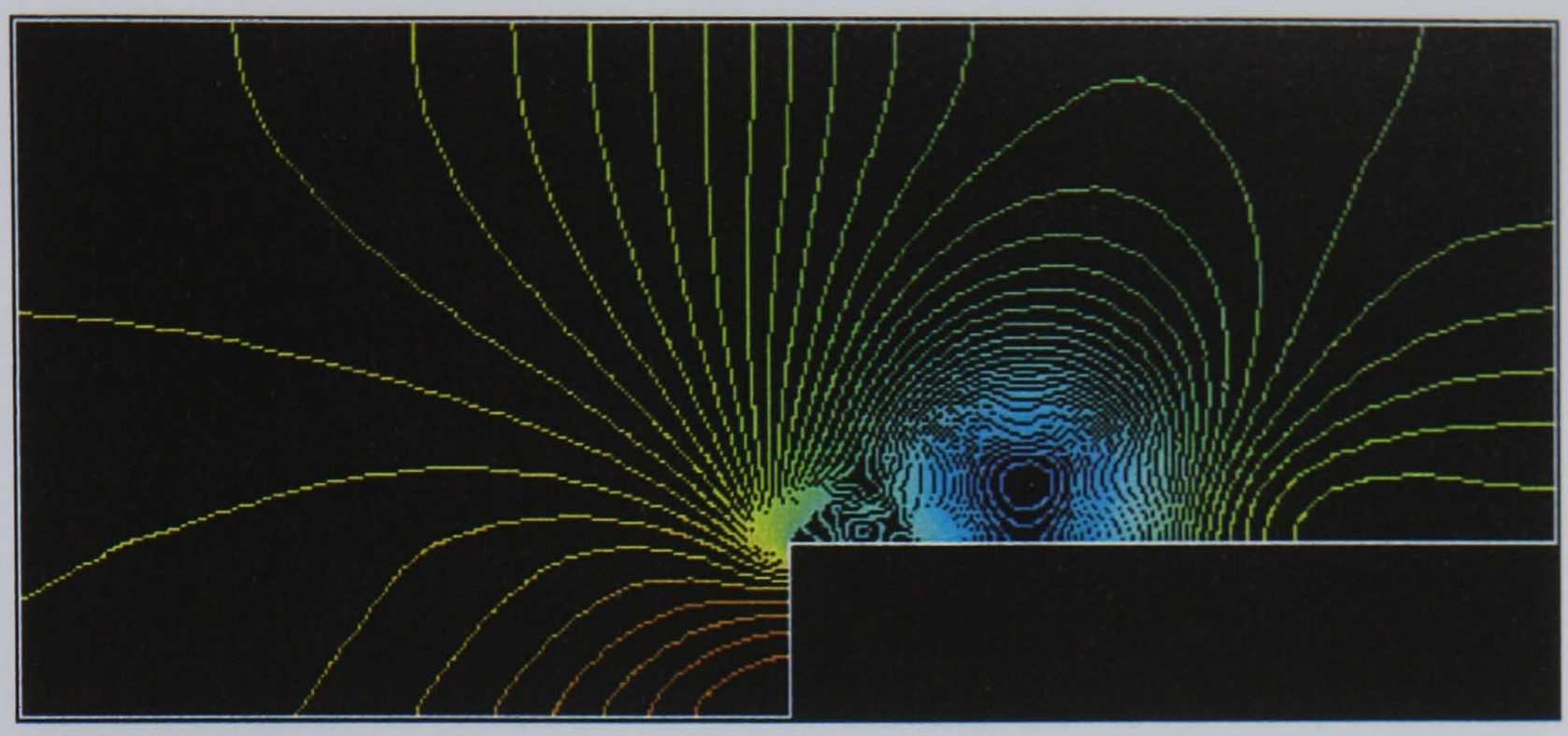

Figure 4.17 : **Pressure distribution contour plot for the flow over a clifftop. (Red - high pressure. Blue - low pressure).**

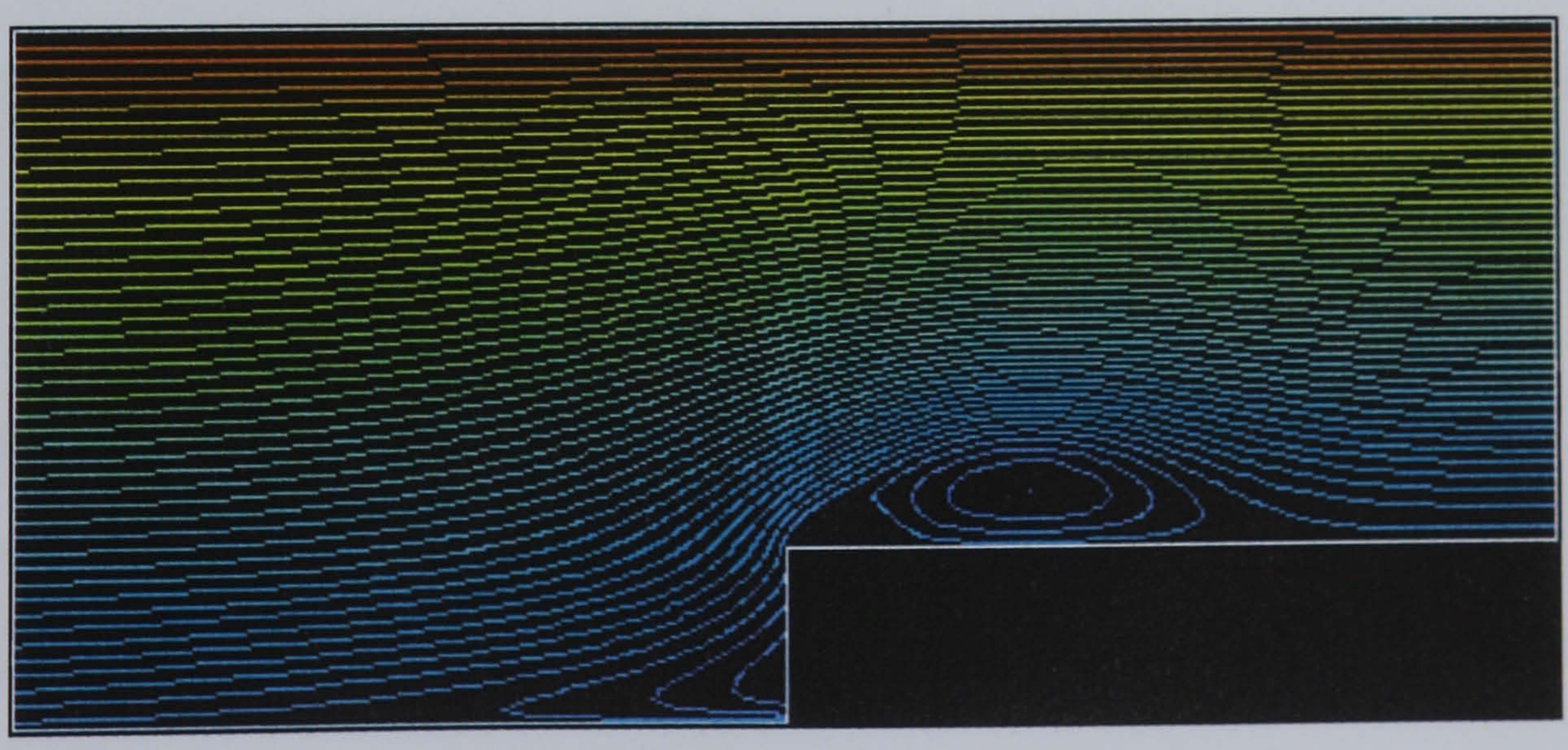

Figure 4.18 : **Streamline contours for flow over a clifftop, showing the vortex on the upper surface near to the cliff edge.**

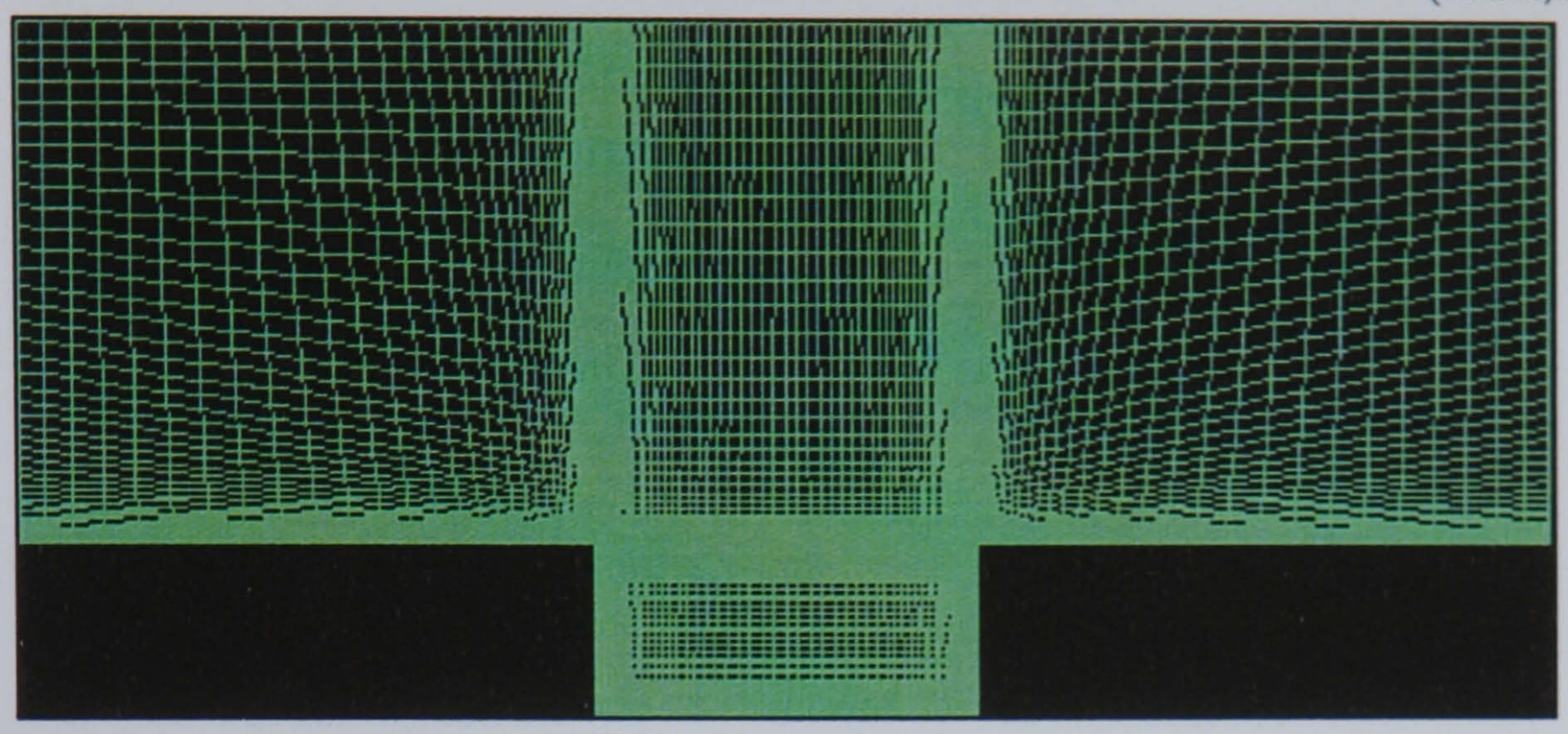

Figure 4.19 : **Grid generated for modelling the flow across a valley. The valley is *100m* wide x *50m* deep.**

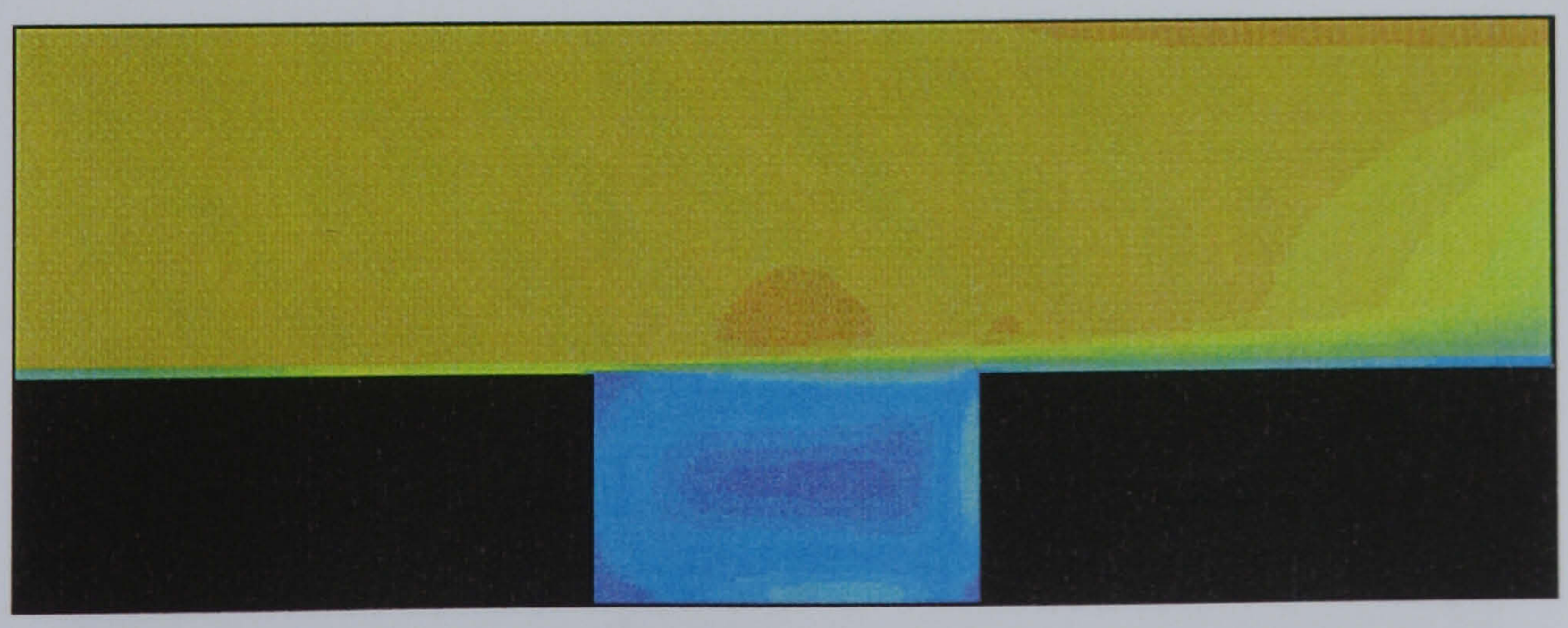

Figure 4.20 : **Contour of velocity magnitudes for the flow across a valley. The velocity ranges from 6.05 ms^{-1} (dark orange) to $0ms^{-1}$ (dark blue) at the walls.**

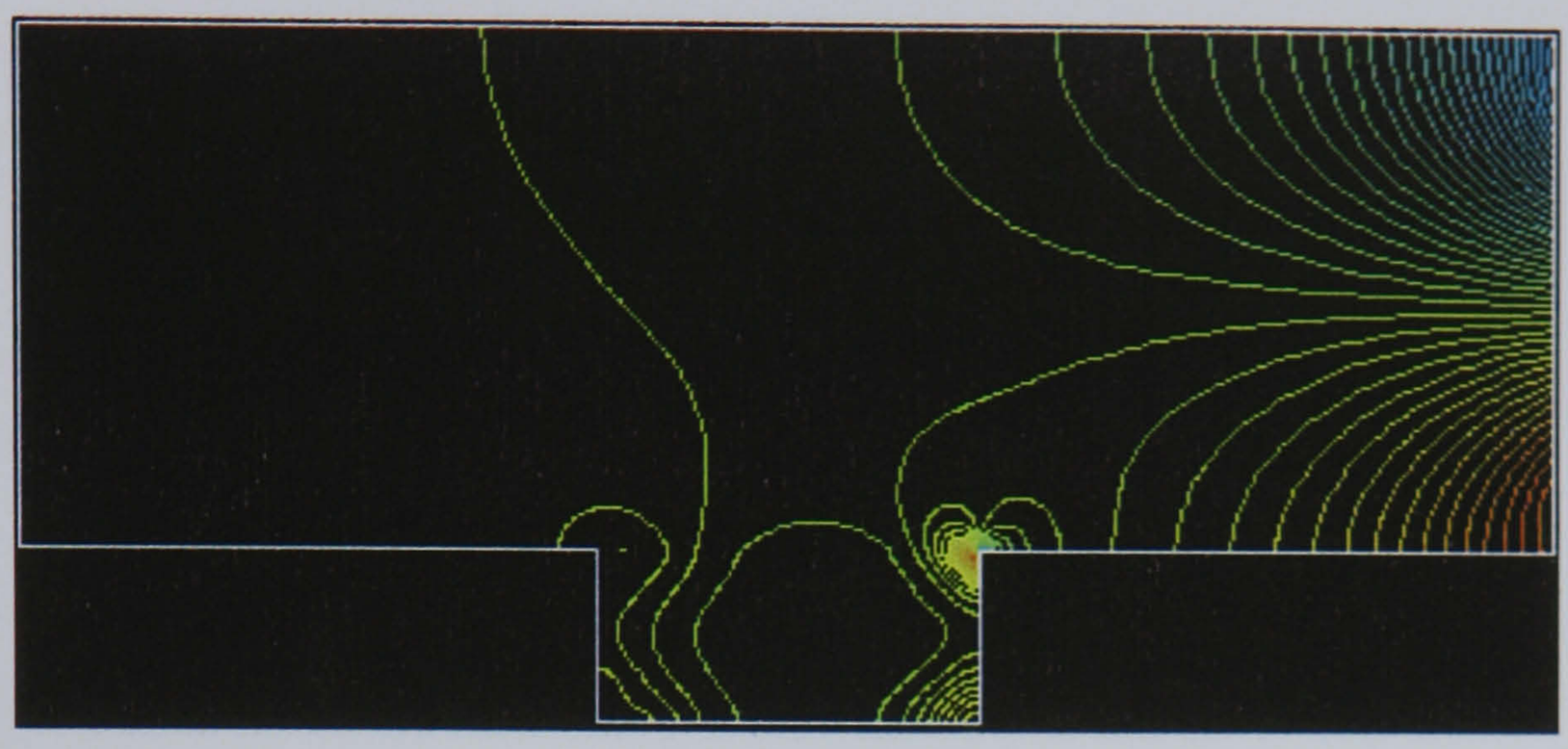

Figure 4.21 : **Pressure contours of the flow across a valley. (Red - high pressure. Blue - low pressure).**

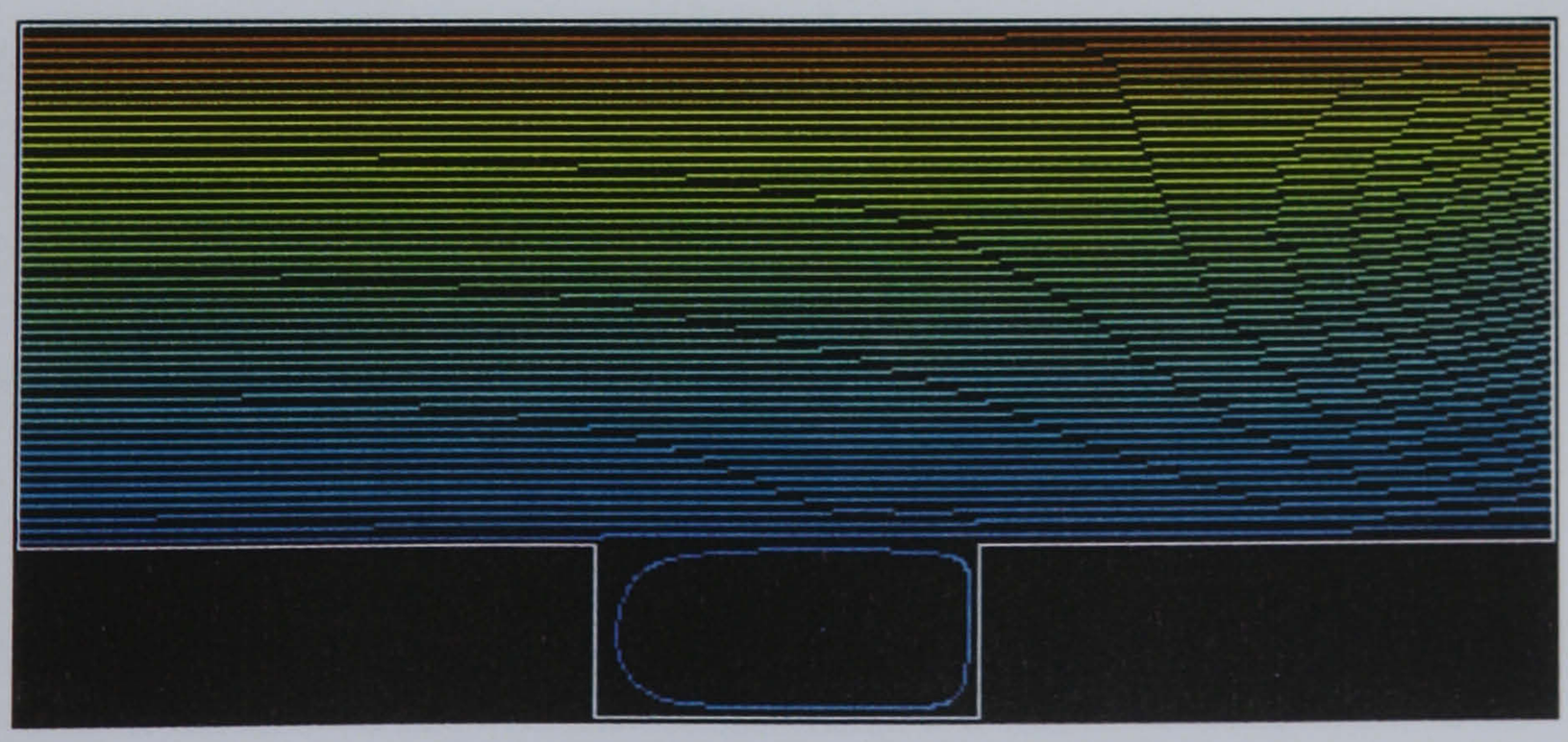

Figure 4.22 : **Stream function contour plot for the flow across a valley. Note the benign vortex which fills the valley centre.**

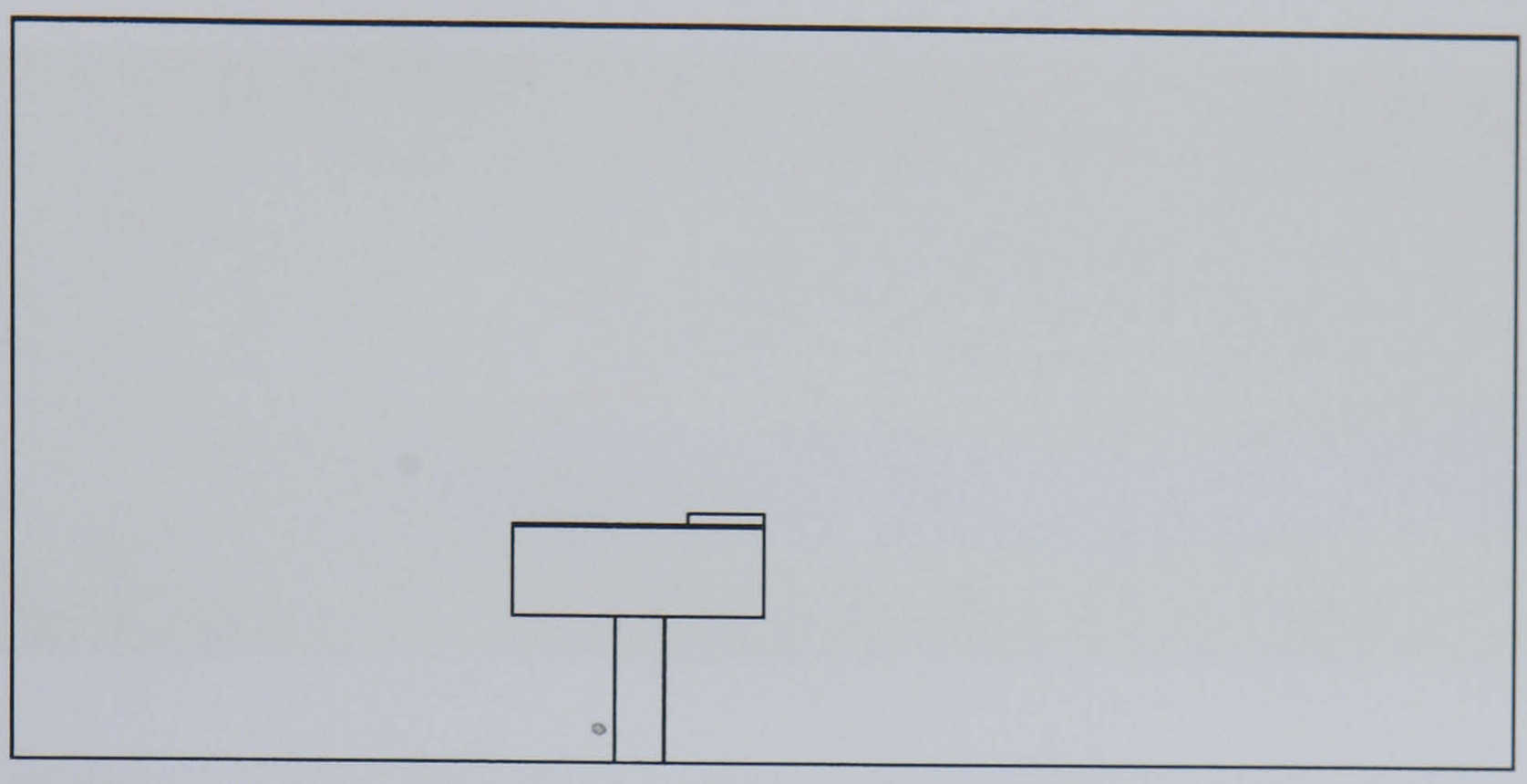

Figure 4.23 : **The geometry of Brent Charlie North sea rig.**

(600m,250m)

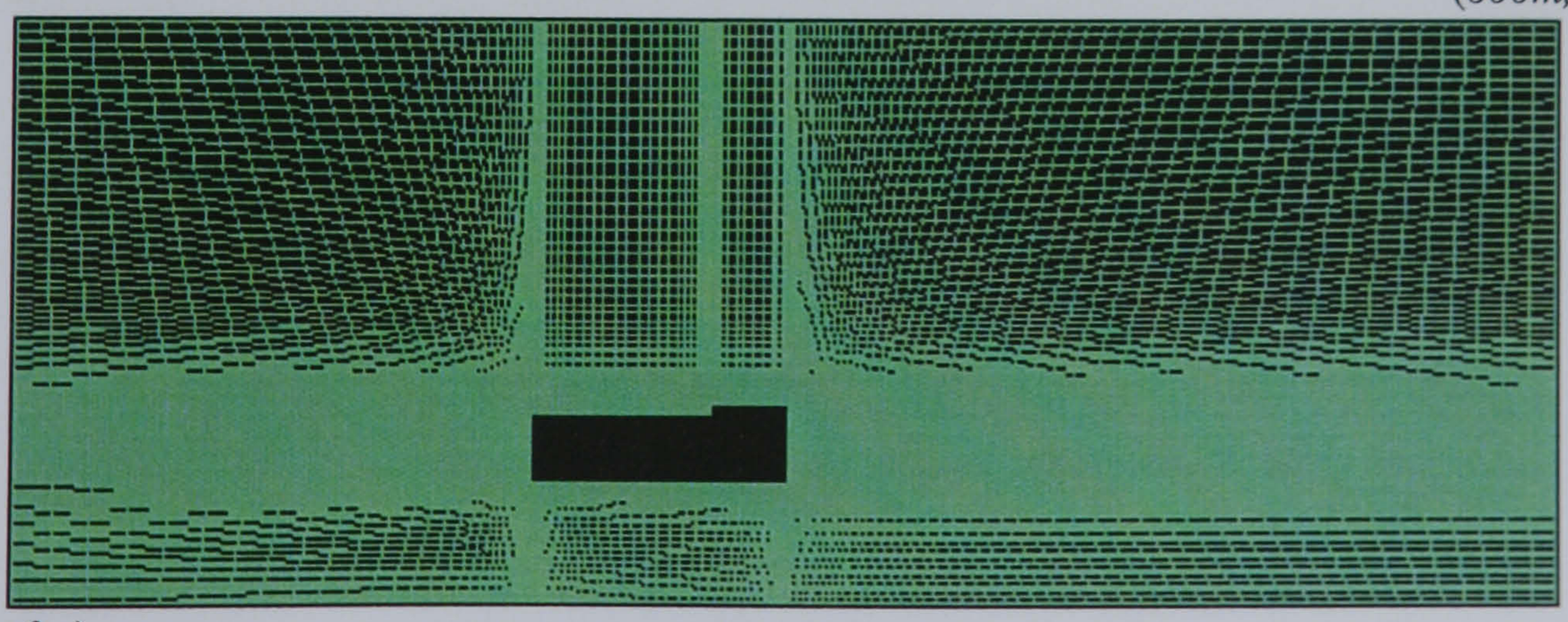

(0m,0m)

Figure 4.24 : **CFD Grid around an offshore oil platform (unsupported rig variant).**

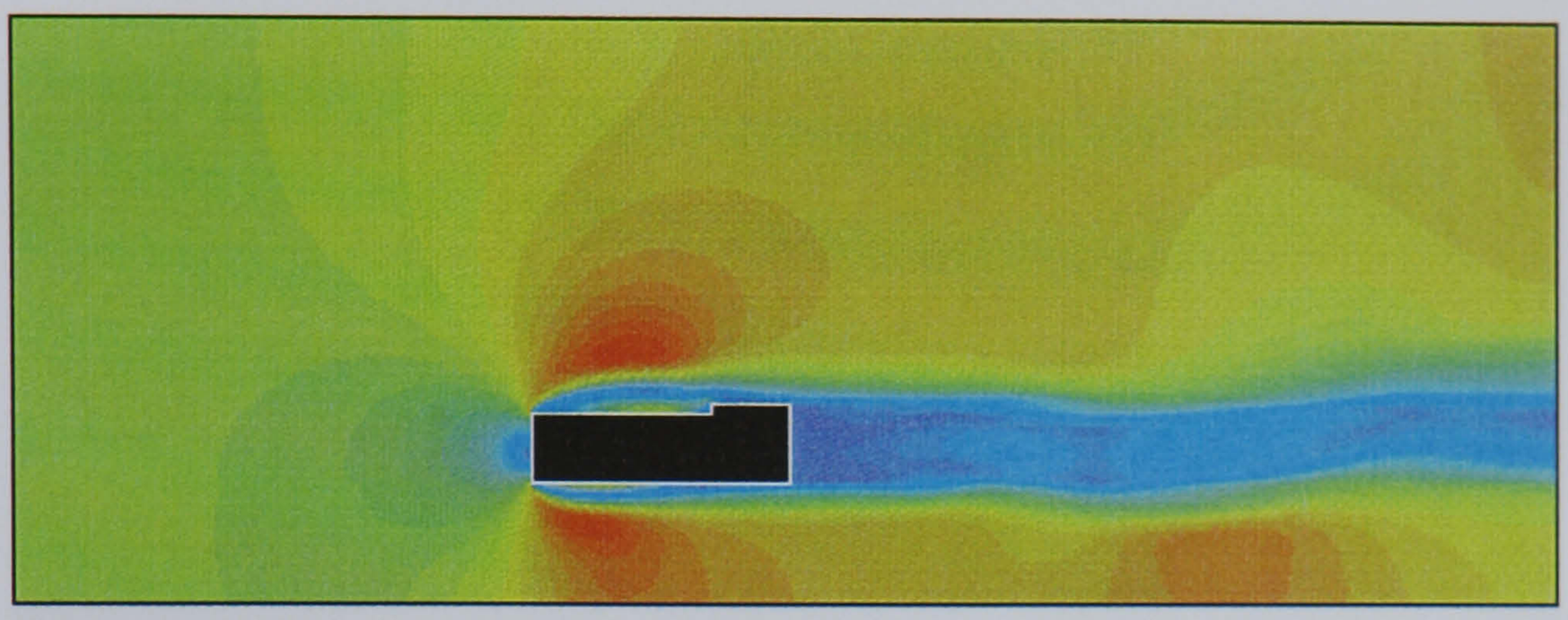

Figure 4.25 : **Velocity magnitude contours of flow around an offshore oil platform (unsupported rig variant). The velocity ranges from 7.74 ms^{-1} (dark red) to 0ms^{-1} (dark blue).**

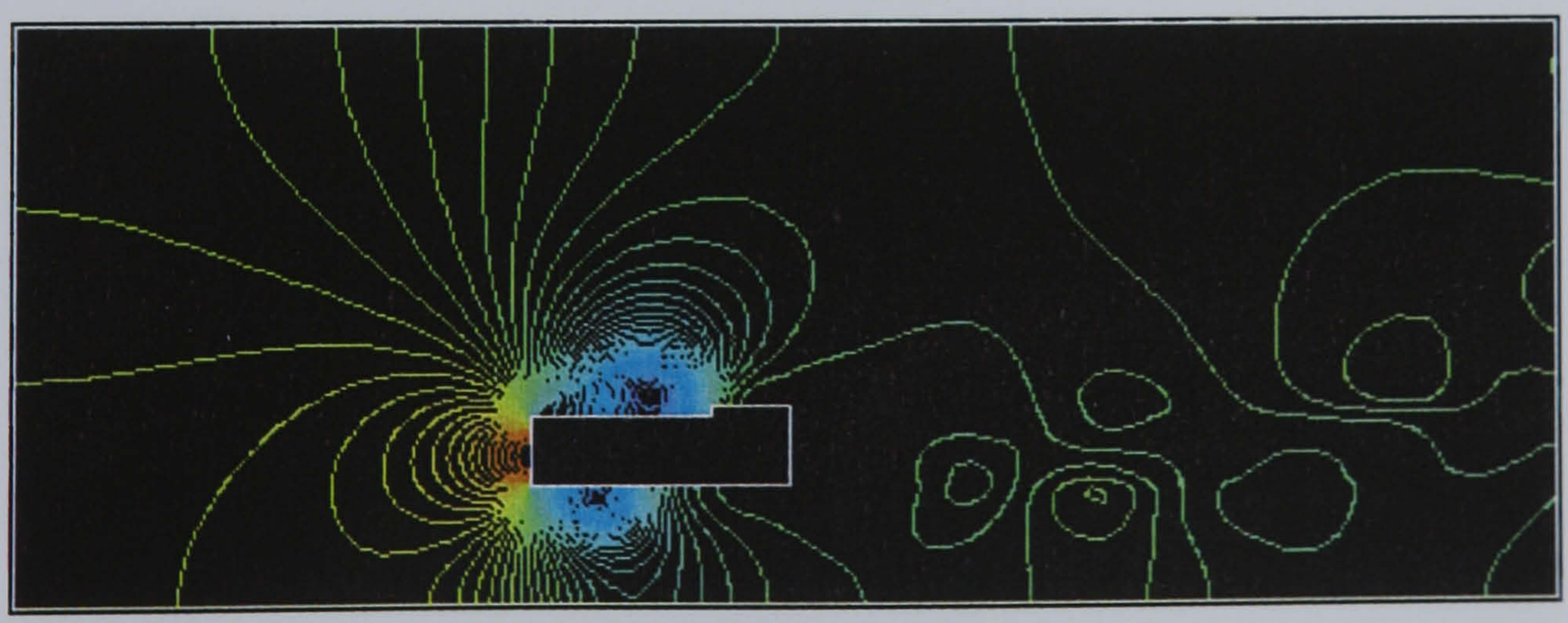

Figure 4.26 : **Pressure contours of flow around an offshore oil platform (unsupported rig variant). (Red - high pressure. Blue - low pressure).**

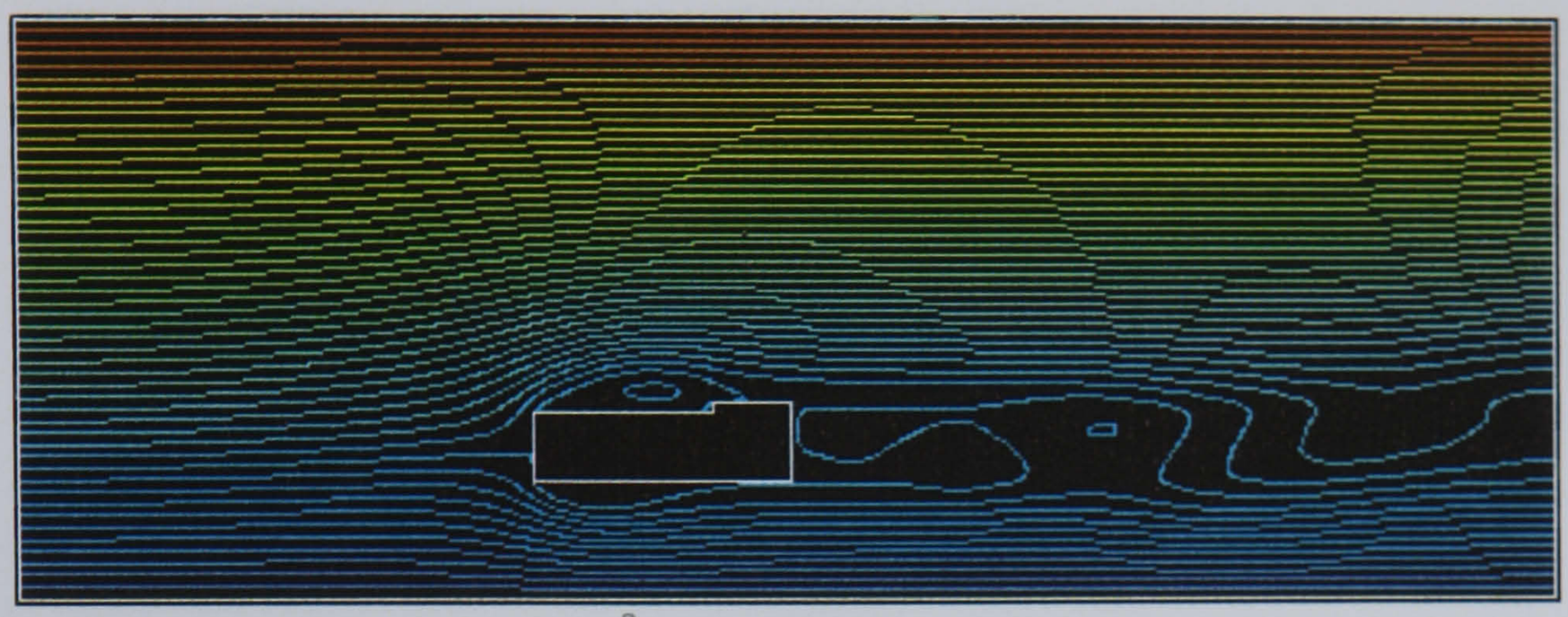

Figure 4.27 : **Stream function of flow around an offshore oil platform (unsupported rig variant).**

(600m,250m)

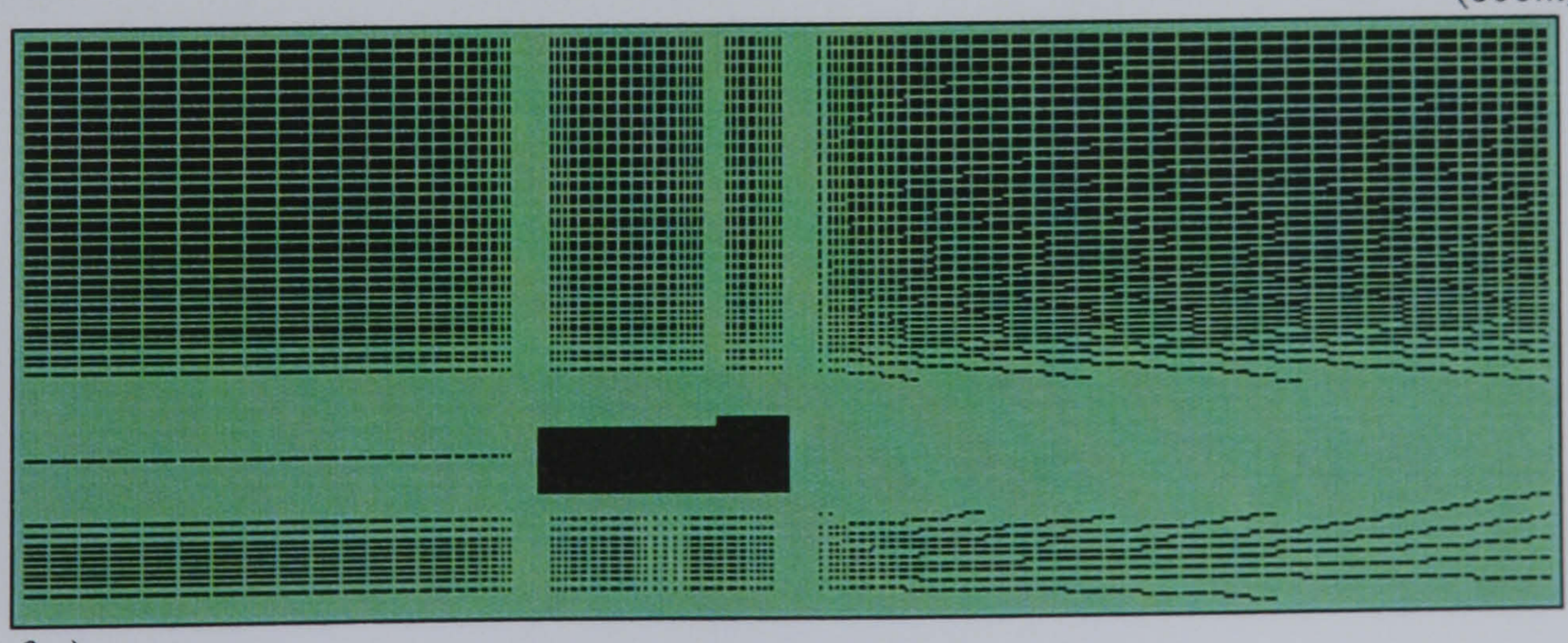

(0m,0m)

Figure 4.28 : **CFD Grid around an offshore oil platform (supported rig variant).**

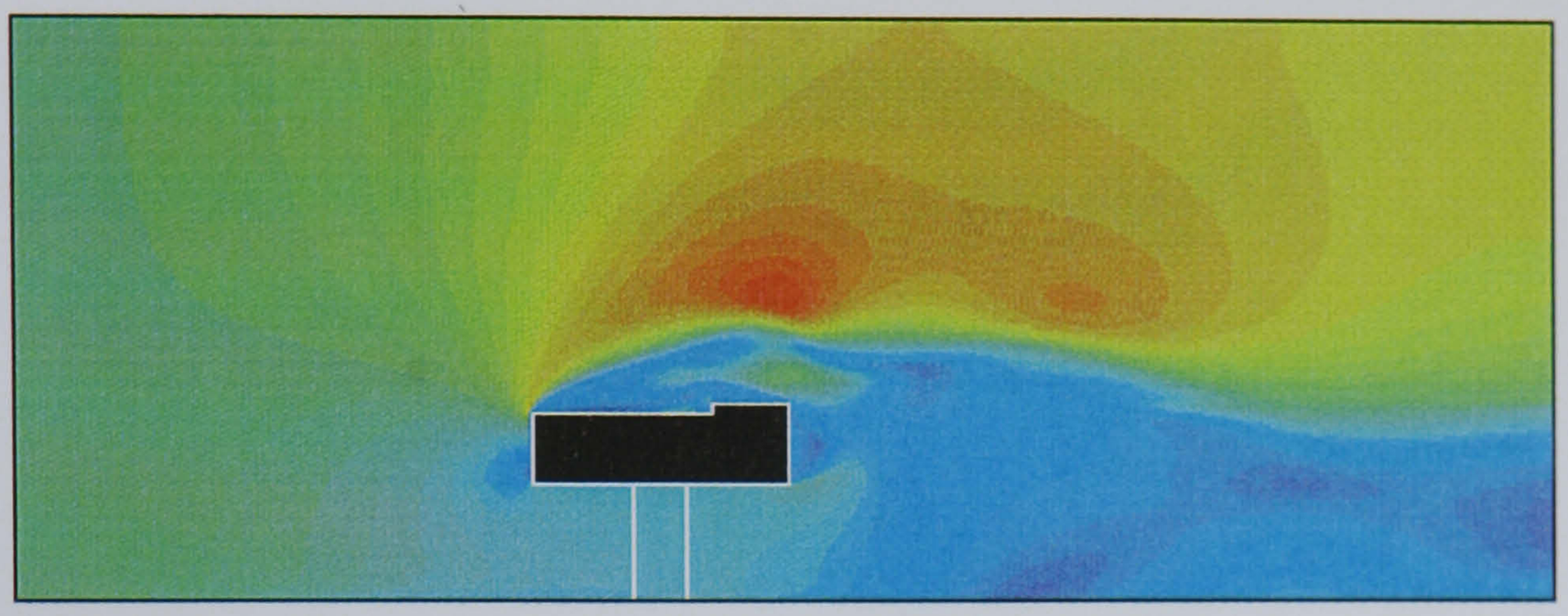

Figure 4.29 : **Contours of velocity magnitude around an offshore oil platform (supported rig variant). Velocity ranges between 10.1ms^{-1} max (dark red) and 0ms^{-1} (dark blue).**

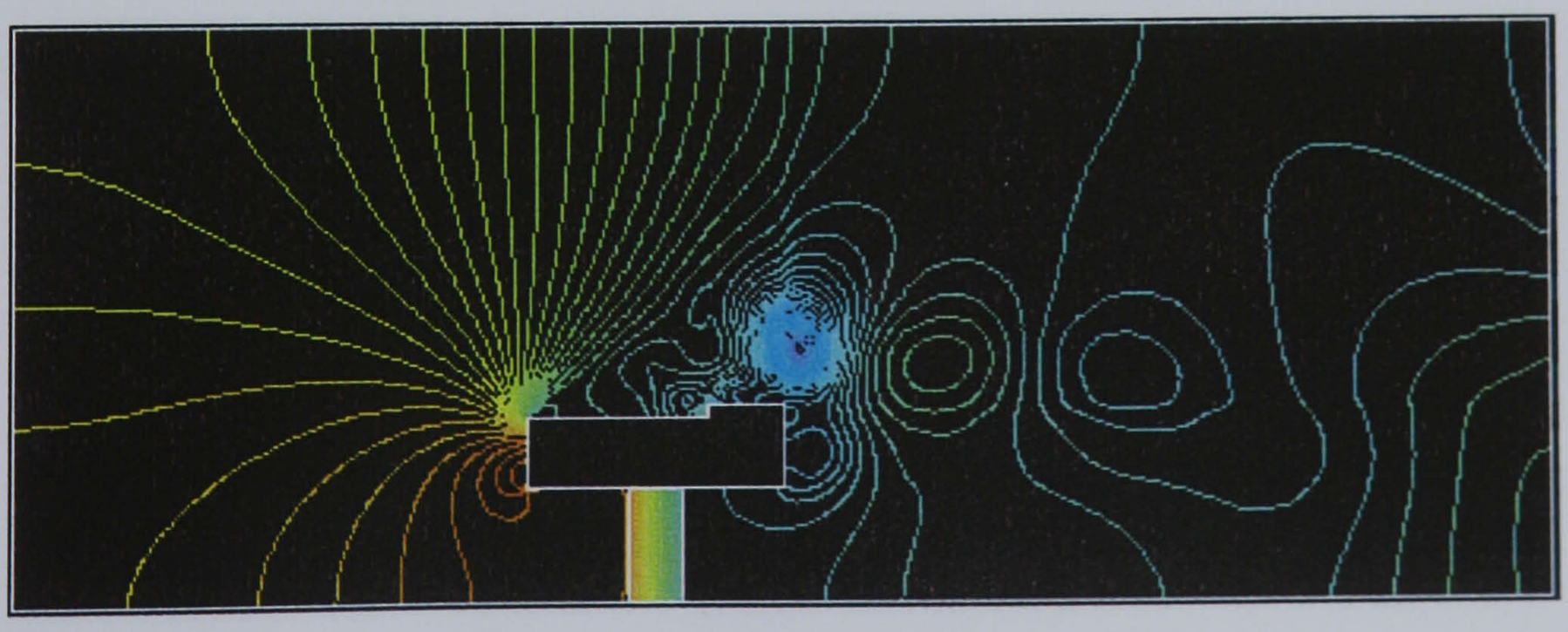

Figure 4.30 : **Pressure contours for the flow around an offshore oil platform (supported rig variant). High pressure - Red, low pressure - Blue. Note the intense vortex above the helideck.**

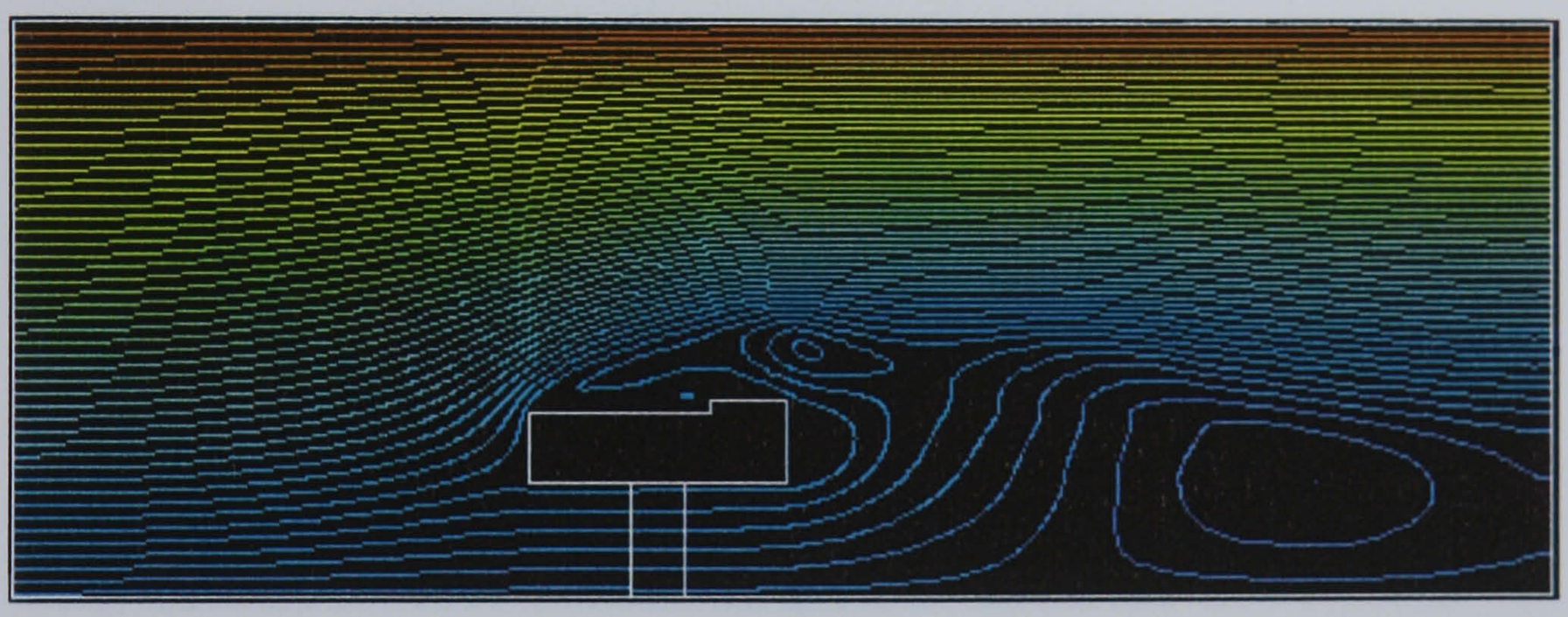

Figure 4.31 : **Stream function for the flow around an offshore oil platform (supported rig variant).**

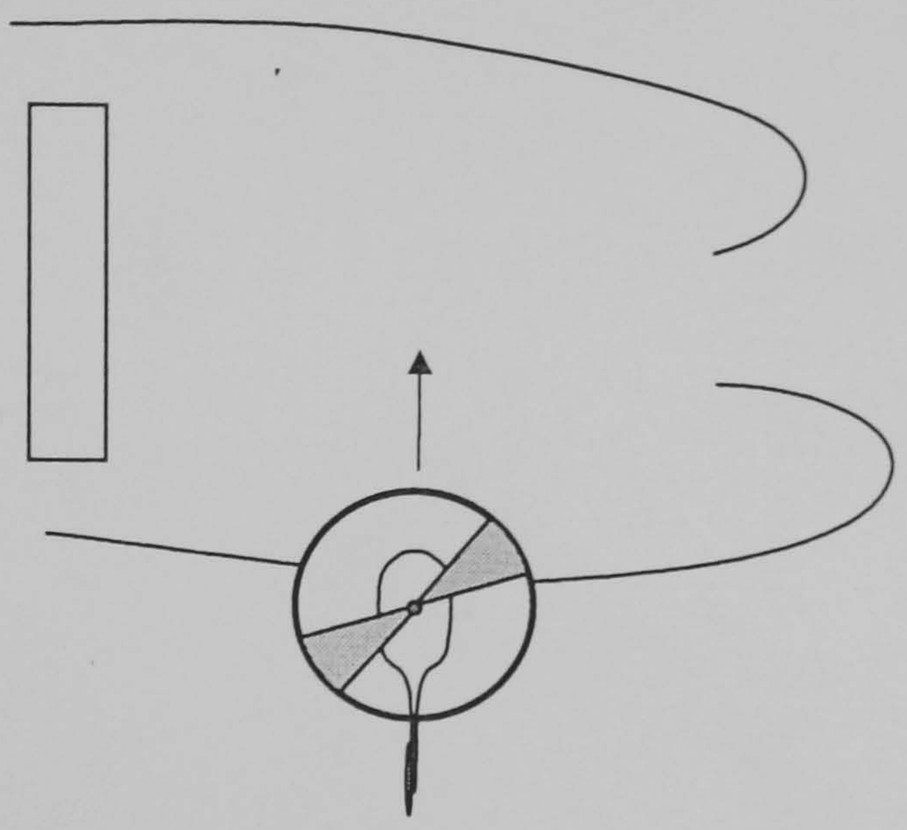

Figure 4.32 : **The initial trim condition for the flight past a tower block example.**

Figure 4.33 : **The starting point and direction of flight for the flight over a cliff top example.**

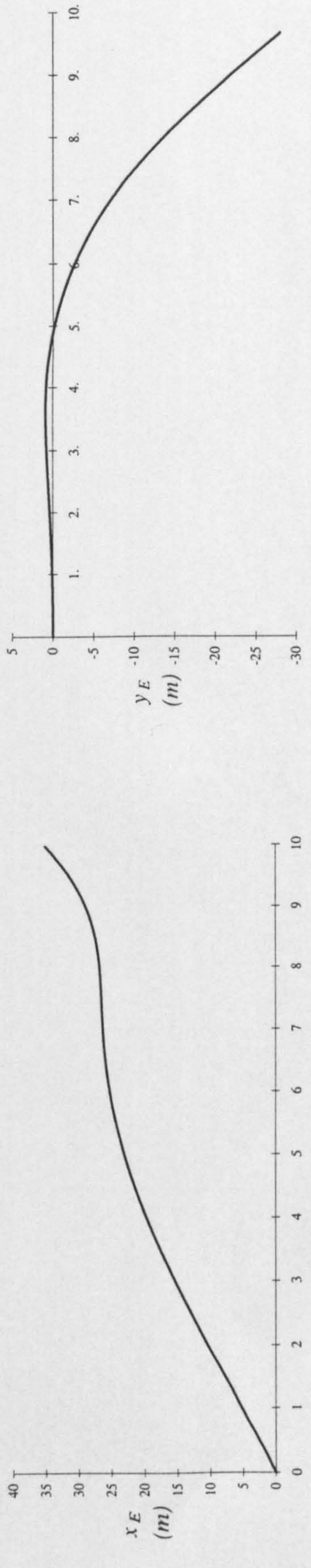

Figure 4.34 : Ground track position for simulated flight past a tower block.

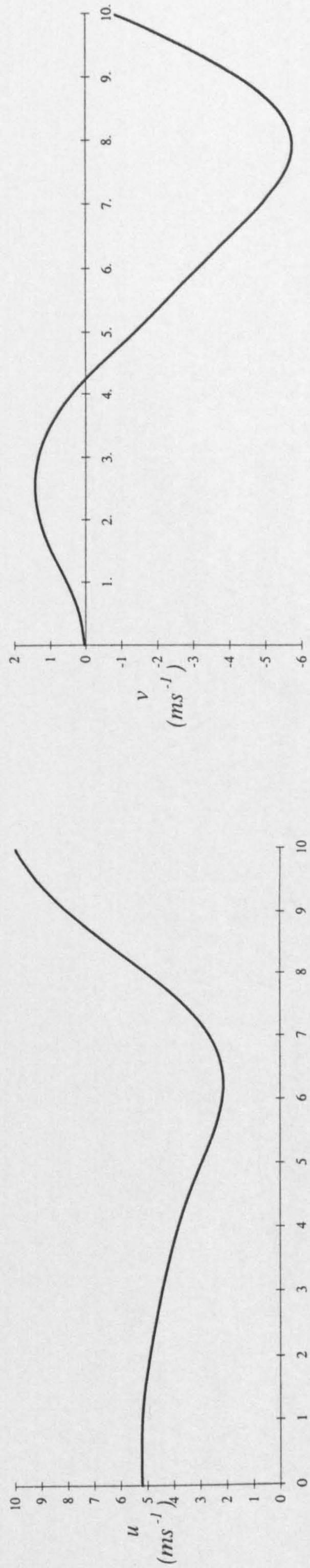

Figure 4.35 : Body axes velocity for simulated flight past a tower block.

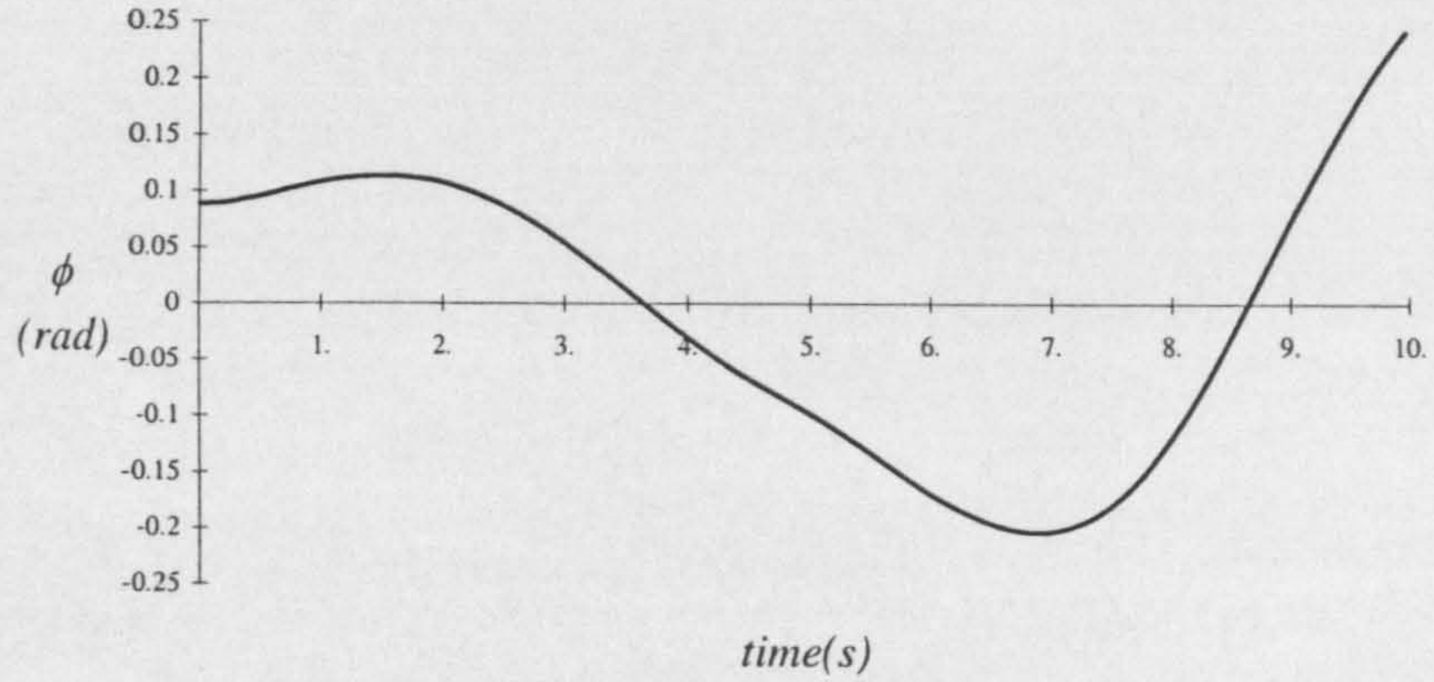

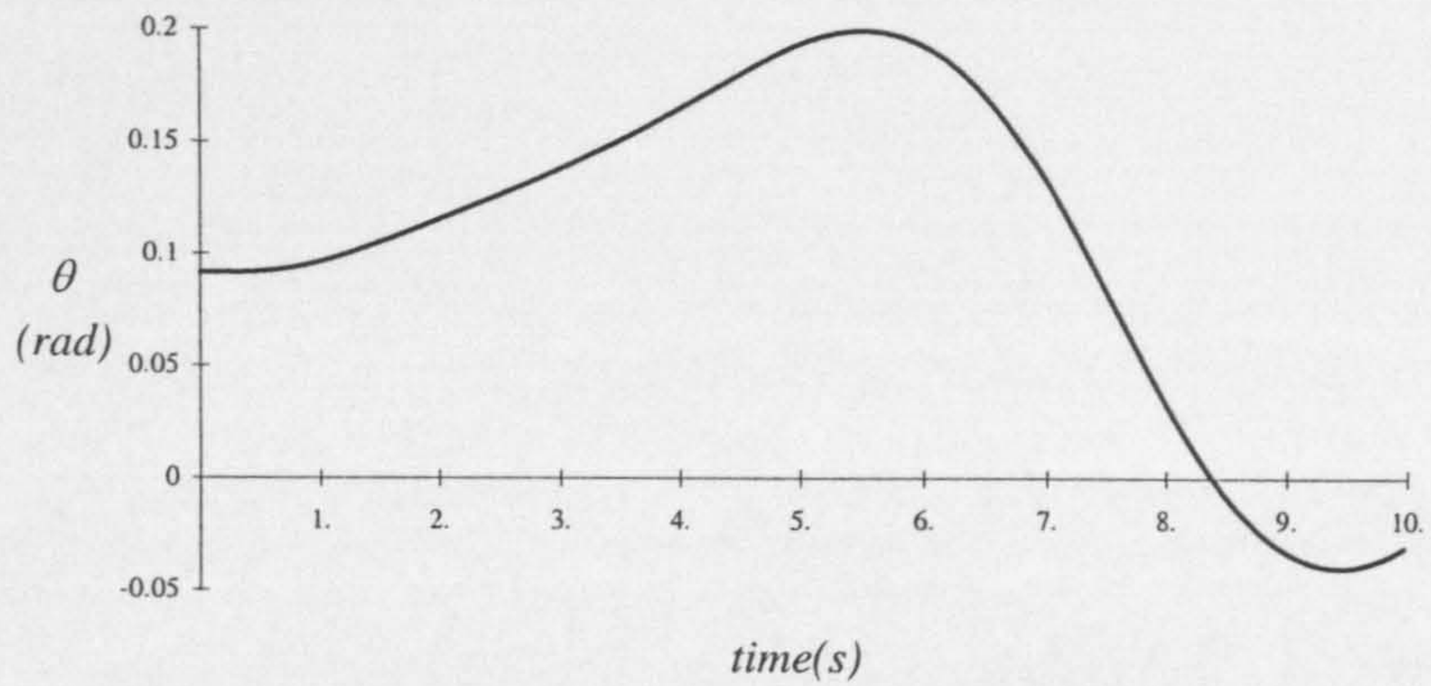

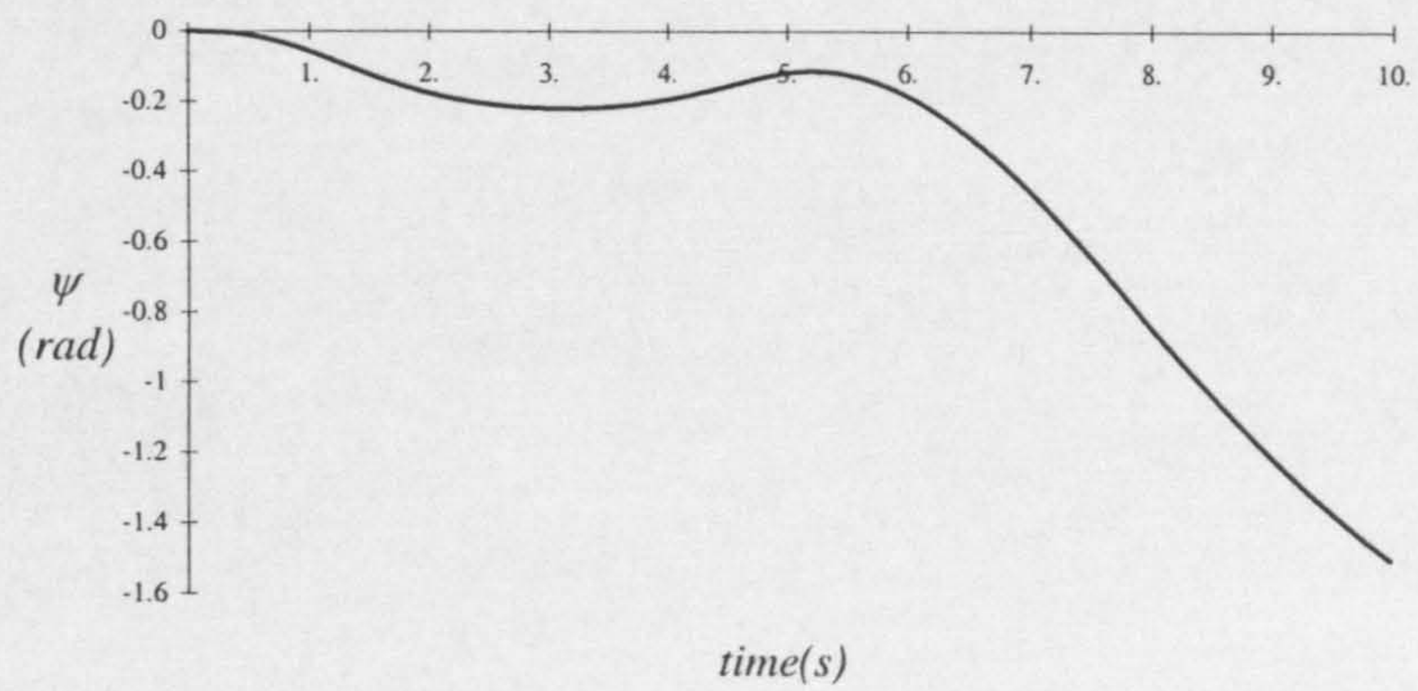

Figure 4.36 : Time histories of the Euler angles for simulated flight past a tower block.

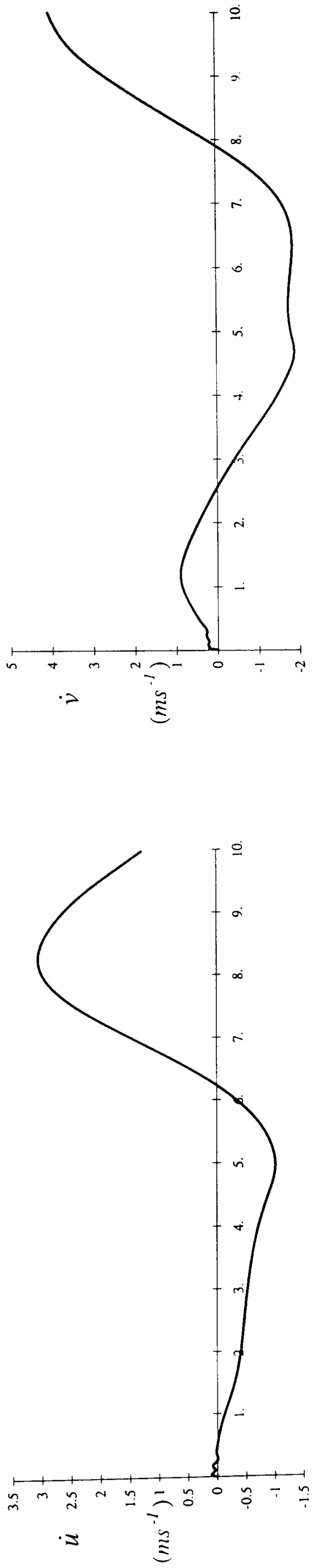

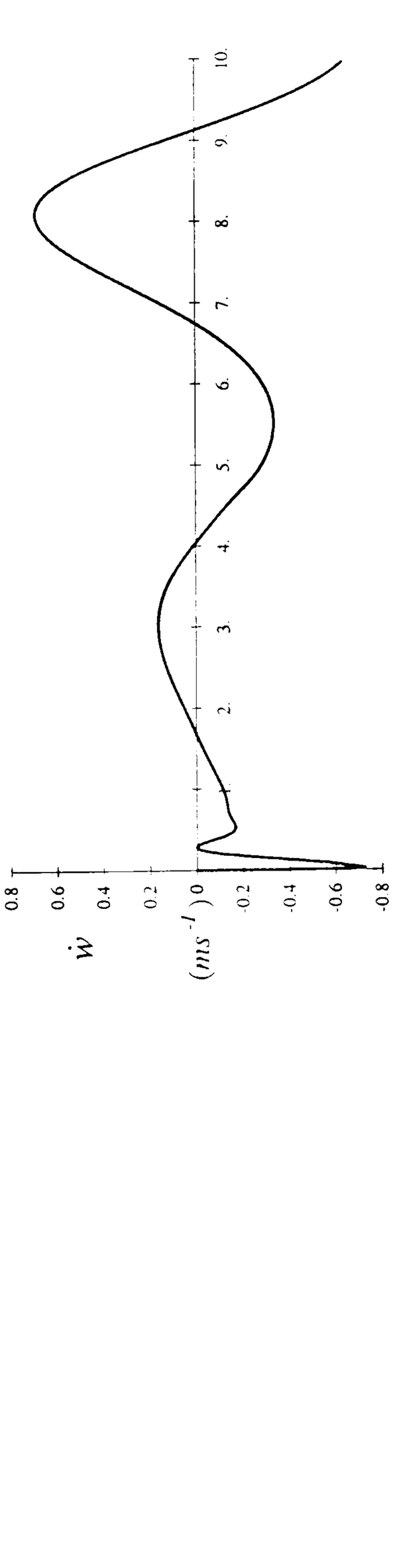

Figure 4.37 : Body axes accelerations for simulated flight past a tower block.

Figure 4.38 : Ground track positions for simulated flight over a cliff top.

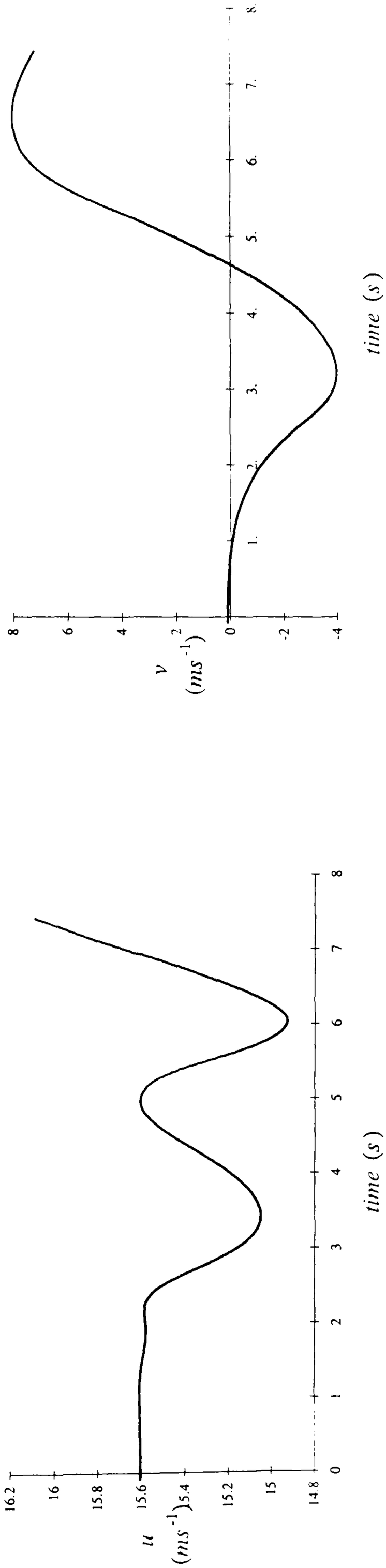

Figure 4.39 : Body axes velocities during simulated flight over a cliff top.

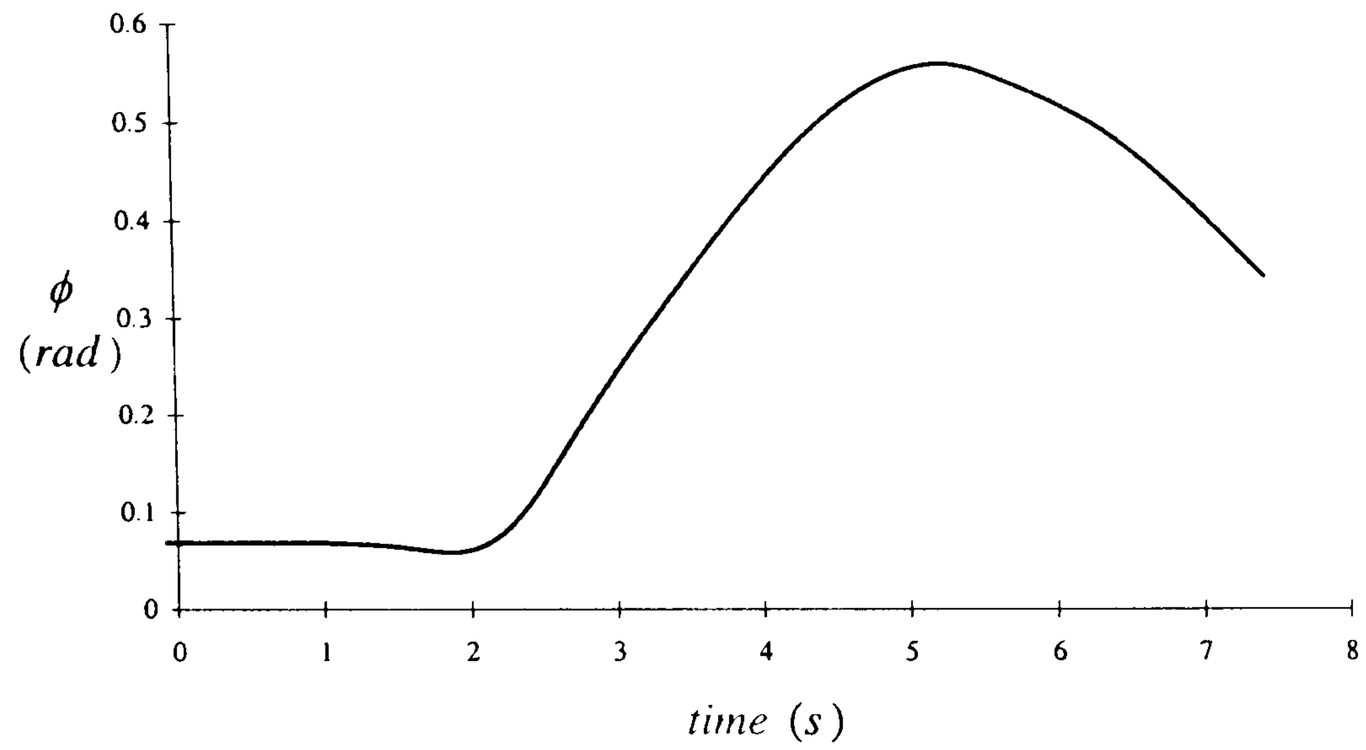

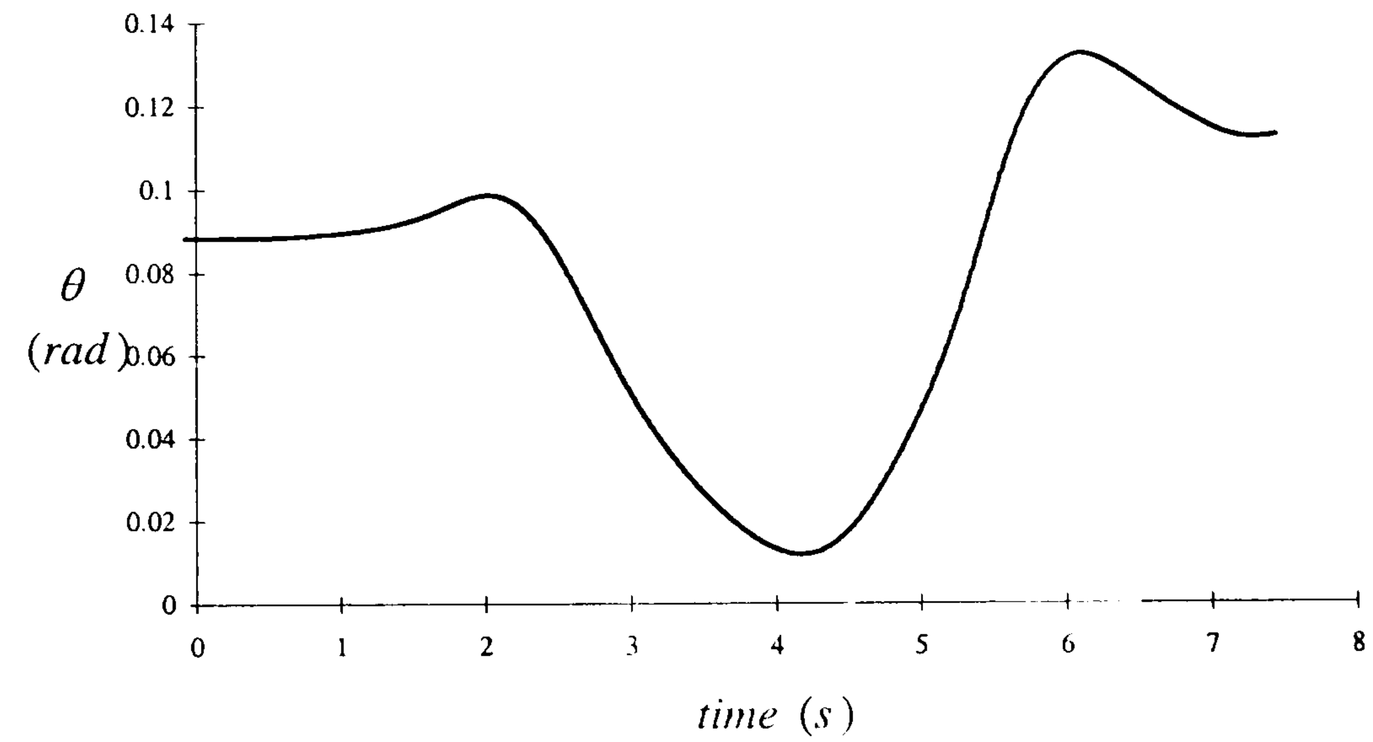

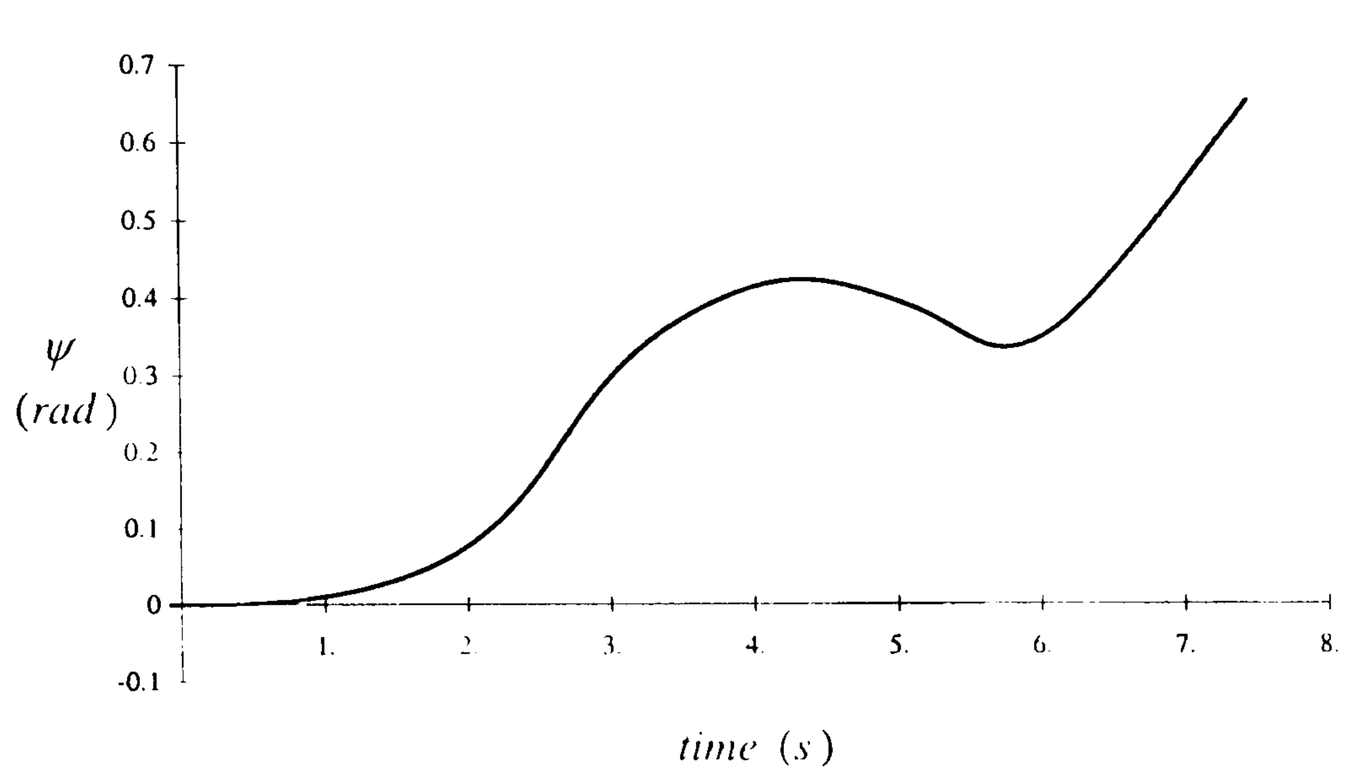

Figure 4.40 : **Time histories of Euler angles during simulated flight over a cliff top.**

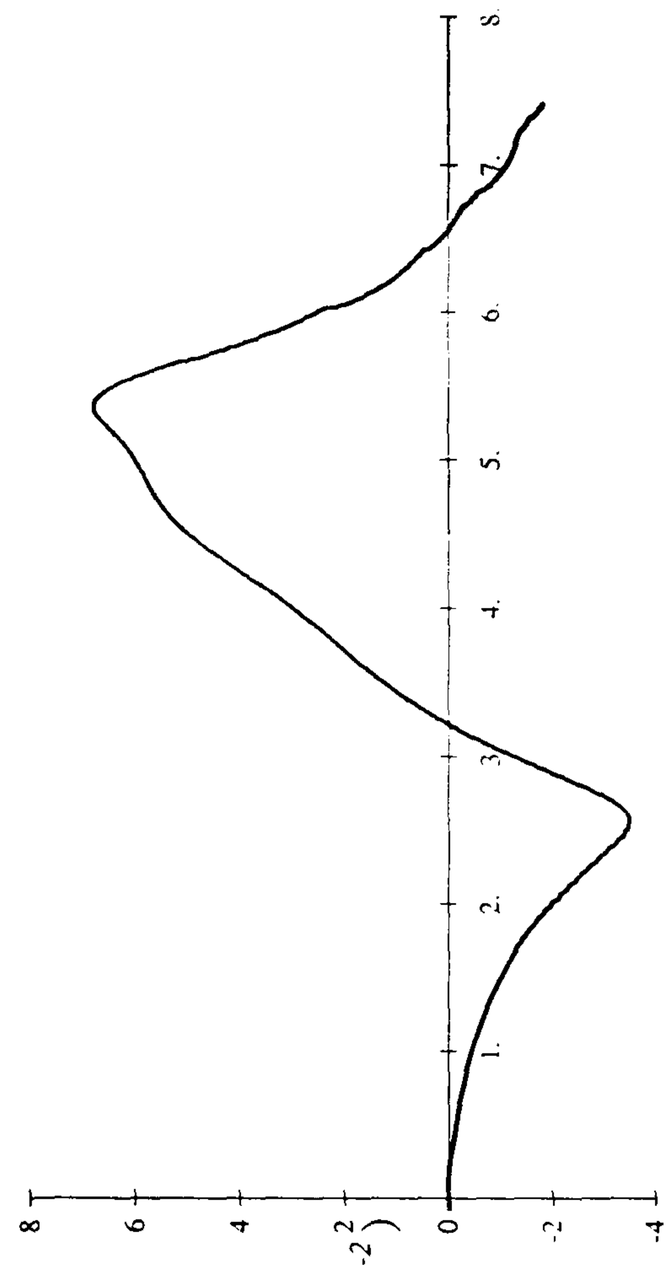

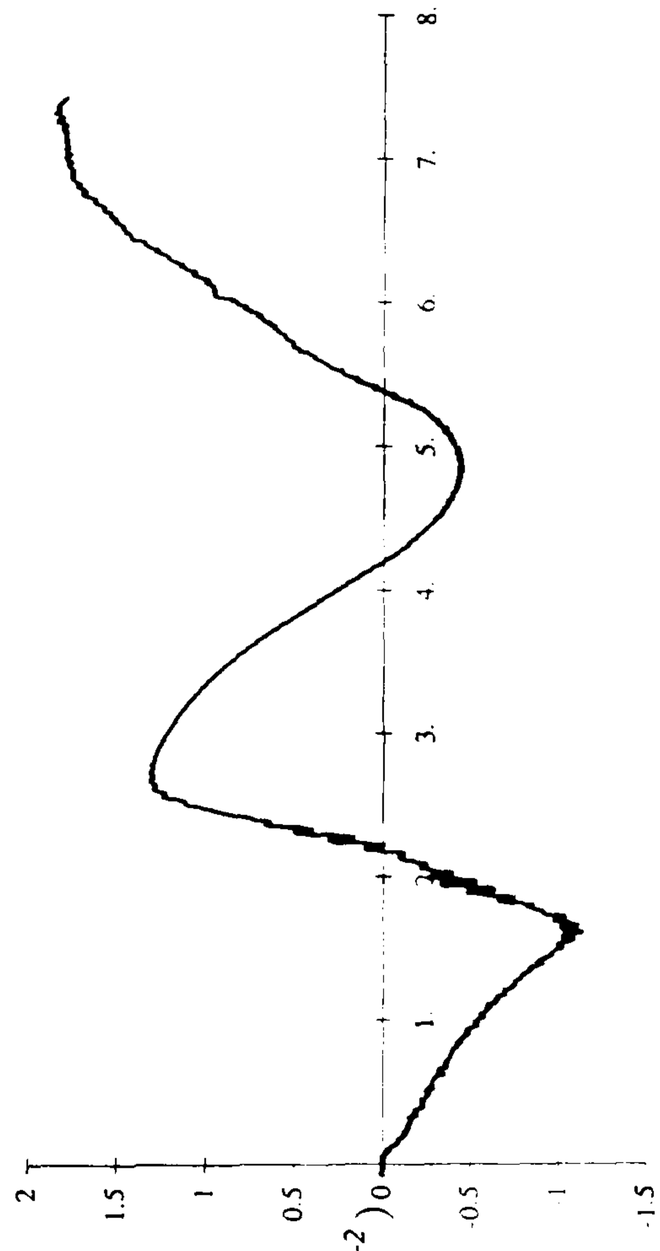

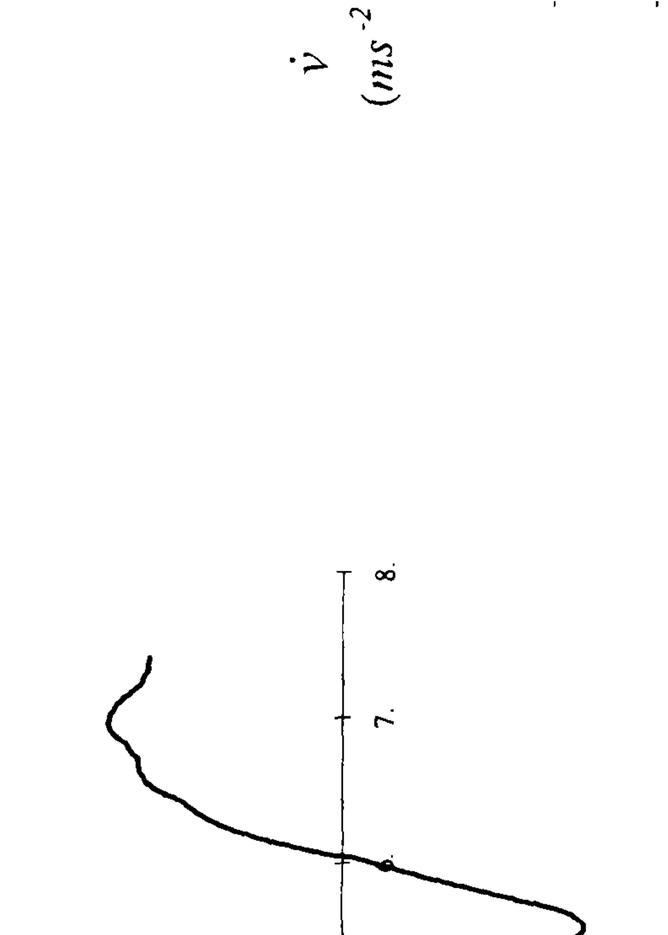

Figure 4.41 : Body axes accelerations during simulated flight over a cliff top.

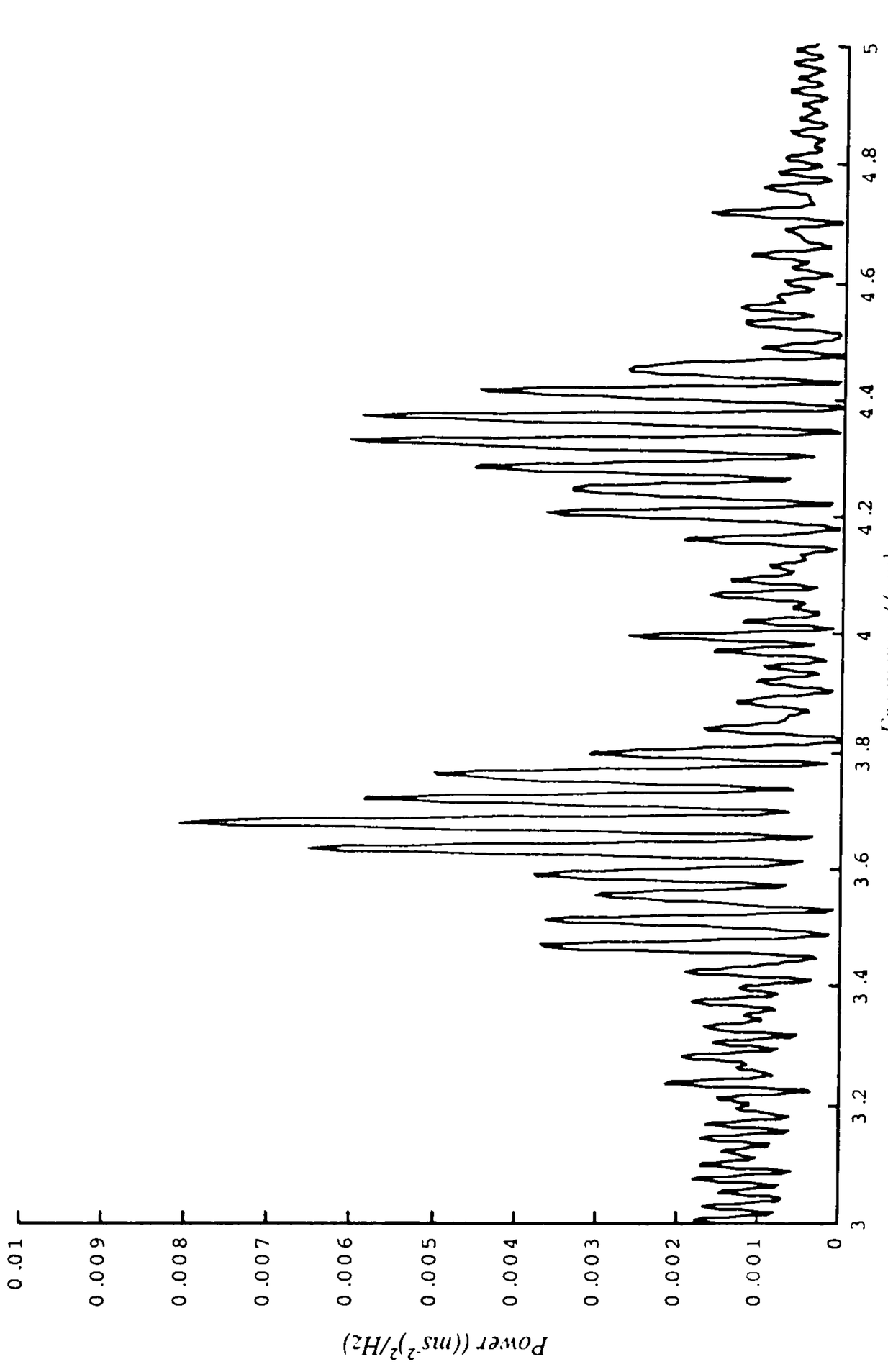

Figure 4.42 : The PSD of w resulting from flight over a cliff top.

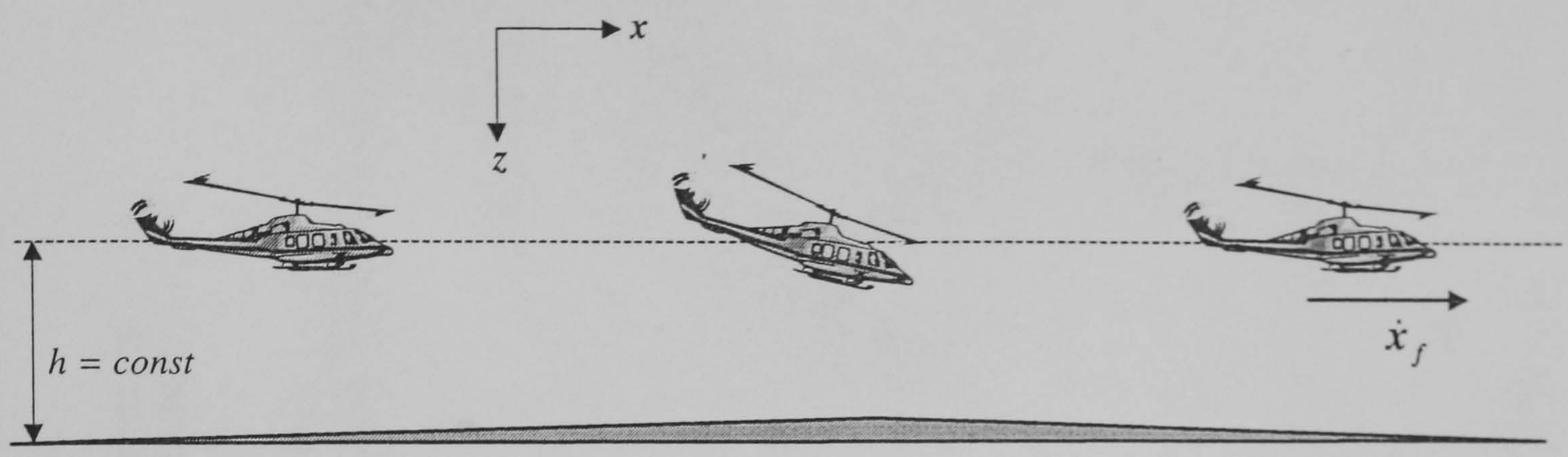

Figure 5.1 : **Illustration of the manoeuvre discussed in the simple example of §5.3.**

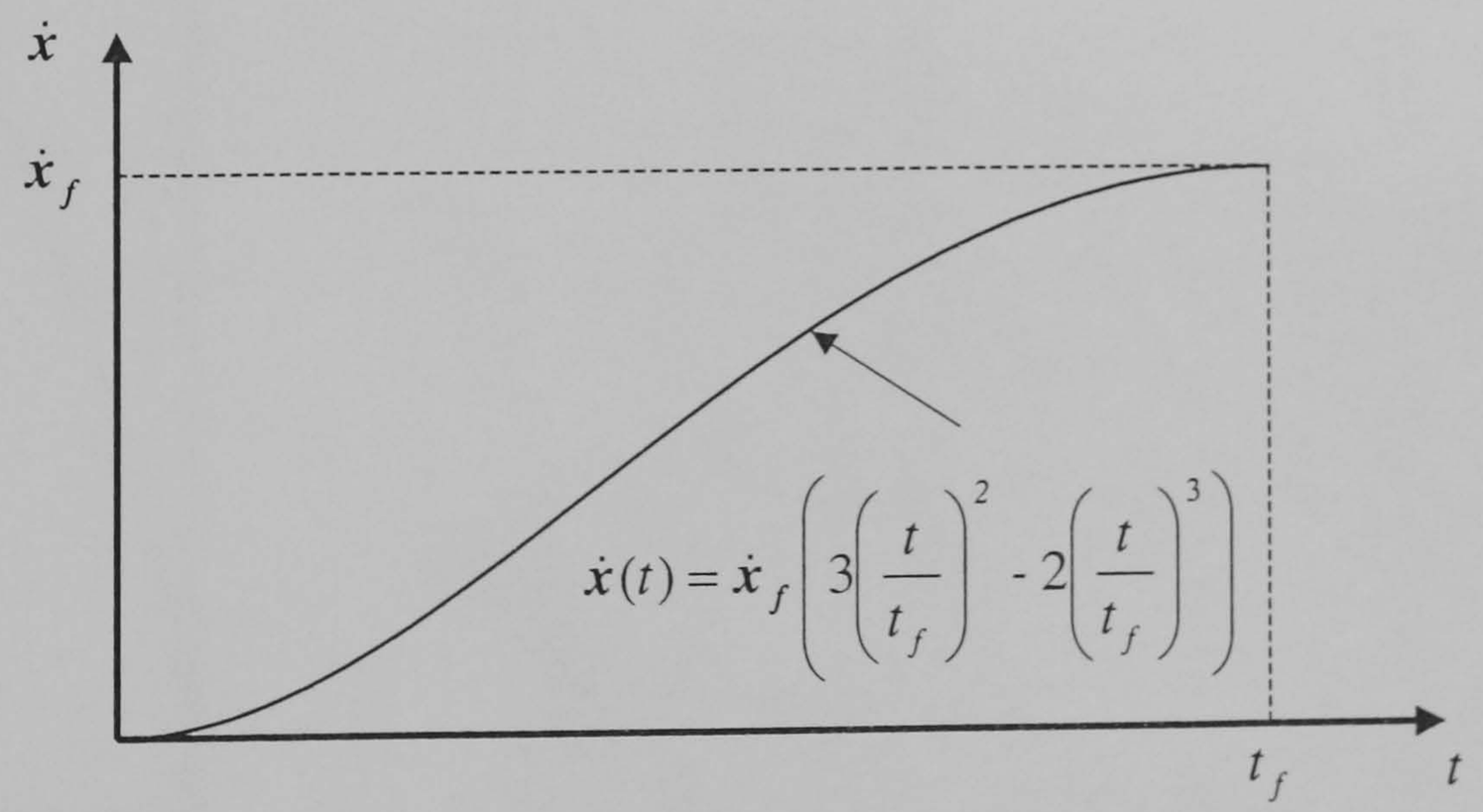

Figure 5.2 : **Velocity profile of the simple example discussed in §5.3.**

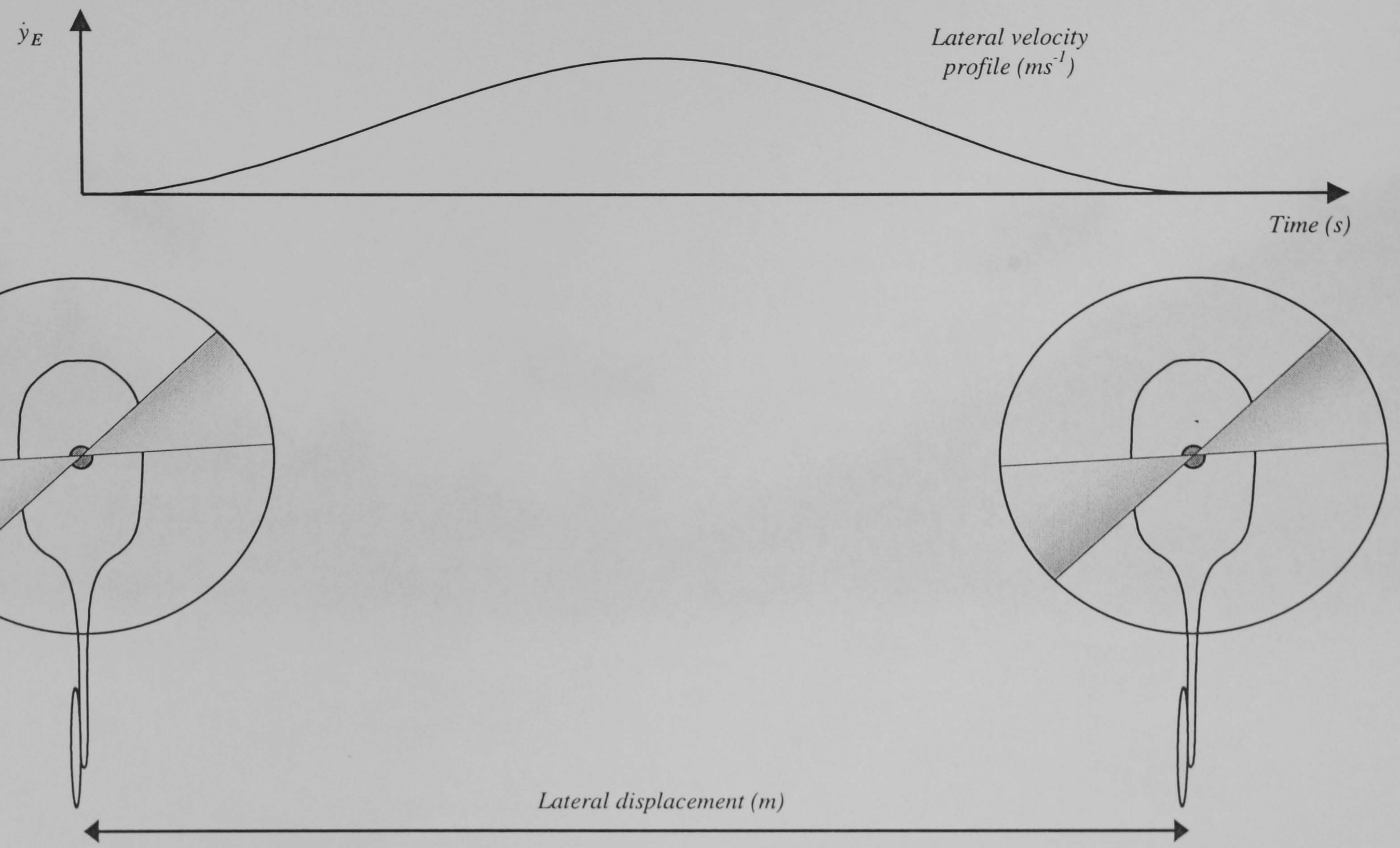

Figure 5.3 : **Side- step manoeuvre expressed as a boundary value polynomial.**

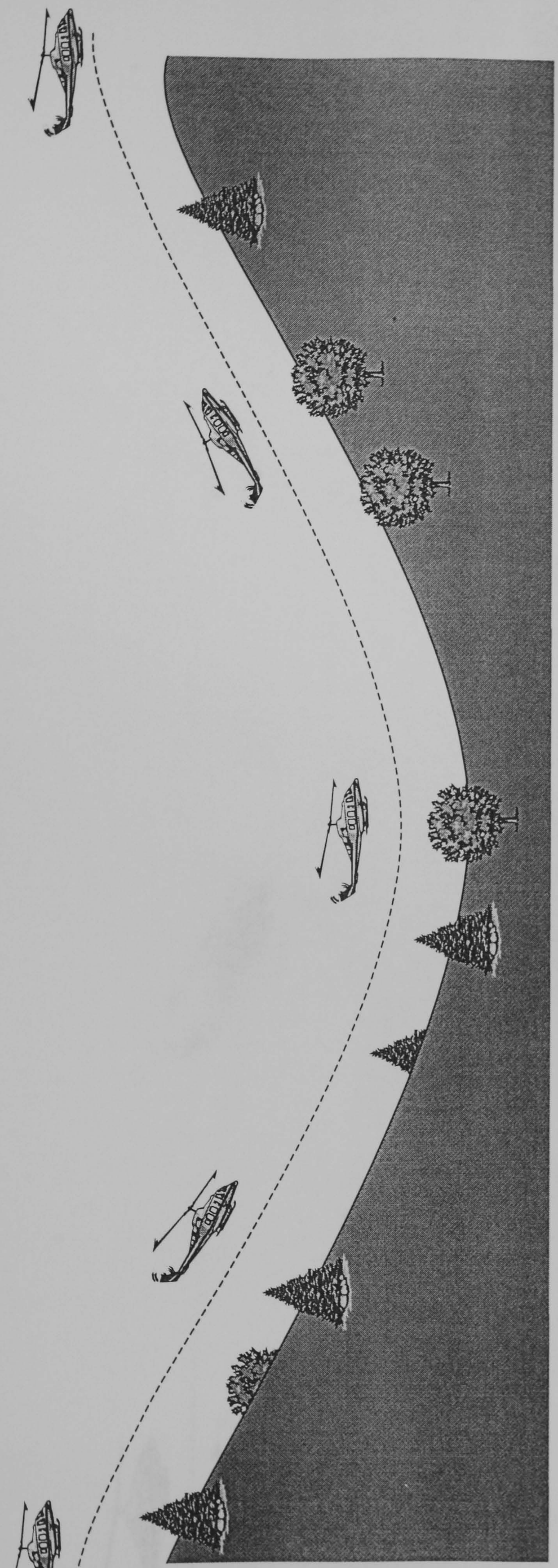

Figure 5.4 : Inverse hurdle-hop manoeuvre expressed as a boundary value polynomial.

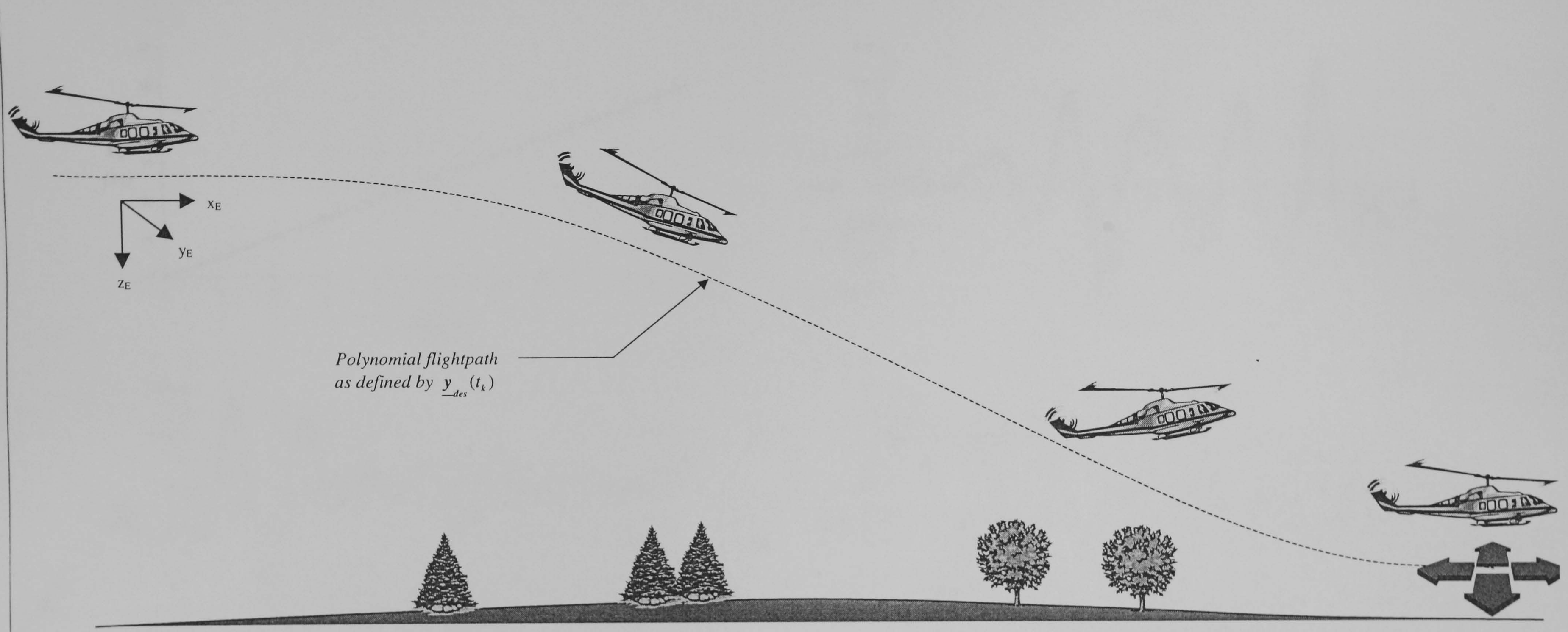

Figure 5.5 : **Flare to hover manoeuvre expressed as a boundary value polynomial.**

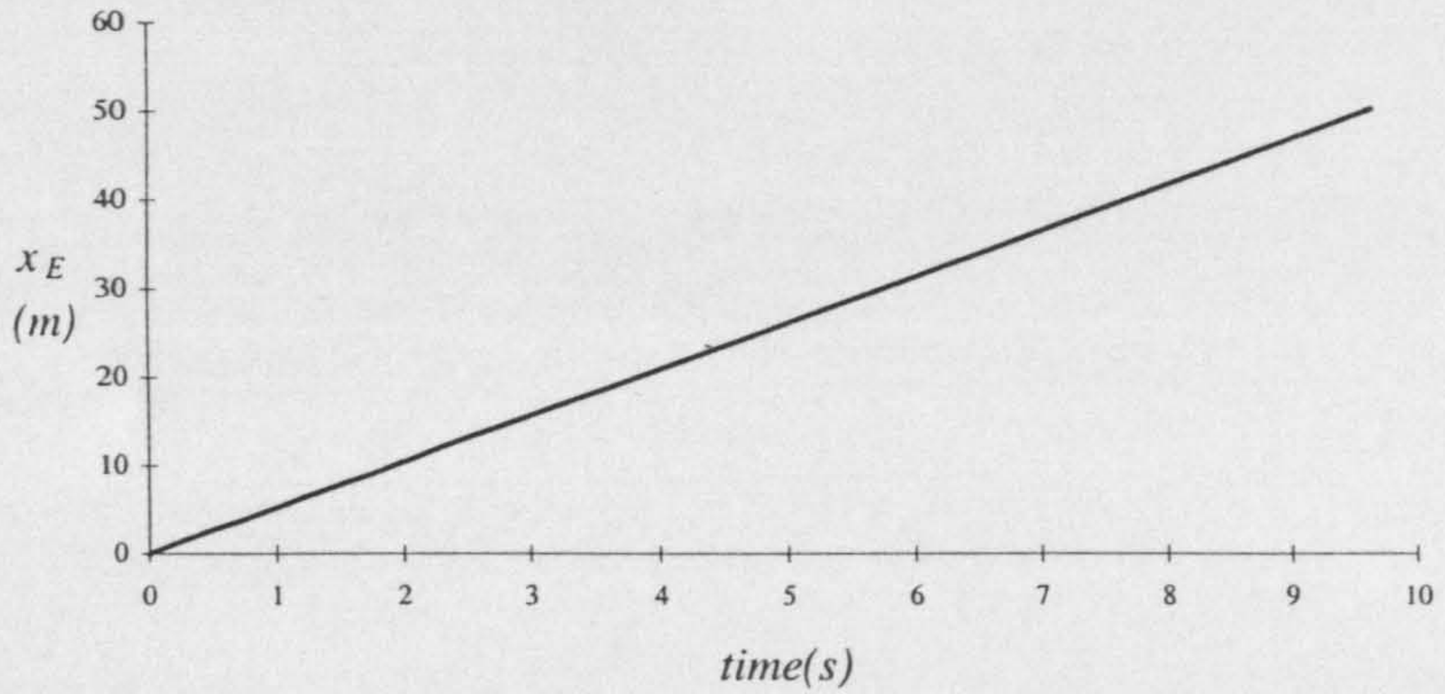

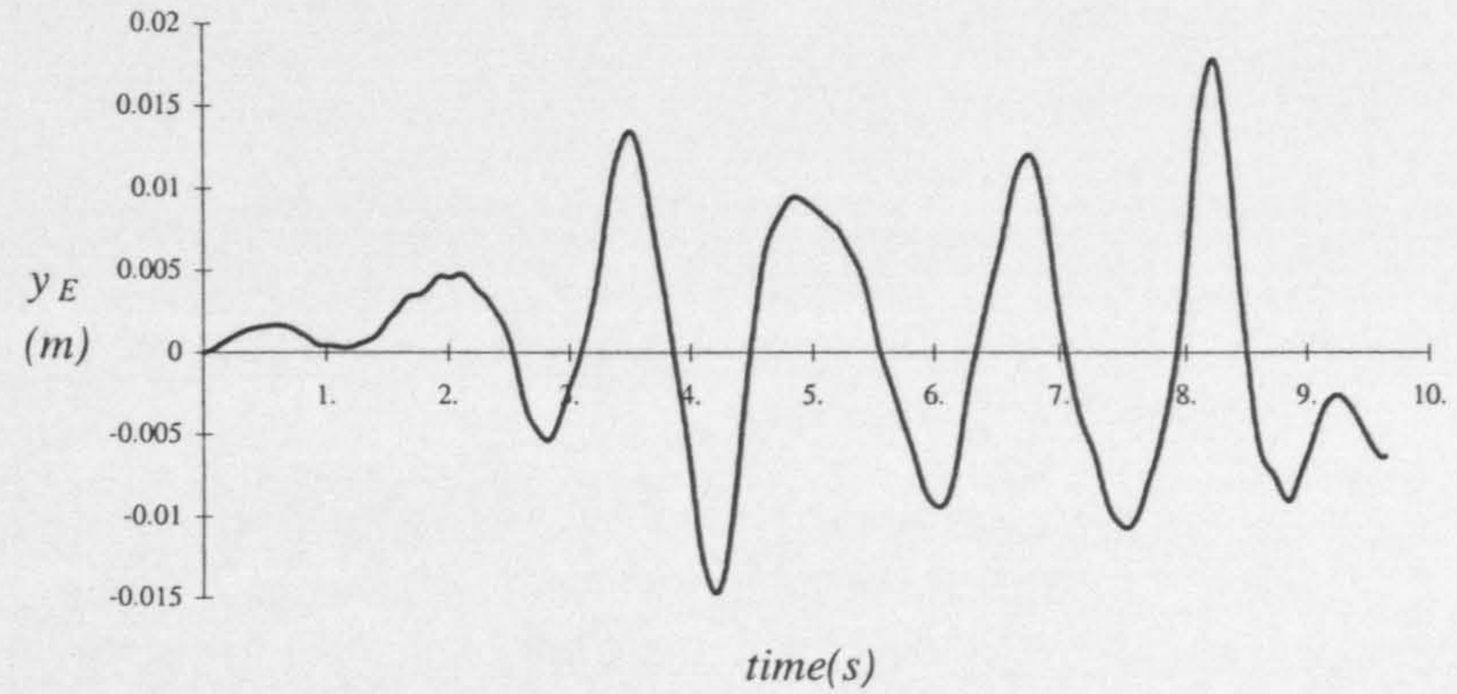

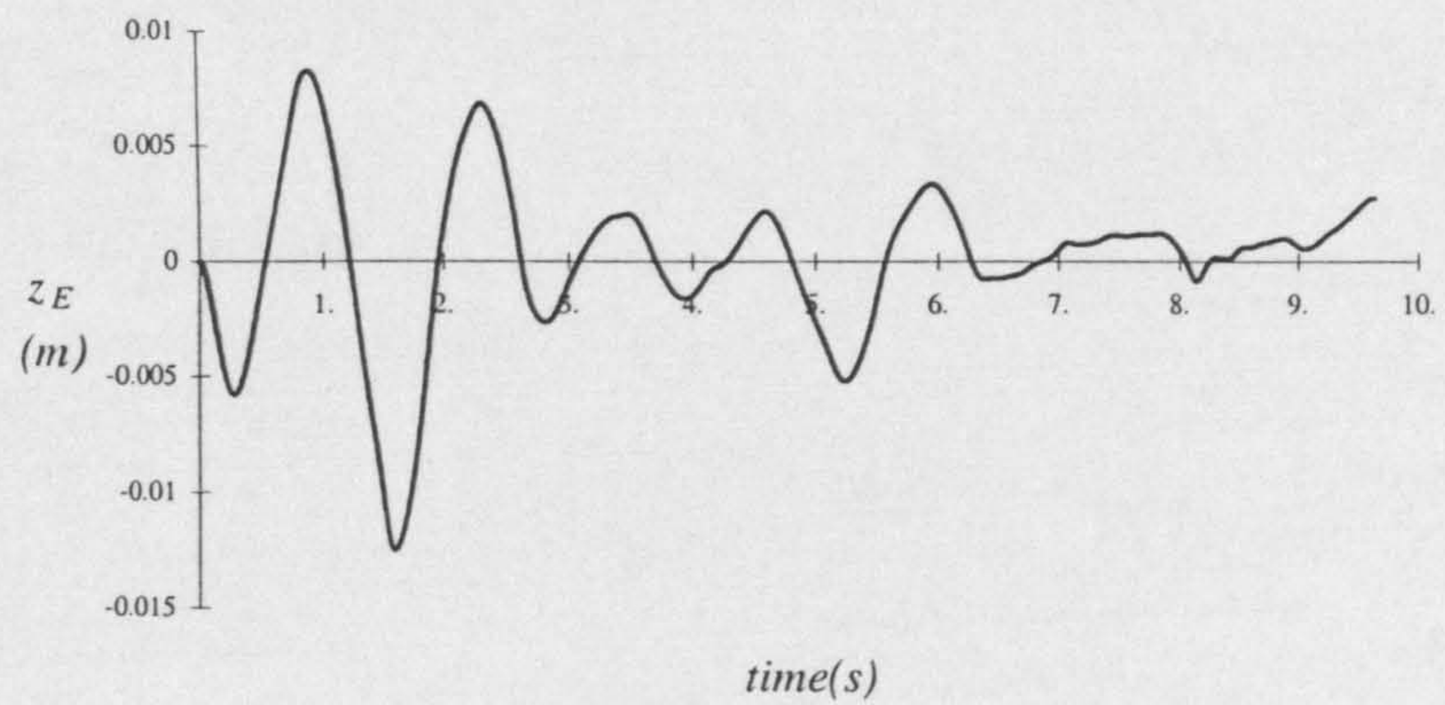

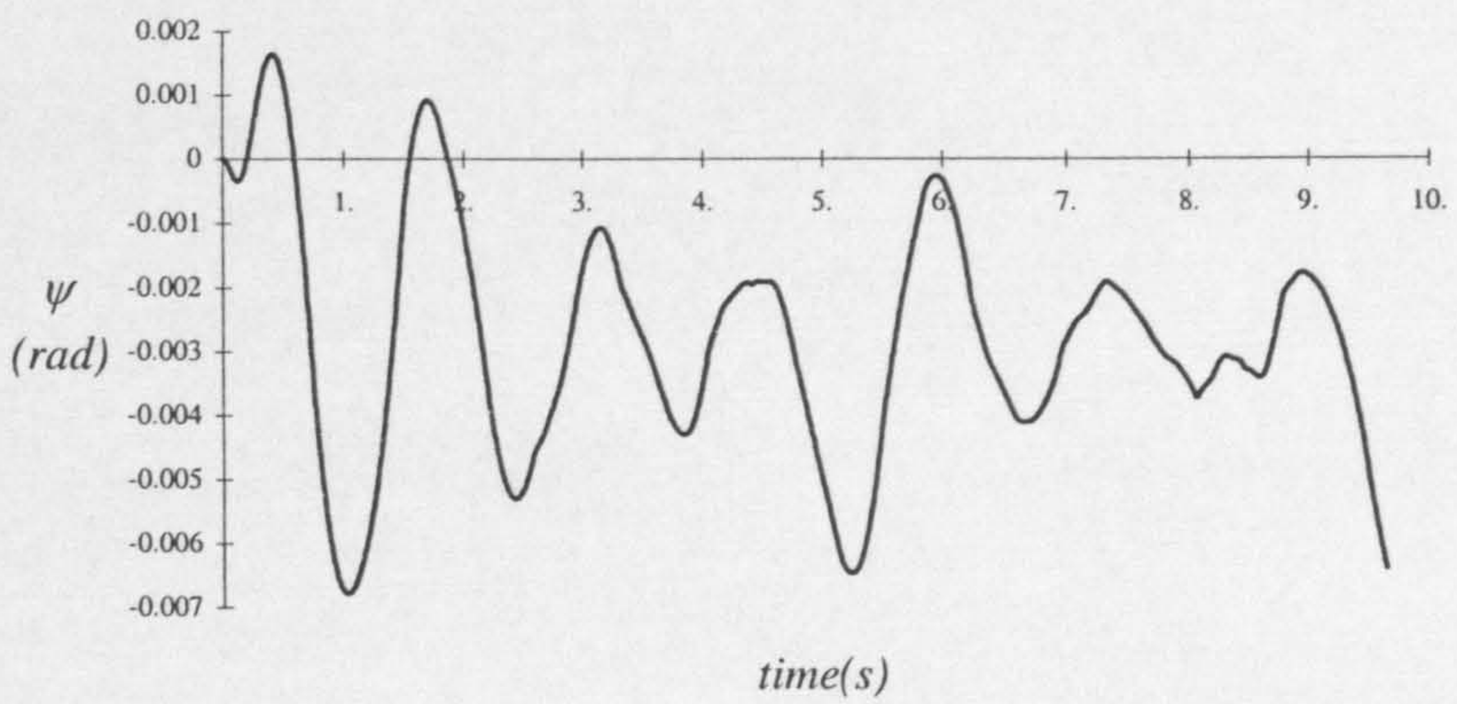

Figure 5.6 : **Time histories of the primary constraint variables of the Puma maintaining trim in inverse simulation using the *unmodified* version of the GENISA algorithm.**

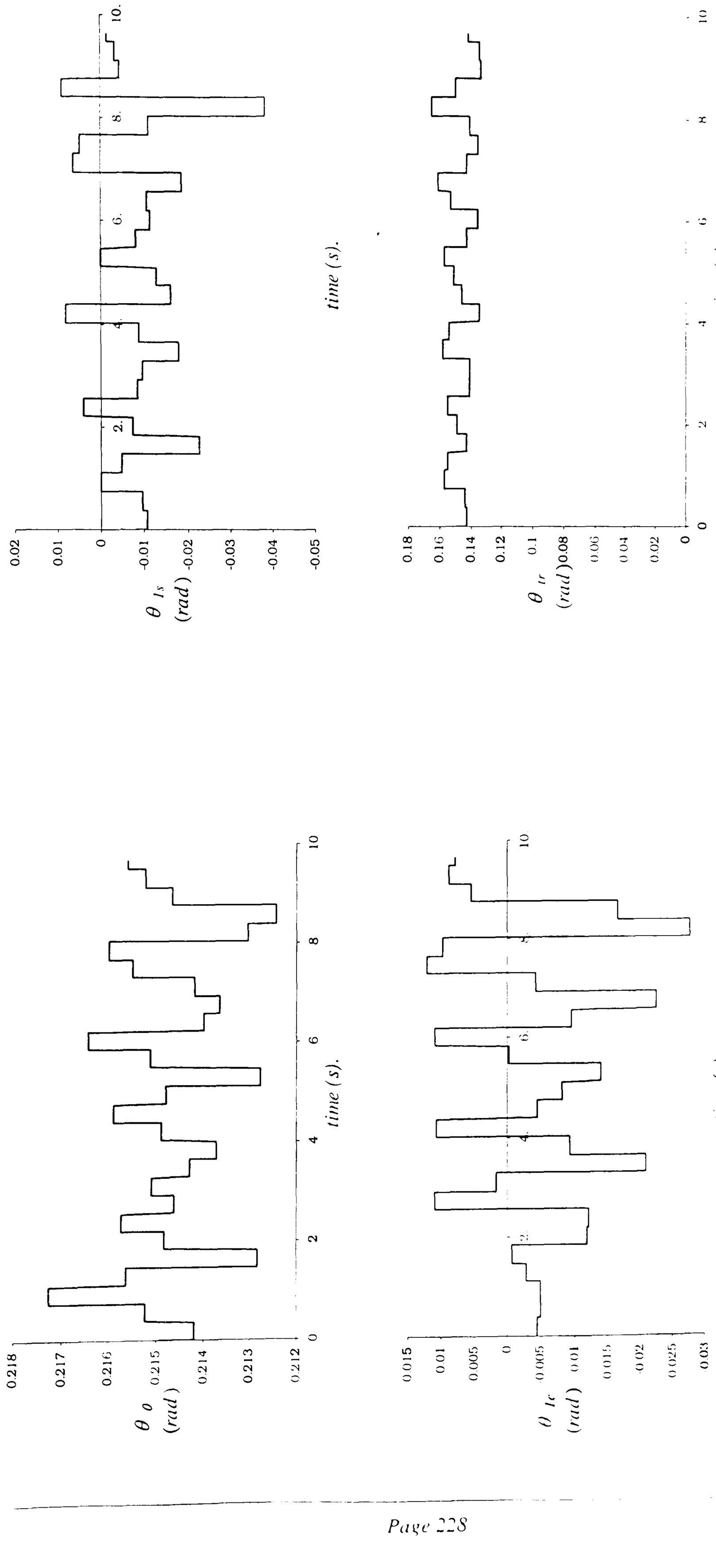

Figure 5.7 : **Time histories of the applied controls of the Puma maintaining trim in inverse simulation using the *unmodified* version of the GENSA algorithm.**

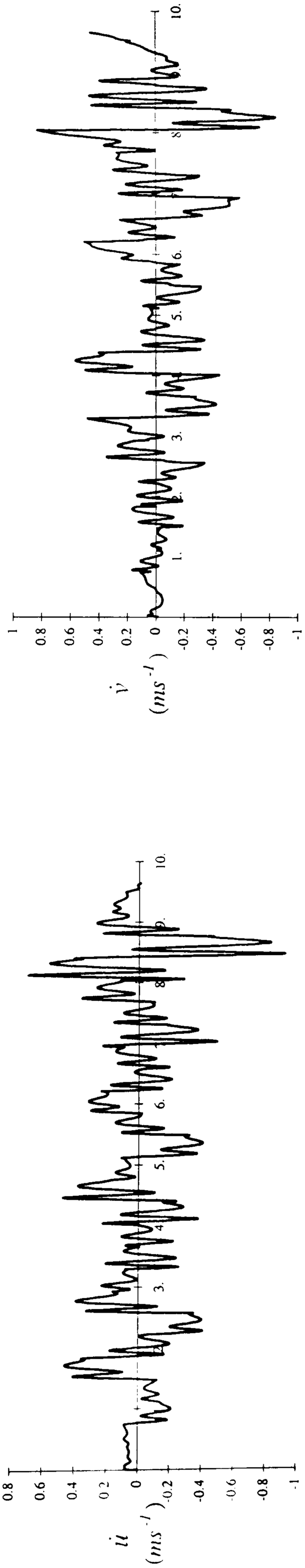

Figure 5.8 : Time histories of the body axes accelerations of the Puma maintaining trim in inverse simulation using the *unmodified* version of the GENISA algorithm.

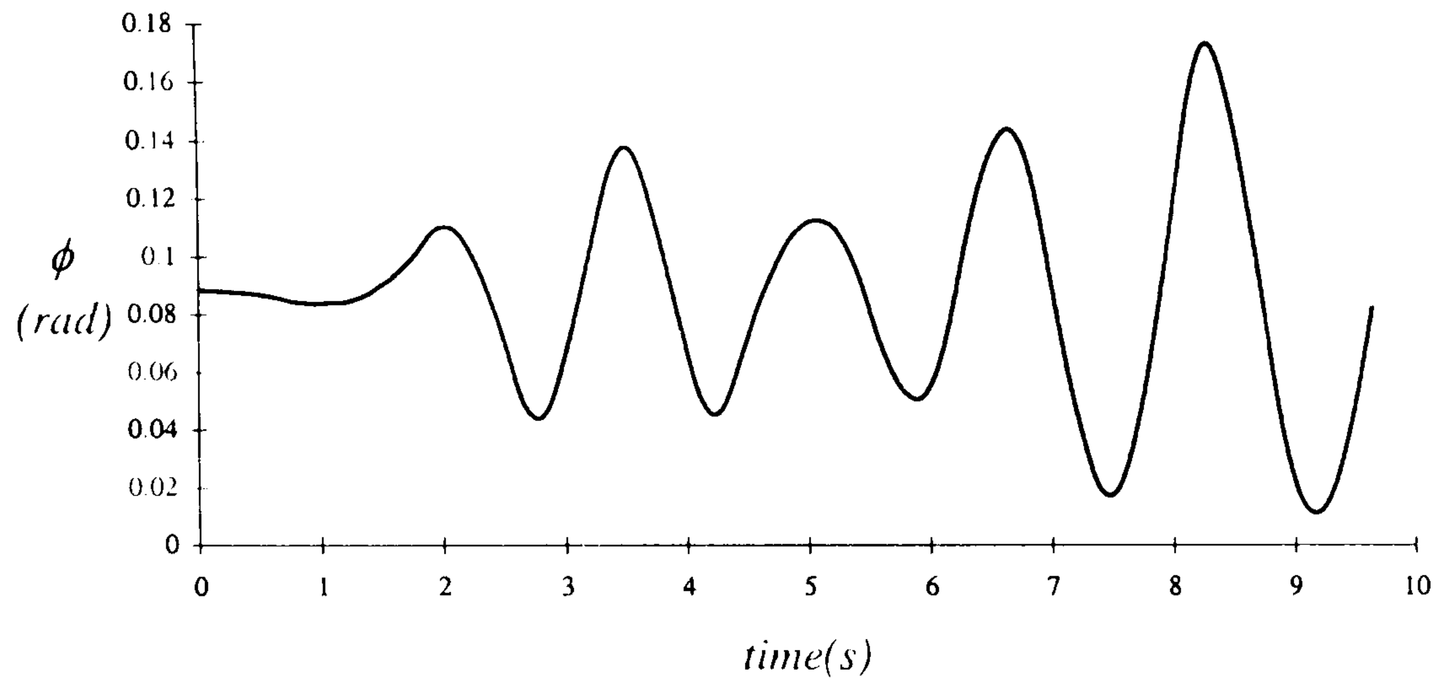

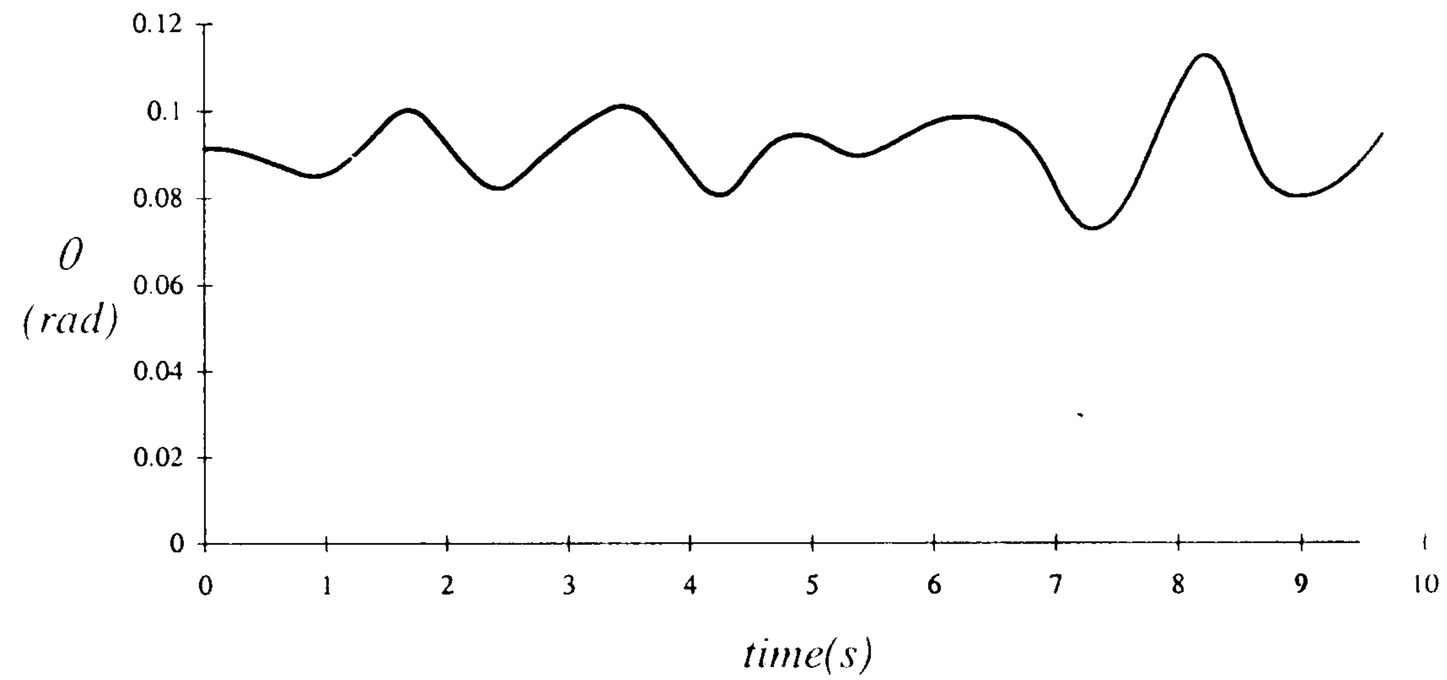

Figure 5.9 : Time histories of the unconstrained body attitudes of the Puma maintaining trim in inverse simulation using the ***unmodified*** version of the GENISA algorithm.

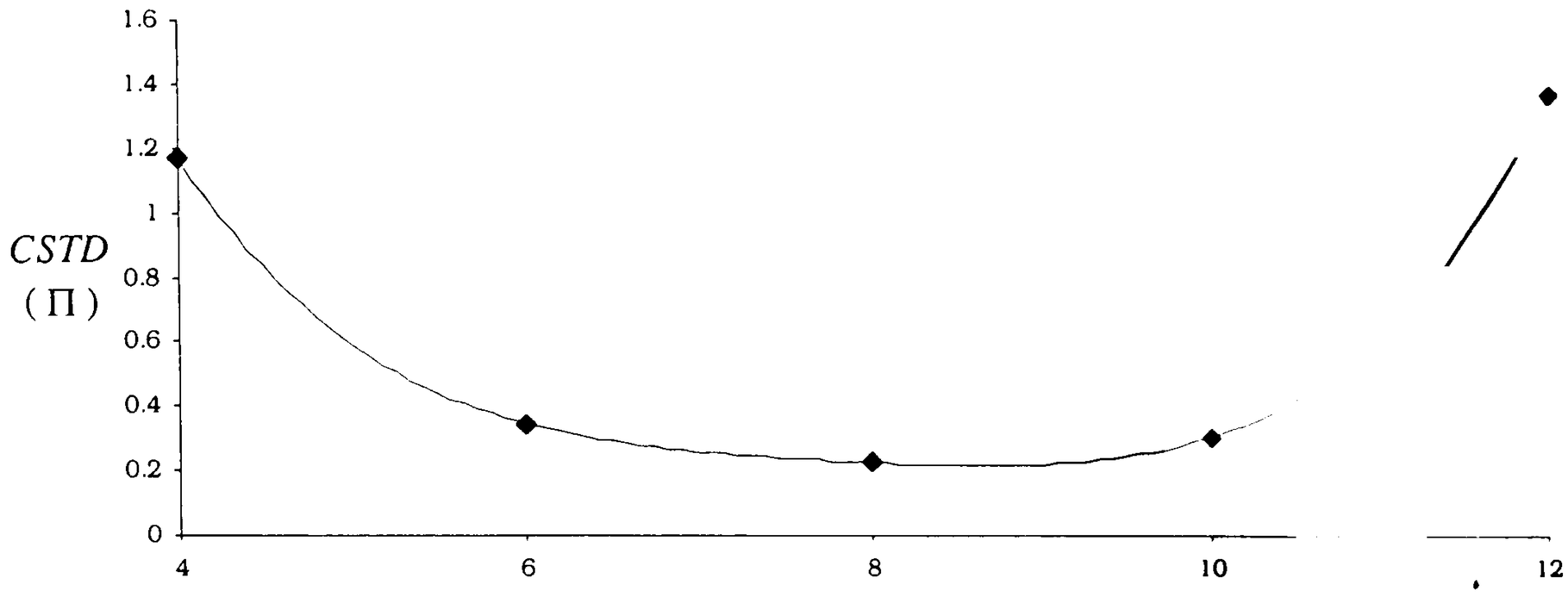

Figure 5.10 : **Distribution of the cumulative standard deviation distribution coefficient with respect to the control application interval**

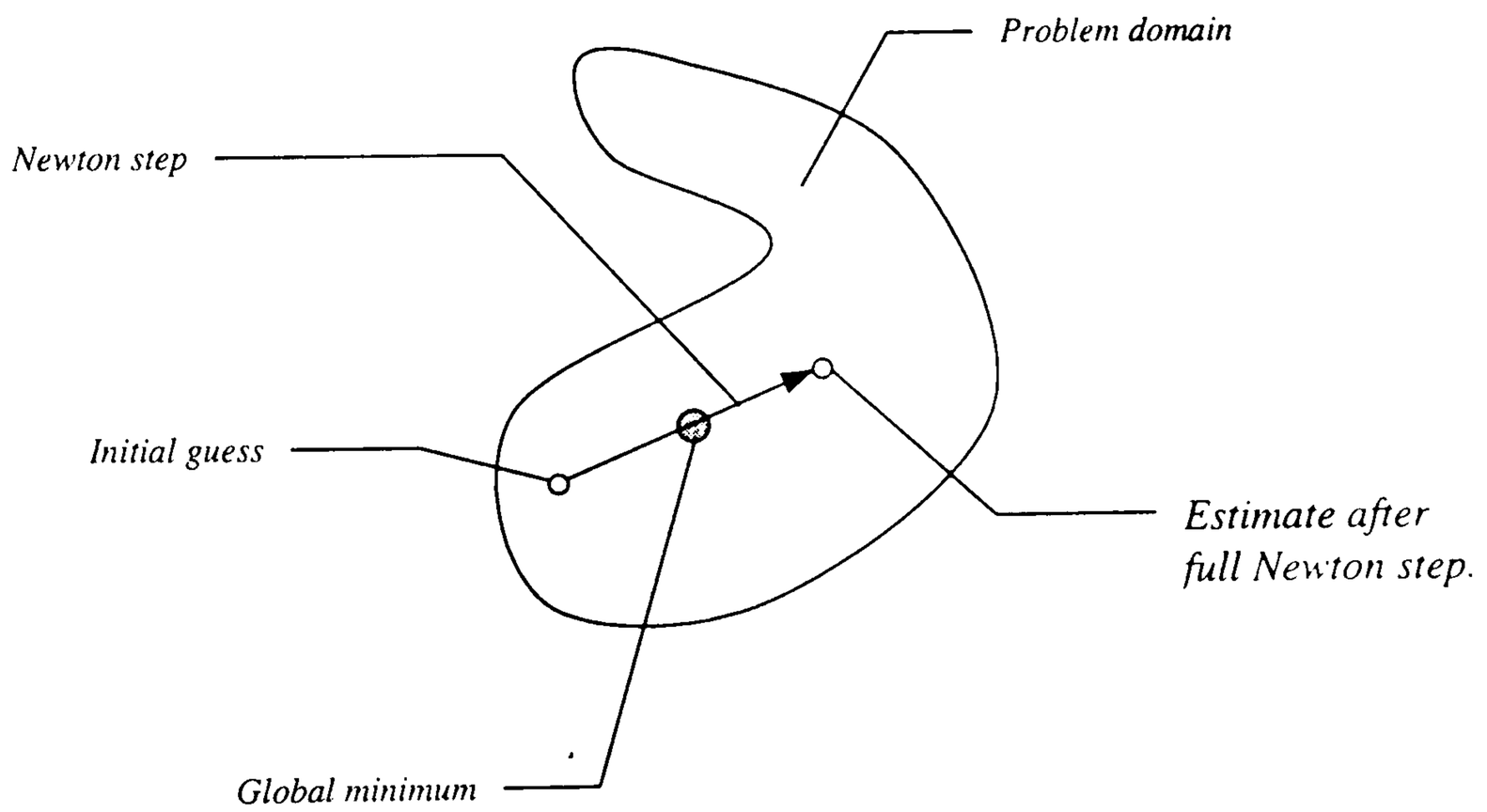

Figure 5.11 : **Multidimensional function minimisation using the full Newton step.**

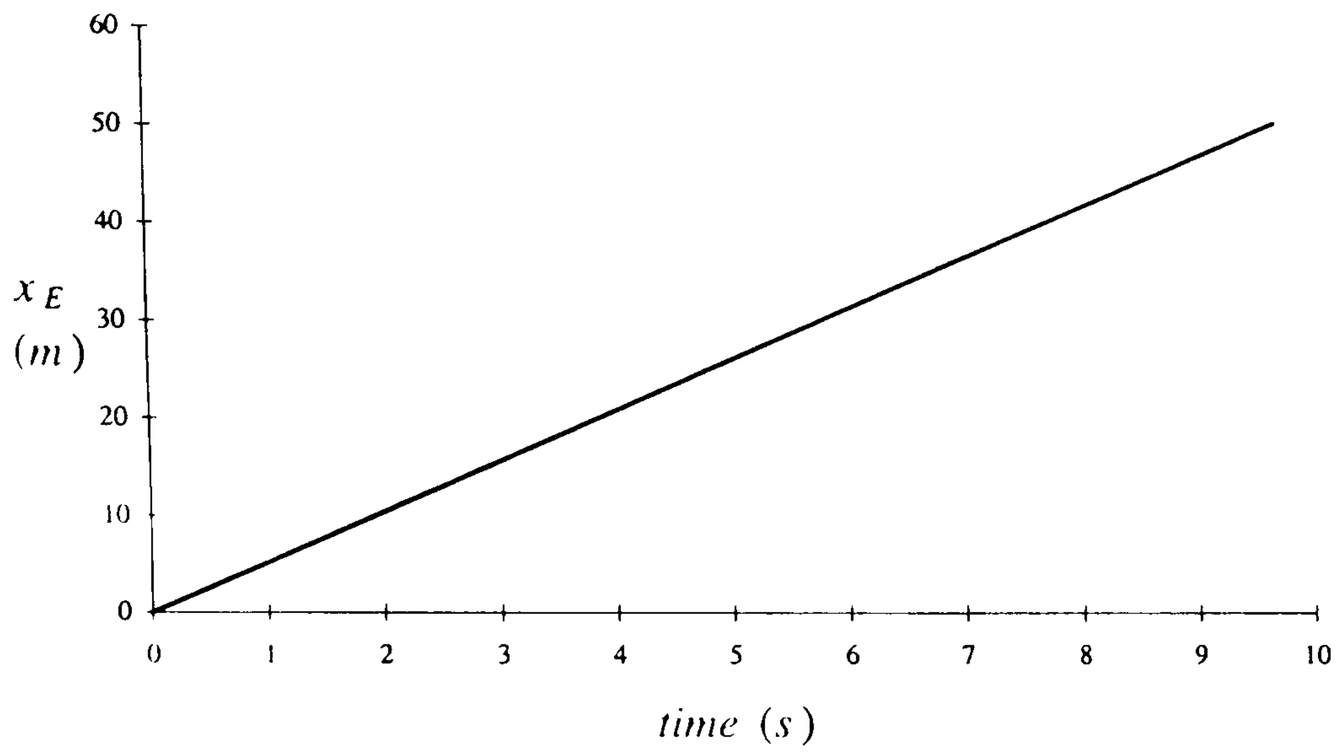

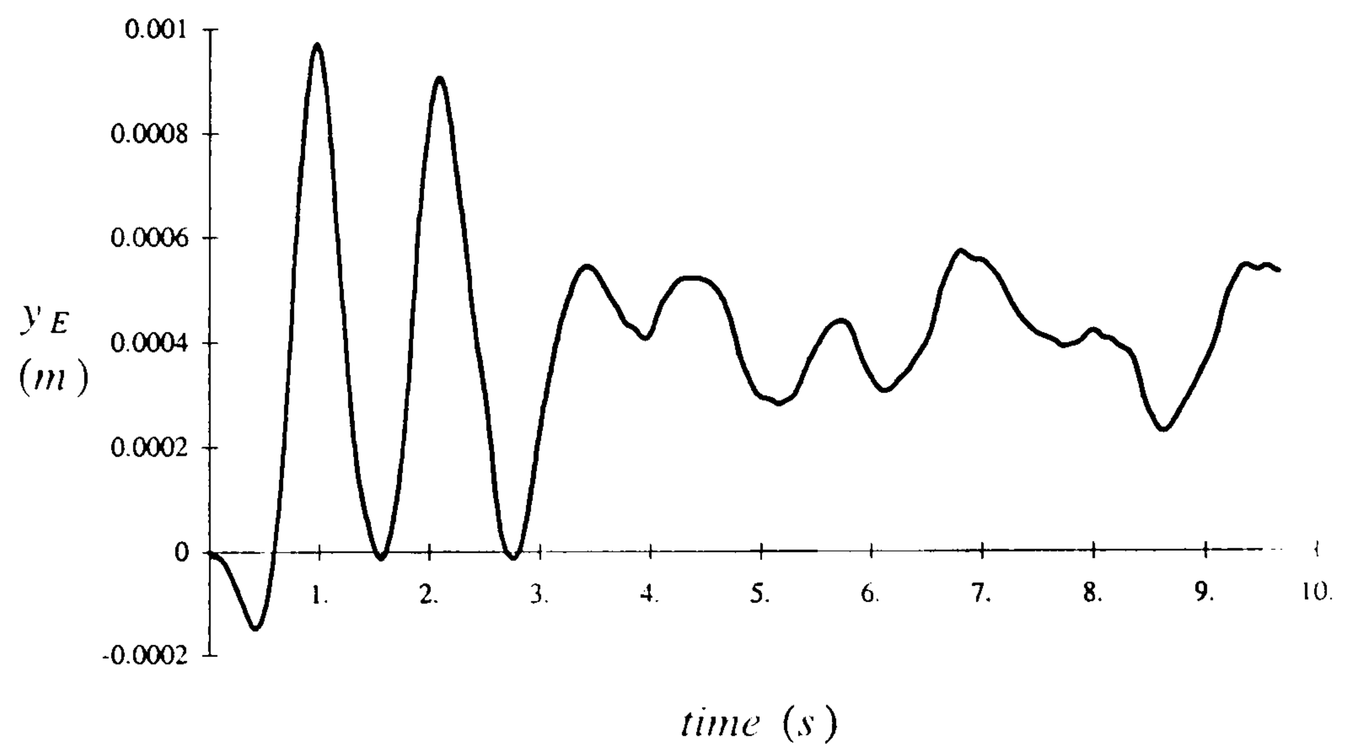

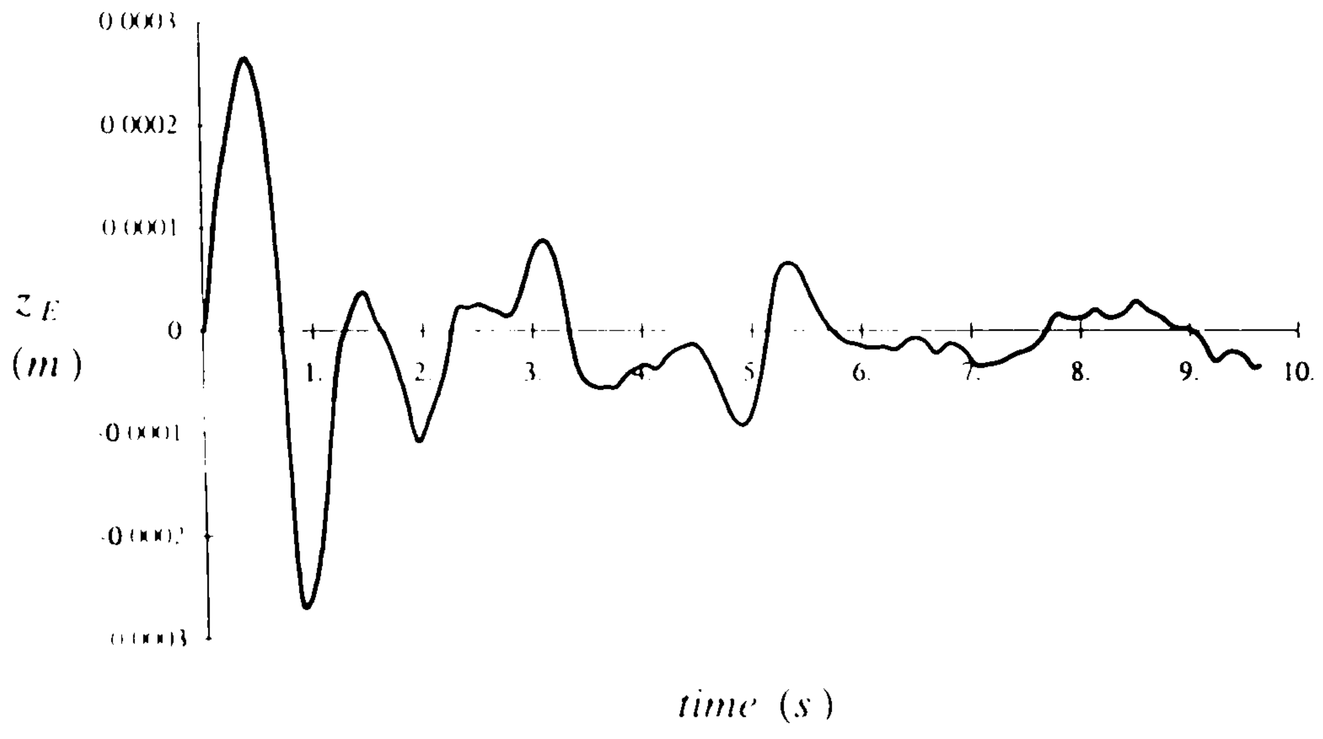

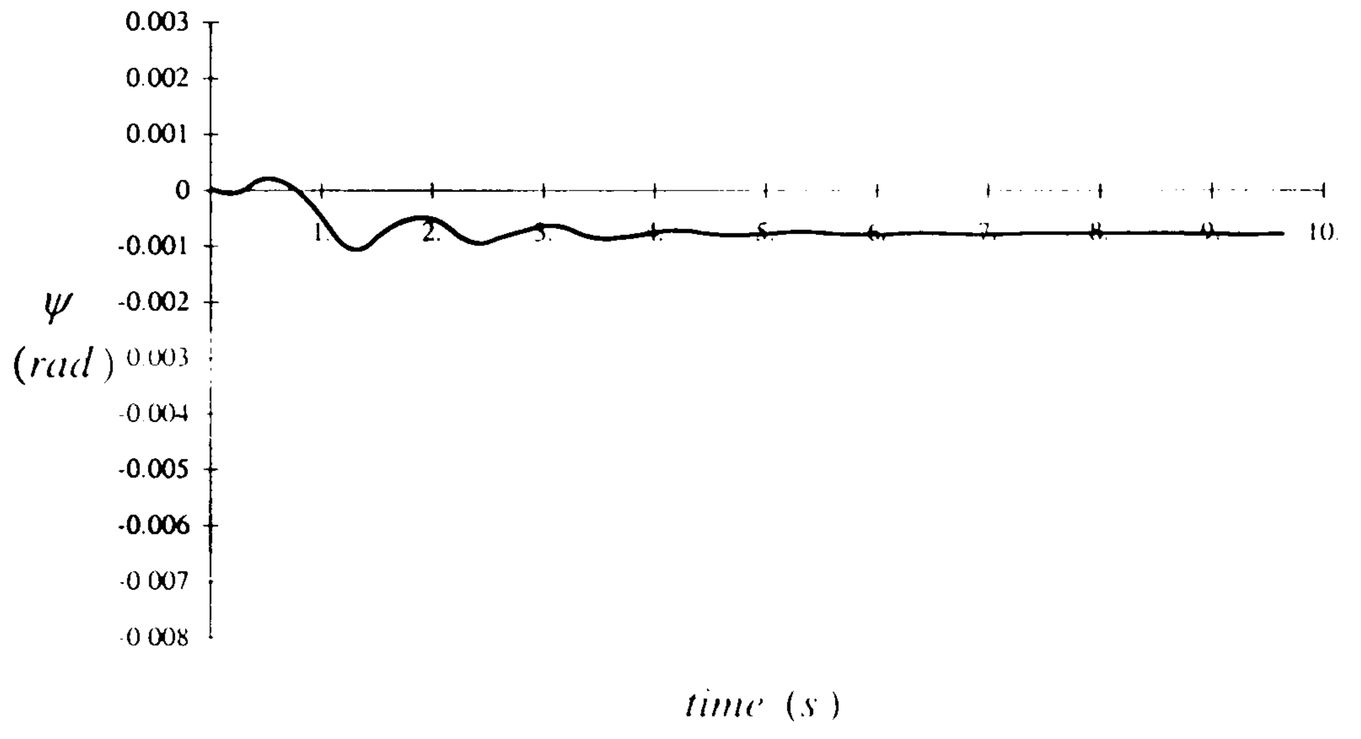

Figure 5.12 : **Time histories of the primary constraint variables of the Puma maintaining trim in inverse simulation using the *enhanced* version of the GENISA algorithm.**

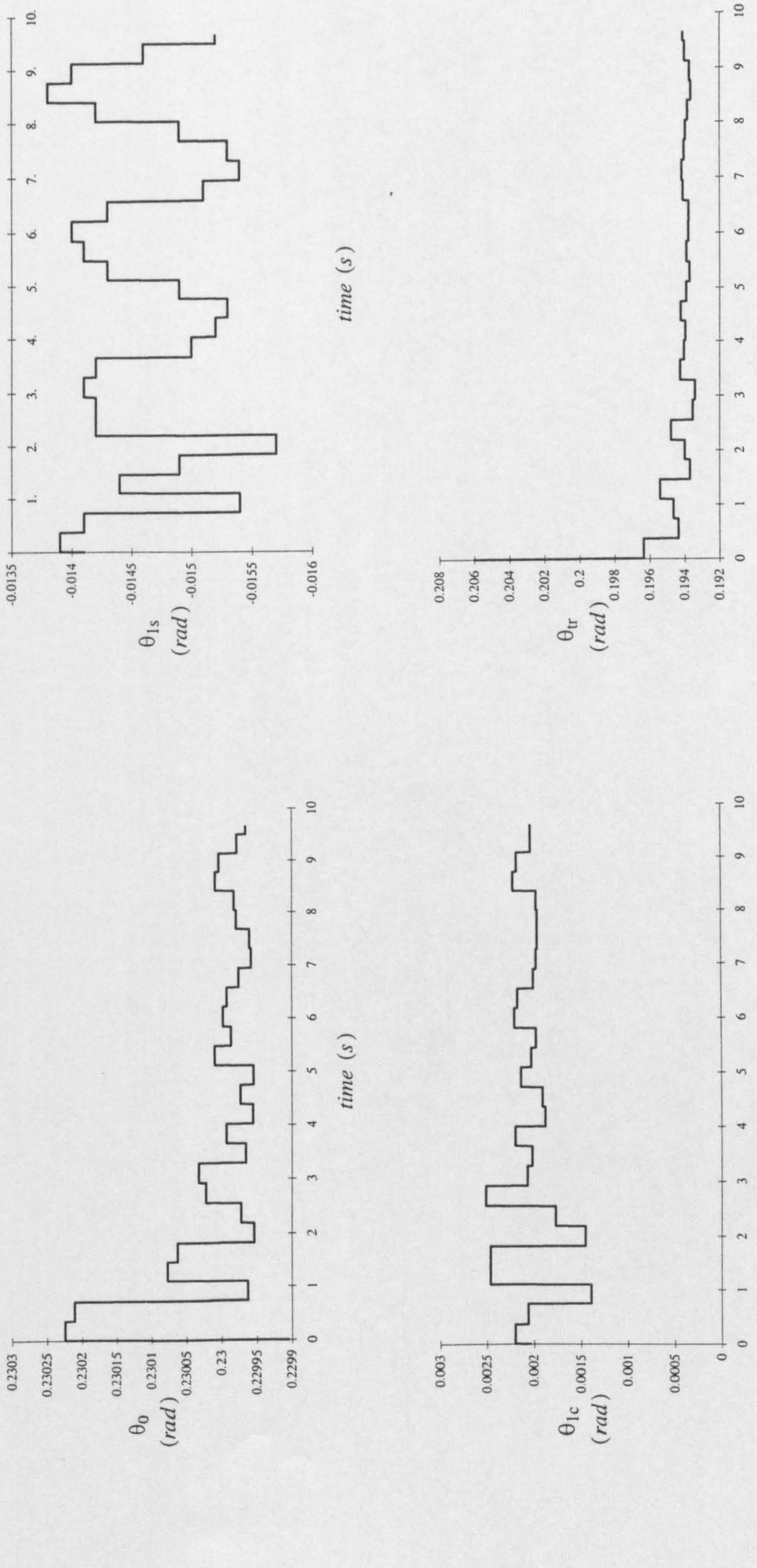

Figure 5.13 : Time histories of the applied controls of the Puma maintaining trim in inverse simulation using the *enhanced* version of the GENISA algorithm.

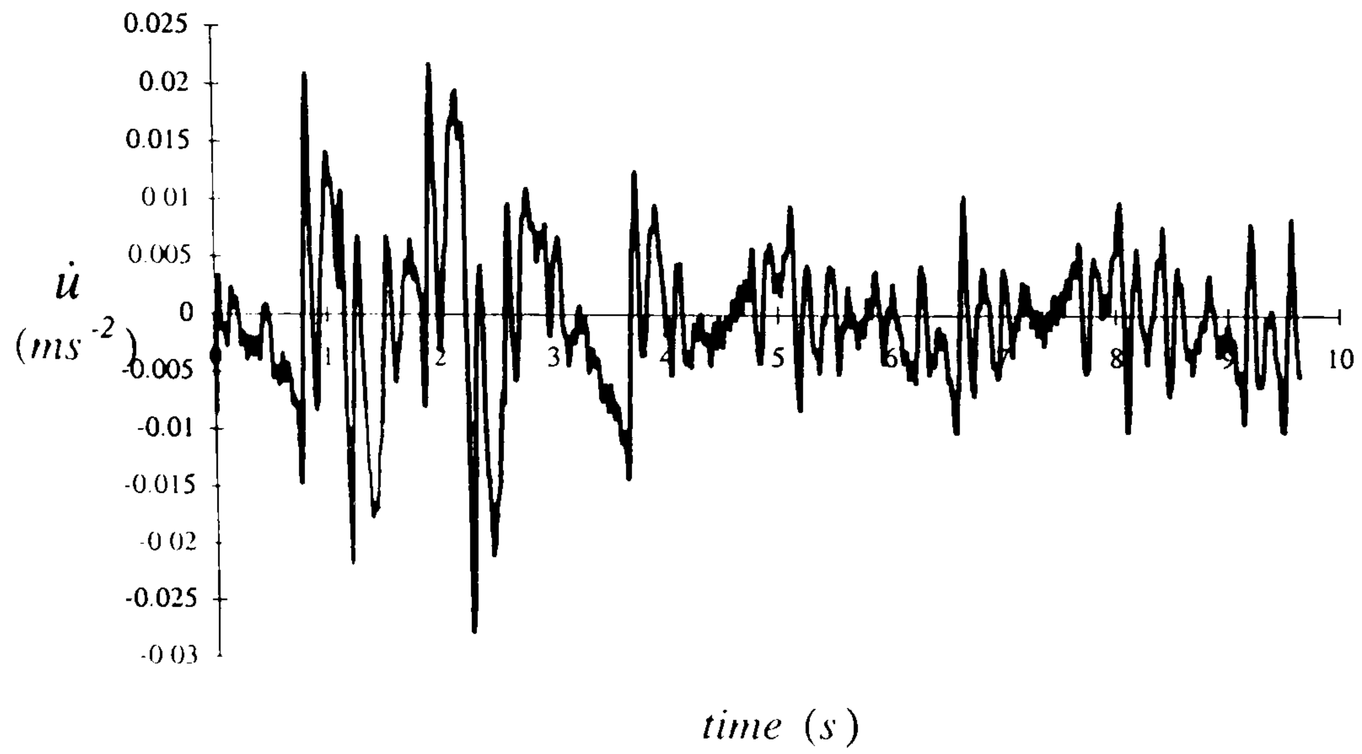

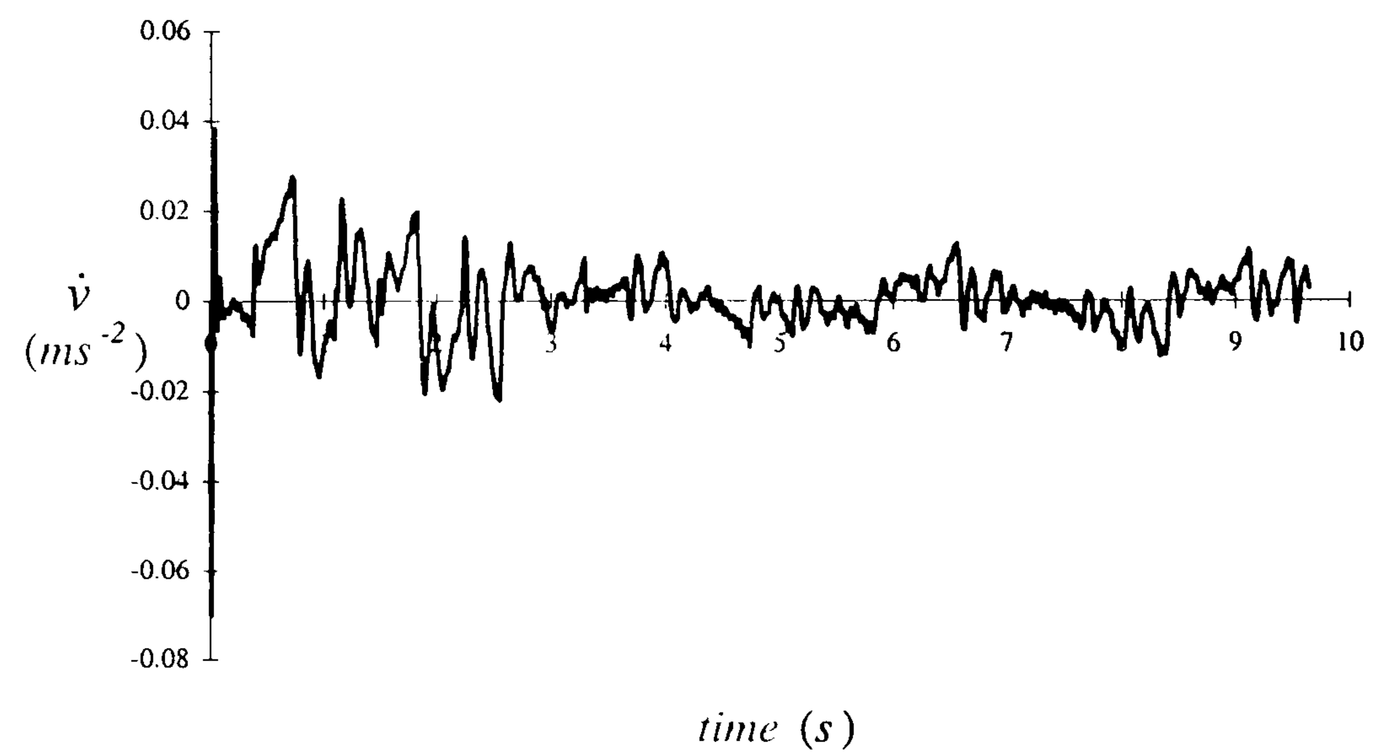

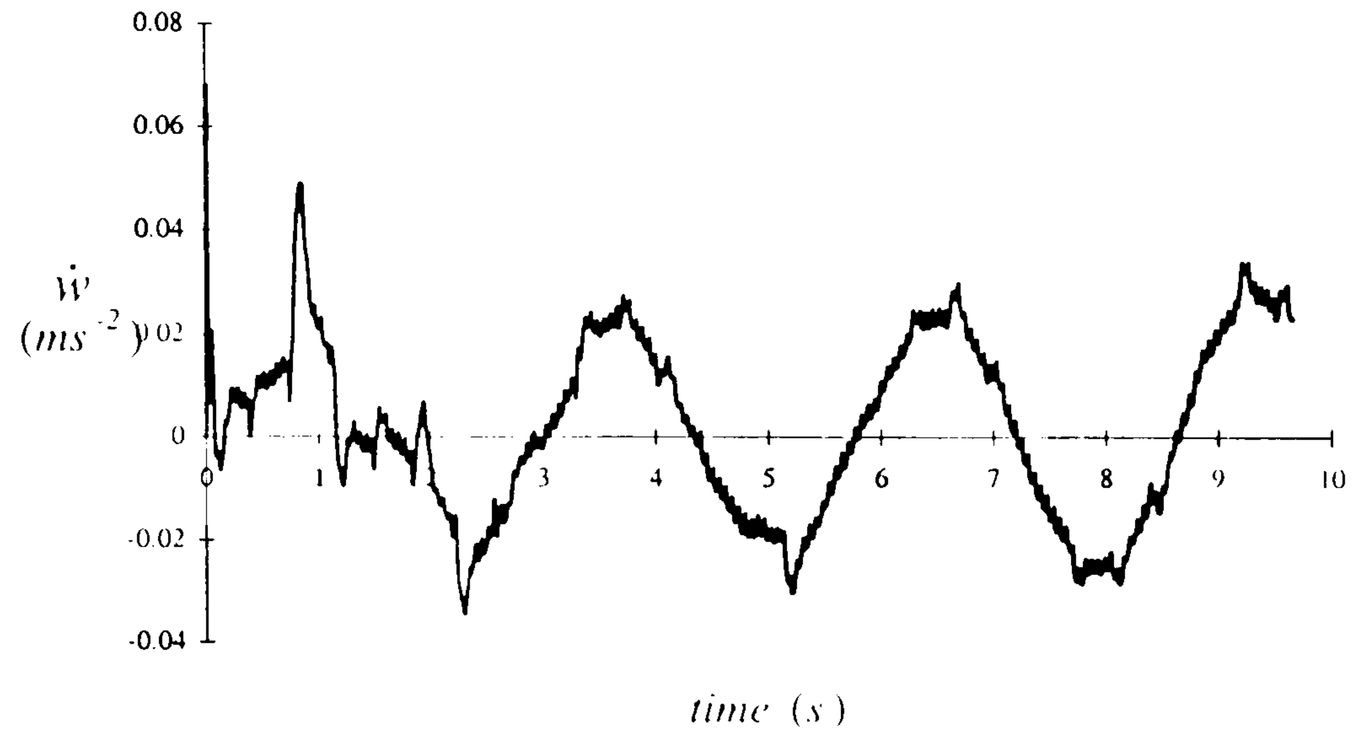

Figure 5.14 : **Time histories of the body axes accelerations of the Puma maintaining trim in inverse simulation using the *enhanced* version of the GENISA algorithm.**

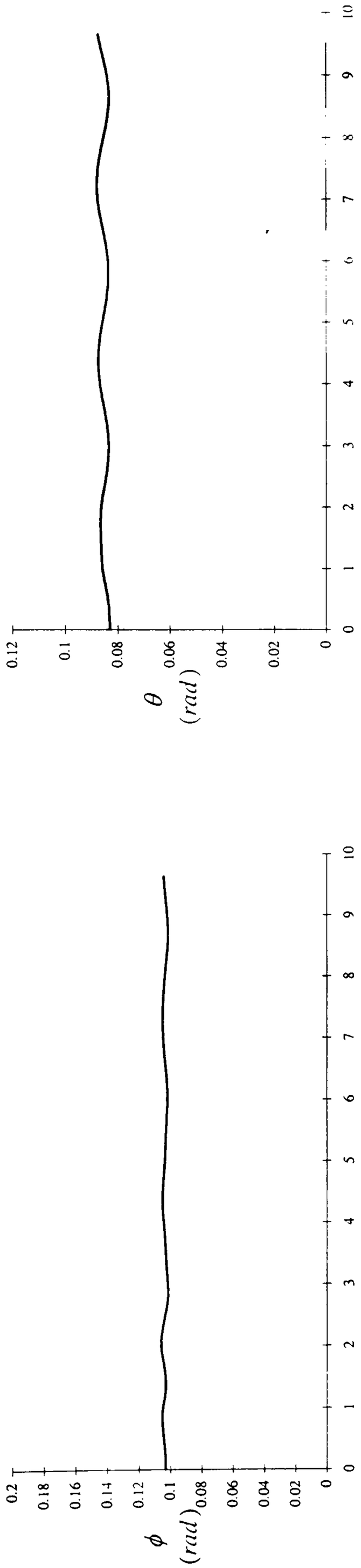

Figure 5.15 : Time histories of the unconstrained body attitudes of the Puma maintaining trim in inverse simulation using the *enhanced* version of the GENISA algorithm.

System matrix (A)

$$\begin{bmatrix}
-0.021 & -0.022 & 0.030 & 0.017 & 0.403 & 0.099 & -0.010 & -9.218 & 0 \\
0.015 & -0.053 & 0.005 & -0.432 & 0.411 & -5.107 & 9.049 & -0.162 & 0 \\
-0.076 & -0.011 & -0.343 & -0.047 & 5.527 & -0.842 & -0.953 & -0.921 & 0 \\
0.022 & -0.052 & 0.008 & -1.624 & 0.809 & -0.226 & -0.744 & -0.087 & 0 \\
0.005 & 0.006 & -0.001 & -0.052 & -0.521 & -0.021 & 0.008 & -0.166 & 0 \\
0.008 & 0.011 & 0.010 & -0.183 & 0.127 & -0.441 & -0.073 & -0.011 & 0 \\
0 & 0 & 0 & 1.003 & 0.008 & 0.090 & 0 & 0 & 0 \\
0 & 0 & 0 & 0 & 0.999 & -0.088 & 0 & 0 & 0 \\
0 & 0 & 0 & 0 & 0.089 & 1.003 & 0 & 0 & 0
\end{bmatrix}$$

Control matrix (B)

$$\begin{bmatrix}
5.122 & -27.620 & 1.270 & -0.665 \\
0.825 & 11.246 & 32.770 & -5.351 \\
-62.635 & -5.627 & 4.753 & 4.062 \\
0.695 & -0.598 & 53.847 & 1.444 \\
1.036 & 13.436 & -0.117 & -0.636 \\
-12.580 & 0.301 & 7.336 & 8.950 \\
0 & 0 & 0 & 0 \\
0 & 0 & 6.337 & 0 \\
0 & 0 & 6.179 & 0
\end{bmatrix}$$

Constrained System matrix (A_c)

$$\begin{bmatrix}
-0.338 & -0.2578 & 5.1821 & -11.8835 \\
0.0961 & -0.1869 & -4.0366 & -1.3432 \\
0.152 & 0.877 & 0.6113 & -1.3518 \\
1.0005 & 0 & 0 & 0
\end{bmatrix}$$

Figure 5.16 : **Systems and control matrices for the free and inverse simulations of a Puma maintaining a 10 knot trim.**

Eigenvalue	*Damping*	*Frequency (rad/s)*
0.325 ± 3.08i	-0.105	3.09
-0.281 ± 2.26i	0.123	2.28

Table 5.17 : **The eigenvalues and transient characteristics of the inverse system matrix A_c.**

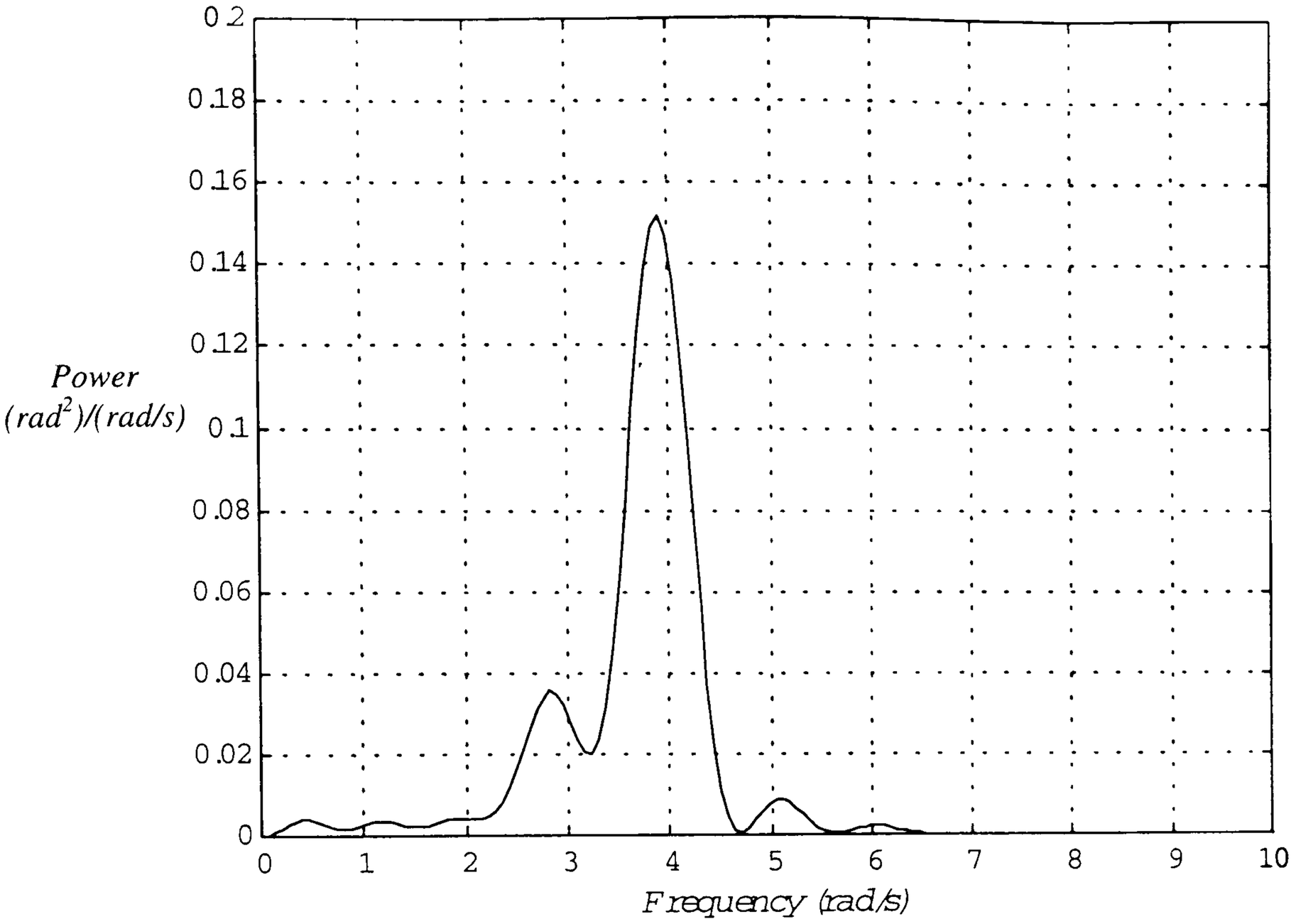

Figure 5.18 : **The PSD of the roll angle time history obtained using the original version of GENISA.**

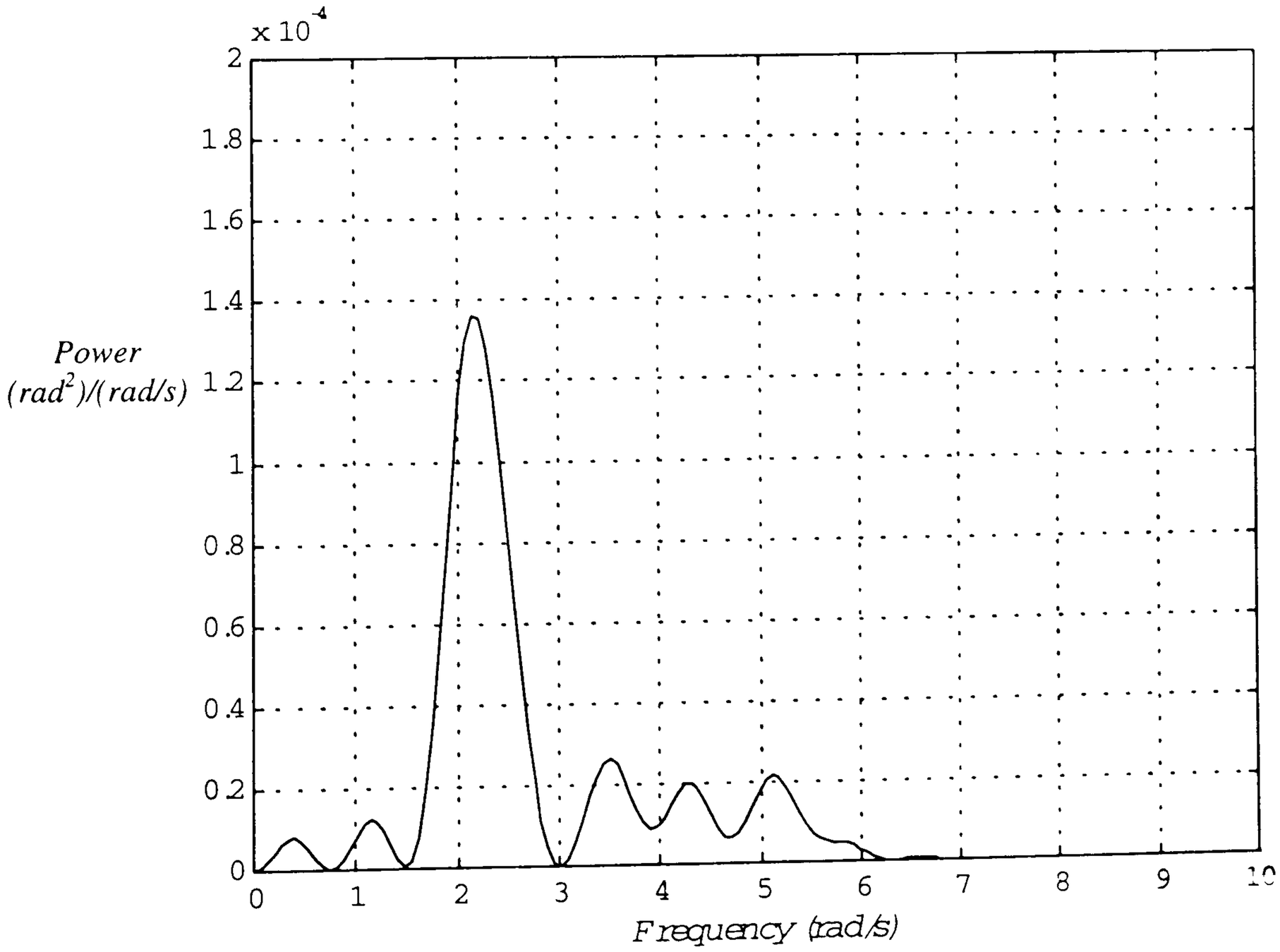

Figure 5.19 : **PSD of the roll angle time history using the modified version of GENISA.**

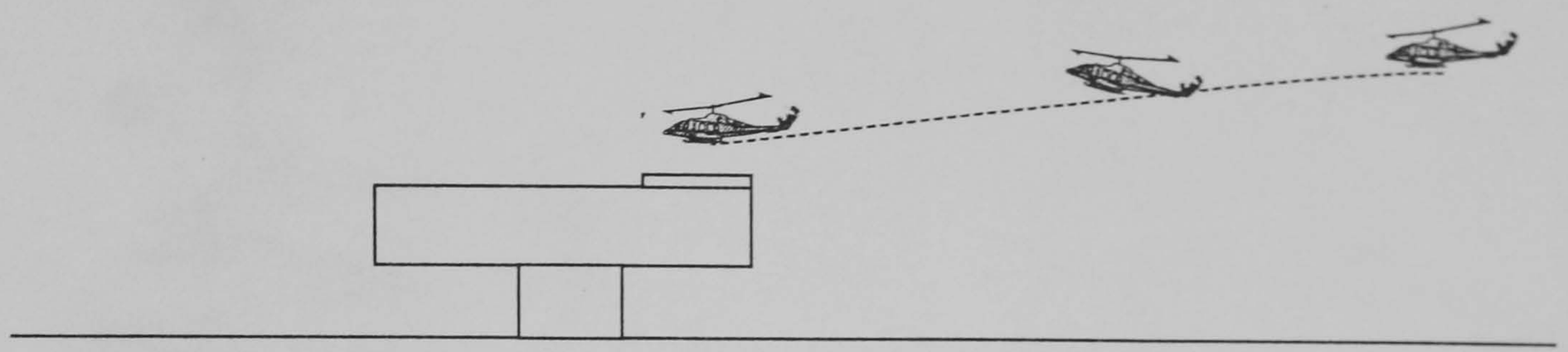

Figure 5.20 : **Manoeuvre profile for the test case flare to hover inside the turbulence field of the flow around a supported oil platform.**

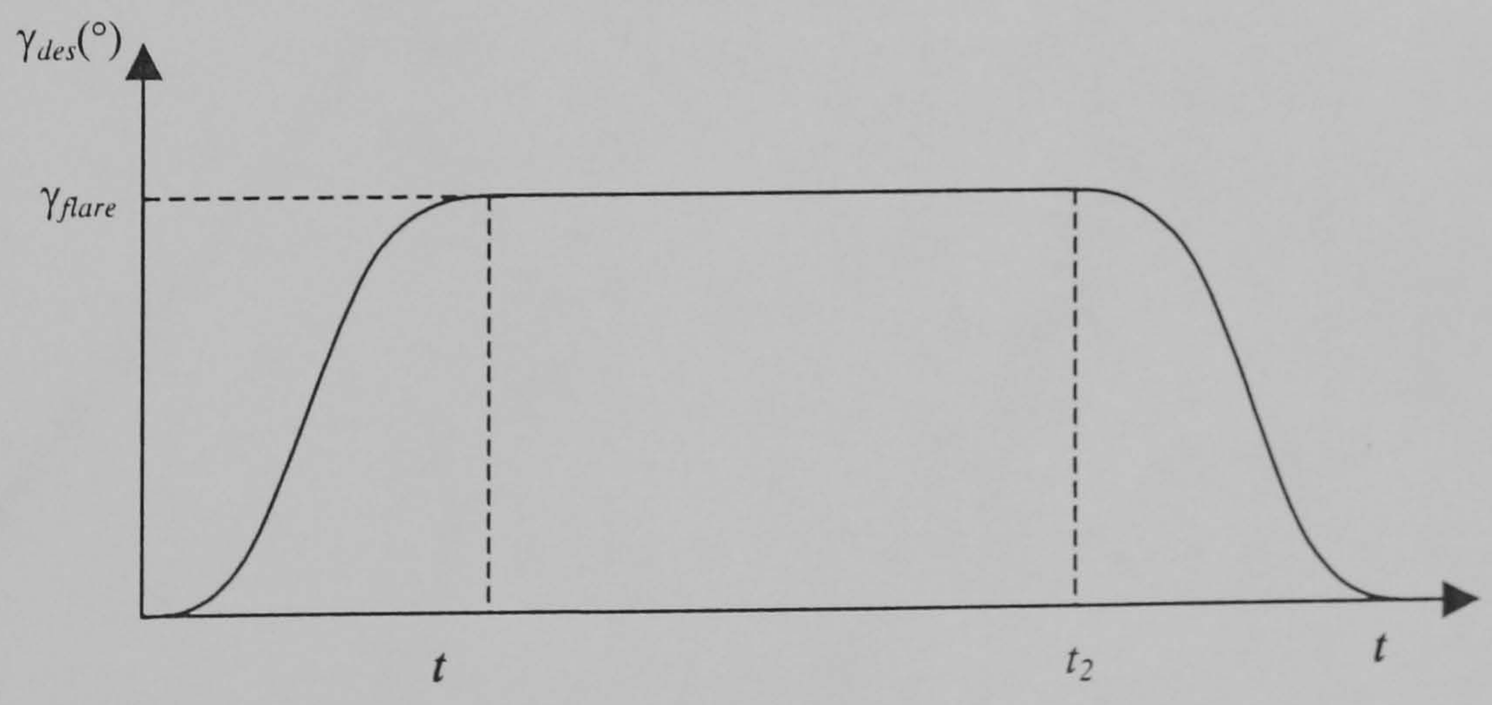

Figure 5.21 : **Piecewise polynomial of the desired flight path for the flare to hover manoeuvre.**

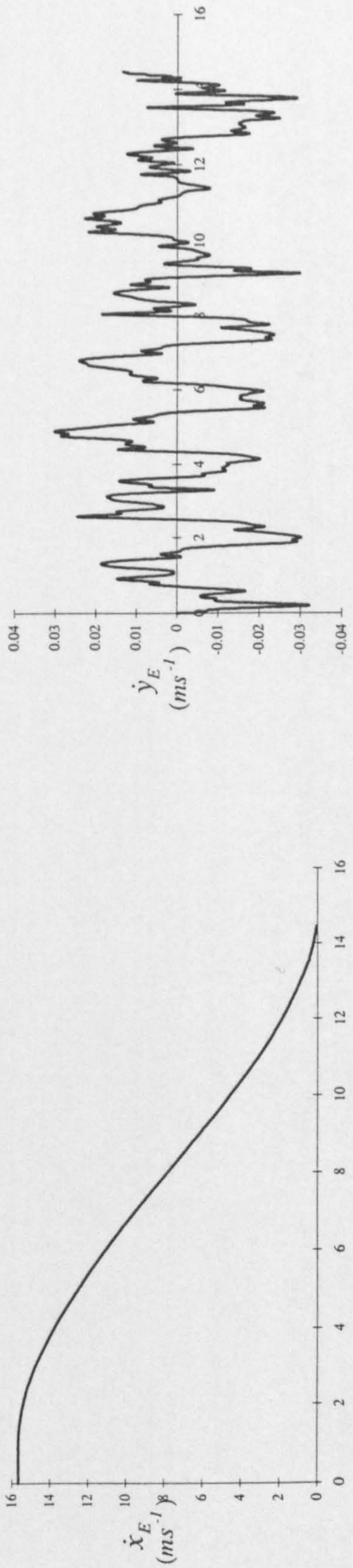

Figure 5.22 : Time histories of the primary constraint variables of the Puma flying the flare to hover manoeuvre on approach to an offshore oil platform.

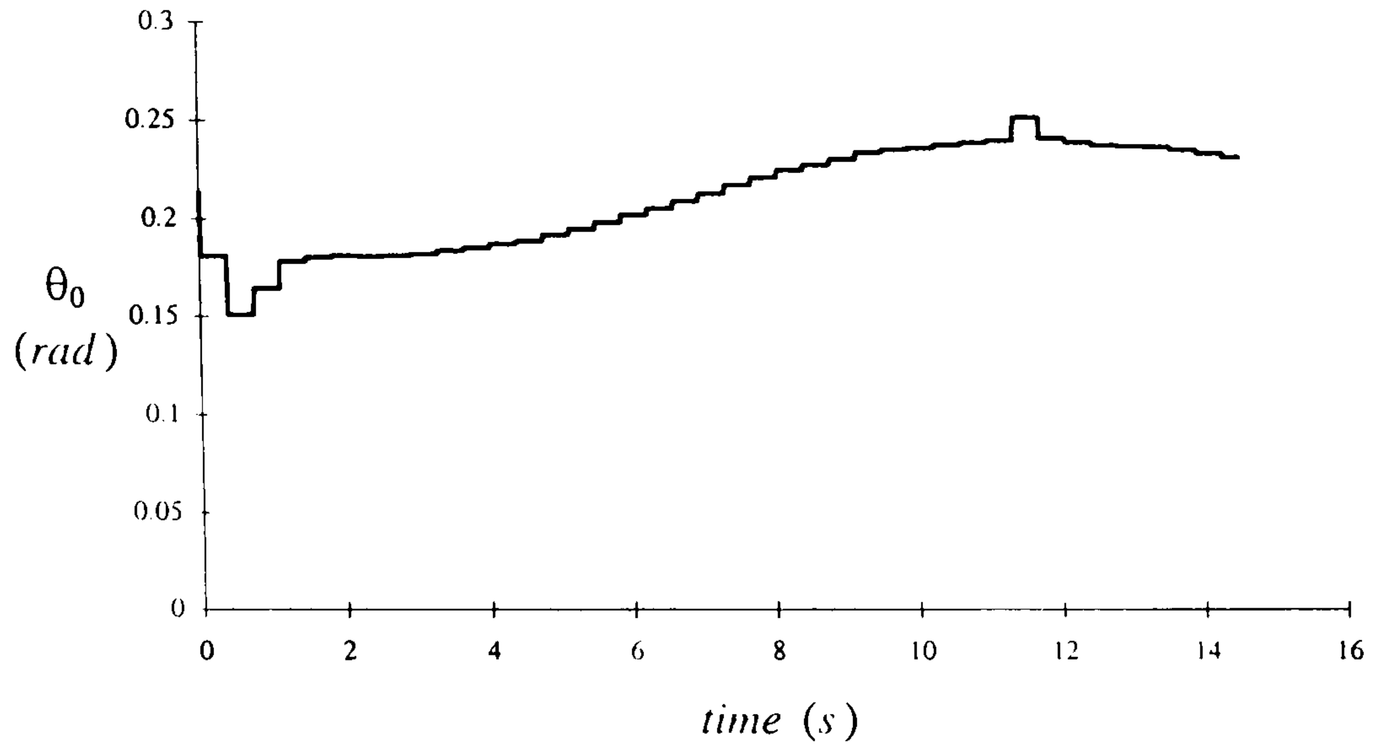

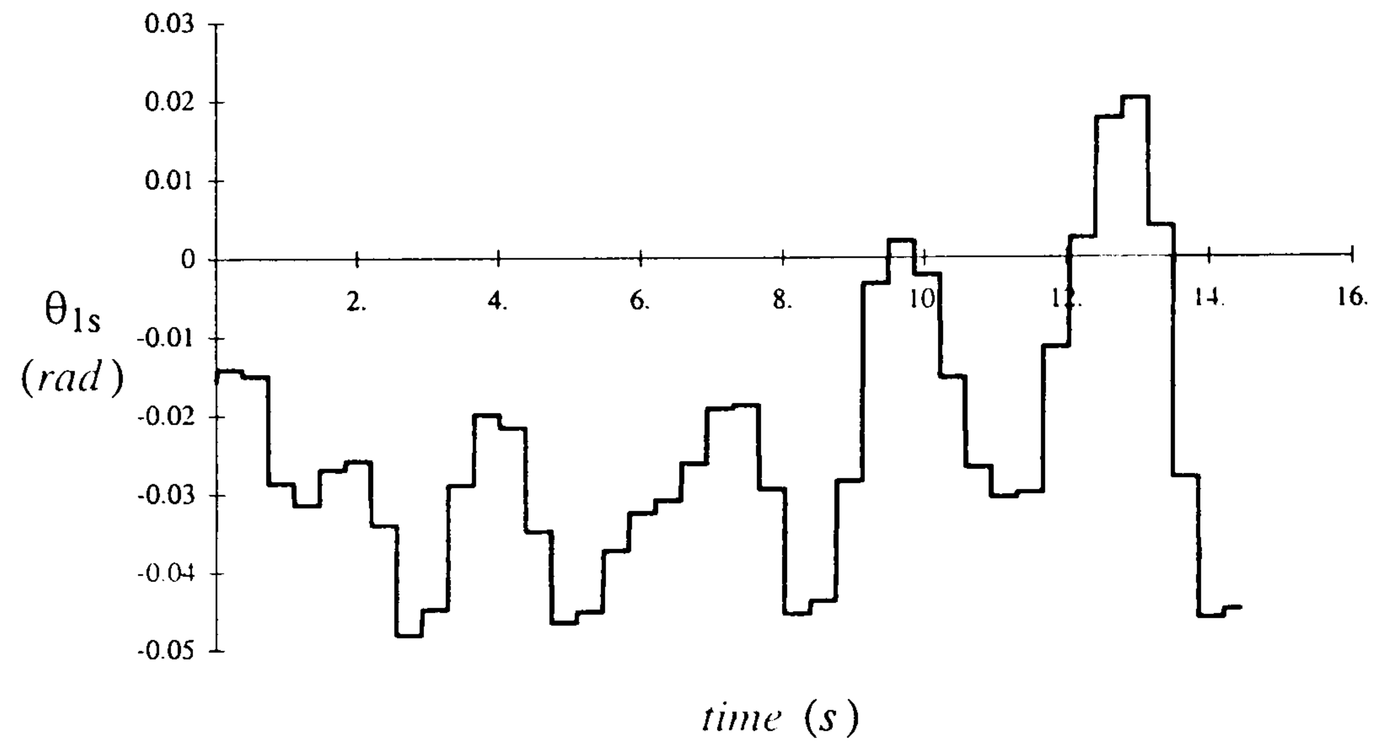

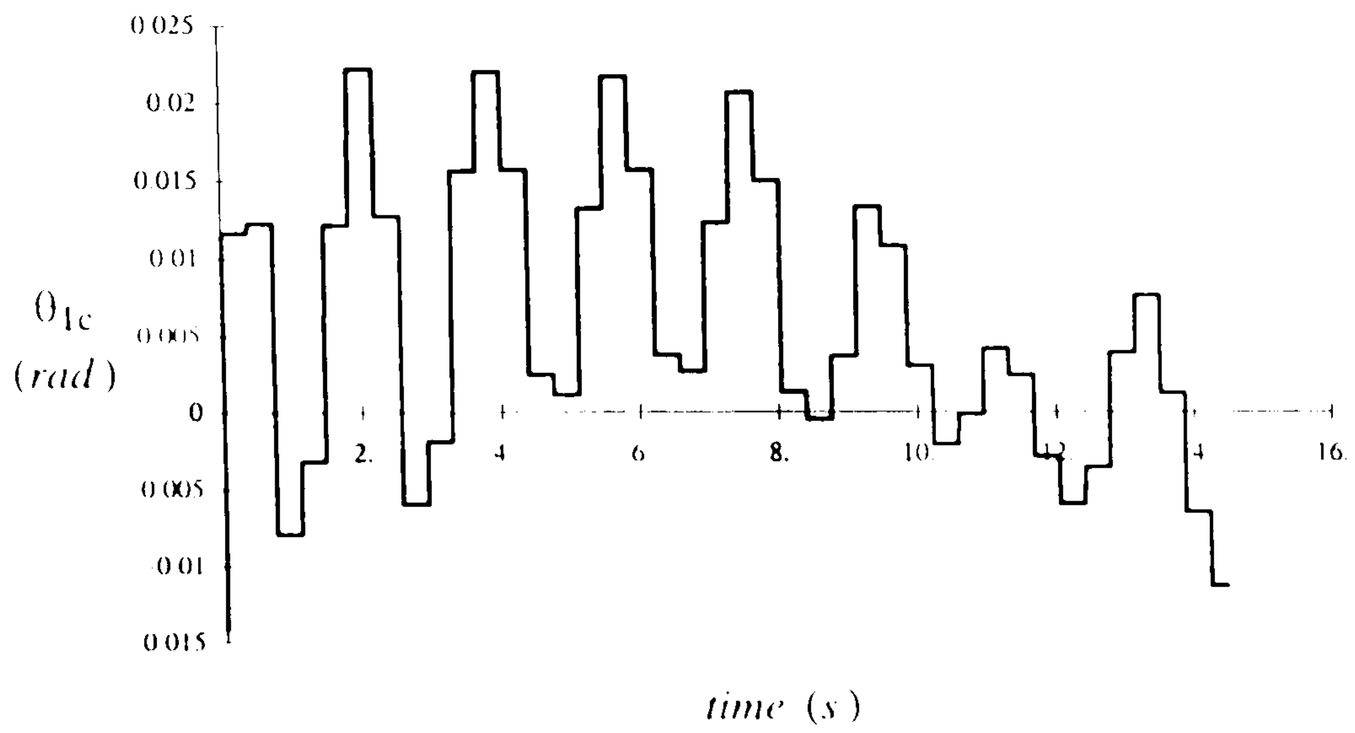

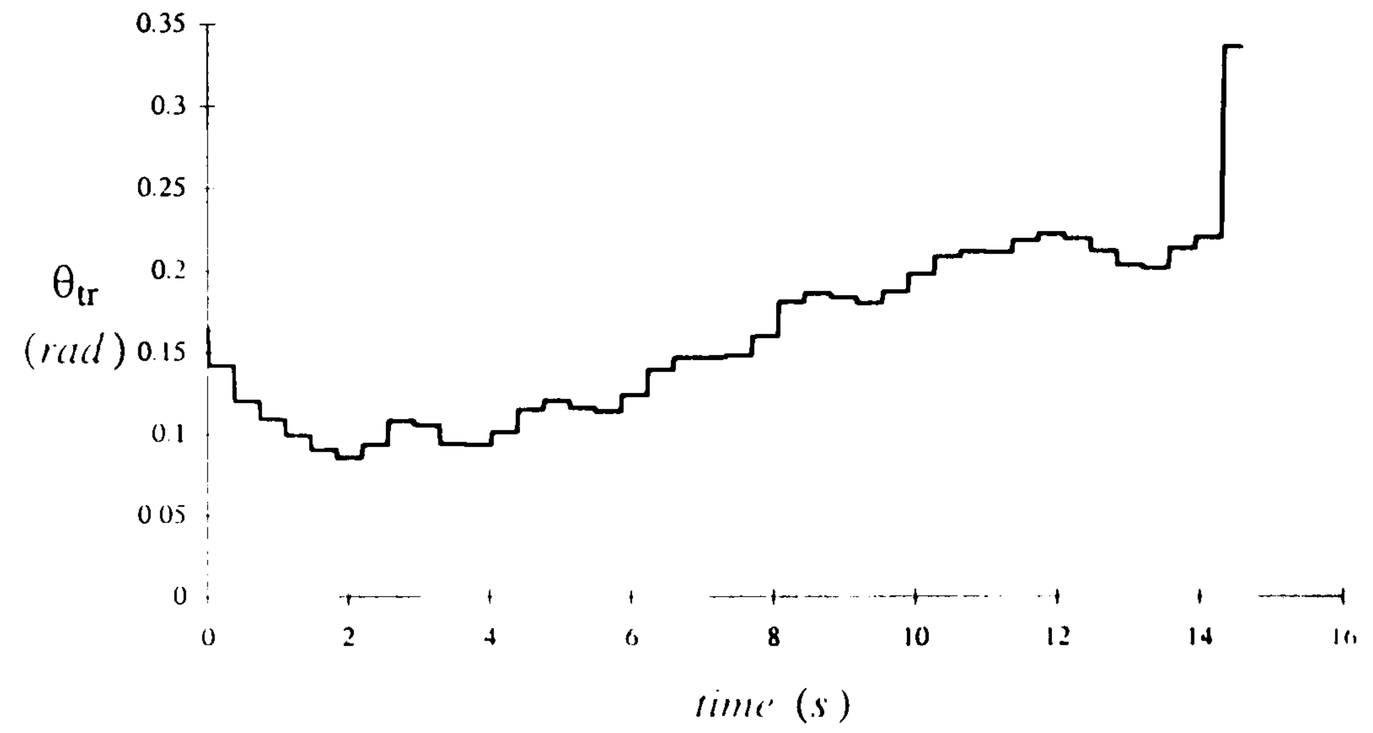

Figure 5.23 : **Time histories of the control inputs of the Puma flying the flare to hover manoeuvre on approach to an offshore oil platform.**

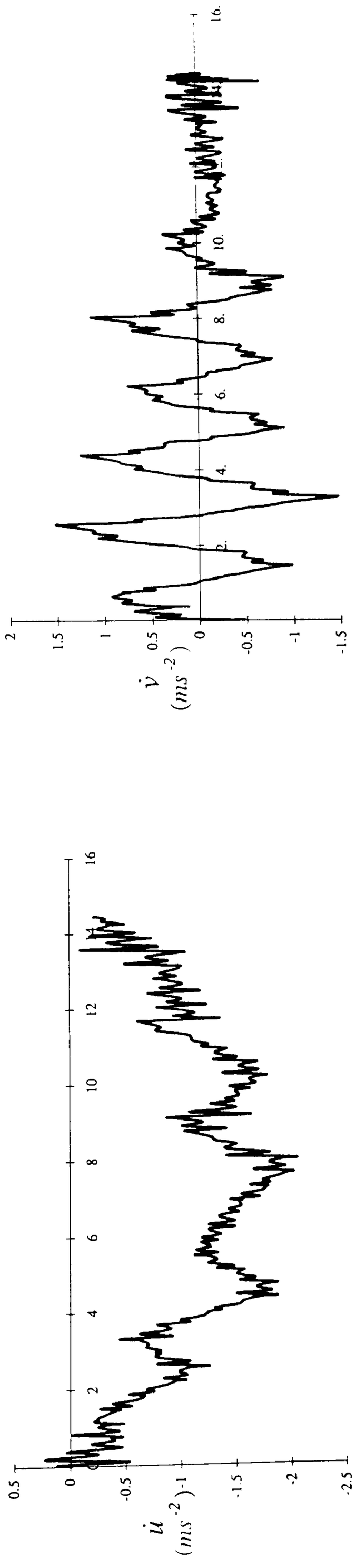

Figure 5.24 : Time histories of the body axes accelerations of the Puma flying the flare to hover manoeuvre on approach to an offshore oil platform.

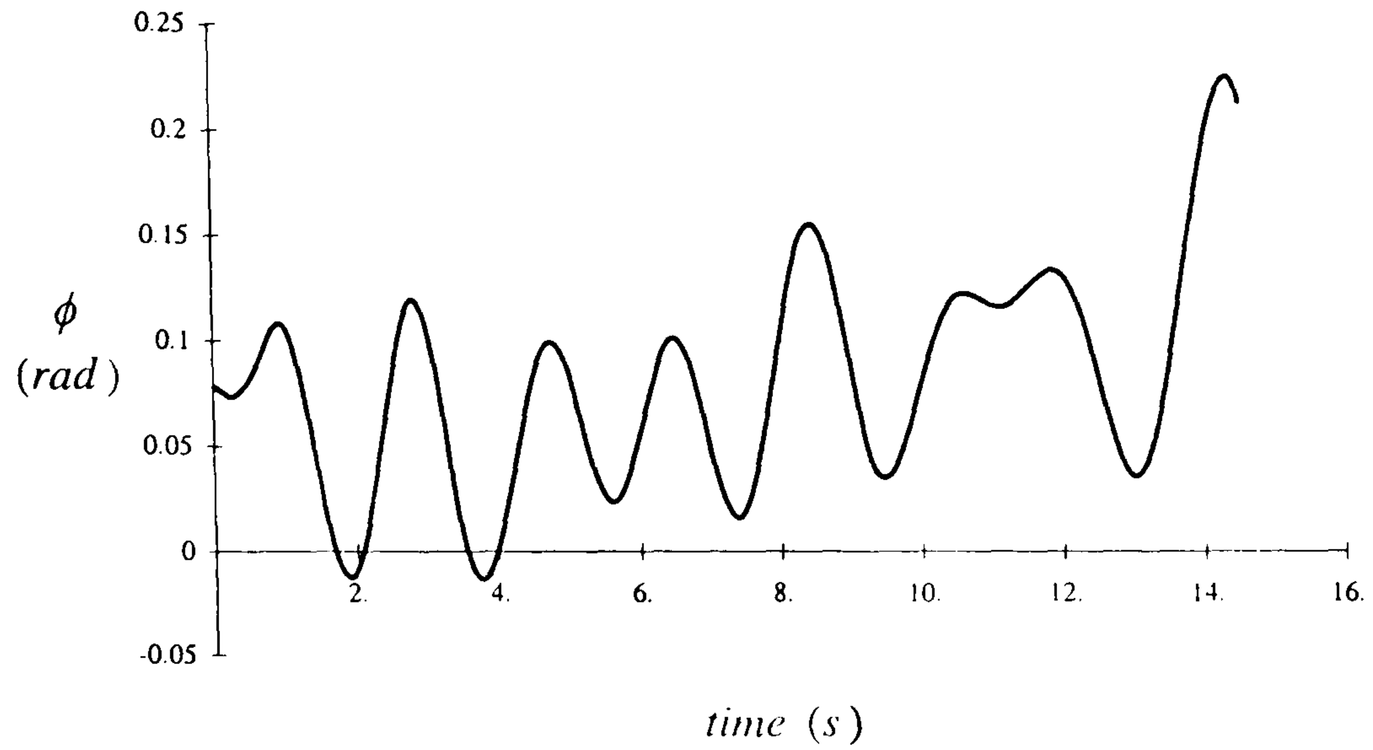

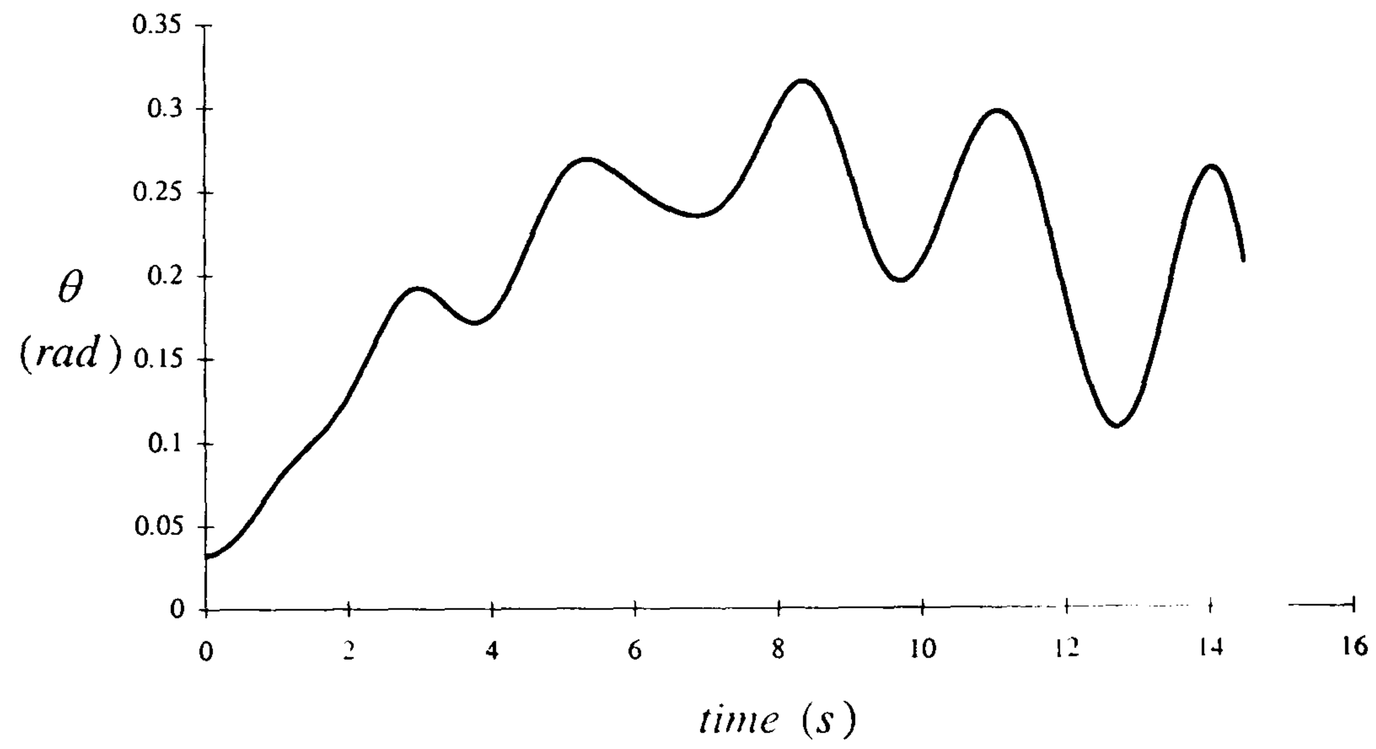

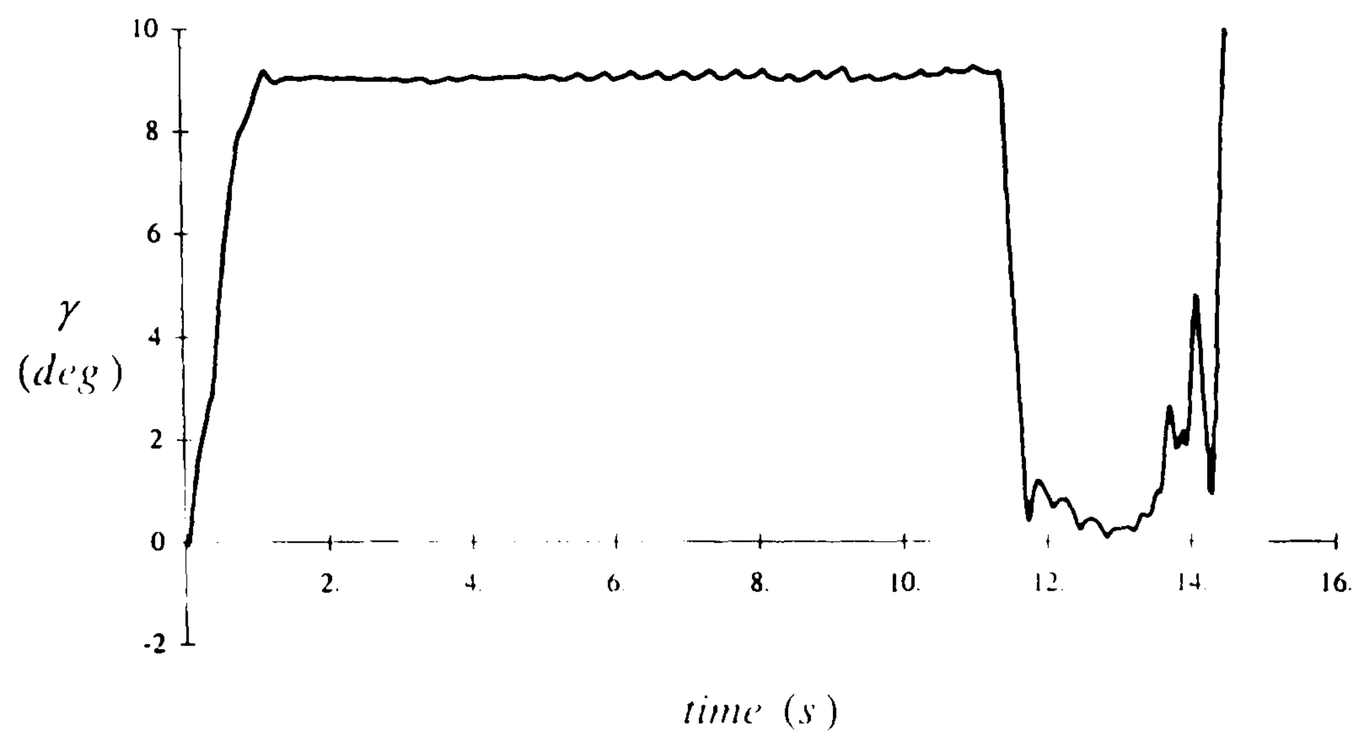

Figure 5.25 : **Time histories of the body axes attitudes and flight path angle of the Puma flying the flare to hover manoeuvre on approach to an offshore oil platform.**

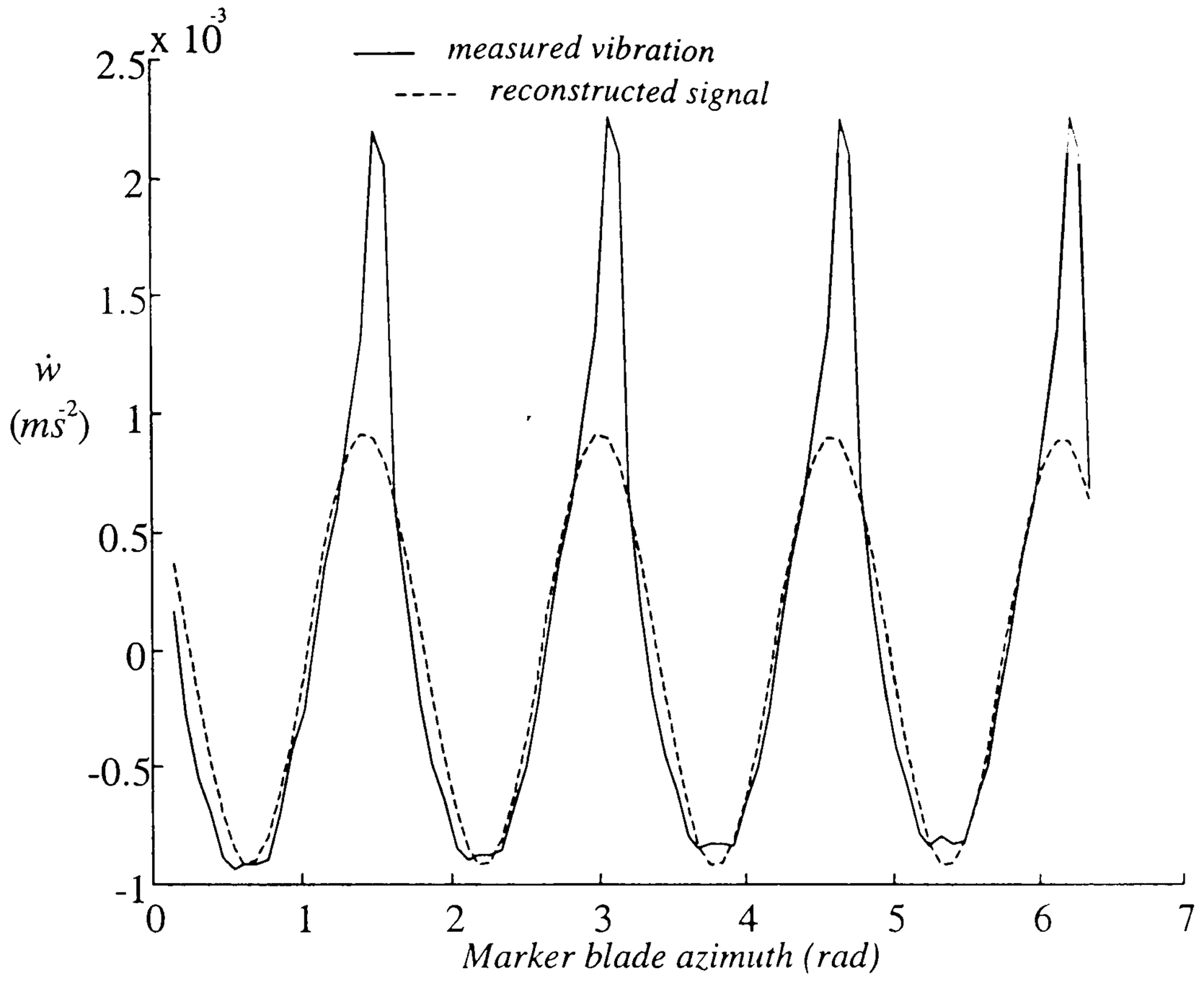

Figure (6.1) : **Vibration signal reconstructed from the N/rev Fourier coefficients obtained from harmonic analysis.**

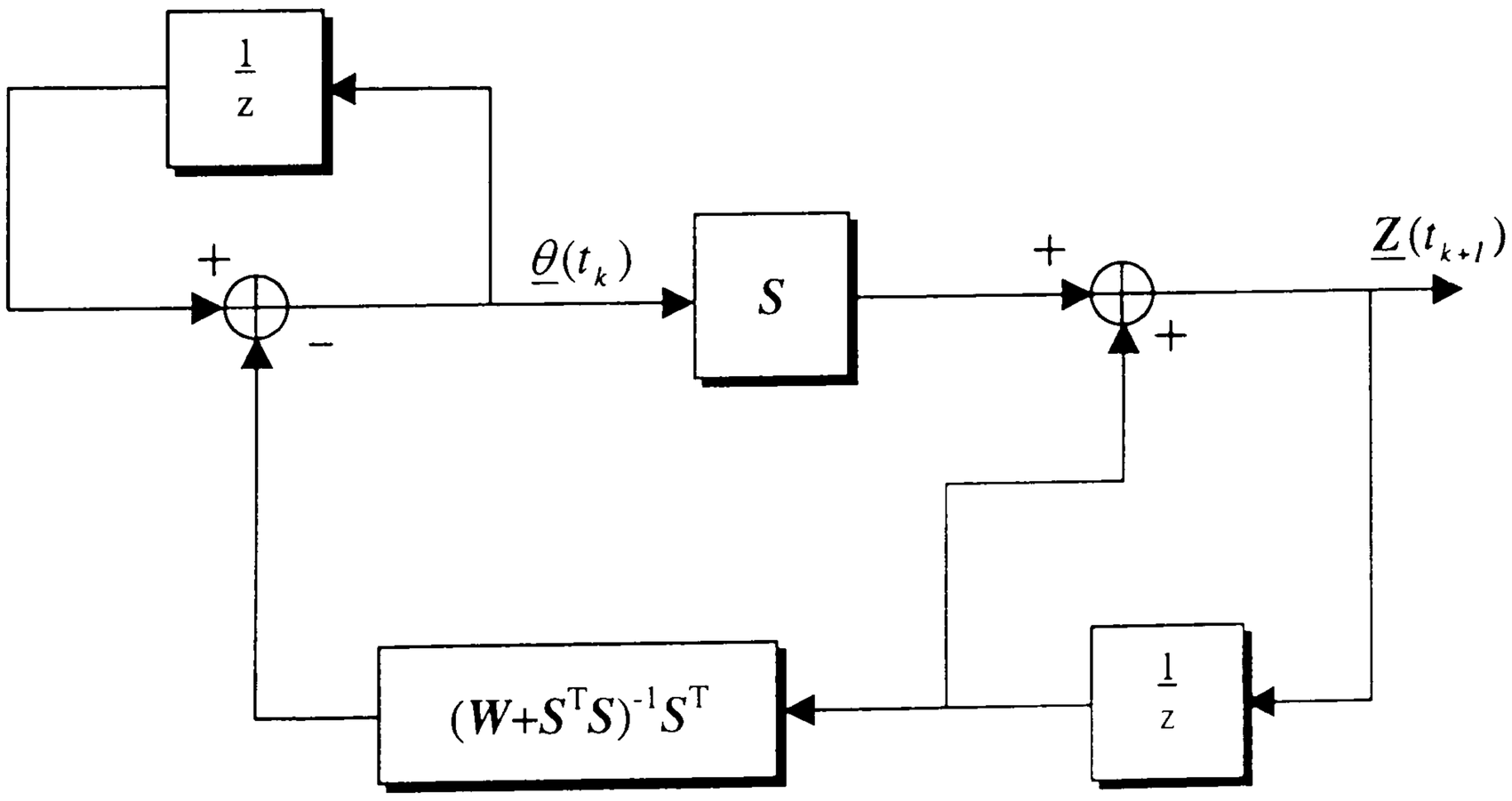

Figure (6.2) : **Block diagram of the variational Higher Harmonic Control algorithm. The blocks containing 1/z are unit time delays in the digital domain.**

Figure (6.3) : **Time History Illustrating the Performance of the Optimal HHC algorithm in attenuating still-air vibration at 20knots.**

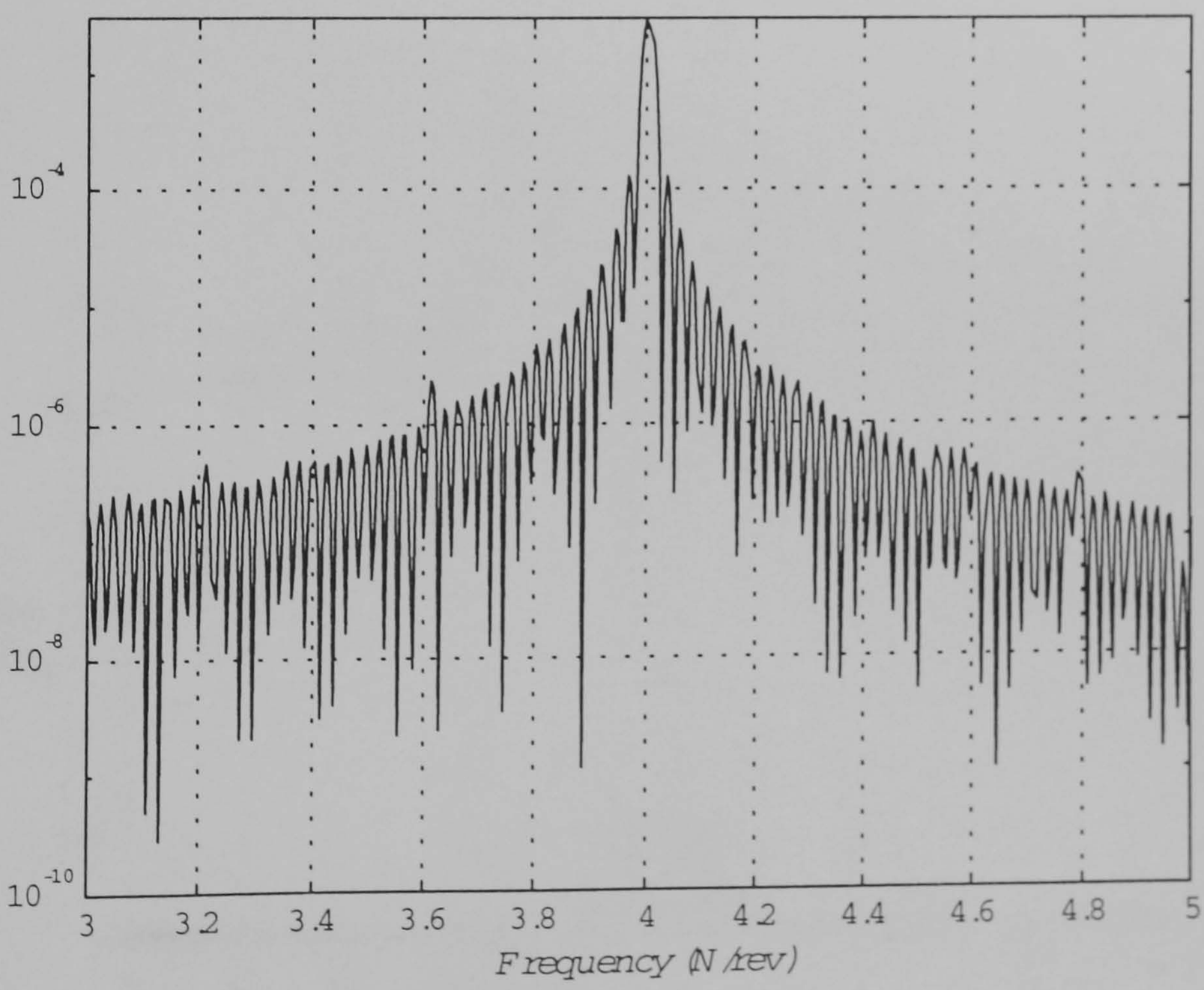

Figure (6.4) : **Power Spectral Density plot of uncontrolled still-air vibration at 20knots.**

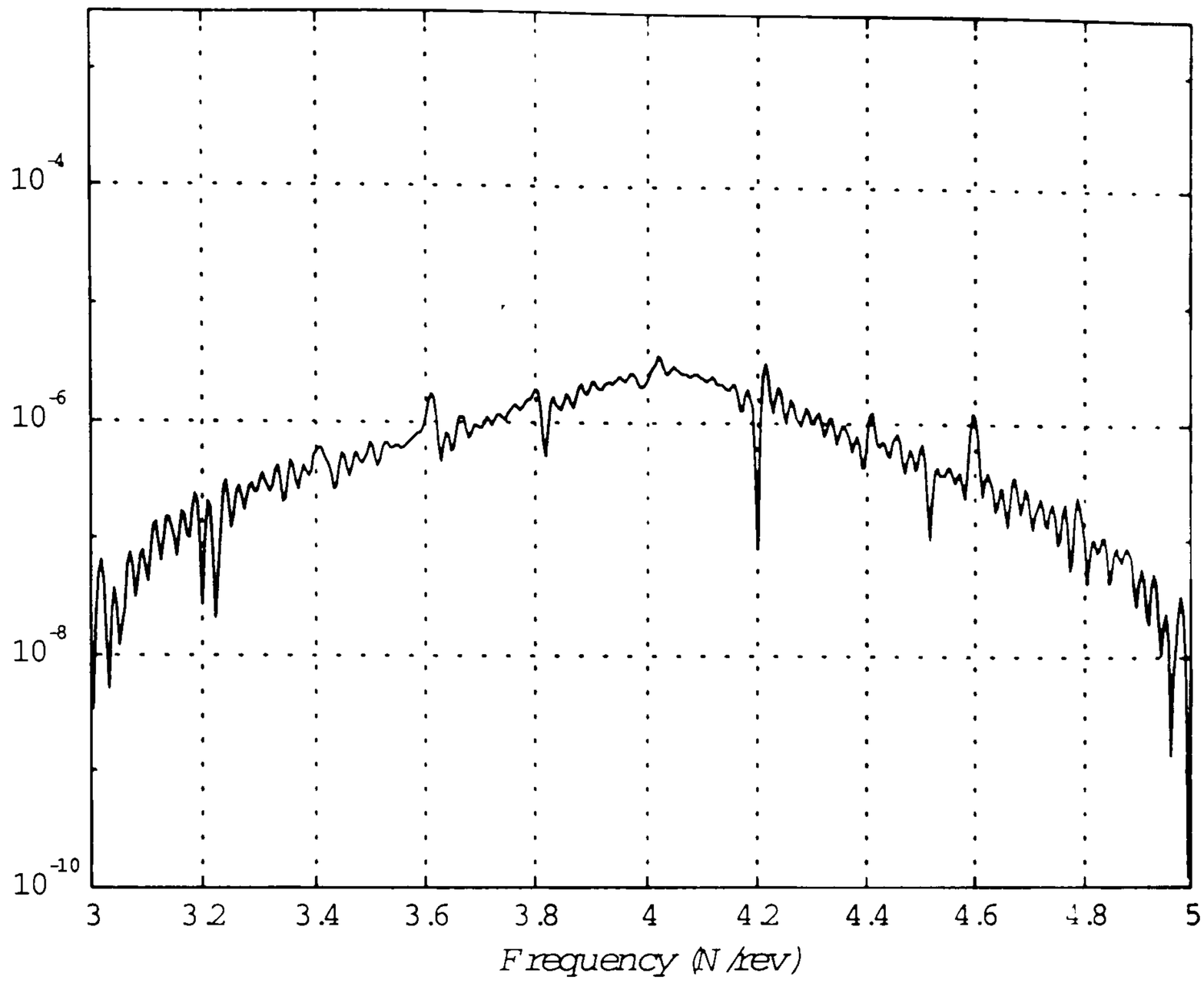

Figure (6.5) : **Power Spectral Density plot of still-air vibration at 20knots with HHC algorithm operating.**

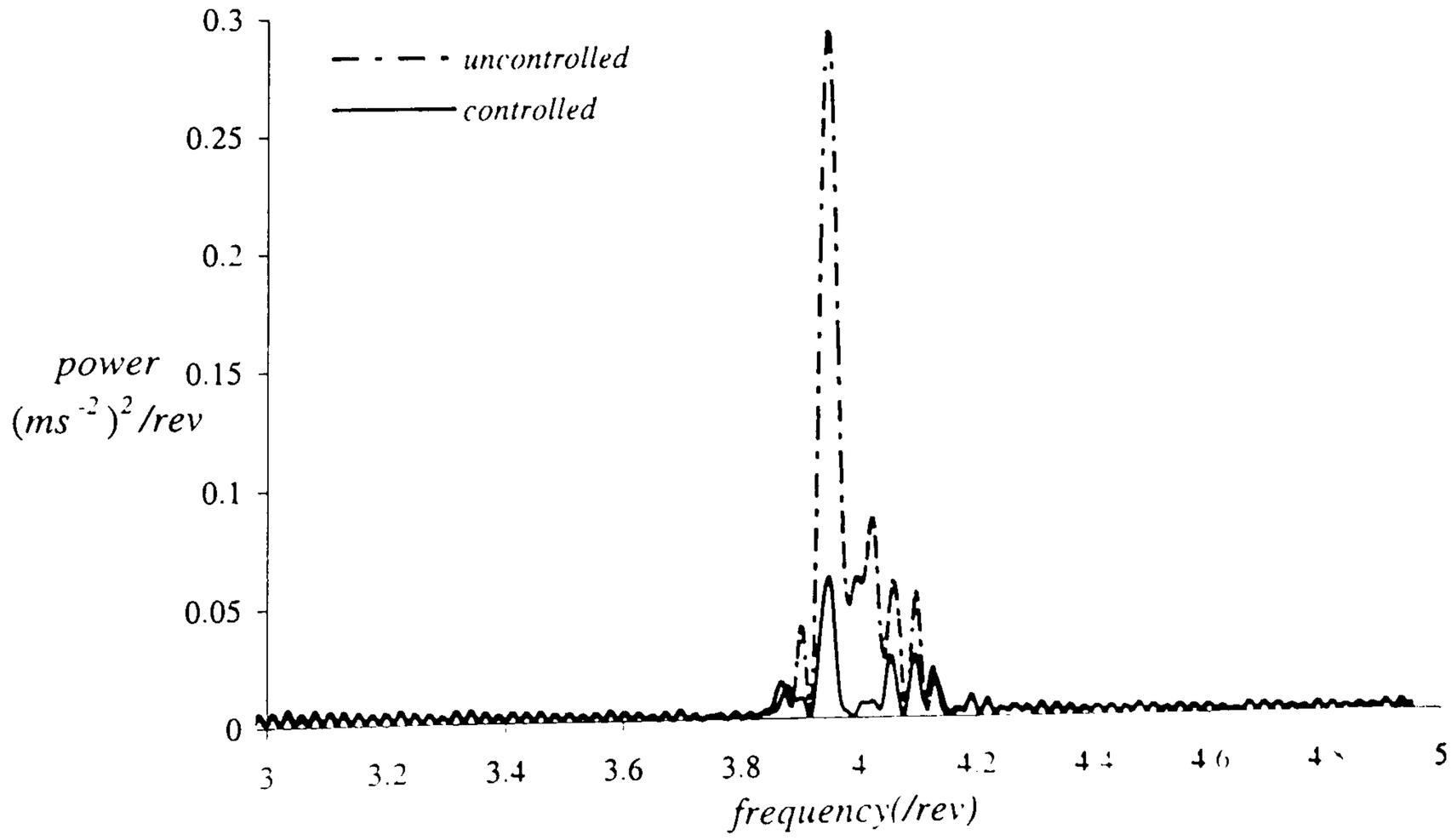

Figure 6.6 : **Effectiveness of the optimal HHC to gust-induced vibration at 5 knots.**

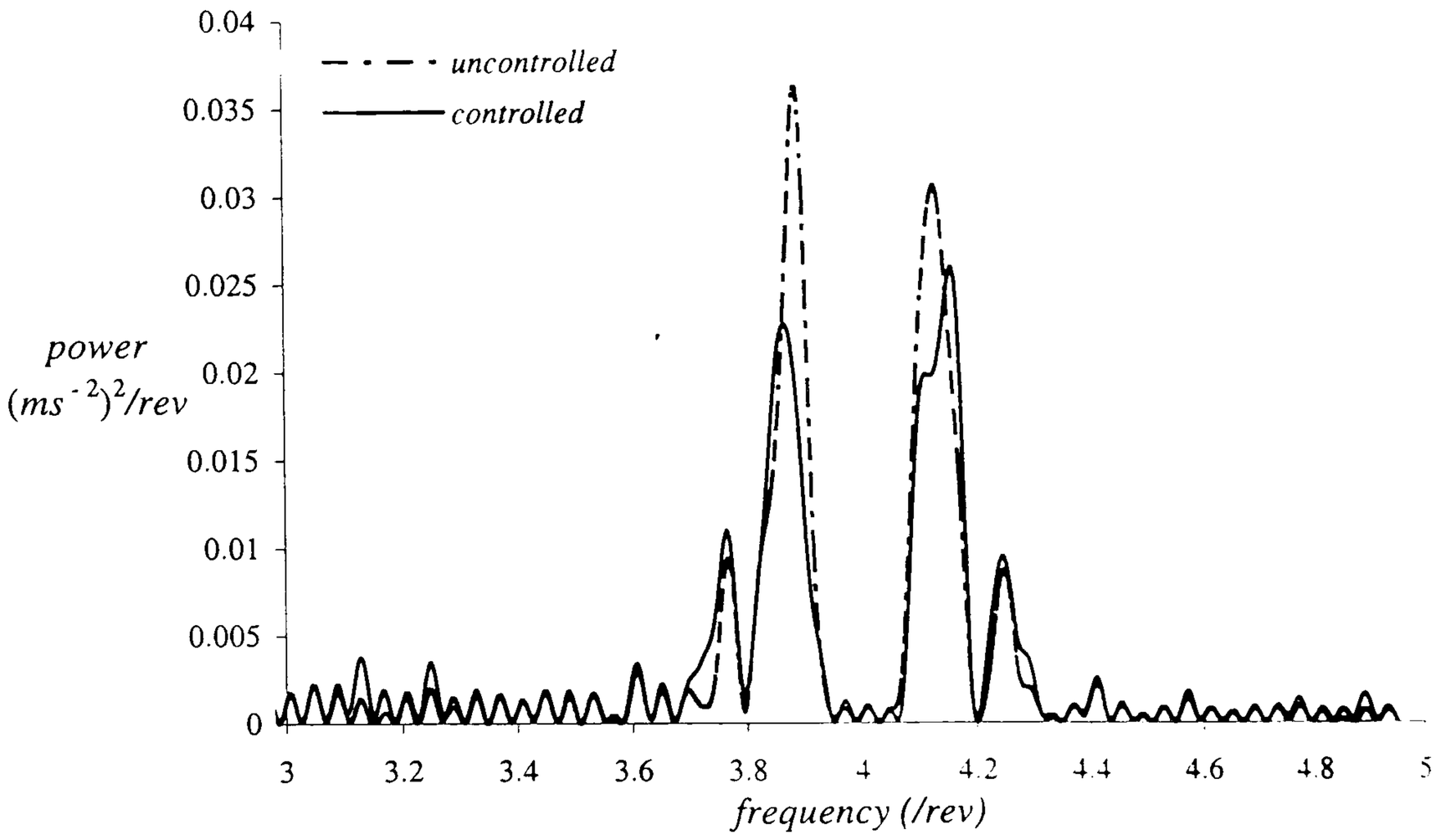

Figure 6.7 : **Effectiveness of the optimal HHC to gust-induced vibration at 10 knots.**

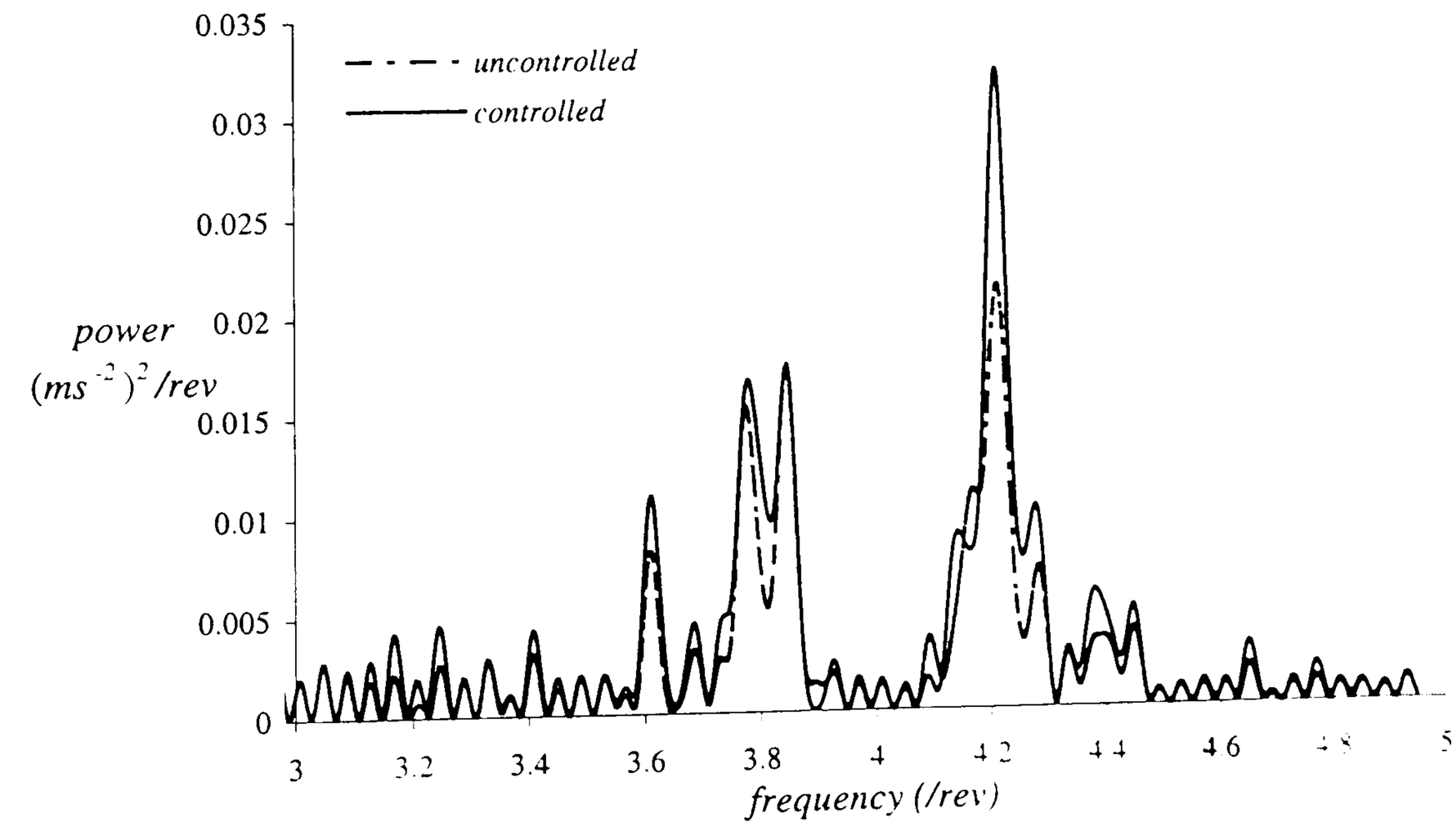

Figure 6.8 : **Effectiveness of the optimal HHC to gust-induced vibration at 15 knots.**

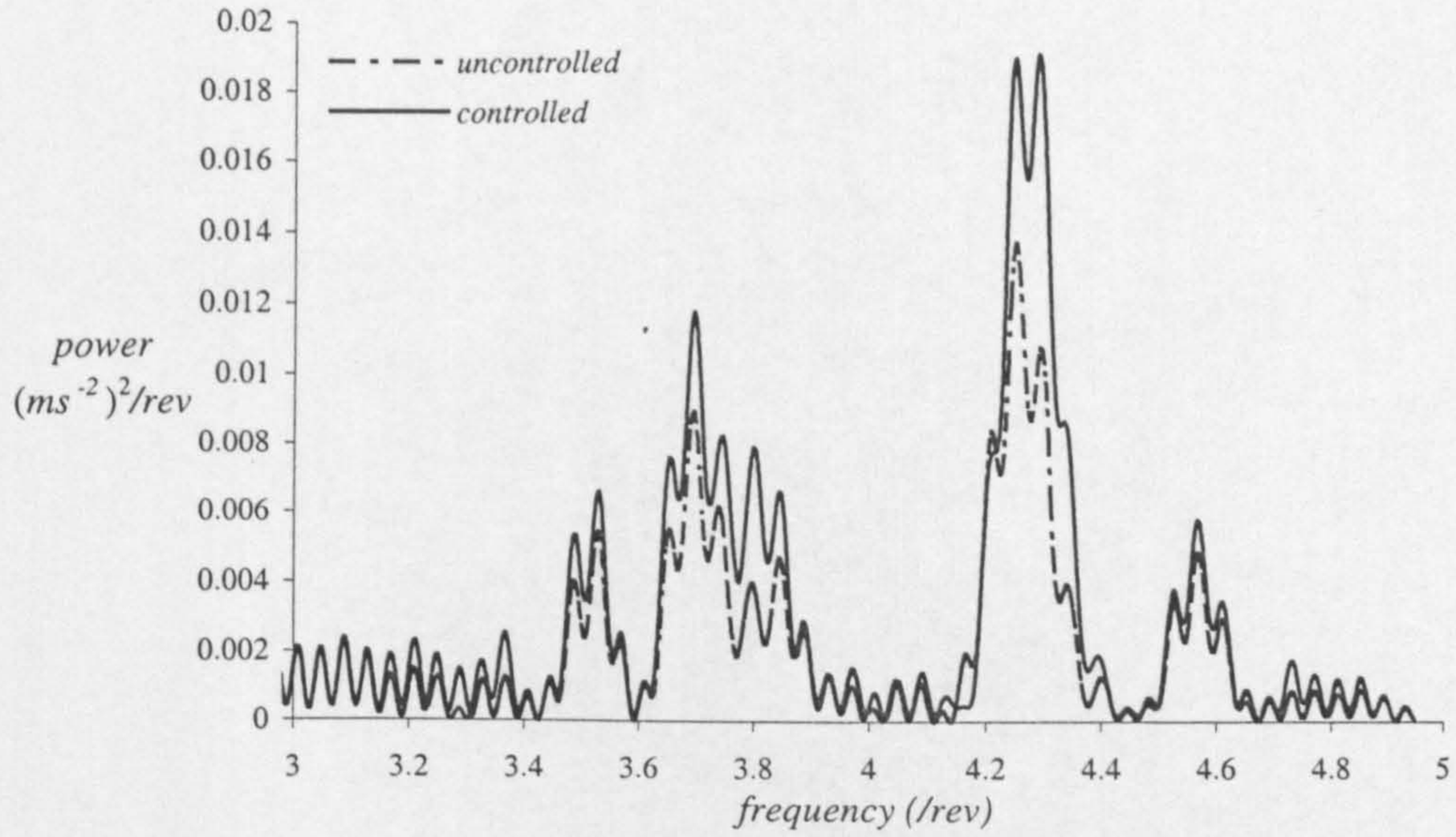

Figure 6.9 : **Effectiveness of the optimal HHC to gust-induced vibration at 20 knots.**

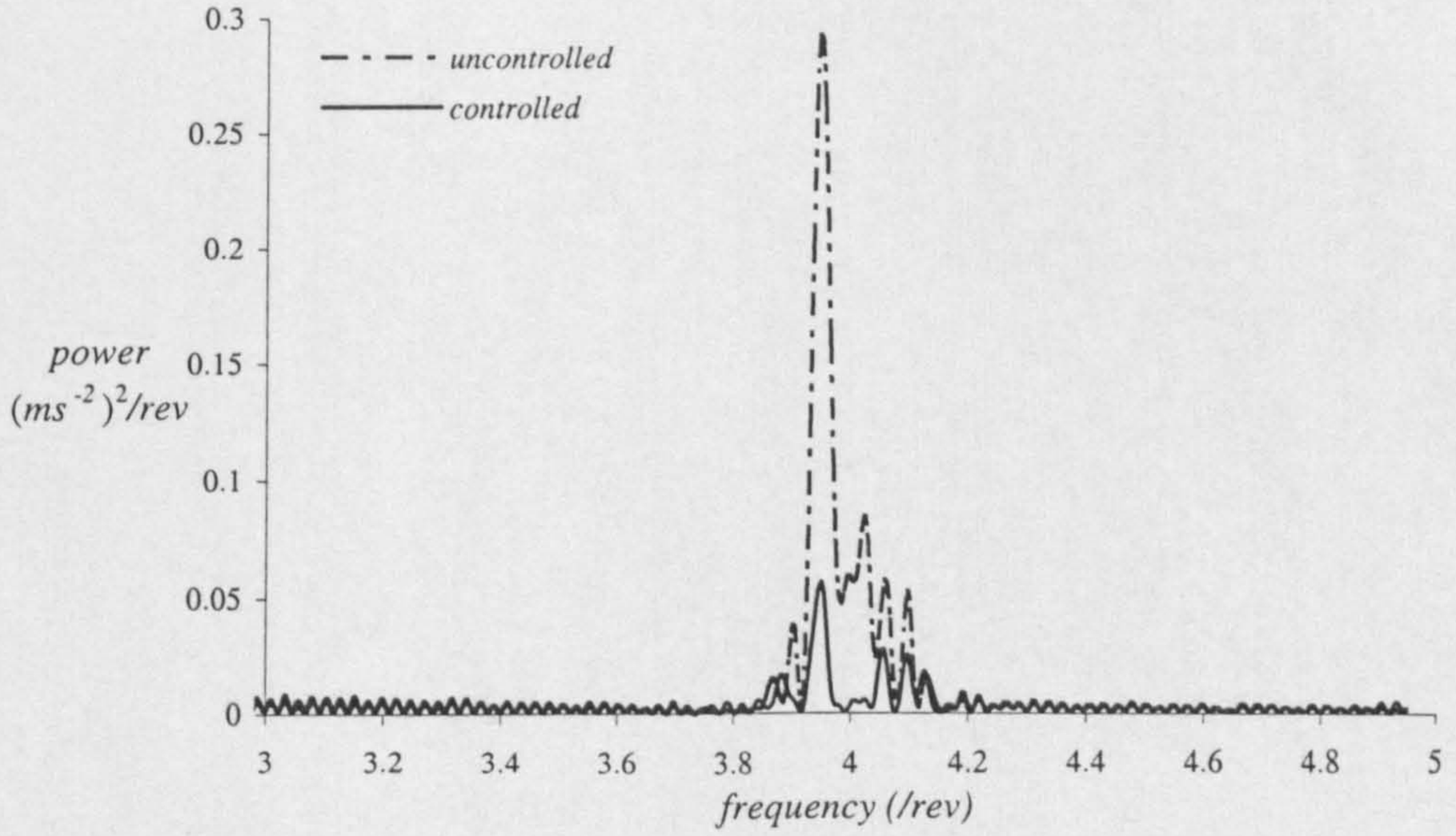

Figure 6.10 : **Effectiveness of the multiharmonic optimal HHC to gust-induced vibration at 5 knots.**

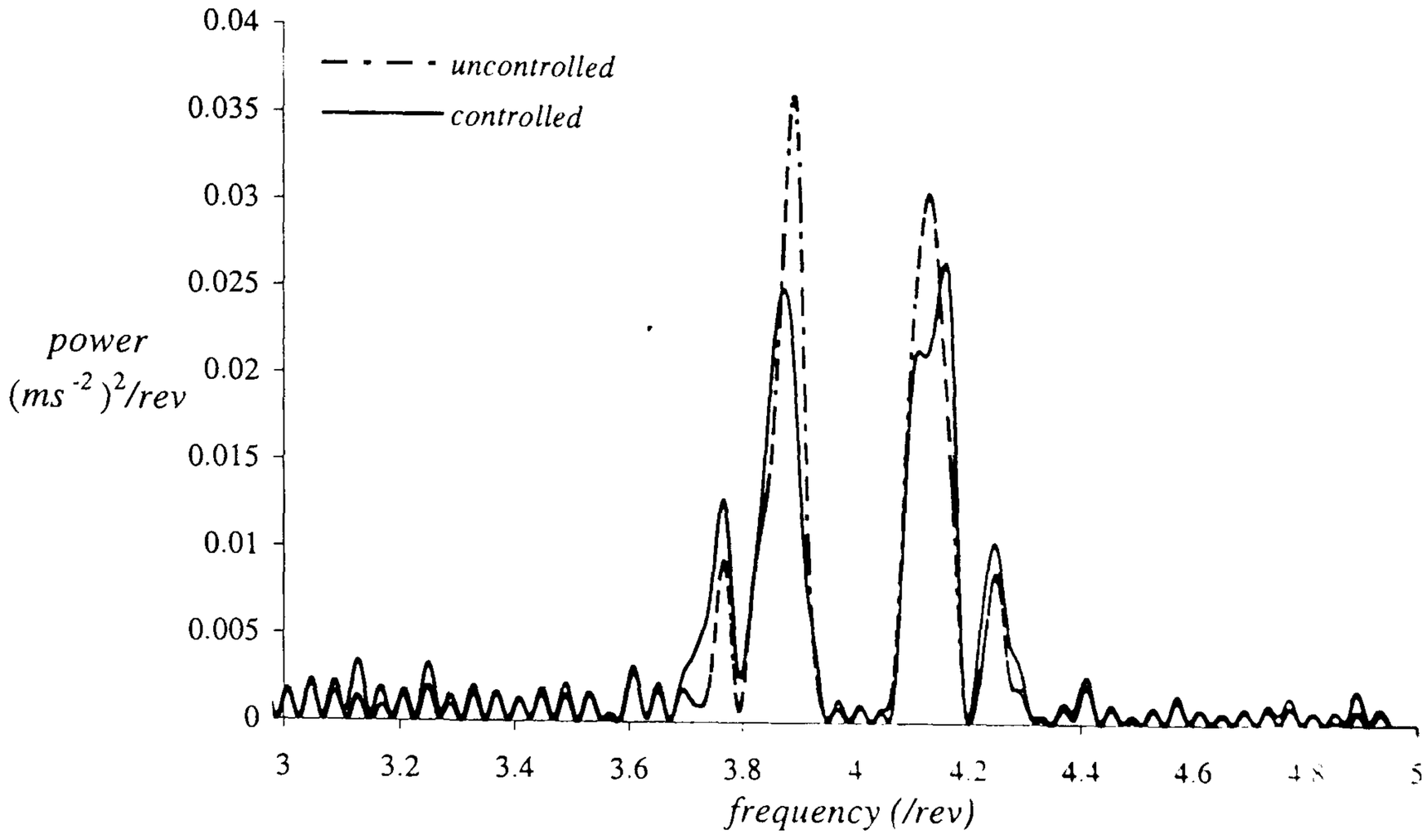

Figure 6.11 : **Effectiveness of the multiharmonic optimal HHC to gust-induced vibration at 10 knots.**

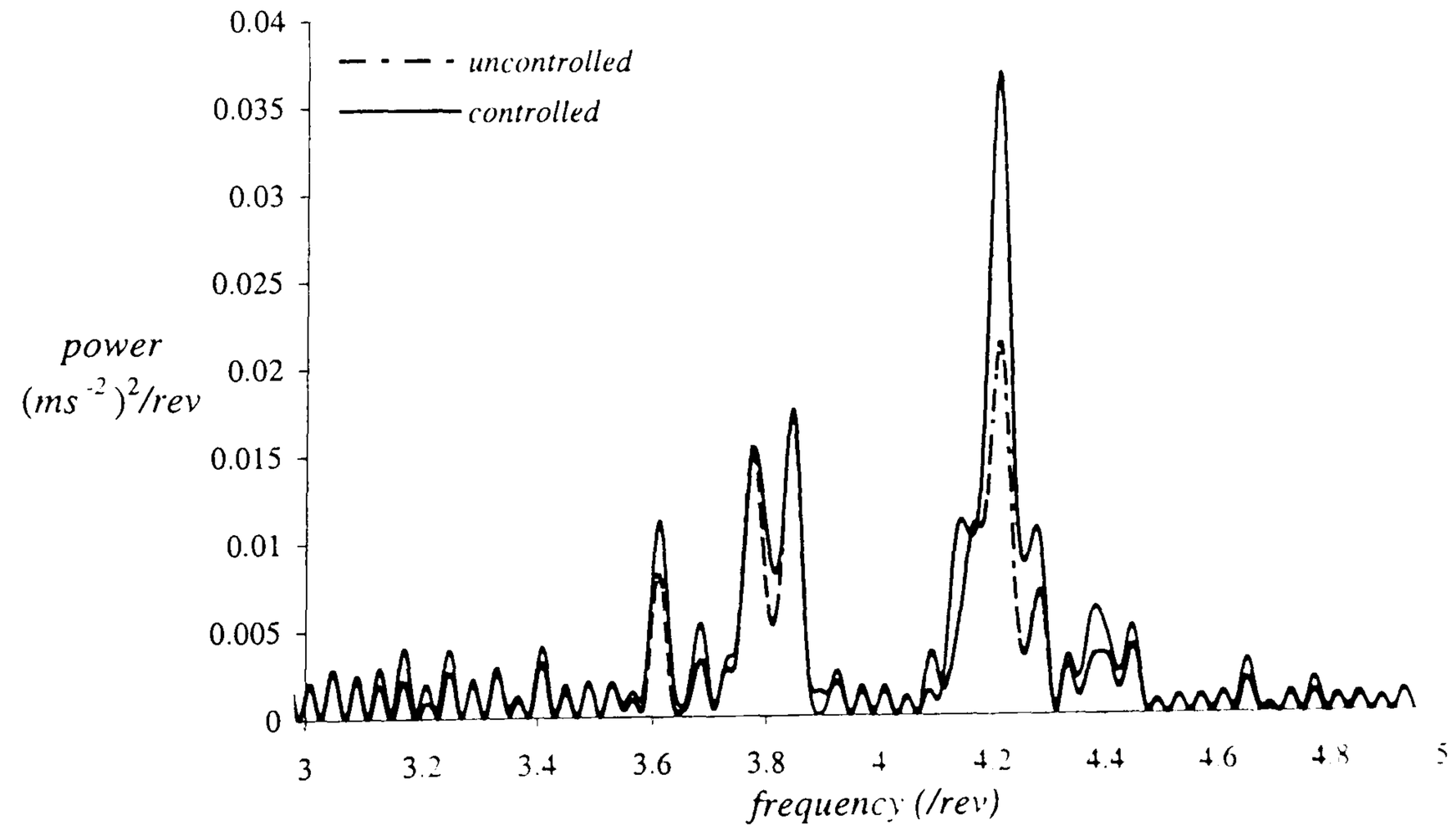

Figure 6.12 : **Effectiveness of the multiharmonic optimal HHC to gust-induced vibration at 15 knots.**

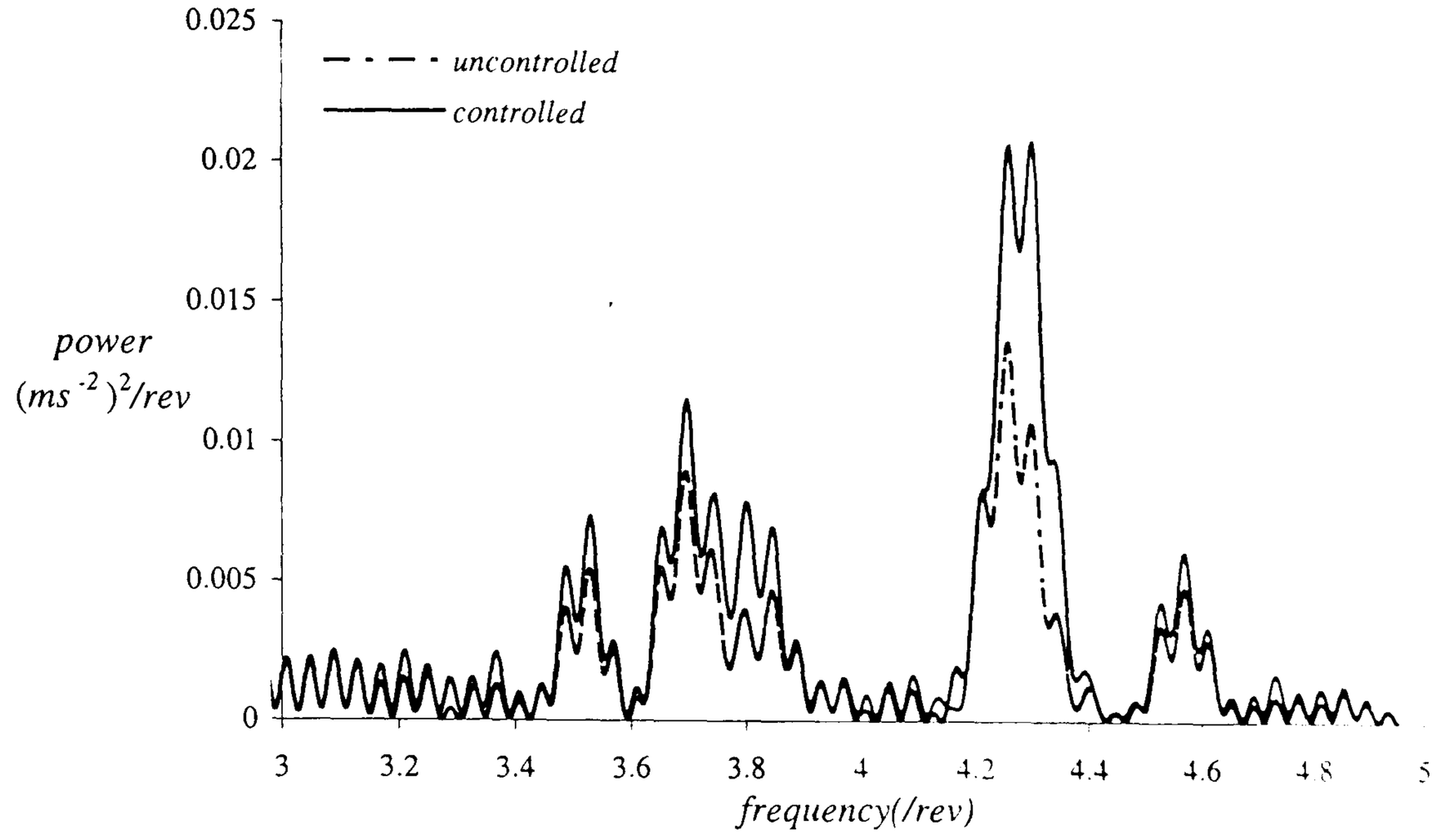

Figure 6.13 : **Effectiveness of the multiharmonic optimal HHC to gust-induced vibration at 20 knots.**

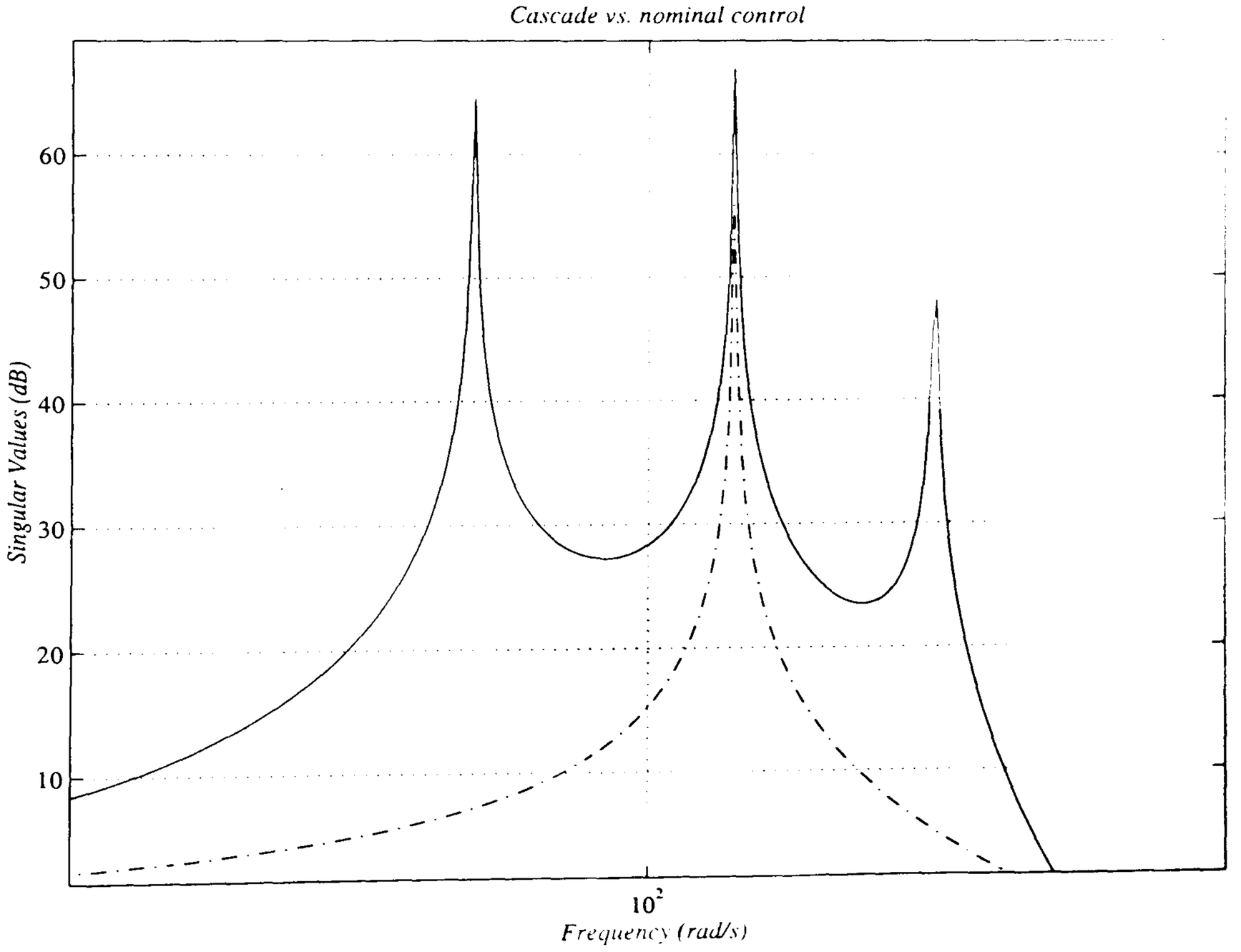

Figure 6.14 : **Bode magnitude plot of 3,4 and 5 /rev harmonic inputs in a cascade arrangement.**

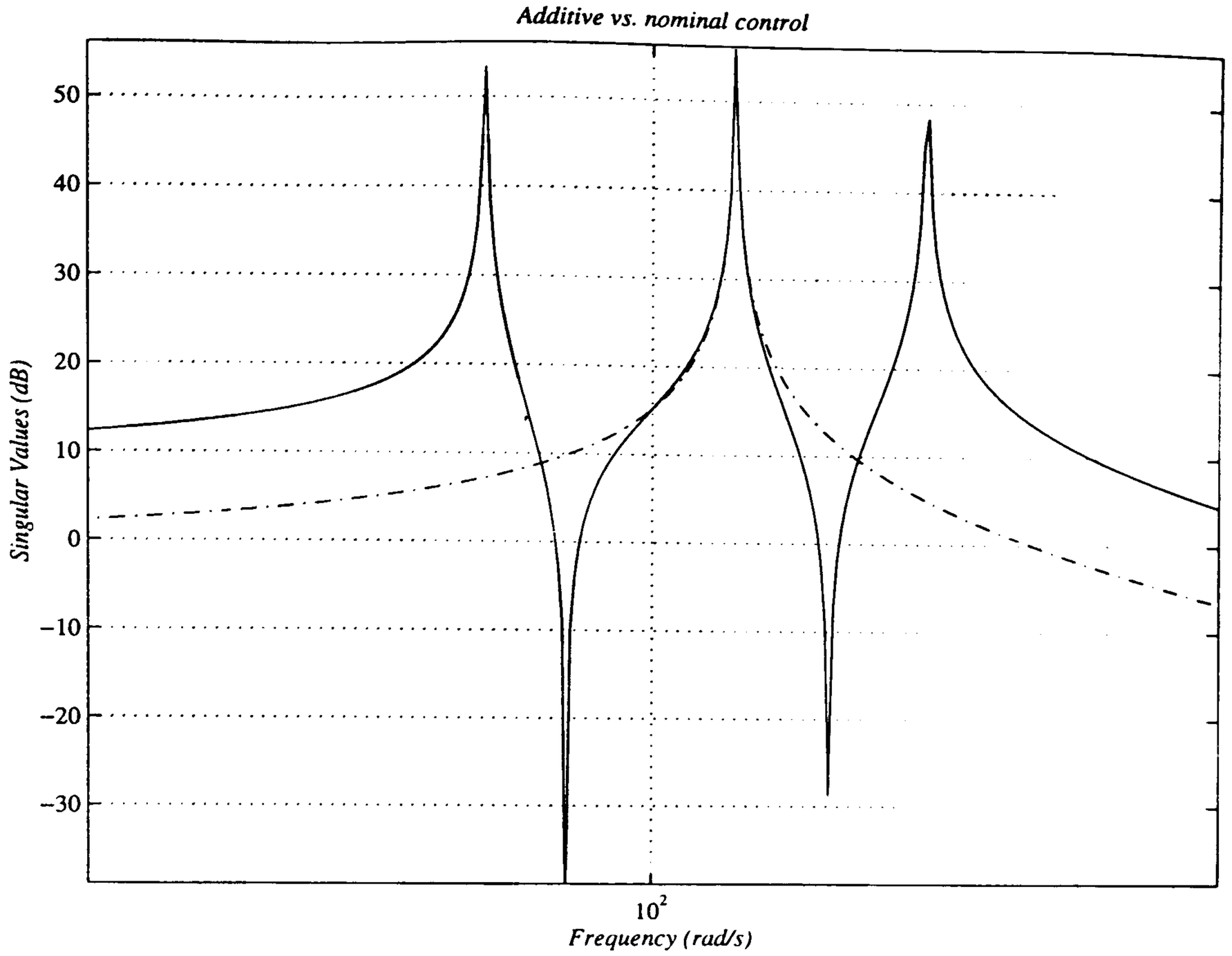

Figure 6.15 : **Bode magnitude plot of 3,4 and 5 /rev harmonic inputs in a parallel summation arrangement.**

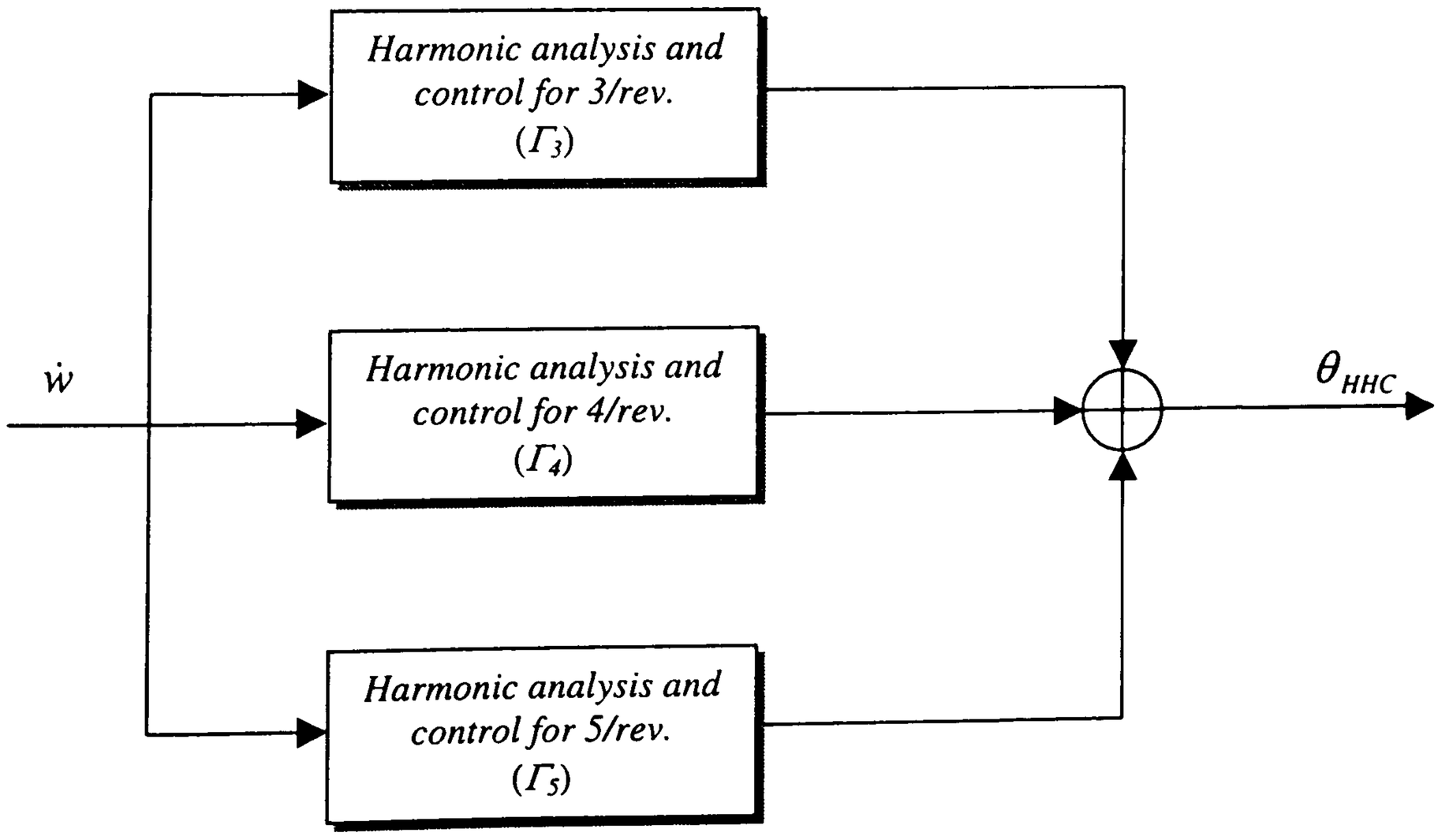

Figure 6.16 : **Block diagram of the linear multi-harmonic control strategy.**

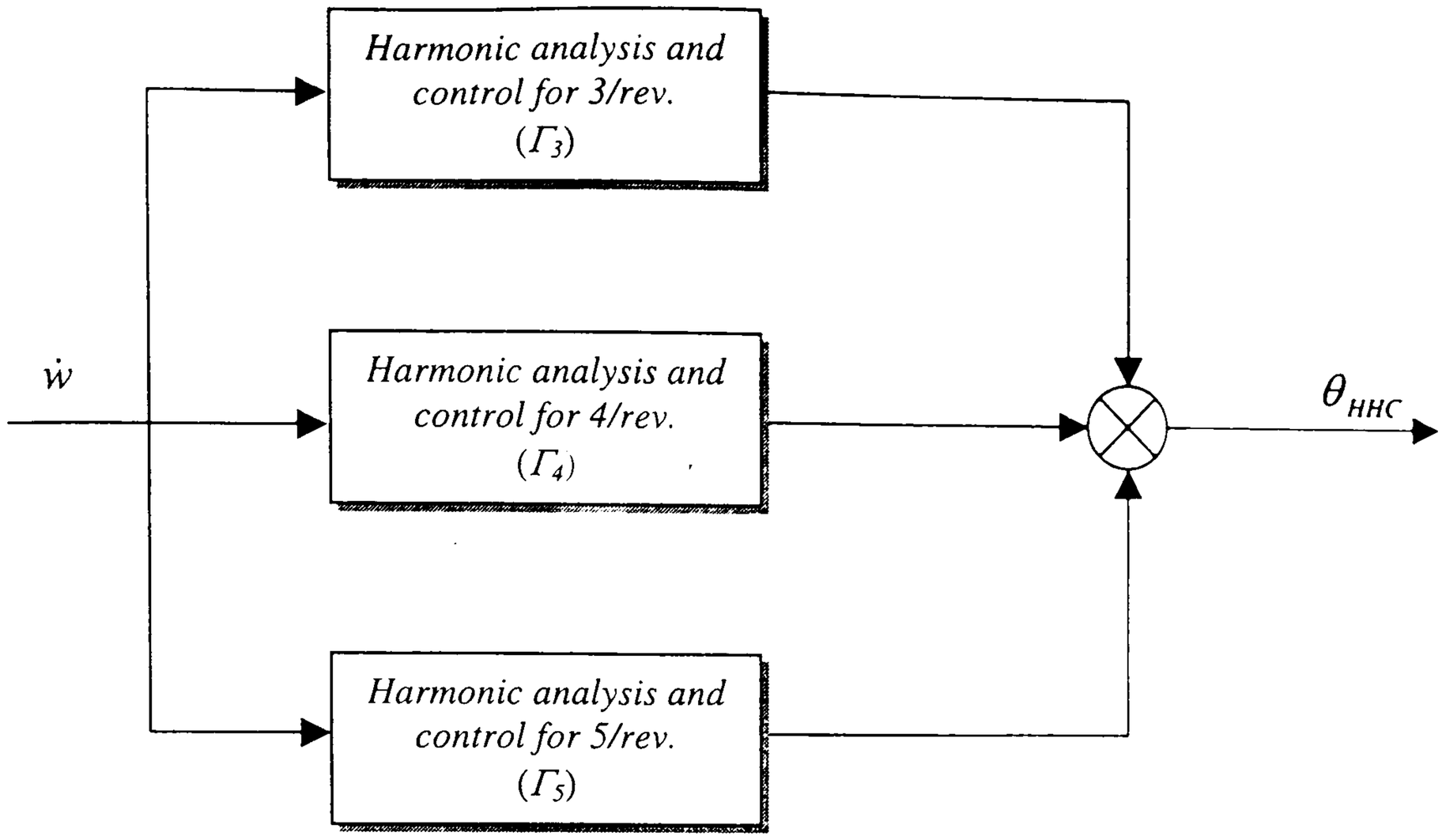

Figure 6.17 : **Block diagram of the nonlinear multi-harmonic control strategy.**

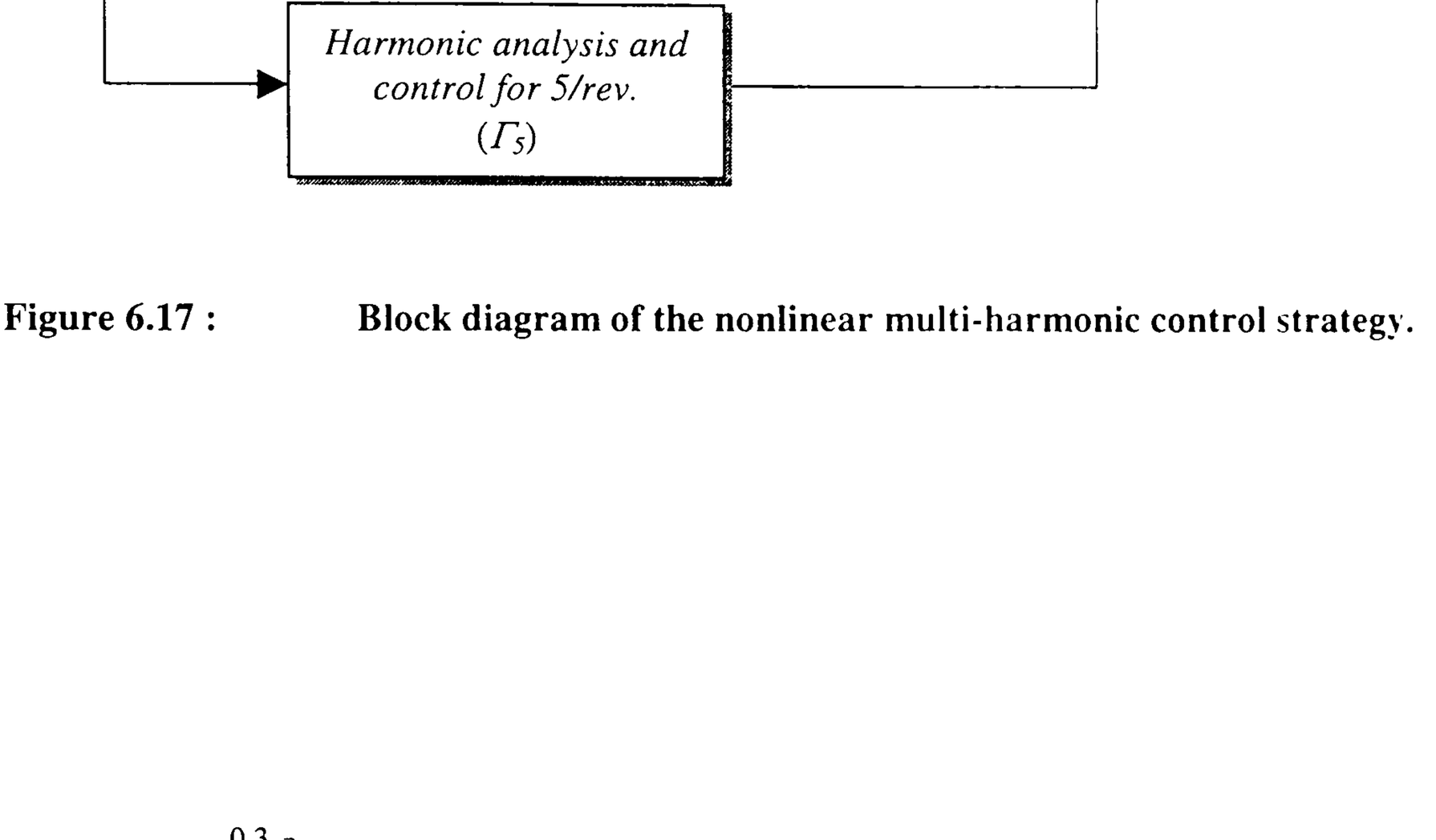

Figure 6.18 : **Effectiveness of the optimal HHC with disturbance feedforward to gust-induced vibration at 5 knots.**

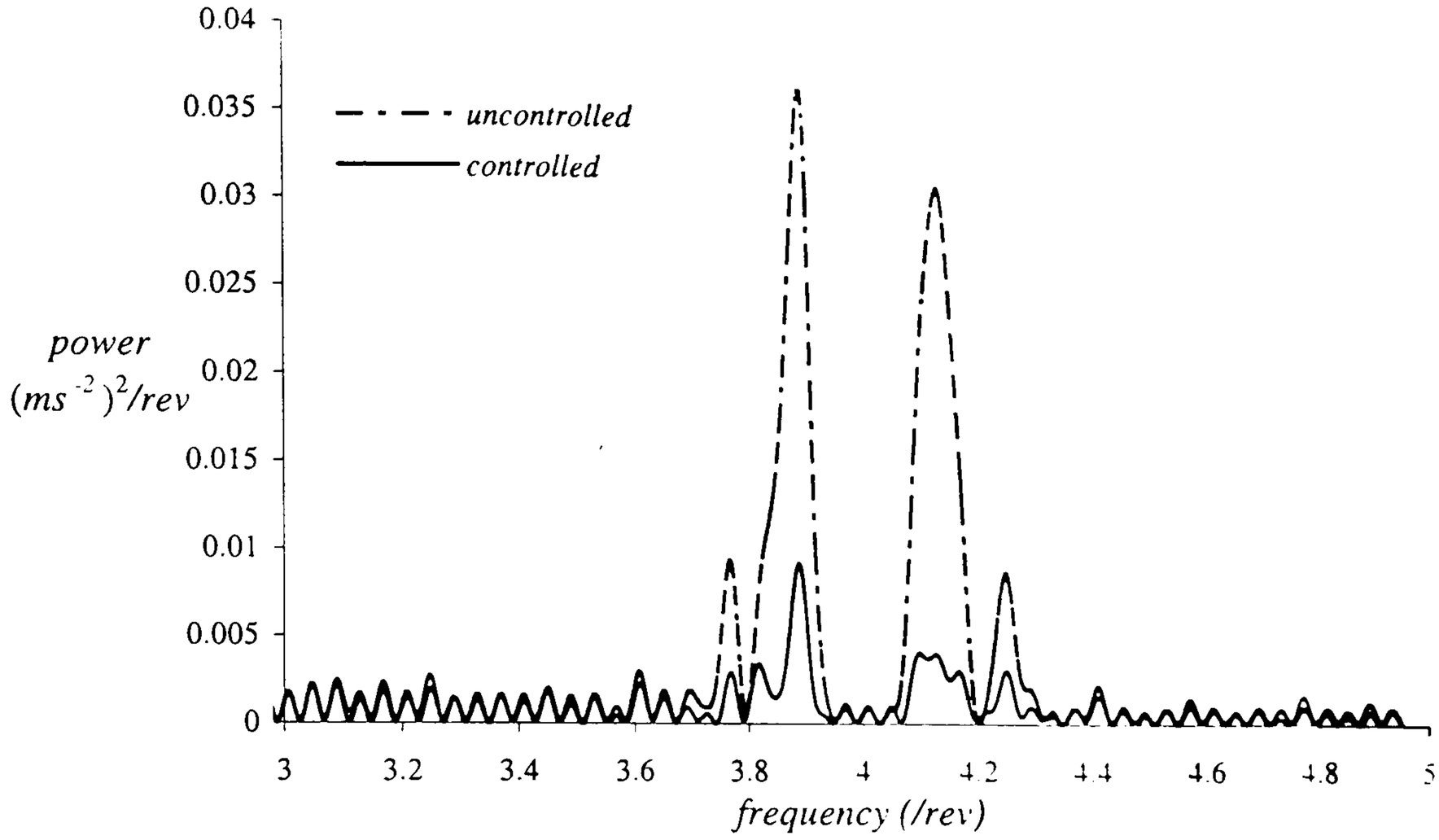

Figure 6.19 : **Effectiveness of the optimal HHC with disturbance feedforward to gust-induced vibration at 10 knots.**

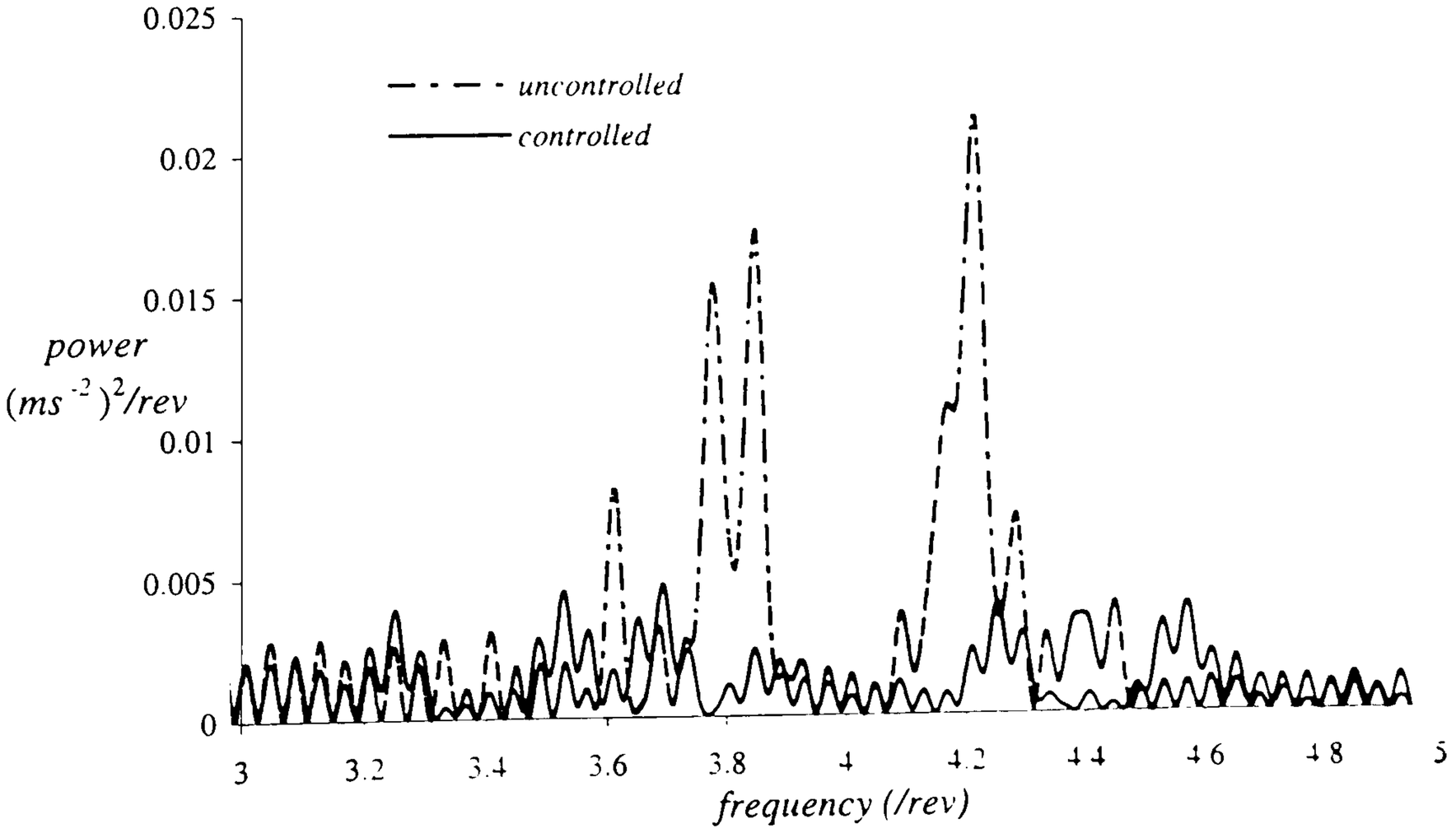

Figure 6.20 : **Effectiveness of the optimal HHC with disturbance feedforward to gust-induced vibration at 15 knots.**

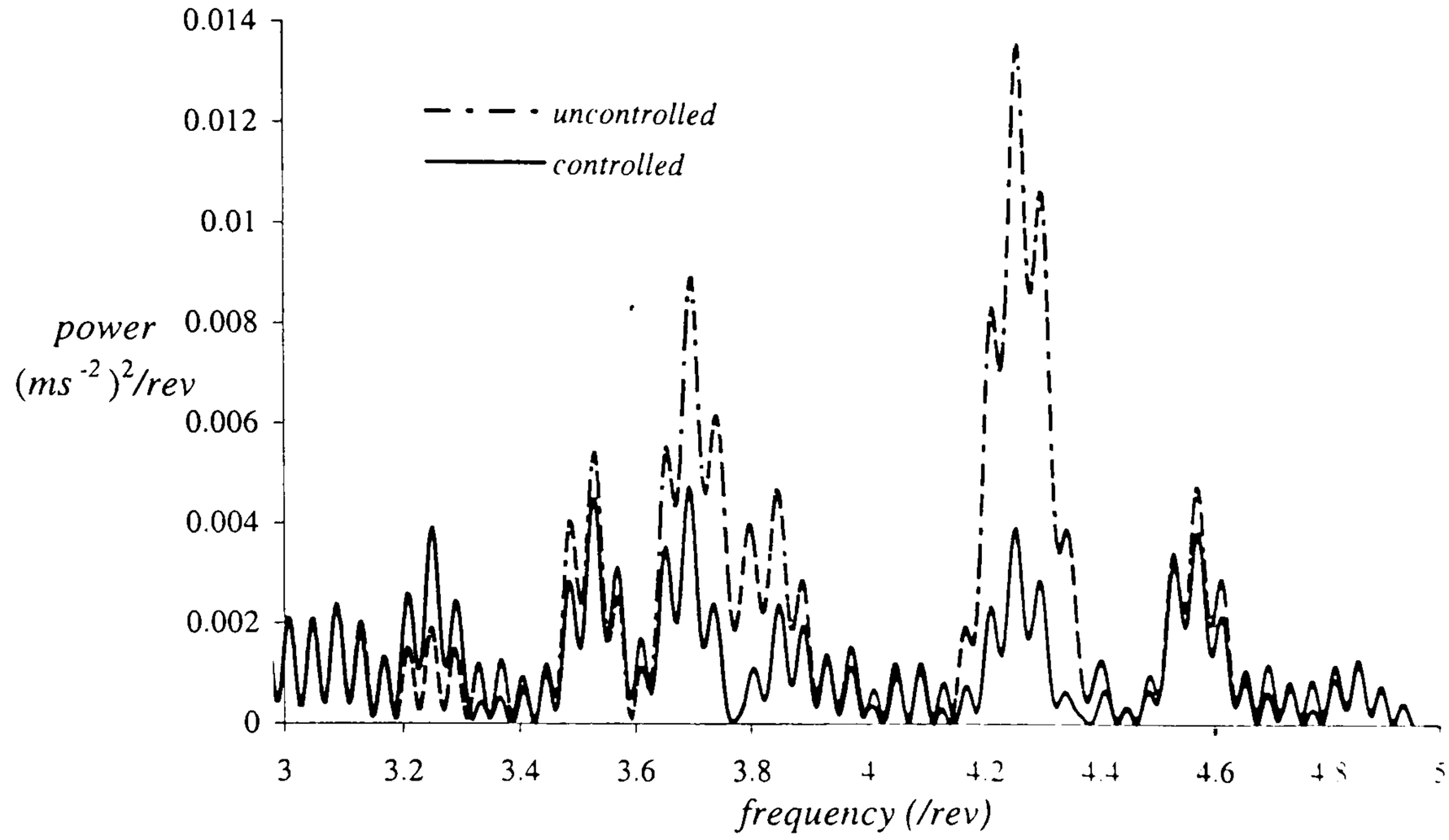

Figure 6.21 : **Effectiveness of the optimal HHC with disturbance feedforward to gust-induced vibration at 20 knots.**

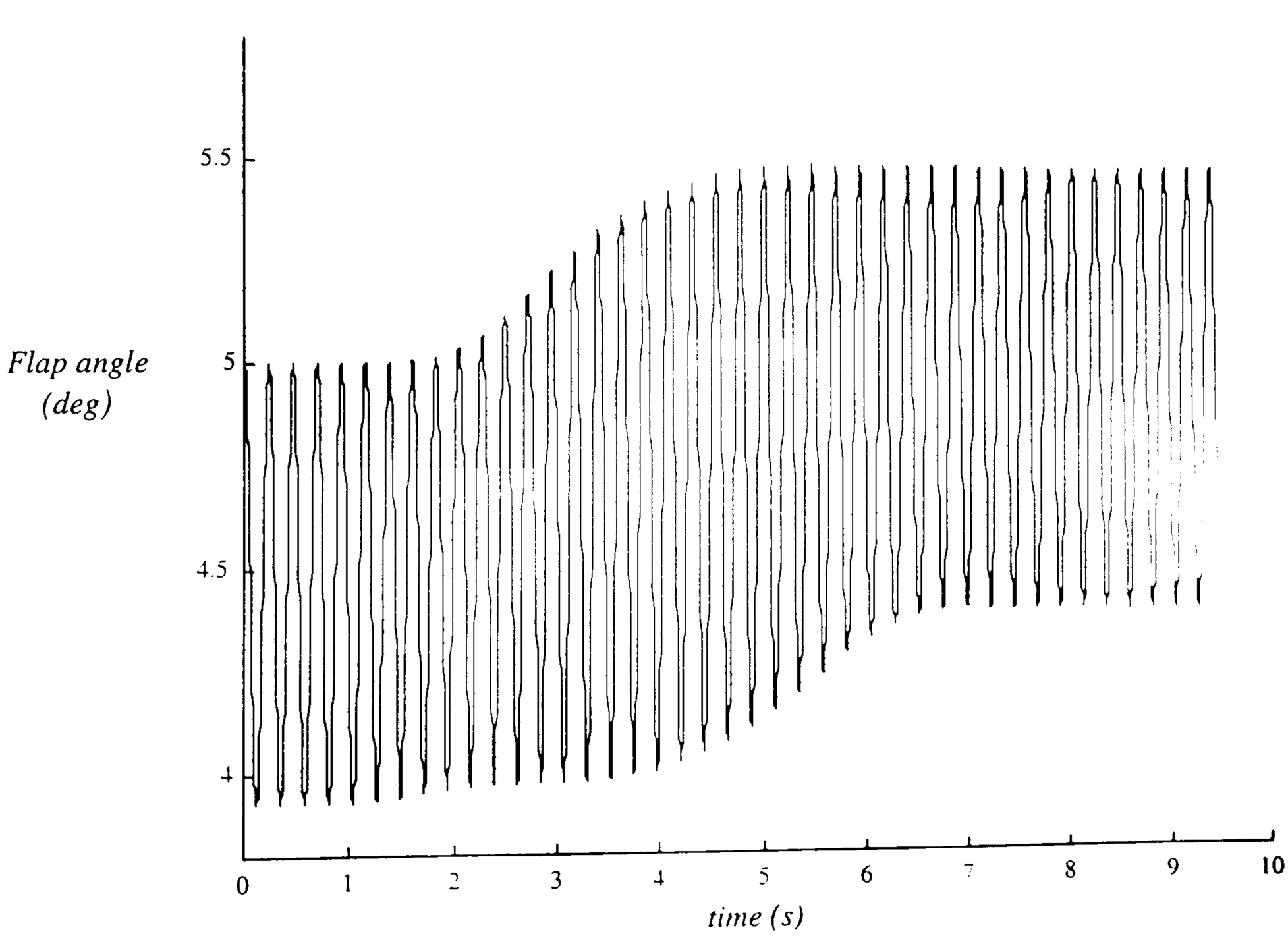

Figure 6.22 : **Flap angle response to rotor immersion into a sharp-edged gust.**

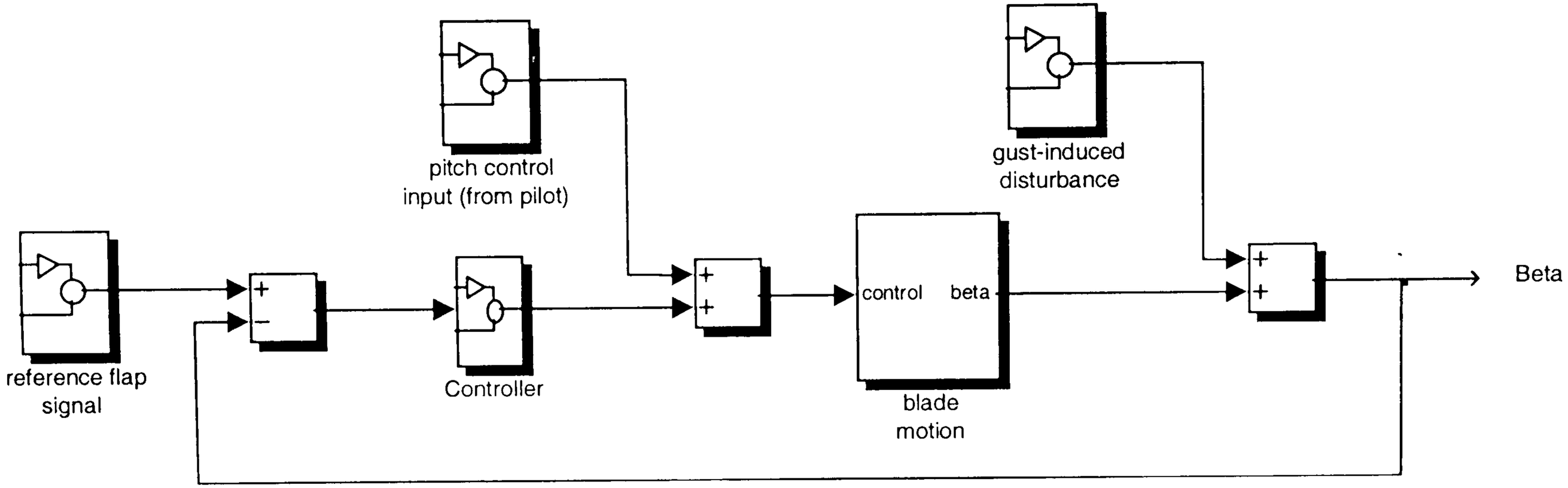

Figure 6.23 : SIMULINK model of flap regulated IBC feedback loop subjected to gust disturbance.

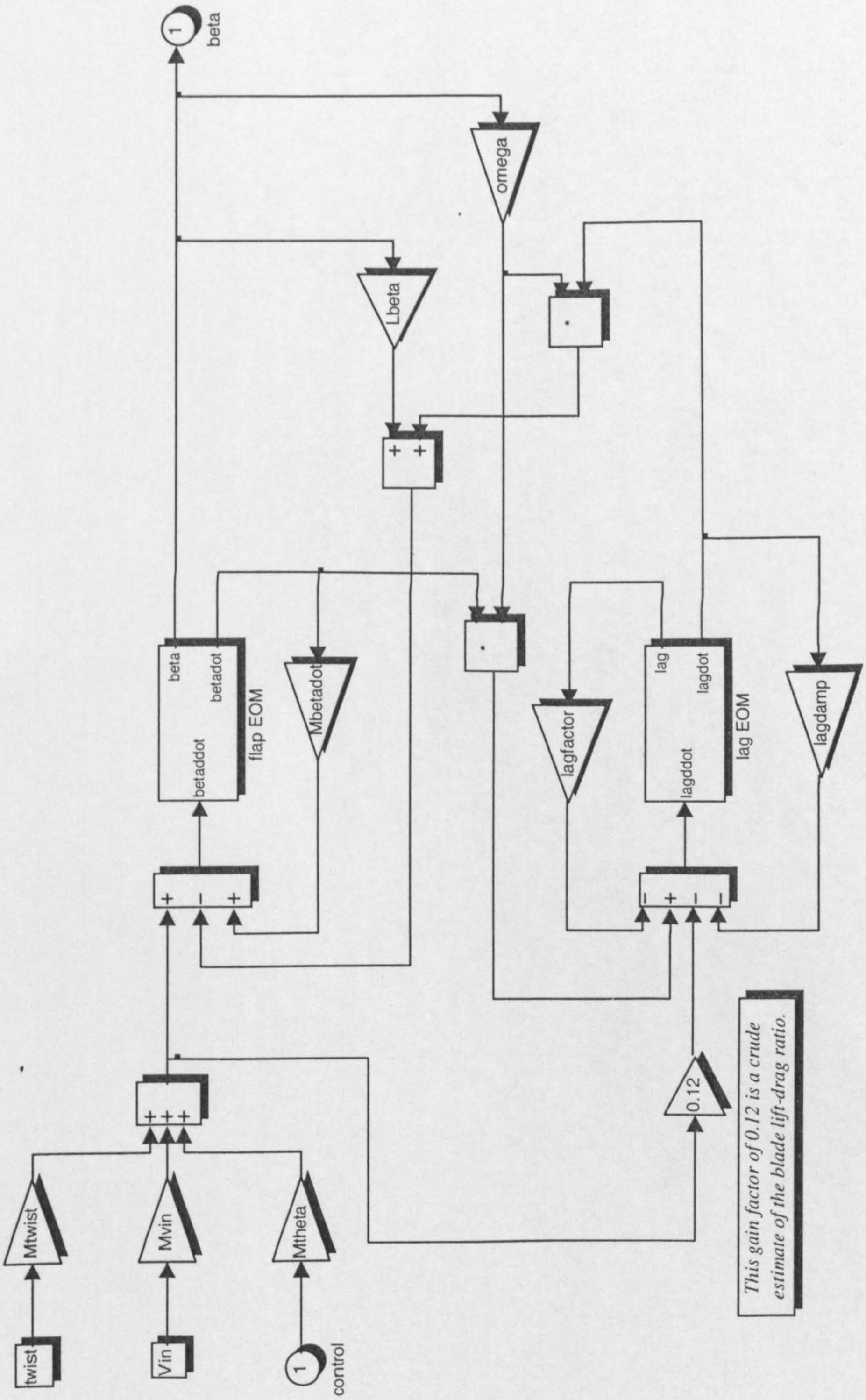

Figure 6.24 : SIMULINK model of coupled flap-lag equations of motion in hover.

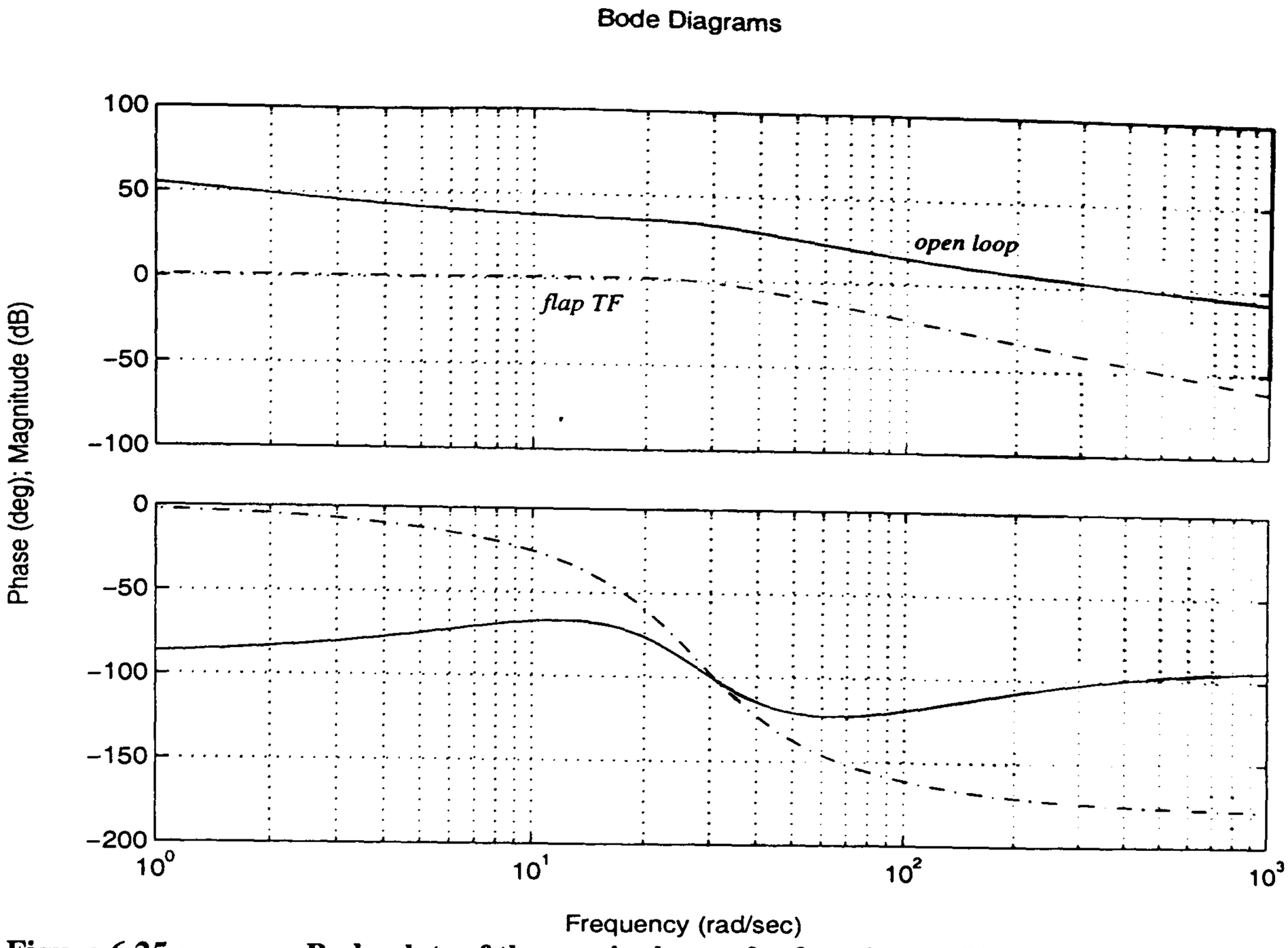

Figure 6.25 : **Bode plots of the nominal transfer function vs. PID compensator open loop TF.**

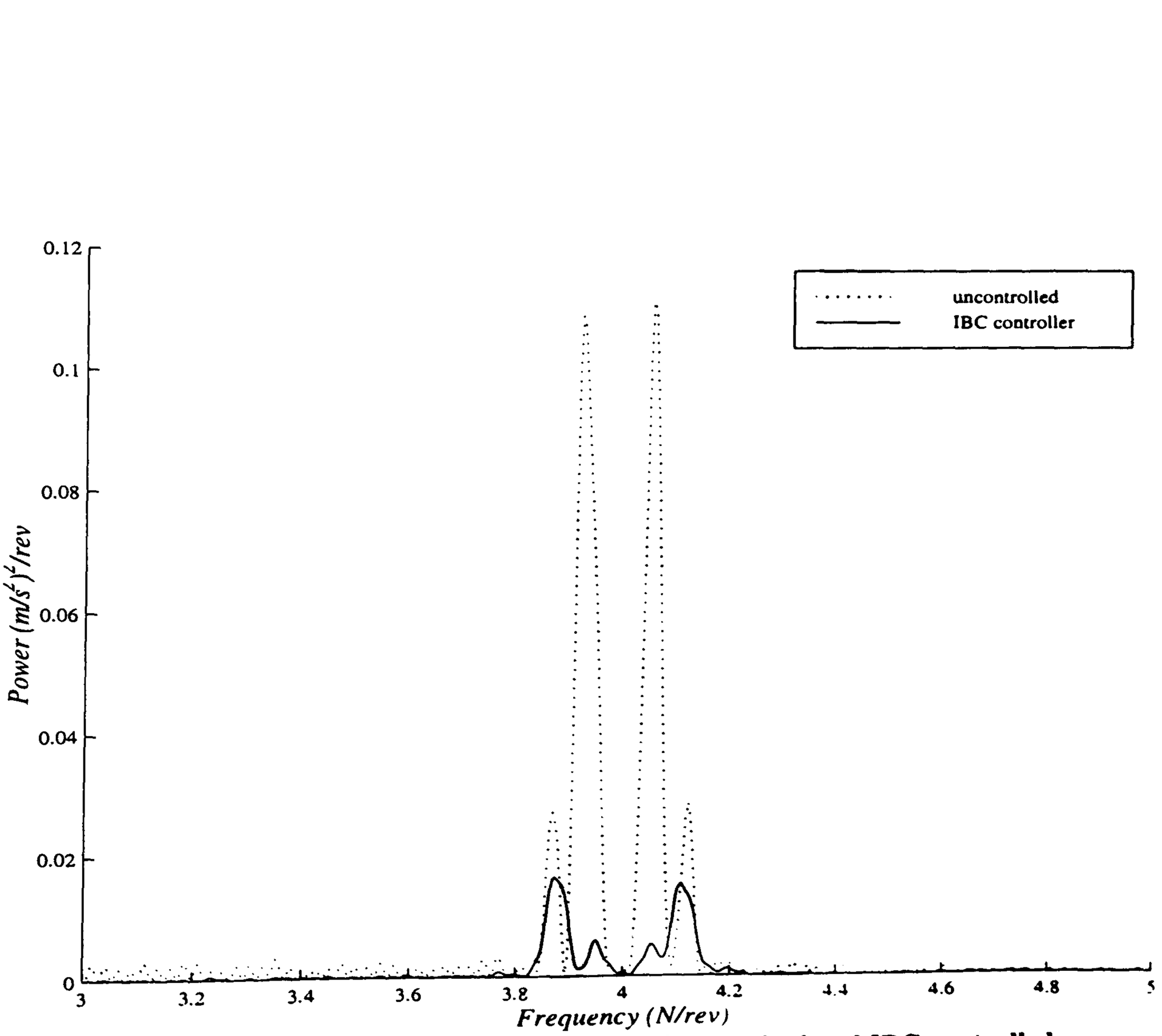

Figure 6.26 : **PSD's of fuselage vibration under nominal and IBC controlled gust immersion.**

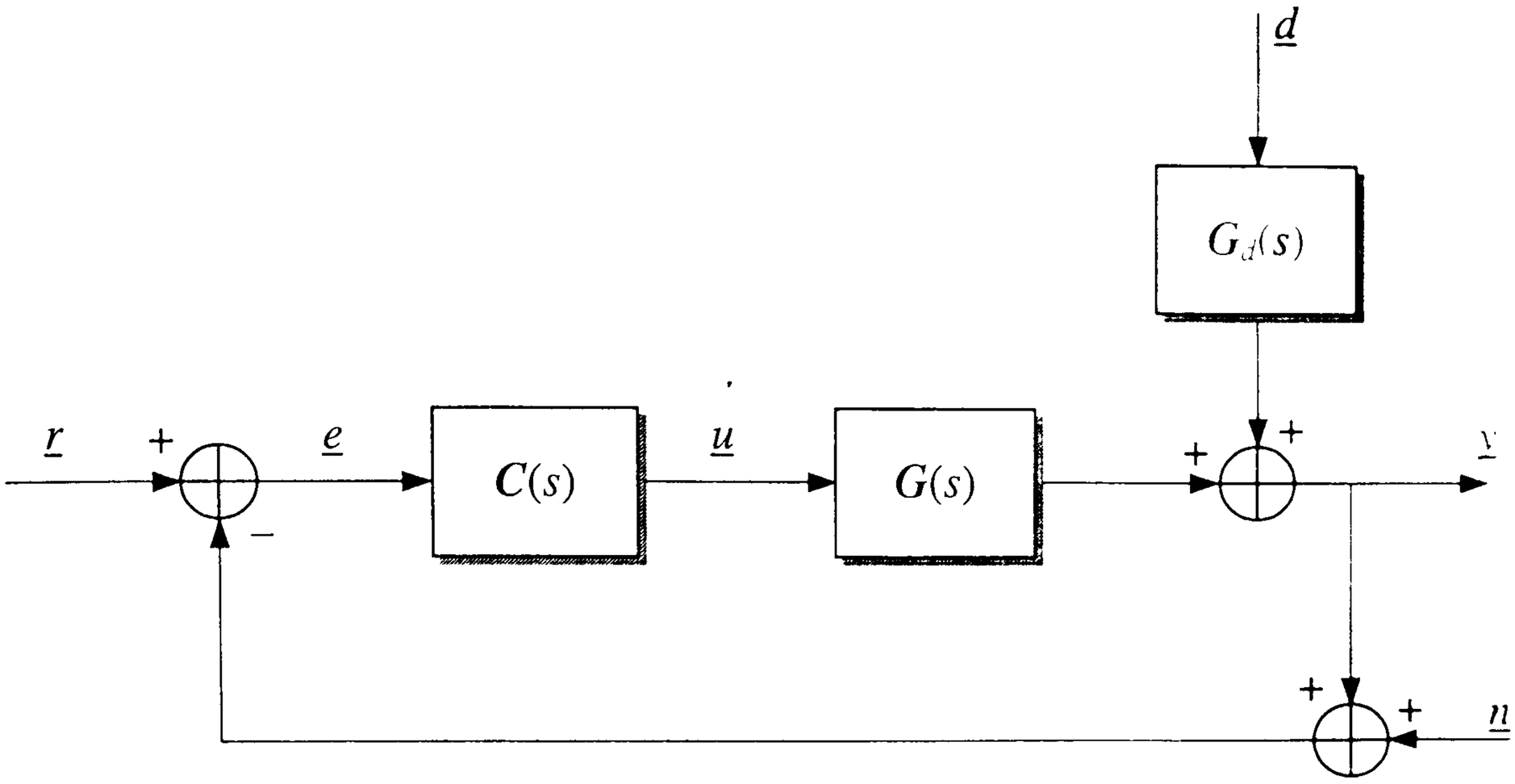

Figure 7.1 : **Block diagram of a general 1 degree of freedom feedback loop.**

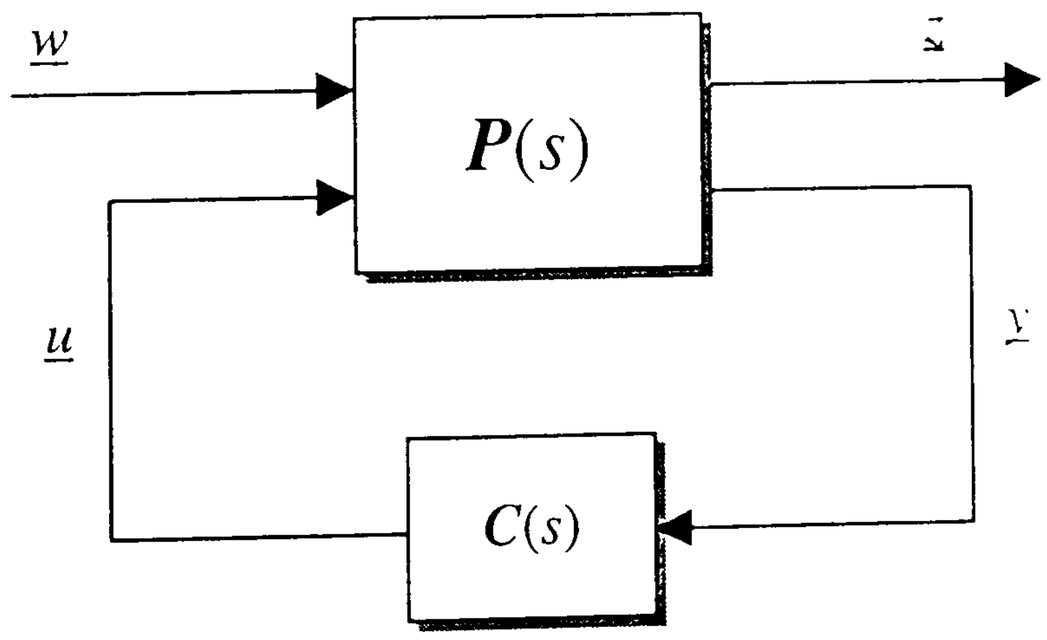

Figure 7.2 : **Standard 4-Block control problem configuration.**

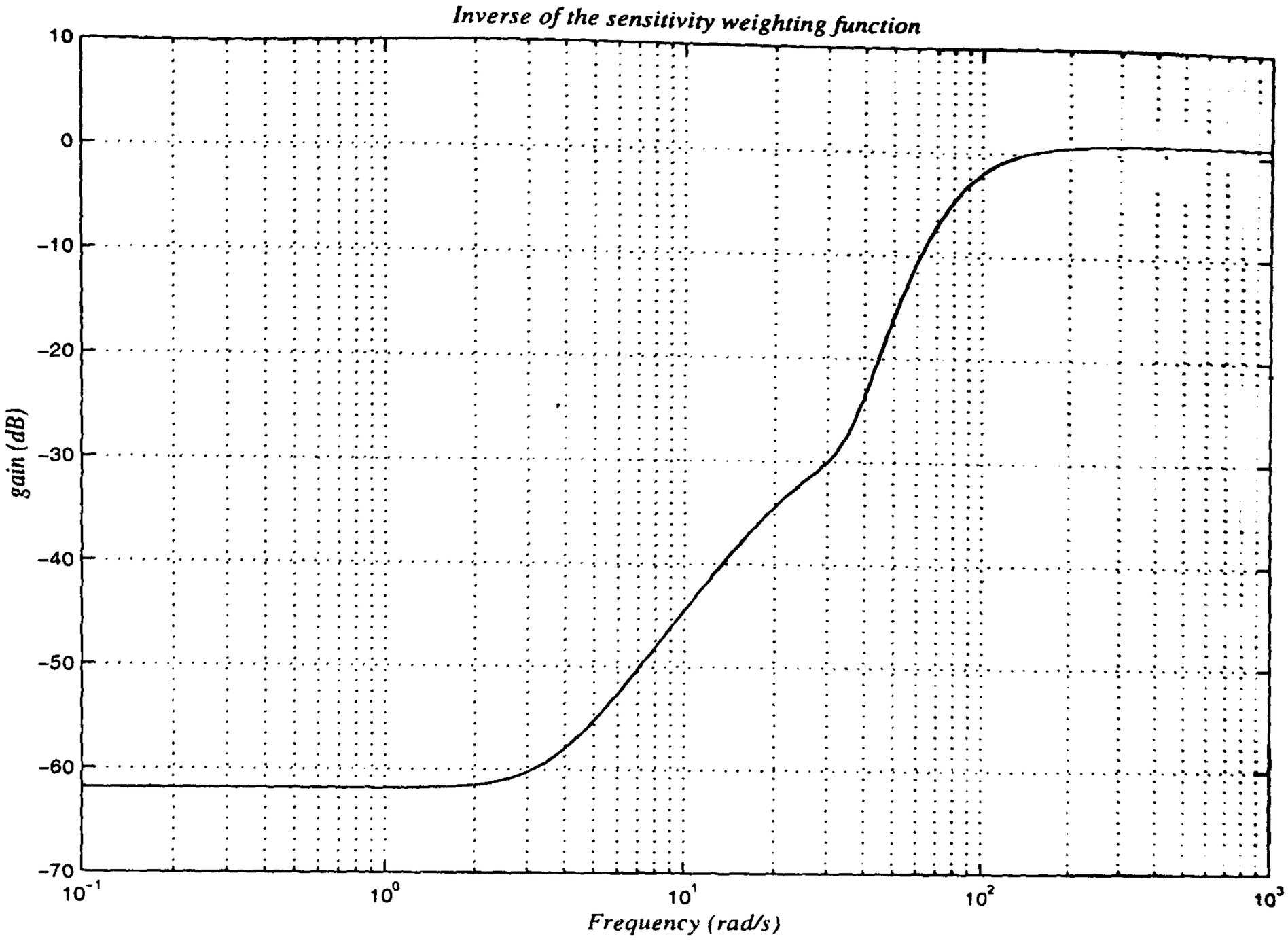

Figure 7.3 : Sensitivity weighting function for H_∞ design No 1.

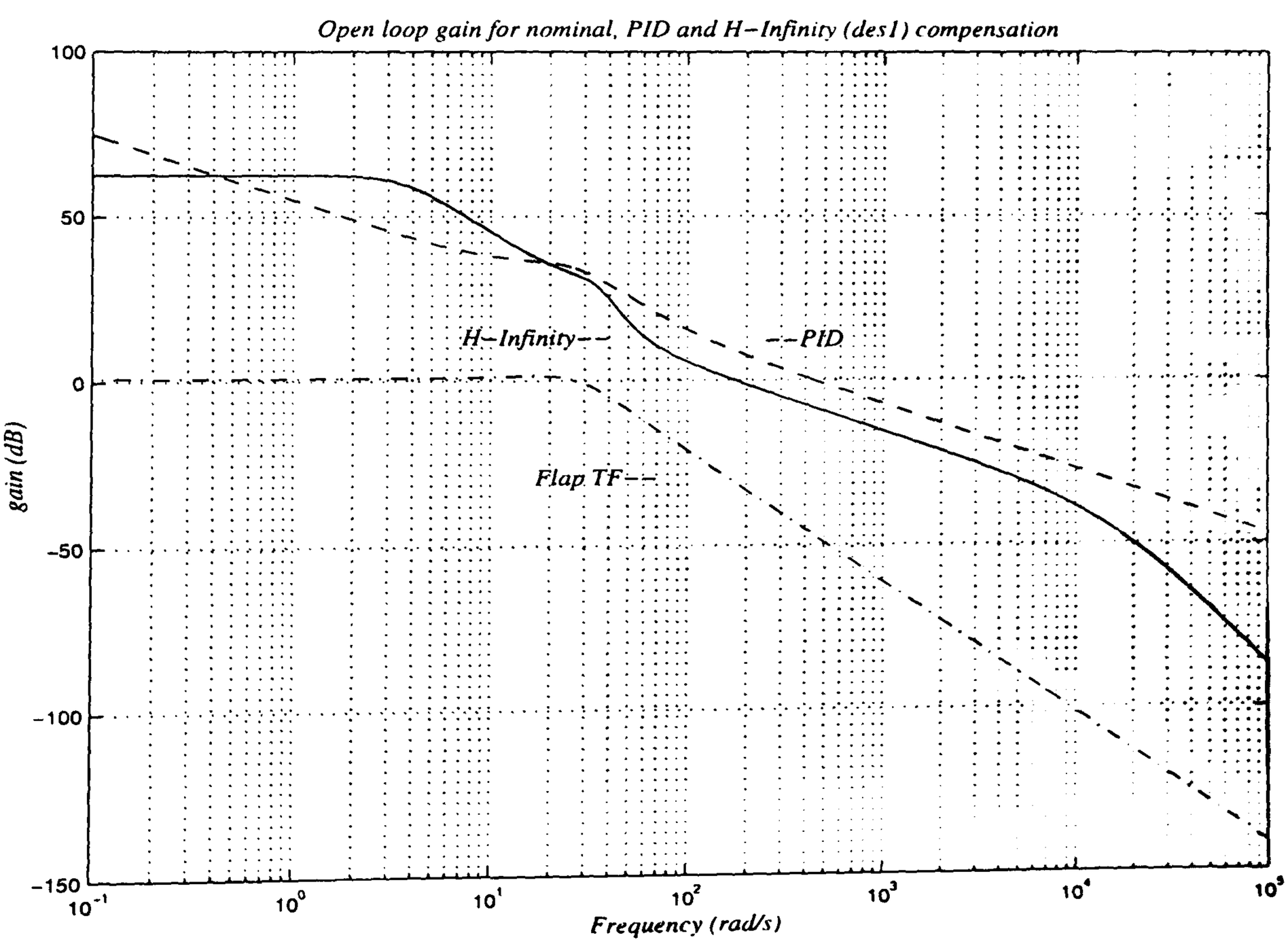

Figure 7.4 : Open-loop gain for nominal, PID and H_∞ (design No 1) compensated plants.

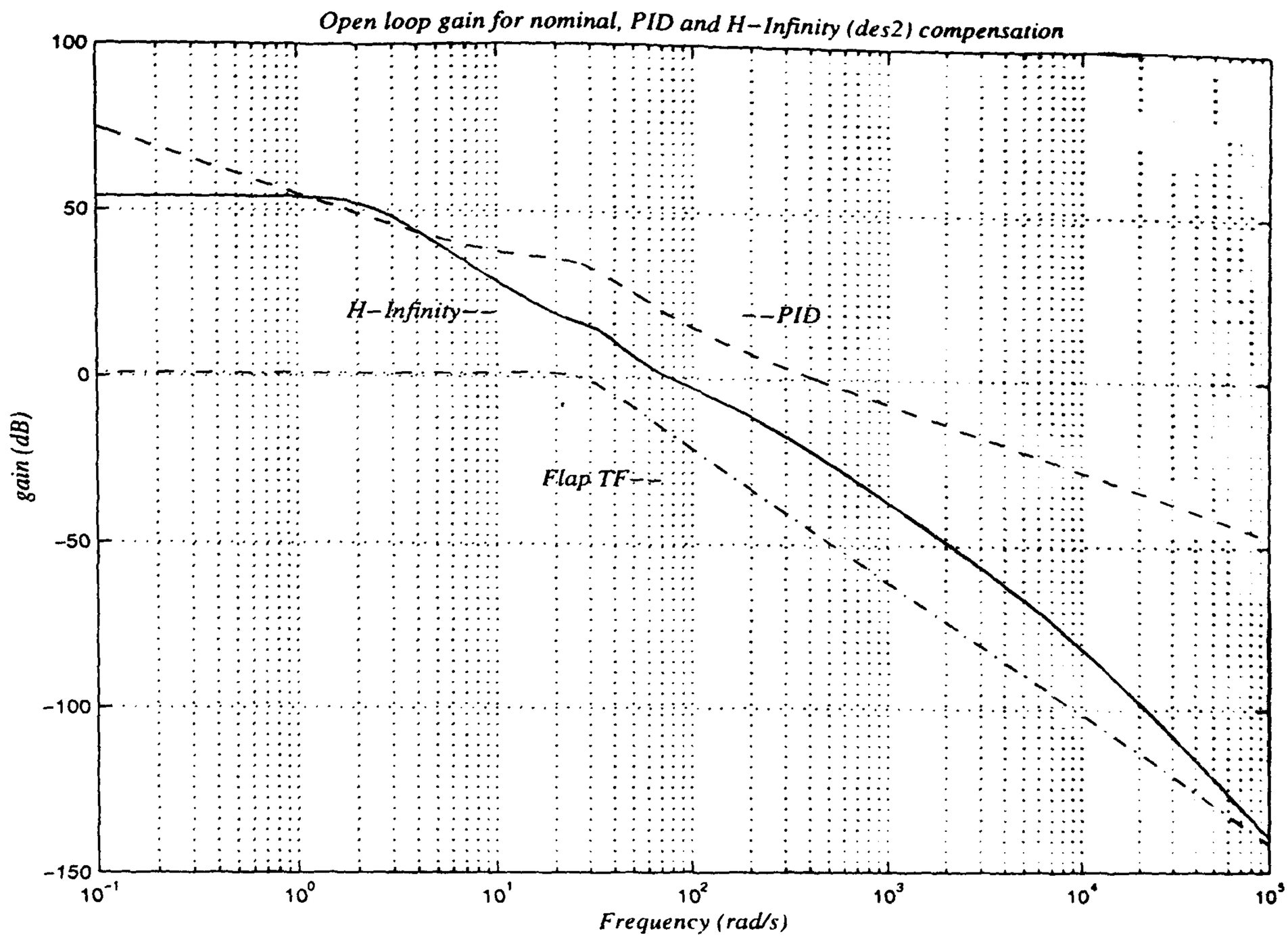

Figure 7.5 : **Open-loop gain for nominal, PID and H_∞ (design No 2) compensated plants.**

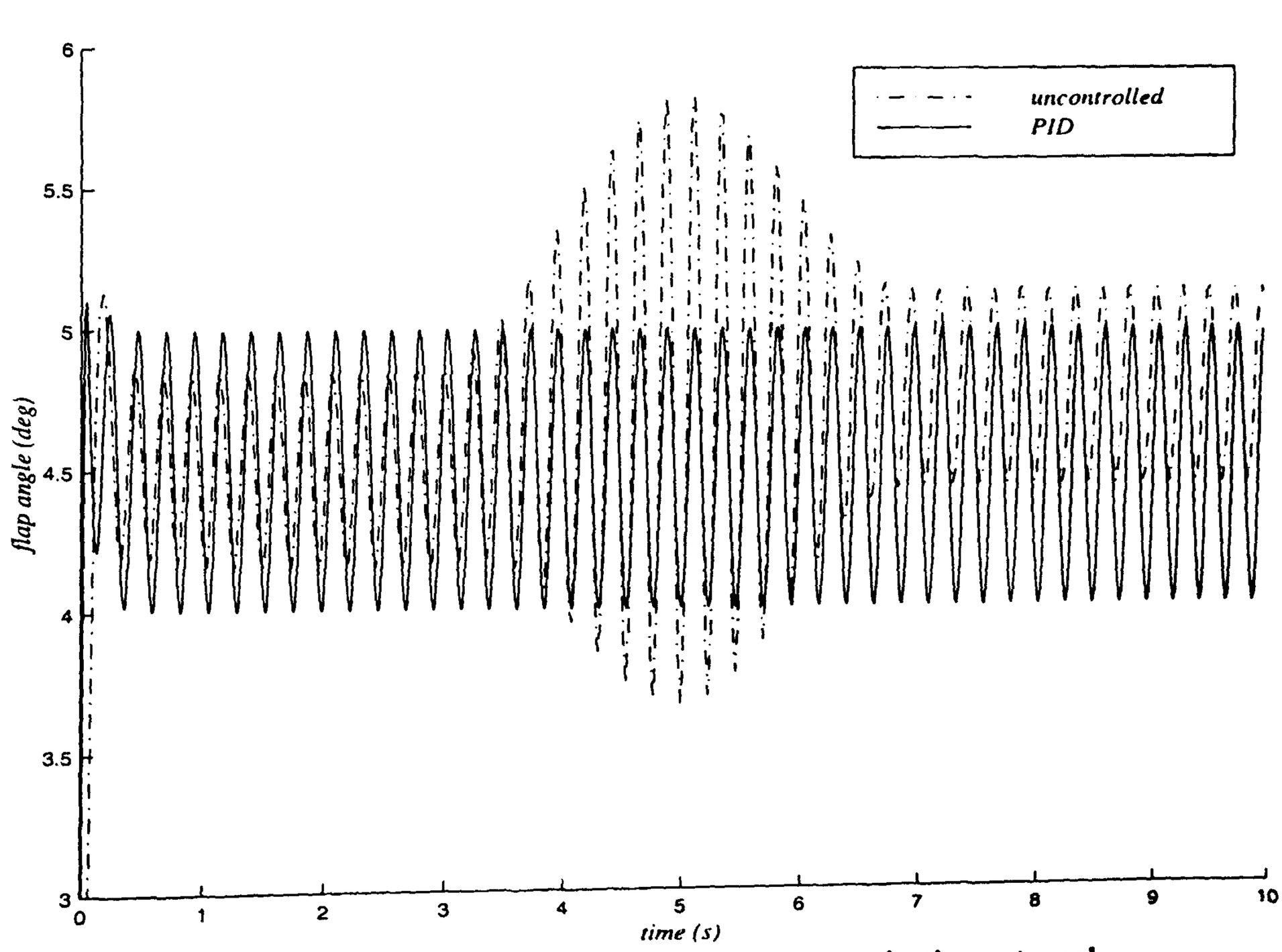

Figure 7.6 : **Effectivness of the PID compensator at rejecting external disturbance.**

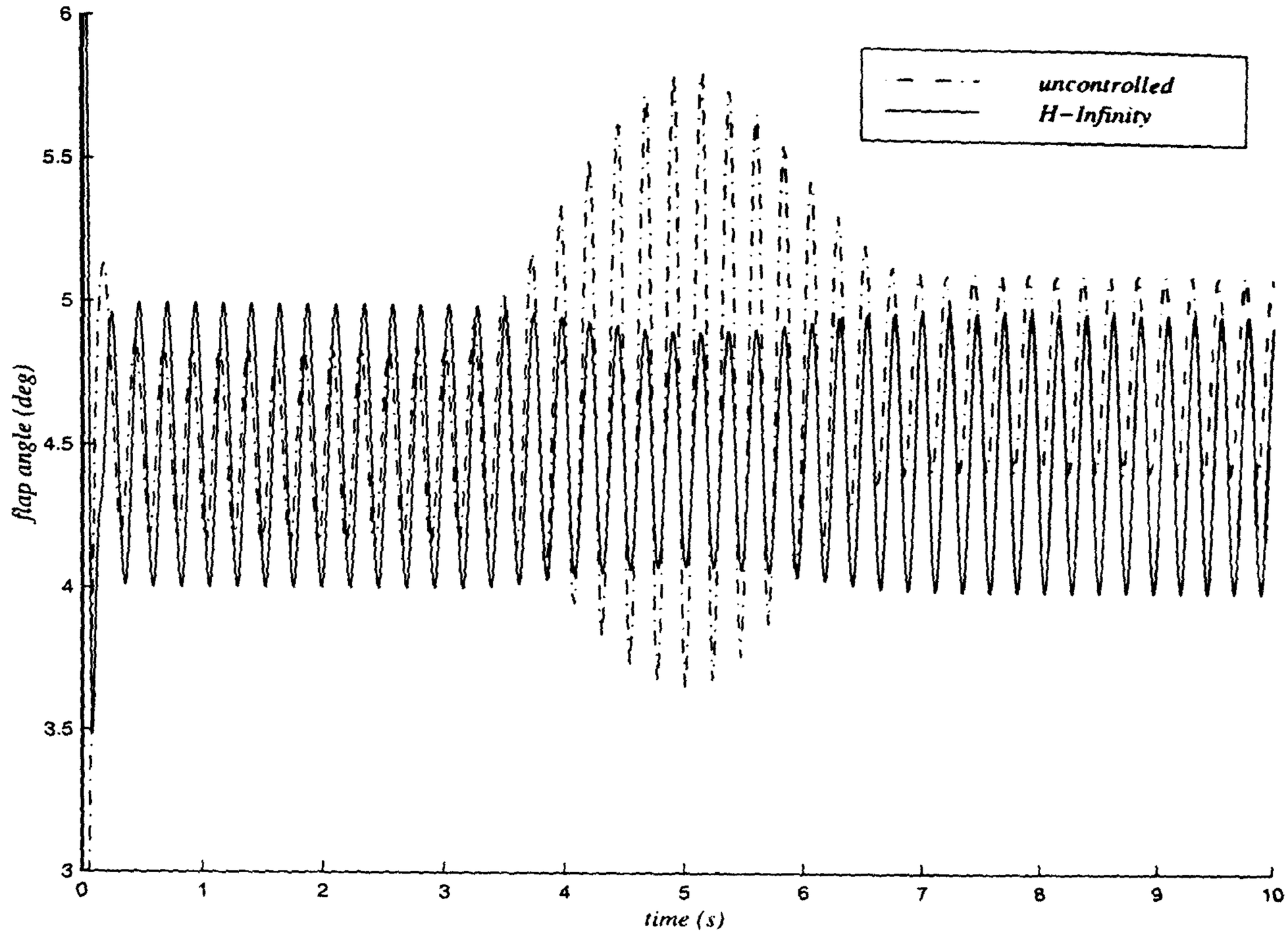

Figure 7.7 : **Effectivness of the H_∞ compensator at rejecting external disturbance.**

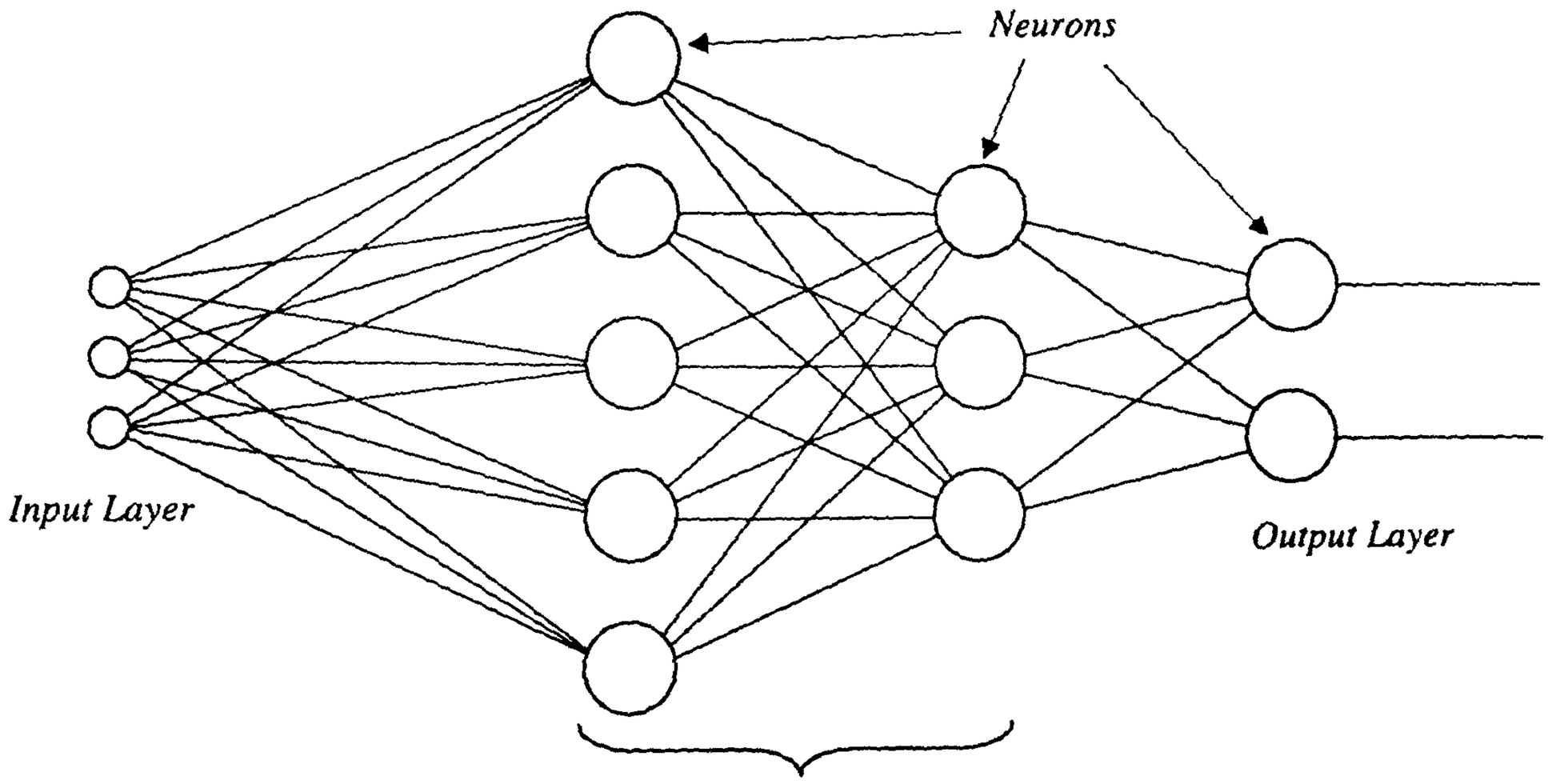

Figure 7.8 : **Architecture of a 3 layer, feedforward, multilayer neural network.**

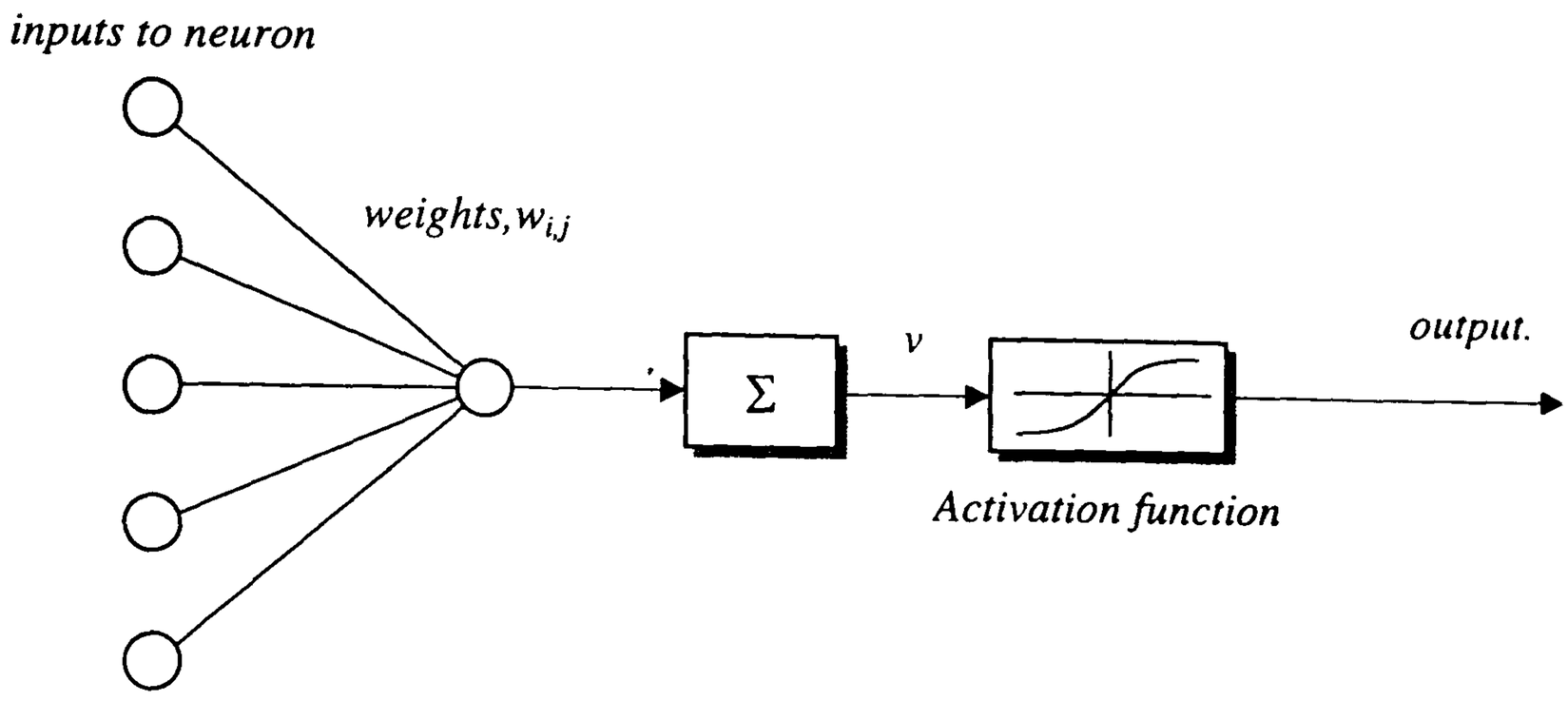

Figure 7.9 : Model of a neuron.

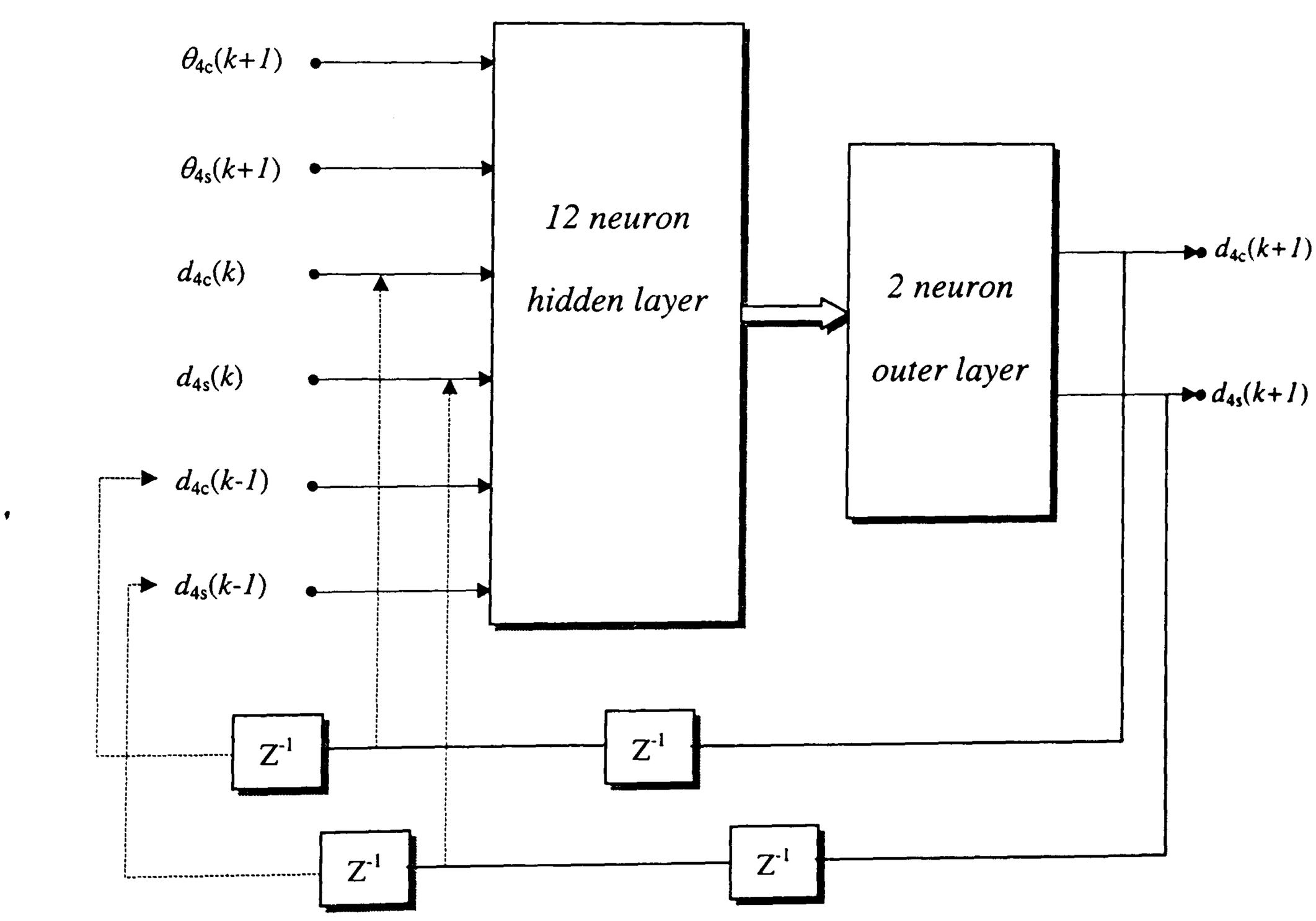

Figure 7.10 : Schematic of the Neural Network architecture designed for predicting gust-induced vibration Fourier coefficients.

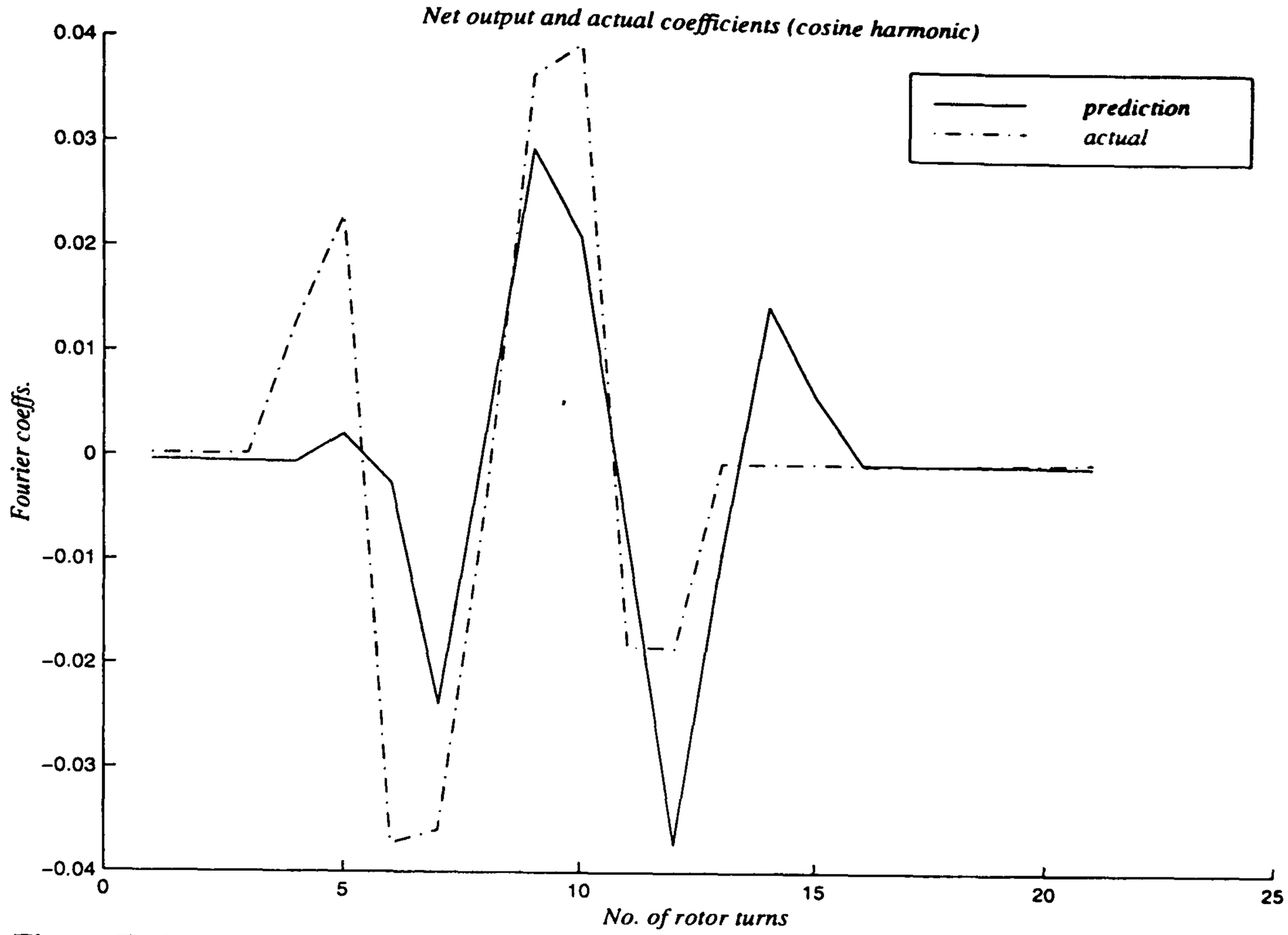

Figure 7.11 : **Comparison of the actual and predicted cosine harmonics of the Fourier coefficients of gust induced vibration.**

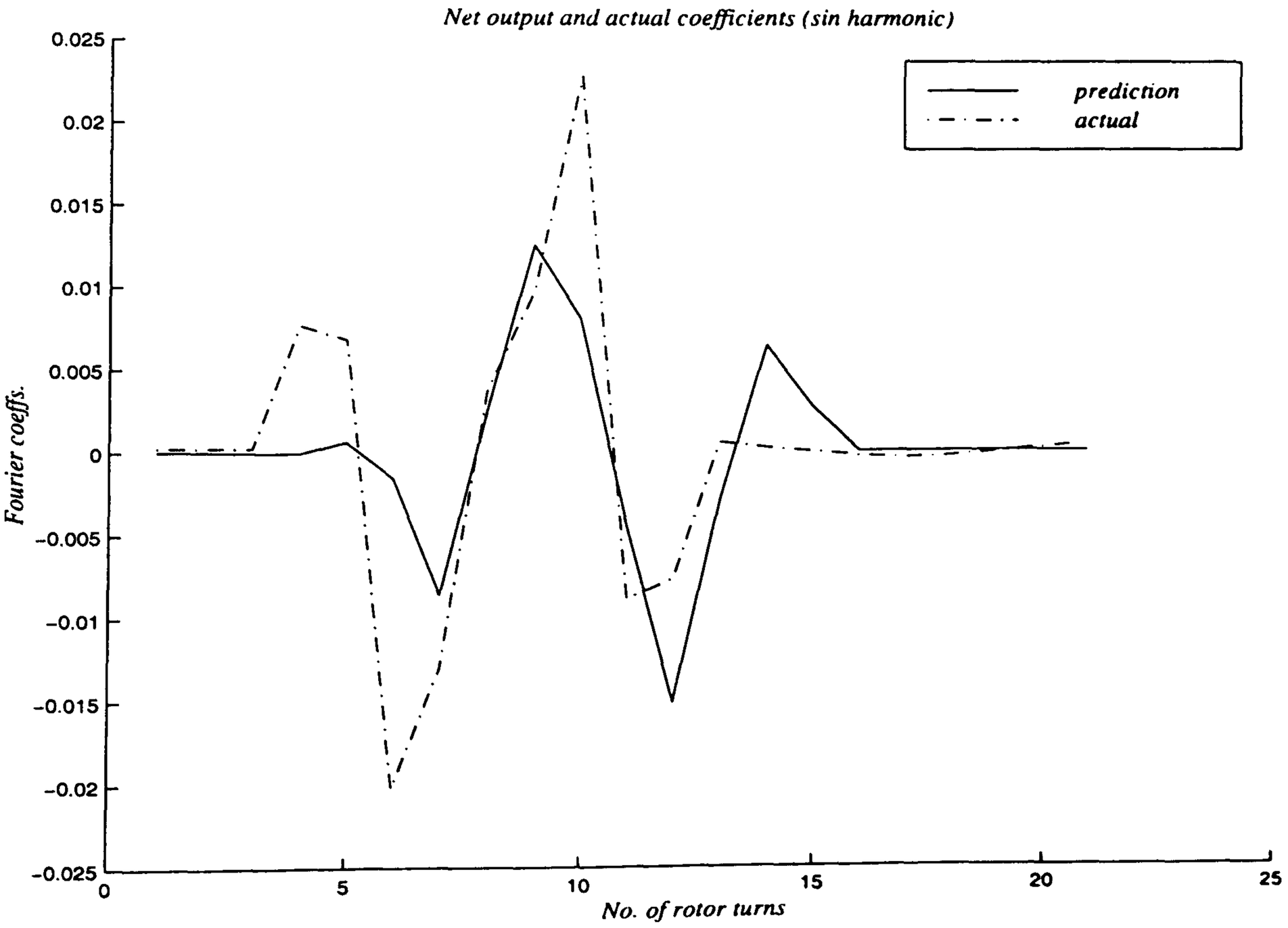

Figure 7.12 : **Comparison of the actual and predicted sine harmonics of the Fourier coefficients of gust induced vibration.**

References

Achache, M., Polychroniadis, M., '*Development of an Experimental System for Active Control of Vibrations on Helicopters-Development Methodology for an Airborne System*', Vertica, Vol. 11, No. 1/2, 1987.

Anon., "*Handling Qualities Requirements for Military Rotorcraft*", Aeronautical Design Standard ADS-33D, United States Army Aviation and Troop Command, July 1994.

Arnold, U.T.P, Müller,M., Richter,P., '*Theoretical and Experimental Prediction of Individual Blade Control Benefits*', 23rd European Rotorcraft Forum, Dresden, Germany, Sept. 1997.

Azuma, A., Saito, S., "*Study of Rotor Gust Response by means of Local Momentum Theory*", Journal of the American Helicopter Society, January, 1982.

Balmford, D.E.H., '*The Control of Vibration in Helicopters*', Aeronautical Journal, Feb. 1977.

Beal, T.R., "*Digital Simulation of Atmospheric Turbulence for Dryden and von Karman Models*", Journal of Guidance, Control and Dynamics, Vol. 16, No. 1, January-February 1993.

Belo, E.M., Marques, F.D., '*Vibration Alleviation of a Hingeless Helicopter Rotor Blade by State Feedback*', ICAS Conference Proceedings, paper 4.5.1, 1996.

Bradley,R, Sinclair,M., Jones, J.G., Turner, G. "*Wavelet Analysis of Helicopter Response to Atmospheric Turbulence In Ride Quality Assesment*", 20th European Rotorcraft Forum, Amsterdam, October 1994

Bramwell, A.R.S., "Helicopter Dynamics", Arnold 1976.

Braun, D., '*Development of Anti-Resonance Force Isolators for Helicopter Vibration reduction*', 6th European Rotorcraft Forum, Bristol, 1980.

Brinson, P., Mullen, G., Howitt, J., Woodrow, I., "*Experimental Investigation of Control System Design Methods for Helicopters*", Twenty-First European Rotorcraft Forum, Saint-Petersburg, Russia, 1995, Paper VII-2.

Calico,R.A.,Wiesel,W.E., '*Control of Time-Periodic Systems*', Journal of Guidance, Vol. 7,No. 6, Nov.-Dec. 1984.

Calico,R.A.,Wiesel,W.E., '*Stabilisation of Helicopter Blade Flapping*', Journal of the American Helicopter Society, October 1986.

Caradonna, F.X., Strawn, R.C., and Bridgeman, J.O., "*An Experimental and Computational Study of Rotor-Vortex Interactions*", 14th European Rotorcraft and Powered Lift Aircraft Forum, Milano, Italy, September, 1988.

Celi, R., Kim, F.D., Tischler, M.B., "*High-Order State Space Simulation Models of Helicopter Flight Mechanics*", Journal of the American Helicopter Society, October, 1993.

Chen, W.-Y., "*Application of Rice's Exceedance Statistics to Atmospheric Turbulence*," AIAA Journal, Vol.10, Aug 1972, pp. 1103-1105.

Chen, R.T.N., "*A Survey of Nonuniform Inflow Models for Rotorcraft Flight Dynamics and Control Applications*", Paper 64, 15th European Rotorcraft Forum, Amsterdam, Netherlands, September 1989.

Cheney, W., Kincaid, D., "*Numerical Mathematics and Computing. Second Edition*", Brooks/Cole Publishing, 1985.

Collins Dictionary, HarperCollins Publishers, 1995.

Costello, M. F., Prasad, J. V. R., Schrage, D.P., and Gaonkar, G. H., "*Some issues on Modelling Atmospheric Turbulence Experienced by Helicopter Rotor Blades*" Journal of the American Helicopter Society, Vol 37, (2), Apr 1992.

Doyle, J.C., Glover, K., Khargonekar, P.P., and Francis, B.A., "*State-Space Solutions to Standard H_2 and H_∞ Control Problems*", IEEE Trans. Automatic Control, Vol. 34, No. 8, August 1989.

Du Val, R.W., Gregory, C.Z., Gupta, N.K., '*Design and evaluation of a State-Feedback Vibration Controller*', Journal of the American Helicopter Society, July 1984.

Ellis, C.W., and Jones, R., "*Application of an Absorber to Reduce Helicopter Vibration Levels.*", Journal of the American Helicopter Society, July 1963.

Fradenburgh, E.A., and Chuga, G.M., "*Flight Program on the NH-3A Research Helicopter.*", Journal of the American Helicopter Society, January 1968.

Friedmann, P.P., Millott, T.A., '*Vibration reduction in Rotorcraft Using Active Control: A Comparison of Various Approaches*', Journal of Guidance, Control and Dynamics, Vol. 18, No. 4, July-August, 1995.

Glauert, H., '*A General Theory of the Autogyro*', R&M No. 1111, British A.R.C., 1926.

Grimble, M.J., Johnson, M.A., '*H_∞ robust control design- a tutorial review*', Computing and Control Engineering Journal, November 1991.

Gupta, N.K., '*Frequency-Shaped Cost Functionals: Extension of Linear-Quadratic-Gaussian Design Methods*', Journal of Guidance and Control, Vol. 3,No. 6, Nov-Dec. 1980.

Gupta, N.K., Du Val, R.W., '*A New Approach for Active Control of Rotorcraft Vibration*', Journal of Guidance, Vol. 5,No. 2, March-April 1982.

Haas, D.J., Milano, J., Flitter, L., "*Prediction of Helicopter Component Loads Using Neural Networks*", Journal of the American Helicopter Society, Jan 1995.

Halwes, D.R., '*LIVE- Liquid Inertia Vibration Eliminator*', Proc. 35th American Helicopter Soc. Conf., Paper No. 80-22, 1980.

Ham, N.D., Maser, H.H. and Zvara, J., "*Investigation of rotor response to vibratory aerodynamic inputs*", W.A.D.C. Tech Report 58-87. Part I, 1958.

Ham, N.D., "*Some Conclusions from an Investigation on Blade-Vortex Interaction*", Journal of the American Helicopter Society, Vol. 20, pp 26-31, October, 1975.

Ham, N.D., '*A Simple System for Helicopter Individual-Blade-Control Using Modal Decomposition*', Vertica, Vol. 4, 1980.

Ham, N.D., Behal, B.L., McKillip, R.M., '*Helicopter Rotor Lag Damping Augmentation through Individual-Blade-Control*', Vertica, Vol. 7, No. 4, 1983.

Ham, N.D., "*Helicopter Individual-Blade-Control Research at MIT 1977-1985*", Vertica, Vol 11, No.1/2, pp. 109-122, 1987.

Ham, N.D., '*Helicopter Individual Blade Control: Promising Technology for the future Helicopter*', 21st European Rotorcraft Forum, St. Petersburg, Russia, Aug-Sept. 1995.

Haverdings, H., "*A Control Model for Manoeuvering Flight for Application to a Computer-Flight-Testing Program*", Vertica Vol 7, No3,pp. 259-269, 1983.

Haykin, S., '*Neural Networks – a comprehensive foundation*', Macmillan College Publishing Inc., 1994.

Hess, R.A., Gao, C., Wang, S.H., "*Generalised Technique for Inverse Simulation Applied to Aircraft Manoeuvres*", Journal of Guidance, Control, and Dynamics, Vol. 14, No.5, 1991.

Hess,R.A., Gao,C., "*Inverse Simulation of Large Amplitude Aircraft Manoeuvres*", Journal of Guidance, Control and Dynamics, Vol. 16, No.4,1993.

Hess, R.A., "*Rotorcraft Handling Qualities in Turbulence*", Journal of Guidance, Control and Dynamics, Vol. 18, No. 1, January-February 1995.

Hoblit, F, M. "*Gust Loads on Aircraft: Concepts and Applications*" American Institute of Aeronautics and Astronautics, 1988.

Hooper, W.E., "*The vibratory airloading of helicopter rotors*", Vertica Vol. 8, No. 2, pp 73-92, 1984.

Horner, M.H., Stewart, J.N., Galbraith, R.A.McD.,Grant, I., Coton, F.N., and Smith, G.H., "*Preliminary Results from a Particle Image Velocimetry Study of Blade-Vortex Interaction*", 19th European Rotoreraft and Powered Lift Aireraft Forum, Cernobbio, Italy, September, 1993.

Houston, S.S., Tarttelin, P.C., "*Validation of Mathematical Simulations of Helicopter Vertical Response Characteristics in Hover*", Journal of the American Helicopter Society, Vol 36, No 1, pp45-57, 1991a.

Houston, S.S., "*Rotoreraft Aeromechanics Simulation for Control AnaLysis-Mathematical Model Description.*", University of Glasgow, Department of Aerospace Engineering, Internal Report No.9123, 1991b.

Houston, S.S., Hamilton, R.A., "*Modelling, Simulation and Characterisation of Helicopter Response to Atmospheric Turbulence*", 19th European rotoreraft forum, Paper G18, September 1993.

Houston, S.S., "*Validation of a non-linear individual blade rotoreraft flight dynamics model using a perturbation method*", Journal of the Royal Aeronautical Society, August/September, 1994.

Howitt, J., Howell, S.E., Brinson, P.R., Mullen, G.J., Woodrow, I.J., Hayhurst, C., '*Experimental Evaluation of High-Bandwidth Helicopter Flight Control System Design Exploiting Rotor State Feedback*', 23rd European Rotoreraft Forum, Dresden, Germany, 1997.

Hunt, K.,Sbarbaro, D., Zbikowski, R. & Gawthrop, P.J., '*Neural Networks for Control Systems – A Survey*', Automatica, Vol. 28, No. 6, 1992.

Ingle, S., Celi, R., "*Effects of Higher Order Dynamics on Helicopter Flight Control Law Design*", Journal of the American Helicopter Society, July, 1994.

Johnson, W., "*Helicopter Theory*", Princeton University Press, 1980.

Jones, J.P., "*The influence of the wake on the flutter and vibration of Rotor blades*", The Aeronautical Quarterly, Vol. IX, August, 1958.

Jones, J.P., "*Helicopter vibrations*", Journal of the Royal Aeronautical Society, Vol. 64, December 1960.

Jones, J.G., "*A Theory for Extreme Gust Loads on an Aircraft Based on the Representation of the Atmosphere as a Self-Similar Intermittent Random Process*," Royal Aircraft Establishment, TR-68030, Feb. 1968.

Jones, J.G., "*A Unified Discrete Gust and Power Spectral Treatment of Atmospheric Turbulence*," Proceedings of the RAS/CASI/AIAA Conference on Atmospheric Turbulence, Royal Aerospace Society, London, Paper No. 41, 1971.

Jones, J. G., "*Statistical-Discrete-Gust Method for Predicting Aircraft Loads and Dynamic Response*," Journal of Aircraft, Vol.26, April 1989.

Jones, J.G., Foster, G.W., Earwicker, P.G., "*Wavelet Analysis of Gust Structure in Measured Atmospheric Turbulence Data*," Journal of Aircraft, Vol.30, No.1, Jan-Feb, 1993.

Judd, M., Newman, S.J., "*An Analysis of Helicopter Rotor Response due to Gusts and Turbulence*", Vertica, Vol. 1, pp 179-188, 1977.

Kaminer, I., Khargonekar, P.P., Robel, G., "*Design of Localiser Capture and Track Modes for a Lateral Autopilot Using H-Infinity Synthesis*", IEEE Control Systems Magazine, 1990.

Kessler, Ch., Reichert, G., '*Active Control to Augment Rotor Lead-Lag Damping*', 22nd European Rotorcraft Forum, Brighton, UK, Sept. 1996.

Kolmogorov, A., N., "*Local Structure of Turbulence in an Incompressible Liquid for Very Large Reynolds Numbers*," Comtes Rendus (Doklady) de l'Academie des Sciences de l'URSS, Vol. 30, 1941, pp. 299-303.

Kuethe, A.M., Chow, C.Y., "*Foundations of Aerodynamics, Bases of Aerodynamic design*", John Wiley & Sons, 1986.

Kwakernaak, H., "*Robust Control and H_∞ Optimisation – Tutorial Paper*", Automatica, Vol. 29, No. 2, 1993.

Lehmann, G., '*The Effect of Higher Harmonic Control (HHC) on a Four Bladed Hingeless Model Rotor*', Vertica, Vol. 9, No. 3, 1985.

Lightbody, G., Wu, Q.H., Irwin, GH.W., '*Control applications for feedforward networks*', Neural Networks for Control and Systems, Pergammon Press, 1992.

Lin, K.C., Lu, P., Smith, M., "*The Numerical Errors in Inverse Simulation*", AIAA-93-3588-CP, 1993.

Loewy, R.G., "*A two dimensional approximation to the unsteady aerodynamics of rotary wings.*", C.A.L. Report No. 75, 1955.

Low, E., Garrard, W.L., "*Design of Flight Control Systems to meet Rotorcraft Handling Qualities Specifications*", Journal of Guidance, Control & Dynamics, Vol. 16, No. 1, January-February 1993.

Lynn, R.R., "*Dynamic Absorbers in the Rotating System of Helicopters.*", Journal of the American Helicopter Society, October 1960.

Madhavan, R., Gaonkar, G.H., "*Effects of Rotating Frame Turbulence and Dynamic Stall on Gust Response of Helicopter Blades*", Fifteenth European Rotorcraft Forum, September 1989, Amsterdam, paper No. 40.

McCloud, J.L, '*The Promise of Multicyclic Control*', Vertica Vol. 4, 1980.

McKillip, R.M., '*Periodic Control of the Individual-Blade-Control Helicopter Rotor*', Vertica, Vol. 9, No. 2, pp. 199-225, 1985.

Molusis, J.A., Hammond, C.E., Cline, J.H, '*A Unified Approach to the optimal Design of Adaptive and Gain Scheduled Controllers to Achieve Minimum Helicopter Rotor Vibration*', Journal of the American Helicopter Society, April 1983.

Munson, B.R., Young, D.F., Okiishi, T.H., "*Fundamentals of Fluid Mechanics*", John Wiley and Sons, 1990.

Murphy, I.S., '*Advanced Calculus for Engineering and Science Students: Third edition*', Arklay Publishers, 1989.

Napolitano, M.R., Kincheloe, M., "*On-line Learning Neural-Network Controllers for Autopilot Systems*", Journal of Guidance, Control and Dynamics, Vol. 33, No. 6, Nov.-Dec., 1995.

Newman, S., "*The Foundations of Helicopter Flight*", Edward Arnold, 1994.

Narendra, K.S., Parthasarathy, K., '*Identification and Control of Dynamical Systems Using Neural Networks*', IEEE Trans. Neural Networks, Vol. 1, No. 1, March, 1990.

Nguyen, D.H., Widrow, B., "*Neural Networks for Self-Learning Control Systems*", IEEE Control Systems Magazine, 1990.

O'Leary, J., Miao, W., '*Design of Higher Harmonic Control for the ABC*^{TM}', Journal of the American Helicopter Society, January 1982.

Paul, W.F., '*Development and Evaluation of the Main Rotor BIFILAR Absorber*', 25th Forum American Helicopter Soc., 1969.

Padfield, G.D., '*Helicopter Flight Dynamics*', Blackwell Science Ltd, 1996.

Pearson, J.T., Goodall, R.M., Lyndon, I., '*Active Control of Helicopter Vibration*', Computing and Control Engineering Journal, December 1994.

Peters, D.A., HaQuang, N., "*Dynamic Inflow for Practical Applications*", Journal of the American Helicopter Society, October 1988.

Pitt, D.M., Peters, D.A., "*Theoretical Prediction of Dynamic Inflow Derivatives*", Vertica, Vol. 5, pp. 21 to 34, 1981.

Press, W., Teukolsky, S.A., Vetterling, W.T., Flannery, B.P., "*Numerical Recipes in Fortran. The Art of Scientific Computing. Second Edition*", Cambridge University Press, 1992.

Prouty, R.W., "*Helicopter Performance, Stability and Control*", Robert E Kreiger Publishing Co, ISBN 0-89464-457-2, 1990.

Pototzky, A.S., Zeiler, T.A., Perry, B., "*Calculating Time-Correlated Gust Loads using Matched Filter and Random Process Theories*", Journal of Aircraft, Vol.28, May 1991.

Richter, P., Eisbrecher, H.-D., Klöppel, V., '*Design and First Tests of Individual Blade Control Actuators*', 16th European Rotorcraft Forum, 1990.

Reighert, G.,'*Helicopter Vibration Control-A Survey*', Vertica, Vol. 5, pp1-20, 1981.

Riaz, J., Prasad, J.V.R., Schrage, D.P., Gaonkar, G.H., "*Atmospheric Turbulence Simulation for Rotorcraft Applications*", Journal of the American Helicopter Society, January 1993.

Robinson, P.A., Reid, L.D., "*Modelling of Turbulence and Downbursts for Flight Simulators*", Journal of Aircraft, Vol. 27, August 1990a.

Robinson, P.A., Reid, L.D., "*Augmenting Flight Simulator Motion Response to Turbulence*", Journal of Aircraft, Vol. 27, August 1990b.

Rumelhart, D.E., Hinton, G.E., Williams, R.J., '*Learning internal representations by error propagation'*, In Parallel Distributed Processing: Explorations in the Microstructure of Cognition, Vol. 1, Chapter8, MIT Press, 1986.

Rutherford,S.,Thomson,D.G., "*Development of a Generic Inverse Simulation Algorithm*", University of Glasgow, Department of Aerospace Engineering, Internal Report No. 9410, July 1994.

Rutherford, S., Thomson, D.G., "*Helicopter Inverse Simulation Incorporating an Individual Blade Rotor Model*", Paper 3.6.3, ICAS Congress, Sorrento, Italy, September 1996.

Rutherford, S., "*Simulation Techniques for the Study of the Manoeuvring of Advanced Rotorcraft Configurations*", PhD Thesis Submitted to the Department of Aeronautical Engineering, University of Glasgow, March, 1997.

Sadhukhan, D., Feteih, S., "*F8 Neurocontroller Based on Dynamic Inversion*", Journal of Guidance, Control and Dynamics, Jan.-Feb., 1996.

Saito, S., Azuma, A., Nagao, M., "*Gust Response of Rotary Wing Aircraft and its Alleviation*", Vertica, Vol. 5, pp. 173-184, 1981.

Saito, S., '*Application of an Adaptive Blade Control Algorithm to a Gust Alleviation System*', Vertica, Vol. 8, No. 3, 1984.

Shaw, J., '*Higher Harmonic Blade Pitch Control for Helicopter Vibration Reduction: A Feasibility Study*', Massachusetts Institute of Technology S.M. Thesis, May 1967.

Shaw, J., Albion, N., '*Active Control of the Helicopter Rotor for Vibration Reduction*', Journal of the American Helicopter Society, July 1981.

Shaw, J., Albion, N., Hanker, E.J., Teal, R.S., '*Higher Harmonic Control: Wind Tunnel Demonstration of Fully Effective Vibratory Hub Force Suppression*', Journal of the American Helicopter Society, January 1989.

Shipman, D., '*Nodalisation Applied to helicopters*', SAE-Paper, 1973.

Shipman, D.P., White, J.A., Cronkhite, J.D., '*Fuselage Nodalisation*', Proc. 28th Forum American helicopter Soc., 1972.

Skogestad, S., Postlethwaite, I., '*Multivariable Feedback Control: Analysis and Design*', John Wiley and Sons, 1996.

Smollen, L.E., Marshall, P., and Gabel, R., "*Active Vibration Isolation of Helicopter Rotors.*", Journal of the American Helicopter Society, April 1962.

Stefani, R.T., Savant, C.J., Shahian, B., Hostetter, G.H., '*Design of Feedback Control Systems: third edition*', Saunders College Publishing, 1994.

Stevens, B.L., Lewis, F.L., '*Aircraft Control and Simulation*', J. Wiley and Sons, USA, 1992.

Tettenborn, G., Kessler, Ch., Reichert, G., '*Comparison of IBC with Active Controllers Using a Conventional Swashplate to Suppress Ground and Air Resonance*', Proceedings, 23rd European Rotorcraft Forum, Dresden, September 1997.

Thomson, D.G., "*A Documentation Note on the Helicopter Inverse Simulation Package: HELINV*", University of Glasgow, Department of Aerospace Engineering, Internal Report No. 8814, 1988.

Thomson, D.G., Bradley, R., "*Modelling and Classification of Helicopter Combat Manoeuvres*", Proceedings of ICAS Congress, Stockholm, Sweden, September 1990a.

Thomson,D.G. and Bradley,R., "*Prediction of the Dynamic Characteristics of Helicopters in Constrained Flight*", The Aeronautical Journal, December 1990b.

Thomson, D.G., Bradley, R., "*The Contribution of Inverse Simulation to the Assessment of Helicopter Handling Qualities*", Paper 7.3.2, Proceedings of the 19th ICAS Conference, Anaheim, U.S.A., September 1994.

Thomson, D.G., Talbot, N., Taylor, C., Bradley, R., Ablett, R., "*An Investigation of Piloting Strategies for Engine Failures During Takeoff from Offshore Platforms*", The Aeronautical Journal, January 1995.

Thomson, D.G.T., Bradley, R., "*The Principles and Practical Application of Helicopter Inverse Simulation*", Simulation, Practice and Theory, 1997.

Thompson, WT., '*Theory of Vibration with Applications: Third edition*', Prentice Hall, 1989.

Turnour, S. R., Celi, R., "*Modelling of Flexible Rotor Blades for Helicopter Flight Dynamics Applications*", Journal of the American Helicopter Society, January 1996.

Venkatesan,C., Udayasankar,A., '*Sensor Locations and Active Vibration Control in Helicopters*', 23rd European Rotorcraft Forum, Dresden, September 1997.

Verma, M., Jonckheere, E., '*L_∞-compensation with mixed sensitivity as a broadband matching problem*', Systems and Control letters, Vol. 4, 1984.

Webb, S.G., Calico,R.A., Wiesel,W.E., '*Time-Periodic Control of a Multiblade Helicopter*', Journal of Guidance, Vol. 14, No. 6, Nov-Dec. 1991.

Widrow, B., Hoff, M.E., '*Adaptive Switching Circuits*', IRE WESCON Convention record, 1960.

Wheatley, J.B., "*An Analytical and Experimental Study of the Effect of Periodic Blade Twist on the Thrust, Torque and Flapping Motion of an Autogyro Rotor*". NACA TR 591, 1937.

Zames, G., '*Feedback and Optimal Sensitivity: Model reference transformations, weighted seminorms and approximate inverses*', Proc. 17th Allerton Conf., 1979.

Zvara, J., Ham, N.D., "*Helicopter Rotor Model Research at Massachusetts Institute of Technology.*" Journal of the American Helicopter Society, January 1960.